

# Hard X-ray spectro-polarimetric study of black hole binary Cygnus X-1

A thesis submitted in partial fulfillment of  
the requirements for the degree of

**Doctor of Philosophy**

*by*

**Abhay Kumar**

(Roll No. 17330002)

Under the supervision of

**Dr. Santosh V. Vadawale**

Professor

Astronomy and Astrophysics Division

Physical Research Laboratory, Ahmedabad, India.



DEPARTMENT OF PHYSICS

INDIAN INSTITUTE OF TECHNOLOGY GANDHINAGAR

2022



to  
*my family*



# DECLARATION

I declare that this written submission represents my ideas in my own words and where others' ideas or words have been included, I have adequately cited and referenced the original sources. I also declare that I have adhered to all principles of academic honesty and integrity and have not misrepresented or fabricated or falsified any idea/data/fact/source in my submission. I understand that any violation of the above will be cause for disciplinary action by the Institute and can also evoke penal action from the sources which have thus not been properly cited or from whom proper permission has not been taken when needed.

**Abhay Kumar**

(Roll No: 17330002)

Date:



# CERTIFICATE

It is certified that the work contained in the thesis titled “**Hard X-ray spectro-polarimetric study of black hole binary Cygnus X-1**” by **Abhay Kumar** (Roll no: 17330002), has been carried out under my supervision and that this work has not been submitted elsewhere for degree.

I have read this dissertation and in my opinion, it is fully adequate in scope and quality as a dissertation for the degree of Doctor of Philosophy.

**Dr. Santosh V. Vadawale**  
(Thesis Supervisor)

Professor  
Astronomy & Astrophysics Division  
Physical Research Laboratory  
Navarangpura, Ahmedabad, India

Date:



---

## Acknowledgements

*I convey my sincere gratitude to my supervisor Prof. Santosh Vadawale for his support and advises which has helped me evolve as an independent researcher. I am grateful to my collaborators - Dr. Tanmoy Chattopadhyay, Prof. A.R. Rao, Dipankar Bhattacharya, and CZTI team for the fruitful discussions and ideas that have enriched my knowledge. I acknowledge the members of the doctoral studies committee Dr. Shashikiran Ganesh, Dr. Aveek Sarkar, and Dr. Kinsuk Acharyya for the useful suggestions during the half-yearly meetings. I wish to thank Prof. Sachindra Naik, Prof. Raghavan Rangarajan, and Dr. Mudit Srivastava for the stimulating lectures during the course work. I am deeply thankful to Neeraj, Alka, Sushant, and Vipin for proof reading this thesis. I am grateful to my seniors - Tanmoy Chattopadhyay and Sandeep Rout for continuous support throughout this journey. Tanmoy's supervision during the most challenging phase of my PhD was invaluable. He fostered a sense of comfort and consistently upheld my confidence, never allowing me to doubt my abilities. I convey my regards to all friends and acquaintances in PRL for the good times spent together and helping me when needed. I take this opportunity to thank my batchmates and friends outside the PRL who had directly and indirectly helped me achieved this goal. I would also like to thank my mentor from Dr. Bhimrao Ambedkar University, Agra, Prof. Surekha Tomar, who originally sparked my interest in research and encouraged me to pursue it. I am also thankful to all my teachers for teaching me not only the academic subjects but also the important lessons in life. Lastly, I am grateful to my family for always being supportive.*



---

# Abstract

The study of astrophysical sources is done with the help of electromagnetic radiation emitted by them, starting from  $\gamma$  rays to radio. In the X-ray sky, black hole binaries are one of the most peculiar astrophysical sources to understand the physics in the extreme conditions such as strong gravity, high temperature, and magnetic field. Black hole X-ray binaries are the binary systems in which the primary is a black hole and the secondary is a normal star. The black holes are the region of space time from where even light can not escape. It is very challenging to study black hole because we do not get any radiation directly from it. It is mostly studied through the radiation emitted from the surrounding environment which is under its gravitational influence. Accretion of matter onto black hole gives rise to X-rays along with other wavelengths to study their properties. The typical geometry of accreting environment around the black hole is based on spectroscopic and timing studies.

The X-ray spectrum of a black hole binary consists of three main spectral components: thermal emission from the disk, power law continuum emitted as a result of inverse Comptonization of the thermal disk (or seed) photons from an optically thin medium of electrons (known as corona or Compton cloud), and the emission resulting from the reflection of the continuum photons hitting the disk. It is generally accepted that corona is responsible for the power law emission. However, the composition and geometry of the corona are still unclear. Different competing models have been developed based on timing and spectroscopic observations which successfully produce the powerlaw and other variability properties. Some of the geometries that have been incorporated are spherical, sandwich or slab, lamp post etc., but there is no general consensus on any of them. To break this degeneracy, X-ray polarisation studies can play a vital role. The degree of polarisation and the polarisation angle are the two additional observables that can help in the discrimination between different models. Astrophysical sources exhibit polarisation primarily as a result of scattering and synchrotron emission, which are determined by the geometry, magnetic field strength, and structure of the source.

In order to understand the geometry of the corona and the emission mechanism, we have studied black-hole binary Cygnus X-1 using X-ray spectroscopy timing and polarisation analysis as primary tools. Cygnus X-1 is a galactic black hole binary comprising a black hole of mass  $\sim 21 M_{\odot}$  that accretes from the companion supergiant star (O9.7 type) with a mass of 40.6 solar mass. Its brightness and proximity (distance  $\sim 2.22$  kpc) have made it an obvious choice of study by different instruments. It has been extensively studied using spectroscopy and timing analysis techniques in a wide energy range, but X-ray polarisation analysis remains mostly unexplored due to the requirement of relatively longer exposure times and instrumental limitations. In this thesis, we have used *AstroSat* -CZTI data to study Cygnus X-1. The CZT detectors are of 5 mm thickness and hence have good efficiency for Compton interactions (double pixel events) beyond 100 keV, which are utilized for the polarisation study using CZTI in 100 to 380 keV. We explore the utility of polarisation double pixel events to do spectroscopy above 100 keV. We have used Crab observations, which is the standard calibration source in the X-ray sky, to refine the background selection and subtraction techniques. We get consistent hard X-ray flux and spectral index for Crab, which validates our techniques. We have also used *AstroSat* -LAXPC and SXT observations for the broadband spectroscopy. We have tried to comprehend the emission mechanism and geometry of the corona in Cygnus X-1 with the spectro-polarimetric study in the broad energy range of 1 - 380 keV. We further investigate the different hard X-ray spectral states in Cygnus X-1 and its polarisation dependence. For this, we measure the flux and spectral index in the 22 – 100 keV energy band and the short-term spectral and flux correlation index. We have identified distinct accretion modes in the source based on the hard X-ray data, consistent with the recent *INTEGRAL* results and its polarisation dependence.

We have discussed the implications of these results to understand the coronal geometry of the source and corona/jet contribution in the polarisation. Further, we show the necessity of the Compton spectro-polarimeter below 100 keV to get a complete picture of the source geometry and the emission mechanism. We provide a conceptual design of a Compton spectro-polarimeter and

characterized the absorber's position sensitivity, which detects the scattered photons coming from the scatterer.

**Keywords:** Cygnus X-1, black hole, X-ray polarisation, Compton spectro-polarimeter



---

# List of Publications

## Publications included in the thesis

1. **Kumar, A.**, Chattopadhyay, T., Vadawale, S.V. et al. “Exploring sub-MeV sensitivity of AstroSat–CZTI for ON-axis bright sources”. *J Astrophys Astron* 42, 67,2021. doi: <https://doi.org/10.1007/s12036-021-09711-9>
2. **Kumar, A.**, Chattopadhyay, T., Vadawale, S. V., et al., “Extending the energy range of *AstroSat*-CZTI up to 380 keV with Compton Spectroscopy”, *Monthly Notices of the Royal Astronomical Society*, 2022;, stac2466. doi: <https://doi.org/10.1093/mnras/stac2466>
3. Chattopadhyay, T., **Kumar, A.**, Rao, A. R., Bhargava, Yash, Vadawale, S. V., et al. 2023, “High hard X-ray polarization in Cygnus X-1 confined to the intermediate hard state: evidence for a variable jet component”, arXiv e-prints, arXiv:2306.04057
4. **Kumar, A.**, Chattopadhyay, T., Vadawale, S. V., et al. 2023, “Long-term hard X-ray spectral states dependence of polarisation in Cygnus X-1” (under preparation)
5. **Kumar, A.**, Vadawale, S. V., Chattopadhyay, T., et al. 2023, “Development of a position sensitive absorber for a focal plane Compton X-ray polarimeter (CXPOL)” (to be submitted)

## Additional publications not included in the thesis

6. Chattopadhyay, T., Gupta, S., Sharma, Vidushi, Iyyani, Shabnam, Ratheesh, Ajay, Mithun, N. P. S., Aarthy, E. Palit, Sourav, **Kumar, A.**, et al. 2021, “Sub-MeV spectroscopy with AstroSat-CZT Imager for Gamma Ray Bursts”, *J Astrophys Astron* 42, 82 (2021). doi: <https://doi.org/10.1007/s12036-021-09718-2>

7. Chattopadhyay, T., Gupta, S., Iyyani, Shabnam, Saraogi, Divita, Sharma, Vidushi, Tsvetkova, Anastasia, Ratheesh, Ajay, Gupta, Rahul, Mithun, N.P.S., Vaishnava, C. S., Prasad, Vipul, Aarthy, E., **Kumar, A.** et al. 2022, “X-ray polarization catalog for a 5-year sample of Gamma Ray Bursts using AstroSat CZT-Imager”, *The Astrophysical Journal*, 936(1), 12 (2022). doi: <https://doi.org/10.3847/1538-4357/ac82ef>

# Contents

<b>Abstract</b>	<b>iii</b>
<b>List of Publications</b>	<b>vii</b>
<b>List of Figures</b>	<b>xv</b>
<b>List of Tables</b>	<b>xxv</b>
<b>1 Introduction</b>	<b>1</b>
1.1 X-ray binaries . . . . .	1
1.1.1 Classification of X-ray binaries . . . . .	2
1.1.2 Accretion onto compact objects . . . . .	3
1.1.3 Astrophysical black holes . . . . .	6
1.2 Astrophysical emission mechanisms . . . . .	8
1.2.1 Blackbody radiation . . . . .	9
1.2.2 Bremsstrahlung . . . . .	10
1.2.3 Cyclotron and synchrotron radiation . . . . .	11
1.2.4 Curvature radiation . . . . .	12
1.2.5 Compton scattering . . . . .	12
1.3 Variability of black hole X-ray binaries . . . . .	13
1.3.1 Long-term variability . . . . .	13
1.3.2 Medium time variability . . . . .	15
1.3.3 Rapid variability . . . . .	16
1.3.4 Spectral components of black-hole binaries . . . . .	17
1.3.4.1 Thermal disk . . . . .	17
1.3.4.2 Comptonisation . . . . .	19

1.3.4.3	Reflected emission . . . . .	20
1.3.5	State classification . . . . .	23
1.3.5.1	X-ray properties . . . . .	23
1.3.5.2	Radio properties . . . . .	26
1.4	X-ray polarisation . . . . .	27
1.4.1	Polarisation in accreting black holes . . . . .	29
1.4.1.1	Black hole spin . . . . .	30
1.4.1.2	Geometry of the corona . . . . .	31
1.4.1.3	Lamp post corona model . . . . .	34
1.4.1.4	Extended corona model . . . . .	35
1.5	Cygnus X-1 overview . . . . .	36
1.5.1	Accretion . . . . .	39
1.5.2	Previous polarisation measurements . . . . .	40
1.6	Thesis outline . . . . .	41
<b>2</b>	<b>Instrumentation and data analysis</b>	<b>45</b>
2.1	Instrumentation . . . . .	45
2.1.1	X-ray detectors . . . . .	46
2.1.2	X-ray observatories . . . . .	48
2.1.2.1	<i>AstroSat</i> . . . . .	48
2.1.2.2	Other X-ray observatories . . . . .	51
2.2	Spectral analysis . . . . .	55
2.2.1	X-ray data fitting . . . . .	55
2.2.2	Data reduction . . . . .	56
2.2.3	Spectral models . . . . .	57
2.2.3.1	Empirical models . . . . .	57
2.2.3.2	Absorption models . . . . .	58
2.2.3.3	Thermal disk models . . . . .	59
2.2.3.4	Comptonisation models . . . . .	59
2.2.3.5	Reflection models . . . . .	60
2.3	Temporal analysis . . . . .	60
2.4	Polarisation measurement in X-rays . . . . .	62

2.4.1	X-ray polarisation measurement techniques . . . . .	65
2.4.1.1	Bragg reflection polarimetry . . . . .	66
2.4.1.2	Photo-electric polarimetry . . . . .	68
2.4.1.3	Scattering polarimetry . . . . .	69
2.4.2	Hard X-ray polarimetry using <i>AstroSat</i> /CZTI . . . . .	71
2.4.2.1	Compton event selection . . . . .	72
2.4.2.2	Background selection . . . . .	72
2.4.2.3	Background subtraction . . . . .	73
2.4.2.4	Geometric correction . . . . .	74
2.4.2.5	Polarisation estimation . . . . .	75
<b>3</b>	<b>Hard X-ray polarisation measurement of Cygnus X-1 with</b>	
	<b><i>AstroSat</i>-CZTI</b>	<b>77</b>
3.1	Introduction . . . . .	77
3.2	Observations . . . . .	78
3.3	Analysis method . . . . .	81
3.3.1	Estimation of polarisation fraction and polarisation angle . . . . .	81
3.3.1.1	Modulation curve fitting method . . . . .	81
3.3.1.2	Polarisation estimation using MCMC simulations . . . . .	83
3.3.2	Estimation of polarisation upper limit . . . . .	85
3.4	Results and discussions . . . . .	86
3.5	Summary . . . . .	94
<b>4</b>	<b>Extending the energy range of <i>AstroSat</i>-CZTI up to 380 keV</b>	
	<b>with Compton spectroscopy using Crab</b>	<b>95</b>
4.1	Exploring sub-MeV sensitivity . . . . .	95
4.1.1	Observations and analysis procedure . . . . .	97
4.1.1.1	Single and Compton event selection . . . . .	100
4.1.1.2	Background subtraction: Phase match method . . . . .	101
4.1.1.3	Spectral response . . . . .	104
4.1.2	Results: Single and Compton event spectra (PE and CS) . . . . .	106
4.1.3	Discussion . . . . .	107
4.2	Compton spectroscopy excluding low gain pixels . . . . .	110

4.2.1	Observations . . . . .	111
4.2.1.1	Crab observations . . . . .	111
4.2.1.2	Background observations . . . . .	114
4.2.2	Analysis procedure . . . . .	114
4.2.2.1	Selection of single-pixel and 2-pixel Compton events	114
4.2.2.2	Data cleaning for short-term variation in data . .	116
4.2.2.3	Selection of background for Compton spectroscopy	117
4.2.2.4	Exposure correction in background due to long-term variation in data . . . . .	121
4.2.2.5	Generation of the Compton spectra . . . . .	122
4.2.3	Results . . . . .	123
4.2.3.1	Spectroscopic sensitivity of CZTI in 100 - 380 keV	127
4.2.4	Discussion . . . . .	127
4.3	Summary . . . . .	131
<b>5</b>	<b>Dependence of hard X-ray polarization on spectral states in Cygnus X-1</b>	<b>133</b>
5.1	Introduction . . . . .	133
5.2	Observations . . . . .	135
5.3	Spectral state determination . . . . .	135
5.3.1	Spectral analysis . . . . .	135
5.3.2	Timing analysis . . . . .	140
5.4	Spectral state dependence of polarisation . . . . .	143
5.5	Broad band spectroscopy . . . . .	143
5.6	Discussion . . . . .	148
5.7	Summary . . . . .	149
<b>6</b>	<b>Focal plane hard X-ray Compton spectro-polarimeter</b>	<b>151</b>
6.1	Introduction . . . . .	151
6.2	Compton polarimeter . . . . .	152
6.3	Compton spectro-polarimeter . . . . .	154
6.3.1	Proposed detector configuration . . . . .	155

---

6.3.2	Analytical calculation of modulation factor, efficiency and spectroscopic sensitivity . . . . .	160
6.4	Characterisation of position sensitive absorber - based on the NaI(Tl) - scintillator and SiPM arrays . . . . .	165
6.4.1	Characterisation setup . . . . .	166
6.4.2	Readout electronics . . . . .	167
6.4.3	Data analysis . . . . .	168
6.4.4	Results . . . . .	169
6.4.4.1	Measurement of the position of individual X-ray photons . . . . .	169
6.4.4.2	Measurement of energy . . . . .	169
6.4.4.3	NaI(Tl) background . . . . .	172
6.5	Comparison with the other upcoming missions . . . . .	173
6.6	Discussion and summary . . . . .	175
<b>7</b>	<b>Summary and scope for future work</b>	<b>177</b>
7.1	Summary . . . . .	177
7.2	Future work . . . . .	180



# List of Figures

1.1	A schematic of a typical low-mass black-hole binary showing accretion through Roche-lobe overflow. The important components of the system are labelled. Credits: Rob Hynes . . . . .	3
1.2	From top to bottom: The long term lightcurves of two HMXBs - Cyg X-1 and LMC X-3, and three LMXBs - 4U 1630-472, GX 339-4, and GRS 1716-249 observed with <i>MAXI</i> . . . . .	14
1.3	The long term lightcurve of EXO 2030+375 observed with RXTE/ASM. The Type II outburst are rare and Type I is always present . . . . .	16
1.4	The different types of power-density spectra observed in black-hole binaries during various states (Belloni, 2010a). . . . .	18
1.5	The formation of a thermal Comptonisation spectrum by repeated scattering. (Done, 2010) . . . . .	19
1.6	The formation of a non-thermal Comptonisation spectrum from a single (or at most two) scattering. (Done, 2010) . . . . .	20
1.7	Left panel: Dependence of photoelectric absorption and electron scattering cross-sections with energy. Right panel: Reflected spectrum for different ionization states. The different colors represent the different ionization states of the absorbing material (Done, 2010). . . . .	21
1.8	Top panel shows the a typical HID from a BHB outburst. Bottom panel shows the HRD. Courtesy: (Belloni & Motta, 2016) . . . . .	23

1.9	The absolute rms-intensity diagram for GX 339-4 observed during three epochs. The fractional rms levels are represented by dotted lines (Muñoz-Darias et al., 2011) . . . . .	25
1.10	Hardness-intensity diagram for a black hole with labels indicating the radio properties (Belloni et al., 2011) . . . . .	27
1.11	Lamp post vs Extended corona geometry . . . . .	32
1.12	Top to bottom: Schematic diagram of spherical, sandwich and clumpy corona geometry. Credits: Dovčiak et al. (2012); Schnittman & Krolik (2010); Malzac (2018) . . . . .	32
1.13	Polarisation parameters for different geometry of the extended corona. The solid line is for the total observed flux, dashed lines represents the thermal disk contribution and the dot-dashed lines represents the corona-scattered photons. Credits: Schnittman & Krolik (2010) . . . . .	33
1.14	Polarisation parameters for the different height of the corona. The solid lines is for the Schwarzschild black hole and the dashed line represents the Kerr black holes. Credits: Dovčiak et al. (2011, 2012)	34
1.15	Polarisation parameters for the different inclination of the disk. The solid lines is for the Schwarzschild black hole and the dashed line represents the Kerr black holes. For Kerr black hole the lamp post height can be lower because its event horizon is at $1R_g$ while it is $2R_g$ for the Schwarzschild black hole. Credits: Dovčiak et al. (2011, 2012) . . . . .	35
1.16	HID of Cygnus X-1 (gray circles) for all the RXTE/PCA observations overplotted on the HID of the transient black hole LMXB GX 339-4 (black circle) of the 2002/2003 and 2004/2005 outbursts. The histogram shows the distribution of hardness. Credits: Belloni (2010b) . . . . .	38
1.17	Spectrum of Cygnus X-1 for different accretion states. Credits: McConnell et al. (2002); Jourdain et al. (2012b) . . . . .	39

2.1	The <i>AstroSat</i> observatory. Image courtesy: <a href="https://webapps.isisdc.gov.in/astro/\$archive/archive/Home.jsp">https://webapps.isisdc.gov.in/astro/\$archive/archive/Home.jsp</a> . . . . .	50
2.2	The <i>AstroSat</i> observatory. Image courtesy: <a href="https://www.cosmos.esa.int/web/integral/mission-overview">https://www.cosmos.esa.int/web/integral/mission-overview</a> . . . . .	52
2.3	The <i>Swift</i> observatory. Image courtesy: <a href="https://www.swift.ac.uk/about/instruments.php">https://www.swift.ac.uk/about/instruments.php</a> . . . . .	53
2.4	Schematic view of the NuSTAR observatory in the stowed (bottom) and deployed (top) configurations. The figure is taken from Harrison et al. (2013) . . . . .	54
2.5	The schematic diagram of the X-ray spectrum for a black-hole binary. The blue, red, and green curves represent the thermal disk, Comptonisation, and reflected components respectively. The black curve shows the total spectrum. (Figure courtesy: Gilfanov, 2010) . . . . .	58
2.6	The four steps followed during calculation of power spectrum. Courtesy: Stefano Rapisarada . . . . .	61
2.7	The photon interaction probability at different energy for 5 mm thick Silicon. Different colors represent different interactions as mentioned in the figure . . . . .	66
2.8	Bragg reflection. $d\sin\theta$ is the difference in path length between two waves, $d$ is the crystal plane spacing, $\theta$ is angle of incidence and $\lambda$ is photons wavelength. . . . .	67
2.9	Photo-electron angular distribution due to interaction of linearly polarised photon with the atom. Photo-electron preferentially ejected along the direction of the electric field vector of the incident photon. $\theta$ is the emission angle with respect to the incident direction of the photon and $\phi$ is the angle relative to the electric field vector of the photon. . . . .	69
2.10	The schematic diagram of a Compton polarimeter. . . . .	70

- 3.1 Cygnus X-1 all the observations overplotted on the BAT light curve in 15 - 50 keV. Blue horizontal dashed line represents BAT count rate ( $0.11 \text{ Counts s}^{-1} \text{ cm}^{-2}$ ) which corresponds to  $\sim 500$  mCrab. The green vertical lines represents the observations having exposure greater than 50 ks and the red color vertical lines shows the observations having exposure below 50 ks. The green full vertical lines represents all the observations selected for the analysis having exposure greater than 50 ks and BAT flux  $> 500$  mCrab . . . . . 79
- 3.2 Top panel shows the light curves of Cygnus X-1 (ObsId 4646, one of the segment of the full observation) on the left and background (ObsId 2210) on the right, both fitted with fifth degree polynomials (red curve for Crab and green curve for background). Bottom left figure shows the variation of  $\chi^2$  as a function of shift in the Cygnus X-1 light curve with respect to the background, to determine the time for ‘phase matching’. Bottom right figure shows the ‘phase matched’ background and Cygnus X-1 polynomials, in the green curve and red, respectively. The blue curve represents the background where Cygnus X-1 observation is available. . . . . 83
- 3.3 Modulation curve for ID 2992. Top left: posterior probability distribution for polarisation degree from MCMC iterations. Top right: the modulation curve and the sinusoidal fit shown in solid blue line, along with 100 random MCMC iterations. Bottom left: the contour plot for polarisation angle and degree for 68, 95 and 99% confidence levels. Bottom right: posterior probability distribution for polarisation angle from MCMC iterations. . . . . 87
- 3.4 Top to bottom: Cygnus X-1 polarisation results for ID 0426, ID 0436, ID 0456, ID 4492 in 110 - 380 keV energy band. The left figure shows the modulation curve and the right figure shows the contour plot. . . . . 91

- 3.5 Top to bottom: Cygnus X-1 polarisation results for ID 4638, ID 4646, and ID 4678 in 100 - 380 keV energy range. The left figure shows the modulation curve and the right figure shows the contour plot. . . . . 92
- 3.6 Top panel: Cygnus X-1 polarisation results for ID 2992 for the full energy range of 100 - 380 keV (shown in green band), 100 - 175 keV (PF < 15%), 175 - 230 keV (PF-26±6%, PA-228±12°) and 230 - 380 keV (PF-39±9%, PA-239±11°). The red line shows the respective MDP values. The bottom panel shows the polarisation angle in sky (North to East in an anti-clockwise direction) . . . . 93
- 4.1 Top panel shows the light curves of Crab (ObsId 96) on the left and background (ObsId 276) on the right, both fitted with fifth degree polynomials (red curve for Crab and green curve for background). Bottom left figure shows the variation of  $\chi^2$  as a function of shift in the Crab light curve with respect to the background, to determine the time for ‘phase matching’. Bottom right figure shows the ‘phase matched’ background and Crab polynomials, in the green curve and red, respectively. The blue curve represents the background where Crab observation is available. . . . . 102
- 4.2 The top figure shows the phase matched 2-event Compton spectra (CS) of the blank sky observation UB (red) and background CB (blue) from 100 keV to 500 keV. The ratio of the two spectra is shown in the middle panel and the residuals of the two are shown in the bottom panel. . . . . 103
- 4.3 Broadband spectra of Crab (ObsID 406, 114 ks) fitted with a broken power law. The black, red colors are used for PE, and CS respectively. . . . . 107

- 4.4 Best fit parameter of all the selected observations obtained after simultaneous fitting of PE and CS using broken power law model. Red diamonds represent higher energy slope (*PhoIndx2*) and the blue squares represent low energy slope (*PhoIndx1*). The dashed-dot horizontal lines represent the INTEGRAL value of *PhoIndx1* (blue) and *PhoIndx2* (red) in the corresponding energy regime. . . . . 108
- 4.5 Corner plot of the *phoIndx2* versus *Norm* for all the five ObsIDs plotted together for PE and CS. Different colors of contours represents different observations as shown in legend. The peak value of the *PhoIndx2* is  $2.04^{+0.48}_{-0.44}$  and the *Norm* is  $6.39^{+0.71}_{-0.63}$  . . . . . 109
- 4.6 Estimated flux of the selected observations after fitting PE and CS simultaneously using broken power law . The blue diamond represents the CZTI value of the Crab flux. The dashed-dot horizontal line represent the INTEGRAL value of the Crab flux in the corresponding energy band. . . . . 110
- 4.7 Crab observation times are plotted against MJD. Blue, red and green color represents PV phase observations, observations having exposure less than 30 ks and above 30 ks, respectively. . . . . 112
- 4.8 Crab observations distribution having exposure greater than 30 ks. 'Good' observations (15) are those after excluding the PV phase (6) and noise dominated observations (2). . . . . 112
- 4.9 Background selection flow chart. Total CZTI observations till 2020 is 2025 (shown in red). After applying the RA, DEC and exposure conditions, 27 are selected (shown in the 3rd box). Further, excluding PV phase observations resulted in 23 observations (shown in the 5th box). Finally, after applying the BAT flux criterion gives 16 blank sky observations as shown in the last box. . . . . 115
- 4.10 Crab spectral analysis flow chart. The red box shows the initial conditions for selecting 15 source regions and 16 background regions. The blue box is for the process, the green rectangular box represents the source outputs, and the green parallelograms represent the background outputs. . . . . 115

4.11	Light curve of the blank sky observation for Crab background (obsId: 2712). From top to bottom, the blue color represents raw light curve with SAA and earth-occultation cuts. The yellow box at the top right corner shows the zoom-in view of one of the orbits. The red light curve is after applying the longitudinal cuts and veto cuts. . . . .	118
4.12	Spectral hardness using a straight line fit in 70 to 190 keV . . . .	119
4.13	Longitudinal variation of the hardness of the Crab and background. Blue is Crab (obsId: 2472) and red is blank sky observation (obsId: 2712) . . . . .	119
4.14	Bottom panel: correlation between the source and background longitudinal hardness variation for different Crab and blank sky background observations. Top panel: standard deviation of the difference in the longitudinal hardness of the source and blank sky backgrounds having a correlation above 0.8. Each colour in the colour bar represents a different source observation. . . . .	120
4.15	Mask weighted and Compton background count rate variation with MJD. The blue line with filled circles represents the Compton background (right hand side scale). The black line with filled circles represents the mask weighted background (left hand side scale). . . . .	122
4.16	Broadband spectra of Crab (ObsID 2368, 49 ks) fitted with a broken power law. Blue and red colors are used for PE and CS, respectively. . . . .	123
4.17	PhoIndx vs ObsId plot. Blue and red colors are used for PhoIndx1 and PhoIndx2, respectively, and the dashed line represents the <i>INTEGRAL/SPI</i> reported values. . . . .	124
4.18	Norm vs ObsId. Blue and red colors are used for PE and CS, respectively. The dashed lines represent the mean values. . . . .	125
4.19	Residual plots of remaining observations (14). The blue and red colours are used for PE, and CS residuals, respectively. The ObsID is shown at the center of each panel. . . . .	129

4.20	CZTI Compton sensitivity for $3\sigma$ detection of any source with a flux level above a particular value. Different colors represent different exposures, and dashed lines represent different crab flux levels. . . . .	130
5.1	Cygnus X-1 flux and spectral index distribution for the eight observations obtained from the spectral fitting of CZTI observation.	136
5.2	Density map of the spectral index vs flux. The color coding represents the logarithm of number of the data points within an area (ellipse shown above the color bar) around a given pixel. The horizontal dashed line represents the separation between the hard and soft regime. The vertical dashed lines separates the six plasma states. Rectangular regions: The two examples of the estimation of the density gradient within the soft state using the rectangular regions (for details see Lubiński et al. (2020)). This figure is taken from the Lubiński et al. (2020) . . . . .	137
5.3	Radio flux vs spectral index variation for the six different plasma states (for details see text). This figure is taken from the Lubiński et al. (2020) . . . . .	138
5.4	Cygnus X-1 spectral states based on power law index and flux correlation. Identified spectral state is mentioned following observation ID in the legend . . . . .	139
5.5	The spectral index variation with time for observation ID 4492 (blue color) and ID 4646 (orange color). . . . .	140
5.6	PDS for four representative cases are shown. The observation ID, spectral state and MJD of the observation are given at the top right corner of each panel. . . . .	141
5.7	Cygnus X-1 spectral index (30 - 100 keV) vs fractional rms in 0.1 to 20 Hz (3 - 80 keV) using LAXPC data are shown. Each color represents different observations and spectral states as shown in the legend. . . . .	142

5.8	Broad band spectral fitting of the ID 2992 using the LAXPC, SXT, and CZTI data. Top panel: The unfolded spectrum along with the individual model components. The dotted, solid, threedotdash, dashed, and twodotdash, respectively, the soft Comptonisation, thermal-disk, hard Comptonisation, reflection and powerlaw components (Model 3 below). Residuals for the models are shown in the second to fourth panel: Model 1 - <code>const*TBabs* (diskbb + pexriv+ nthComp)</code> ; Model 2 - <code>const*TBabs (diskbb + pexriv + nthComp + powerlaw)</code> ; Model 3 - <code>const*TBabs*(diskbb + pexriv + nthComp + nthComp + powerlaw)</code> . . . . .	145
6.1	Conceptual design of the spectro-polarimeter. NaI(Tl) scintillators are shown in green, SiPM array in grey and scatterer in orange color. Here 12 absorbers are shown, but for CXPOL like geometry, only 8 are required. . . . .	155
6.2	Schematic of the plastic scintillator scatterer readout by the SiPM array: One end readout is shown on left and readout along the length for the segmented or non-segmented scatterer on the right. . . . .	157
6.3	Energy deposition in the scatterer vs scattering angle for different incident energy photon. . . . .	157
6.4	Scattering geometry of the proposed spectro-polarimeter . . . . .	161
6.5	Top to bottom: Modulation factor, efficiency and figure of merit for the CXPOL like conceptual design. The green and red color represents values corresponding to the 1 keV and 2 keV threshold of the scatterer, respectively. . . . .	163
6.6	Energy resolution of the CXPOL like conceptual design. Different color represents different scattering angle. The value for the position and energy resolution of absorber is taken from the experiment. The scatterer position resolution is assumed to be equal to the size of the each segment of the scatterer. . . . .	165
6.7	Experimental setup for the position measurement . . . . .	167
6.8	Readout electronics schematic . . . . .	168

6.9	Gaussian fitted to the position histogram at different irradiation position and the FWHM of the same. . . . .	170
6.10	Gaussian fitted to ADC1+ADC2 histogram at different irradiation position and the energy resolution. Top panel represents two end readout plots and one end readout plots are shown in bottom panel.	171
6.11	Peak channel vs irradiation position. The right figure represents one end readout and the left figure represents two end readout . . .	171
6.12	Background counts per bin (binsize-2s) in SiPM array 1 (SiPM1) represented in orange color. Blue color represents other end of the scintillator (SiPM2) and green color represents the background in coincidence mode . . . . .	173
7.1	Scatterer energy threshold measurement mechanical setup CAD model. . . . .	182
7.2	Coincidence between the CdTe and the pulse generator experimental setup . . . . .	183
7.3	Readout electronics . . . . .	184
7.4	Flux and spectral index correlation overpotted with the expected polarisation fraction (blue solid line) variation in Cygnus X-1 . . .	185

# List of Tables

3.1	Details of the Cygnus X-1 and blank sky observations. The last four digits of the full observation ID (ObsID) will be used to identify the observation in the rest of the chapter. Cygnus RA: 299.59° and DEC: 35.20° . . . . .	80
3.2	Measured polarisation fractions (PF) and position angles (PA) for the Cygnus X-1 observations in (100 - 380 keV) energy range. . .	89
4.1	Summary of Crab and blank sky observations. Crab RA: 83.63° and DEC: 22.01° . . . . .	99
4.2	Comparison of fitted parameters between <i>INTEGRAL/SPI</i> and <i>AstroSat</i> for broken power law. The errors are reported for 90% confidence interval. The mean value of the parameters of all the observations for different combinations of data is mentioned in the bottom row of each block. . . . .	105
4.3	Summary of Crab and blank sky observations. . . . .	113
4.4	Predefined Veto cut threshold values. . . . .	117
4.5	Comparison of fitted parameters between <i>INTEGRAL/SPI</i> and <i>AstroSat</i> for broken power law. The errors are estimated for 90% confidence interval. * represents a frozen parameter. . . . .	126
5.1	List of all the observations used in this work. In the rest of the chapter, only the last four digits of the ObsIDs are mentioned for simplicity with ID as prefix. RA: 299.59° and DEC: 35.20°. . . . .	135

---

5.2	Flux and photon index obtained after the fitting of CZTI observation. <i>INTEGRAL</i> /ISGRI (Lubiński et al., 2020) values are shown for comparison. The errors are estimated for 90% confidence interval. Flux is in the units of $10^{-10}$ erg cm <sup>-2</sup> s <sup>-1</sup> . . . . .	138
5.3	Best fit parameter of Model 3. . . . .	147
5.4	Flux value for the power law and the nthcomp in the different energy ranges for the broadband fit. . . . .	148
6.1	Details of the scatterer and absorber along with scattering geometry.	158
6.2	Some important characteristics of the SensL (now OnSemi) MicroJ-series, KETEK and Hamamatsu SiPM at $V_{br+} \sim 2.5V$ . . .	159
7.1	Model parameter values. . . . .	187

# Chapter 1

## Introduction

### 1.1 X-ray binaries

X-ray binaries (XRBs) are one of the most luminous X-ray sources consisting two stars, a compact object (i.e., a black hole, a neutron star, or white dwarf) and its optical companion, both co-rotating around the common center of mass (Lewin & Livingston, 1995). Depending upon the nature of the compact object, the XRBs are categories into: (i) Black hole X-ray binary (BH-XRB) (ii) Neutron star X-ray binary (NS-XRB) and (iii) White dwarf X-ray binary (WD-XRB or CV i.e., Cataclysmic Variable) (Reig, 2011; Tan, 2021). These are some of the brightest X-ray sources in the sky. Typical luminosity of XRBs ranges from  $10^{34}$ – $10^{38}$  erg s<sup>-1</sup>, which could even exceed  $\sim 10^{41}$  erg s<sup>-1</sup> for Ultraluminous X-ray binary sources (ULXs; Kaaret et al. 2017). Such events could occasionally outshine the host galaxy, making XRBs as one of the brightest objects in the X-ray sky. The understanding of such bright X-ray sources was possible after the launch of first X-ray satellite UHURU which discovered 339 X-ray sources including two pulsating X-ray sources, Her X-1 and Cen X-3 (Forman et al., 1978). The observation of these sources showed X-ray eclipsing which leads to the recognition that these sources are in binaries.

### 1.1.1 Classification of X-ray binaries

X-ray binaries are broadly classified into two categories based on the nature of the companion star: low-mass (LMXB) and high-mass (HMXB). In LMXBs, the companion is a low-mass evolved star ( $< 2M_{\odot}$ , usually M or K spectral type), while in HMXBs the companion is a massive star ( $> 8M_{\odot}$ ). The process of mass transfer to the compact object is different in these two classes of X-ray binaries, which also have some observable effects. In LMXBs, mass transfer predominantly takes place by Roche-lobe overflow (see Figure 1.1). In this process, the companion/donor star first fills its Roche lobe owing to its evolutionary expansion due to the loss of angular momentum. Further, the matter starts to leak over the primary's Roche lobe through inner-Lagrangian point (Frank et al., 2002). Consequently, infalling matter spirals around the primary due to angular momentum gained from the orbital motion around the center of mass. The spiraling of the matter results in the spreading out of the matter in and out due to the transfer of angular momentum which is governed by viscous stress. This is a simplistic description for the formation of accretion disk around primary object. On the other hand, HMXBs accrete matter from the stellar wind of their massive companion stars. The typical mass loss rate of about  $10^{-6} - 10^{-5}M_{\odot}$  per year from the massive stars like O- or B-type star is a high enough (Puls et al., 2008). These winds travel with the escape velocity of their host stars which is of the order of a few thousand  $\text{km s}^{-1}$  and greatly exceed the local sound speed ( $\sim 10 \text{ km s}^{-1}$ ). Because of their supersonic speed, the gas pressure in the winds becomes less important. The gravitational potential energy of the particles dominates over the kinetic energy, when the wind particles pass close to the compact object, as a result particles get captured and accreted. Although accretion by this process is highly inefficient, the huge mass-loss rate more than compensates the inefficiency and provides enough matter to be accreted. These differences in mass transfer mechanism in the two systems have significant ramifications on the long term variability (see Section 1.3.1).

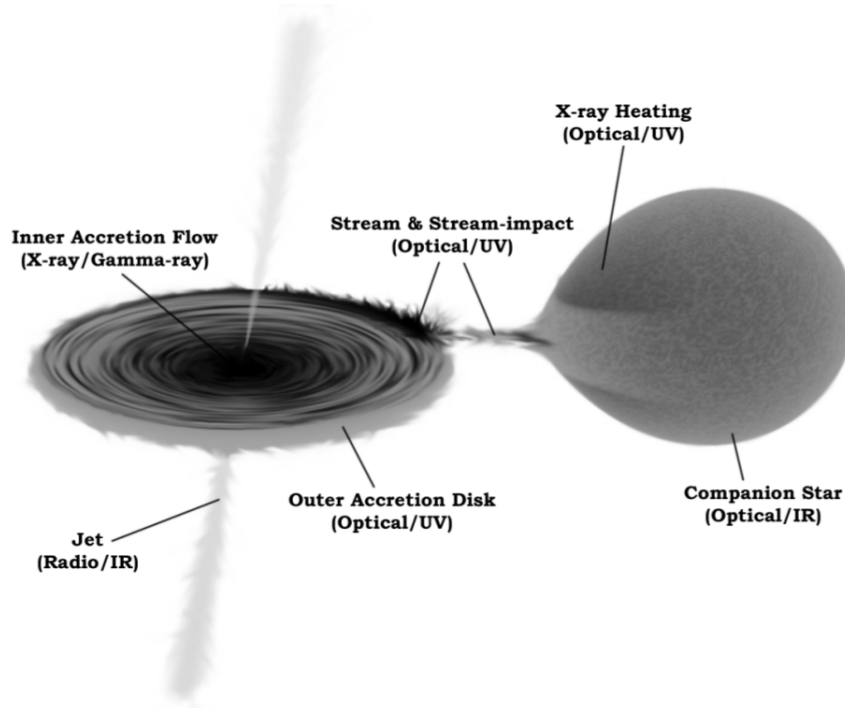


Figure 1.1: A schematic of a typical low-mass black-hole binary showing accretion through Roche-lobe overflow. The important components of the system are labelled. Credits: Rob Hynes

### 1.1.2 Accretion onto compact objects

Accretion is the process of accumulation of matter or gas with high angular momentum onto the gravitating body. The process of accretion got noticed after the discovery of X-ray binaries where it was proposed to explain the copious amount of X-ray flux. When the matter falls onto any object like a black hole or a neutron star, it spirals around the object by losing its angular momentum and transferring it to the outwards. The cause of loss in the angular momentum is viscosity, but the origin of the viscosity is unknown. [Shakura & Sunyaev \(1973\)](#) gave the theory of accretion in the form of geometrically thin and optically thick disk and incorporated viscosity parameter in an adhoc manner. [Balbus & Hawley \(1991\)](#) have suggested that magneto-rotational instability (MRI) in the accretion disk could lead to a viscous dissipation and enhance the angular momentum transport.

The efficiency with which the gravitational potential energy of the material is converted into radiation is highest for accretion. The gravitational potential energy released for a body of mass  $M$  and radius  $R$  by the accretion of

mass  $m$  is given by

$$E_{acc} = GMm/R$$

where  $G$  is the gravitational constant. For example, for a neutron star with  $R \sim 10$  km and  $M \sim M_{\odot}$ , it yields energy about  $10^{20}$  erg per gram. Another physical process of generating huge power is nuclear fusion (burning of hydrogen into helium), which releases energy

$$E_{nuc} = 0.007mc^2$$

where  $c$  is the speed of light. Therefore, the energy released is about  $10^{18}$  erg per gram which is less than the accretion. The maximum efficiency that can be achieved through nuclear fusion is 0.7% while the estimated the accretion efficiency varies between 5.7% - 32.4% depending on the disk's inner extent (Thorne, 1974). Hence, accretion as a source of power is the most efficient method.

The luminosity ( $L$ ) emitted from a source as a result of accretion depends on the mass accretion rate  $\dot{M}$  and given by,  $L = \eta\dot{M}c^2$  where  $\eta$  is the efficiency. There is a limit on this luminosity which any source can emit and that limiting criteria comes from the fact that if luminosity is too high, radiation pressure blow away the infalling matter. This limiting luminosity is called as *Eddington luminosity*. The expression for Eddington luminosity ( $L_{Edd}$ ) is derived by equating the radiative force to the gravitational force.

$$L_{Edd} = \frac{4\pi Gm_p c}{\sigma_T} M \approx 1.26 \times 10^{38} \left( \frac{M}{M_{\odot}} \right) \text{ ergs}^{-1} , \quad (1.1)$$

where  $m_p$  is the mass of proton and  $\sigma_T$  is the Thomson scattering cross-section (see Section 2.4.1.3). However, this is a simplistic picture where it is assumed that accretion of fully ionized hydrogen atoms is steady and spherically symmetric.

If the accretion disk is optically thick then each annular region of the disk will radiate approximately as a blackbody. The typical temperature as a function of the disk radius can be estimated simply by equating luminosity and

thermal emission of the disk. The final expression is given by,

$$T(R) \approx 6.3 \times 10^5 \left( \frac{\dot{M}}{\dot{M}_{Edd}} \right)^{1/4} \left( \frac{M}{10^8 M_\odot} \right)^{1/4} \left( \frac{R}{R_s} \right)^{-3/4} \text{ K} , \quad (1.2)$$

where  $R$  is the radius from the centre and  $\dot{M}/\dot{M}_{Edd}$  is the mass accretion rate in Eddington units. According to equation 1.2, the inner-disk temperature for stellar-mass black holes is about  $10^7$  K and for supermassive black holes ( $M \sim 10^6 - 10^9 M_\odot$ ) it is of the order of  $10^5$  K. So, the disk emits in X-rays for stellar-mass black holes and in optical or ultraviolet for supermassive black holes. The emitted radiation interacts with the surrounding and gets reprocessed across the electromagnetic spectrum.

All these manifestations of accretion, along with their interaction with the surrounding, result in emission of radiation in the entire electromagnetic spectrum. The inner edge of the accretion disk near the compact object attains temperature of the order of  $\sim 10^{5-7}$  K scaled according to the mass. As one moves farther away from the disk the temperature falls as  $R^{-3/4}$  and the thermal emission peaks in longer wavebands. This is why accretion disks are generally modeled as a multi-temperature blackbody. The atmosphere in the vicinity of the compact object consists of an even hotter ( $\sim 100$  keV or  $\sim 10^9$  K), but optically thin, cloud of electrons and protons called as the corona. The emitted photons from the disk are inverse Comptonized in the corona and are detected in the hard X-rays. The outer parts of the accretion disk can be irradiated by X-rays from the inner regions as well as the back-scattered coronal emission leading to an increase in their temperature and consequently emission in higher energies (Gierliński et al., 2008). The jet is known to emit primarily in radio and sub-mm wavebands by synchrotron radiation as the accreting plasma is accelerated through the collimated magnetic field. However, it has been shown that the jet synchrotron emission can also provide significant contribution in shorter wavelengths (Vadawale et al., 2001) or even dominates (Markoff et al., 2001) in hard X-rays. In X-ray binaries, the secondary star can also act as a major source of emission in optical or infrared and during outbursts emit in

ultraviolet due to X-ray irradiation from the central source. As the different components of the system emit in different energies, it is imperative to study these objects in as many wavebands as possible to get the complete picture.

### 1.1.3 Astrophysical black holes

Black holes are one of the most peculiar objects in the universe. In the late 18th century [Michell \(1784\)](#), and later independently, [Laplace \(1799\)](#) hypothesised the existence of the objects of extreme gravity that even light can not escape their gravitational pull. Newton’s particle theory of light and Ole Rømer’s discovery of the finiteness led these pioneers to believe that if the escape velocity of the photon is equal to or greater than  $c$  then the star would be invisible. That is the reason these objects were called as *dark stars*. The escape velocity is given by  $v_{esc} = \sqrt{2GM/R}$ , where  $G$  is the gravitational constant,  $M$  is the mass, and  $R$  is the radius. By replacing  $v_{esc}$  with maximum possible velocity, i.e.  $c$ , the radius of the so-called *dark star* can be written as

$$R_s = \frac{2GM}{c^2} . \quad (1.3)$$

This radius was later termed as “Schwarzschild radius”. [Michell \(1784\)](#) showed that if a star, having density same as that of Sun and radius 500 times the solar radius, then the photons escaping from its surface would return back due to its own gravity. However, such stars could be detected by their gravitational effect on the surrounding medium, for example, other visible objects ([Montgomery et al., 2009](#)). The gravitational effect arises from the curvature of space and time according to the Einstein general theory of relativity. Over a century later, [Schwarzschild \(1916\)](#) gave the first exact solution for the gravitational field of a stationary mass in vacuum using Einstein’s general theory of relativity (see [Schwarzschild, 1999](#), for an English translation by S. Antoci and A. Loinger), which says that the gravitational effect between two massive bodies is due to the warping of the space-time. The two important conclusions from his solutions are: i) At the point of singularity i.e. at the center  $r = 0$ , space-time curvature becomes infinite and ill defined, ii) the presence of imaginary sphere,

termed as event horizon from which nothing can come out, with radius given by equation 1.3. In the following decades, 's solution was re-interpreted and improved by various researchers for the explanation of black holes (e.g., [Eddington, 1924](#); [Finkelstein, 1958](#)). For the formation of an event horizon, a given mass must be squeezed within its Schwarzschild radius. For example, Sun has to be compressed into a sphere of radius 3 km to become a black hole. [Oppenheimer & Snyder \(1939\)](#) showed that after the consumption of the nuclear fuel of a spherically symmetric collapse of a non-rotating star, it could form an event horizon, which can not be escaped even by light. Due to the simplicity of their assumptions, which were of course unreal, doubts remained about the physicality of such collapses. Later, [Penrose \(1965\)](#) firmly described that even after disregarding spherical geometry, the space-time singularities can not be overlooked. For this work, Penrose received Nobel prize in 2020 along with Andrea Ghez and Reinhard Genzel for discovering the supermassive black hole at the centre of Milky Way.

In the mean time, important progress was going on to understand the physics of collapsing stars and compact objects. [Chandrasekhar \(1931\)](#) had calculated the maximum mass of a white dwarf, famously known as Chandrasekhar limit, which could balance the gravitational pull against electron degeneracy pressure (see [Schatzman, 1958](#)). A similar limit (Tolman-Oppenheimer-Volkoff limit) was estimated assuming that neutron degeneracy pressure balanced the star's self gravitation by [Oppenheimer & Volkoff \(1939\)](#), (see [Bombaci, 1996](#); [Kalogera & Baym, 1996](#), for an updated limit). [Baade & Zwicky \(1934\)](#) had proposed that the neutron stars can be formed as a consequence of supernova explosion. In the early 1960s, the high redshift of radio galaxies, such as 3C 273 and 3C 48, had prompted the proposition of very distant and powerful objects ([Schmidt, 1963](#); [Greenstein, 1963](#); [Greenstein & Schmidt, 1964](#); [Lynden-Bell, 1969](#)). In 1964, Edwin Salpeter and Yakov Zeldovich suggested that the properties of these quasi-stellar objects, or quasars, could be explained by matter falling onto massive compact objects ([Salpeter, 1964](#); [Shields, 1999](#)). Their idea was not widely accepted as black holes were still considered to be too exotic but this changed with the advancement in radio and X-ray astronomy. [Shklovsky \(1967\)](#) identified

the first extra-solar X-ray source Sco X-1 (Giacconi et al., 1962) to be a neutron star. Jocelyn Bell, in the same year, discovered radio pulsations from the pulsar PSR B1919+21 (Hewish et al., 1968). After these discoveries, community started seriously thinking about the idea of compact objects (Wolfe & Burbidge, 1970). The first galactic X-ray source, hosting a black hole, was Cygnus X-1 (Giacconi et al., 1967; Bolton, 1972; Webster & Murdin, 1972; Shipman, 1975). So far, black holes have been found to exist in variety of astronomical objects and having a wide range of mass (Kormendy & Richstone, 1995; Celotti et al., 1999; McClintock et al., 2006; Remillard & McClintock, 2006; Done et al., 2007; Kormendy & Ho, 2013).

The process of mass accretion onto the compact object was considered as the primary source of radiations from the binary systems (Prendergast & Burbidge, 1968; Pringle & Rees, 1972; Thorne & Price, 1975). Therefore, X-ray binary systems played a vital role in understanding the process of accretion onto the compact objects and its geometry. Moreover, extreme gravity near black holes provides the excellent laboratories for testing the Einstein's theory of general relativity in the strong field limit. The effects can be tested on the inner accretion disk that can reach as close as  $\sim 2 - 10 R_g$  from the black hole and emission from there experiences strong relativistic effects (Cunningham, 1976; Fabian et al., 1989, 2000; Abramowicz & Fragile, 2013; Bambi et al., 2016, 2017; Bambi, 2018).

## 1.2 Astrophysical emission mechanisms

Astronomy is all about understanding the radiative processes going on in the distant objects that emit light in different wavebands. We tend to go backward from collecting photons to analyzing them, then deciphering the mechanisms of electromagnetic radiation and finally interpreting the nature and properties of the celestial sources. Hence, it becomes imperative to understand the various mechanisms by which light is emitted. Radiation from an astronomical source is the summation of emission from a large number of particles. The energy (or velocity) distribution of these particles defines the shape of the spectrum. If

the particles follow Maxwell-Boltzmann distribution, then the spectrum will be thermal and if the distribution is non-Maxwellian (e.g., power law) the spectrum becomes non-thermal. The radiation can be polarised and unpolarised depending upon the emission mechanism and the source of emission. The asymmetry in the system leads to the polarisation of the photons because symmetry tends to cancel out the polarisation effects. In the following subsections, four commonly encountered emission processes and two common mechanisms of photon interaction with particles are discussed along with the polarisation properties.

### 1.2.1 Blackbody radiation

Blackbody emission is radiated from a source whose particles follow a thermal or Maxwell-Boltzmann distribution and have a large optical depth. Here, the radiated photons are also in thermal equilibrium with one another and the emission is received mostly from a photosphere. The specific intensity due to blackbody radiation is given by the Planck function

$$I_\nu = \frac{2h\nu^3/c^2}{\exp(h\nu/kT) - 1} \quad , \quad (1.4)$$

where  $T$  is the source temperature and  $k$  is the Boltzmann constant. One important point to note is that the specific intensity is an exclusive function of temperature (as  $I_\nu$  only depends on  $T$  and fundamental constants). The flux from a blackbody radiation can be simply calculated as  $F = \sigma T^4$  where  $\sigma$  is the Stefan-Boltzmann constant. In the limits of very low and very high frequencies, Planck's law takes on more simplified and useful forms. For  $h\nu \ll kT$ , the exponential in the denominator approximates the Rayleigh-Jeans law upon Taylor expansion

$$I_\nu = \frac{2\nu^2 c^2}{kT} \quad . \quad (1.5)$$

Similarly, in the limit of  $h\nu \gg kT$  the denominator dominates the equation yielding the Wien's law

$$I_\nu = \frac{2h\nu^3}{c^2} \exp\left(-\frac{h\nu}{kT}\right) \quad . \quad (1.6)$$

It must be noted that the optical depth is dependent on the frequency. A source can be optically thick at some frequencies and optically thin at others.

Since, the particles follow the Maxwell-Boltzmann distribution, motion of particles is isotropic, leading to the symmetry in the system. Asymmetry is required in the system to produce polarised radiations (Huang, 1987). However, polarised radiation can be generated from the thermal radiation, for example, by the Thomson scattering.

### 1.2.2 Bremsstrahlung

Bremsstrahlung, literally meaning “braking radiation”, originates when a charged particle (e.g., electron) decelerates due to Coulomb interaction with another charged particle (e.g., ions or atomic nucleus). The moving charged particle loses kinetic energy, which is then converted into radiation. Bremsstrahlung manifests as a continuous spectrum whose peak intensity moves towards the higher frequency as the change in energy of the electrons increases. It is sometimes mentioned as free-free radiation because the photon emitting electron remains free (i.e., not bound to any atom or molecule) both before and after the interaction. The basic principle by which free-free radiation works is given by the Larmor’s formula

$$P = \frac{2q^2\dot{v}^2}{3c^3} , \quad (1.7)$$

which gives the power emitted due to acceleration (or deceleration) of a charge  $q$ . For a simple case of a single electron-ion interaction, the radiated pulse energy  $W$  is characterized by the impact factor  $b$  and the velocity of the electron  $v$ .

$$W = \frac{\pi Z^2 e^6}{4c^3 m_e^2} \left( \frac{1}{b^3 v} \right) . \quad (1.8)$$

The spectrum of radiation for a single particle, given by the above equation, should be integrated over all collisional parameters and over the velocity (energy) distribution (i.e., Maxwellian or power law) to get the complete energy spectrum. In case of a thermal plasma, the low-frequency part is almost constant with an exponential decrease in higher frequencies owing to decrease in electron

population in the Maxwellian tail. The spectrum also varies with optical depth. In the compact HII region, the characteristic shape of the spectrum consists of a constant intensity for low optical depth regions and a region where the intensity varies as the square of frequency for high optical depth.

### 1.2.3 Cyclotron and synchrotron radiation

According to Larmor’s law, the acceleration of charged particles emits electromagnetic radiation. While acceleration due to electric fields causes free-free radiation, acceleration due to magnetic fields produces synchrotron (or cyclotron) radiation which is why it is also known as “magnetobremstrahlung” or gyromagnetic radiation. In the mildly relativistic regime, i.e., where the electron’s kinetic energy is comparable to its rest mass energy ( $m_e c^2$ ), it produces cyclotron radiation whereas in the ultra-relativistic regime it produces synchrotron radiation. The synchrotron emissivity for an electron in the high frequency limit (Longair, 2011) is given by

$$j(\nu) \propto \nu^{1/2} \exp(-\nu/\nu_c) \quad , \quad (1.9)$$

where  $\nu_c$  is the critical frequency. The critical frequency is given by  $3c\gamma^3/4\pi a$  where  $a$  is the radius of the spiral orbit traversed by the electron and  $\gamma$  is the Lorentz factor. According to the above equation, at frequencies  $\nu > \nu_c$  the spectrum has exponential cut-off and very little power. For low frequency limits of the frequency  $\nu \ll \nu_c$  the spectrum is given by

$$j(\nu) = \left( \frac{eB \sin \alpha}{\gamma m_e} \right)^{2/3} \nu^{1/3} \quad , \quad (1.10)$$

where  $\alpha$  is the pitch angle of the spiral magnetic field. In the low frequency limits, the spectrum is proportional to  $\nu^{1/3}$ . The electrons in most of the synchrotron sources follows a power-law distribution and are not in thermodynamic equilibrium. Thus, these sources are often termed as “non-thermal” sources.

Sources of synchrotron radiation are quite ubiquitous in astronomy, for example, in AGNs, the radio emission coming from the jets is the result of synchrotron process. At frequencies below 30 GHz, the synchrotron process

dominates the radio continuum from star-formation regions in galaxies like our Milky Way. Jupiter's magnetosphere is also believed to be a source of synchrotron emission. Although predominantly observed in radio wavebands, synchrotron emission also dominates other wavebands from infrared (IR) through X-ray in various sources like jets in microquasars, AGNs, and supernova remnants.

### 1.2.4 Curvature radiation

It is emitted if the electron follows the curved magnetic field lines instead gyrating around them. In the relativistic limit, energy emitted is given by

$$E = \frac{3ch}{4\pi R_c} \gamma^3 \quad (1.11)$$

where  $R_c$  is the radius of curvature.

### 1.2.5 Compton scattering

Compton scattering is a process in which a high energy photon collides with a stationary electron and transfers some energy and momentum to it. The energy of the output photon,  $\epsilon_{out}$  is given by

$$\epsilon_{out} = \frac{\epsilon_{in}(1 - \beta \cos \theta_{ei})}{1 - \beta \cos \theta_{eo} + (\epsilon_{in}/\gamma)(1 - \cos \theta_{io})} \quad , \quad (1.12)$$

where  $\theta_{ei}$  is the angle between electron and input photon,  $\theta_{eo}$  between electron and output photon, and  $\theta_{io}$  between input and output photons. The Lorentz factor of the electron  $\gamma = (1 - \beta^2)^{1/2}$  and  $\epsilon_{in} = (h\nu/m_e c^2)$  is the input photon energy.

Depending on the energy of the incoming photons and the electrons, the photons can either impart or extract energy from the electrons. This explains both the Compton (downscattering) and inverse-Compton (upscattering) scattering scenarios. Inverse Compton scattering is not an emission mechanism but a process to boost the energy of the existing photon. It occurs when the energy of the electron is higher (relativistic) than the incident photon energy, and the photon's energy is boosted up at the expense of the electron's kinetic energy. This

effect is called as inverse Compton scattering and plays an important role in hard X-ray emission from hot plasma/corona.

For a thermal electron distribution in the corona, the random velocity typically set by electron temperature  $\Phi = kT_e/m_e c^2$ , since  $v^2 \sim kT_e/m_e$  which implies  $\beta^2 = 3\Phi$ . For an isotropic distribution of electrons and photons, the angle-averaged output energy  $\epsilon_{out}$  can be simplified by Taylor expanding equation 1.12. This gives  $\epsilon_{out} = (1 + 4\Phi + 16\Phi^2 + \dots)\epsilon_{in} \approx (1 + 4\Phi)\epsilon_{in}$  for  $\Phi \ll 1$ . During scattering the change in energy  $\Delta\epsilon$  becomes  $4\Phi\epsilon_{in}$  indicating upscattering of photons. The probability of interaction between the photons and electrons is given by  $e^{-\tau} \approx 1 - \tau$  for  $\tau \ll 1$ .  $\tau$  is the optical depth of the electron cloud and is given by  $\tau = nR\sigma_T$  where  $n$  is the number density of the electrons,  $R$  is the path length, and  $\sigma_T$  is the Thomson cross-section (equation 2.19). The output energy distribution is the resultant of repeated Compton scattering, i.e. thermal Comptonisation. This repeated scattering process continues till the energy of the output photons reaches the limit of the electron energy after  $N$  scatterings, i.e. when  $\epsilon_{out,N} = (1 + 4\Phi)^N \epsilon_{in} \sim 3\Phi$ . The final spectrum is a power law starting from  $\epsilon_{in}$  to  $3\Phi$ . The spectral index,  $\alpha$ , of the power law is estimated by both the optical depth and temperature of the electrons, which is given by  $\log \tau / \log(1 + 4\Phi)$ .

## 1.3 Variability of black hole X-ray binaries

### 1.3.1 Long-term variability

BHBs are divided into two sub-category based on the their variability over a time scale of years- transient and persistent sources. Persistent sources are the one who are in their bright state since their discovery, e.g. the HMXBs LMC X-1, Cyg X-1, and LMC X-3. In general, transient sources live most of their lives in a state of quiescence (i.e., below the sensitivity level of most X-ray detectors exist till now) and become detectable only during violent episodes of outburst, which usually last a few months to a year. These outbursts are quasi periodic with periods ranging from less than a year to decades (Tetarenko et al., 2016a).

The recurrence of times between the outburst depends upon the mass accretion rate (McClintock et al., 2006). Almost all LMXBs show transient behaviour, e.g. GRS 1716–249, 4U 1630–472, GX 339–4 etc. The transient sources show spectral as well as timing variability on a wider range. Figure 1.2 shows the long term light curves for the two types of sources. Out of all the sources, GRS 1915+105 is a unique example which has been in the bright state since its discovery and displays about thirteen variability classes at different time scales (Belloni et al., 2000). Some sources e.g. V404 Cygni, GRO J1655-40, GRS 1716-246, etc. goes into outburst once in a decade. It is believed that long term variability is caused by the hydrogen ionization instability (Lasota, 2001; Frank et al., 2002) aided by the different mass transfer rates from two kinds of companion stars in HMXBs and LMXBs.

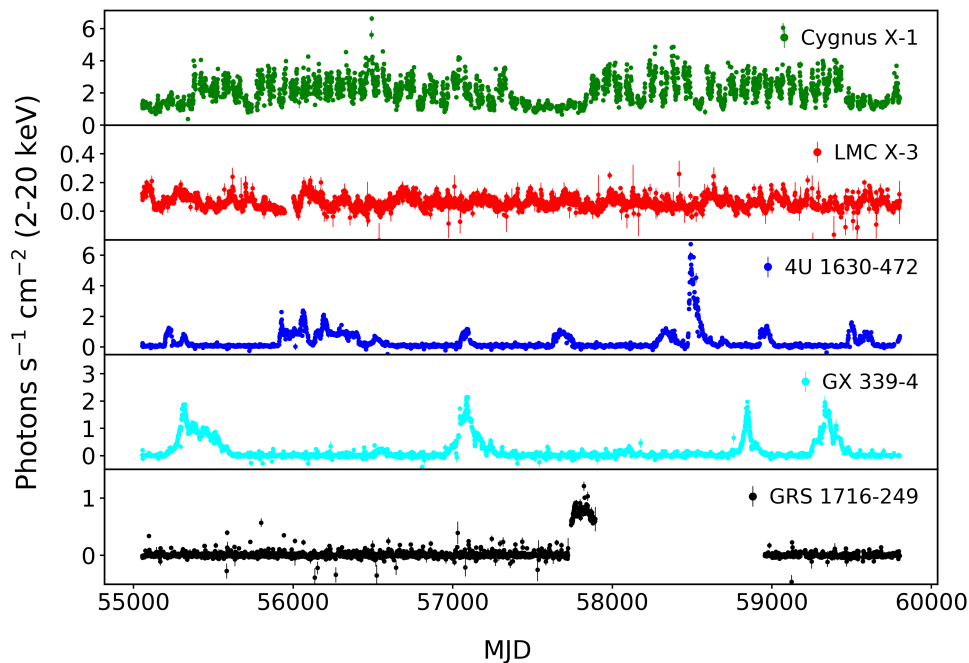


Figure 1.2: From top to bottom: The long term lightcurves of two HMXBs - Cyg X-1 and LMC X-3, and three LMXBs - 4U 1630–472, GX 339–4, and GRS 1716-249 observed with *MAXI* .

### 1.3.2 Medium time variability

There are outburst which happen in much shorter and longer time scale but these are not understood based on disk instability models. However, the original DIM (Disk Instability Models) unable to explain some properties of the outbursts in LMXBTs, such as outburst duration, recurrence time, and decay time, so some other processes such as irradiation must be considered in the modified DIMs to explain it (Dubus et al., 2001).

Some of the sources undergoes frequent outburst on a time scale of weeks to months which is defined with respect to the quiescent state (may correspond to a non-detection state). For example, BHXB SAX J1819.3-2525 went into outburst 24 times in RXTE era (Tetarenko et al., 2016b).

Some of the LMXB Be X-ray binary sources goes into outburst on a time scale of weeks to months. For example, EXO 2030+375 goes into outburst every 46 days, which is the orbital period of the system (Wilson et al., 2008) (see Figure 1.3). Similarly, MXB 1730-33 has bright outbursts, up to 23 in the 16 yr in RXTE era (Yan & Yu, 2015). The BeXB are the X-ray binaries harbouring a fast rotating neutron star which orbits a Be type star. They show two types of outbursting behaviour:

Type I: These are more regular or quasiperiodic outbursts peaking near the periastron passage of the neutron star. These are short lived and less bright having X-ray flux only one order of magnitude compared to pre-outburst state. The neutron star captures gas from the Be Star during the close encounter with the Be disk.

Type II: These type of outbursts are very bright where X-ray flux increases by  $10^3$ - $10^4$  times compared to quiescence state. These are less frequent than Type I outburst. The formation of the accretion disk during Type II outburst may occur. This is also supported by the large and steady spin up rates during the giant outbursts (Wilson et al., 2008).

The long-term X-ray emission is modulated by the orbital period of 46 days in EXO 2030+375. It is believed that the Type II outbursts and Type I outbursts were distinguished by the presence of an accretion disk in the Type II

outburst, while the Type I outbursts proceeded by wind accretion.

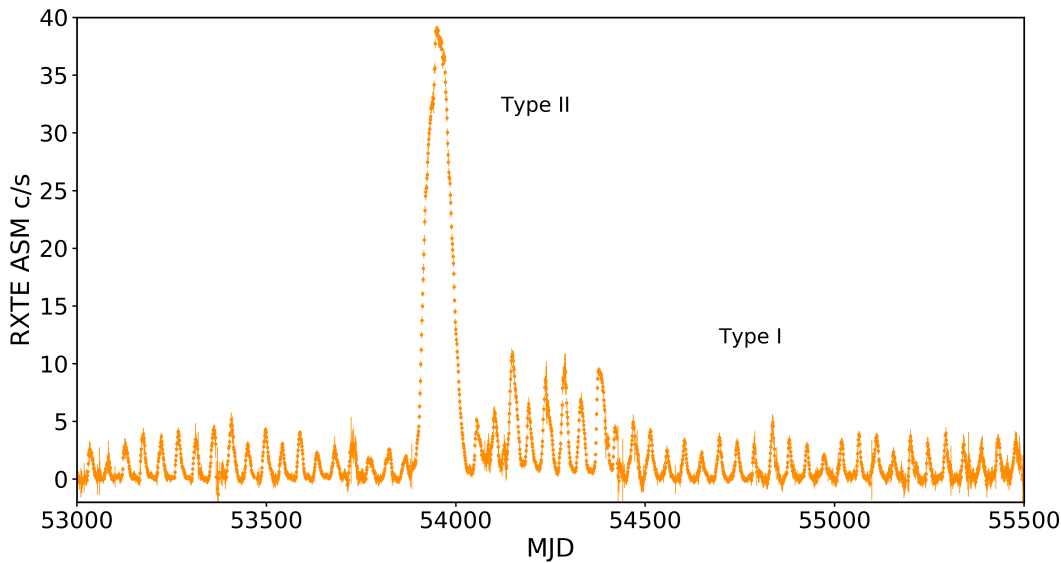


Figure 1.3: The long term lightcurve of EXO 2030+375 observed with RXTE/ASM. The Type II outburst are rare and Type I is always present

### 1.3.3 Rapid variability

In addition to months and years, BHB emissions also show variability at much shorter time scales, sometimes as low as milliseconds. These time scales are associated with the characteristic time scales of accretion flow, such as light crossing, thermal and viscous diffusion, free fall, etc. In addition, there are also time scales associated with Keplerian motion and general relativistic effects such as nodal and Lense-Thirring precession. Therefore, probing any of these time scales of emitted radiation can provide an important insight about the on-going physical mechanism.

The analysis of the time series in the frequency space is the most common method for studying rapid variability. This exercise is performed by Fourier transforming the lightcurve and constructing a power spectrum (see 2.3 for details on the calculation of power spectrum). A power density spectrum (PDS) represents the variation of power as a function of temporal frequency. The PDS constructed during different spectral states (Section 1.3.5) of an outburst is shown in Figure 1.4. As one go from top to bottom, PDS is associated with the states of decreasing hardness and constitutes different noise levels and peaked features.

Various models have been proposed to explain the broadband noise properties. Models based on shot noise are able to explain the broadband noise properties observed in the PDS (Terrell, 1972). However, their strength lays on their ability to reproduce the observations and are unable to explain the physical processes underlying the noise (also see Narayan & Yi, 1995; Uttley et al., 2005). The origin of the  $1/f$  noise is possibly connected to the fluctuations in the mass accretion rate (Kazanas et al., 1997) as their strength increases with increasing rate (Cui et al., 1997b,c,a). The white noise component can be produced due to thermodynamic fluctuations in the inner regions of the disk. Broad peaks on the PDS (apparent in the second, third and fourth PDS in Figure 1.4), known as quasi-periodic oscillations (QPO), are the most abundant features found in BHBs. They are classified into two categories as low frequency ( $\lesssim 30$  Hz) or milli-hertz and high frequency QPOs ( $\gtrsim 40$  Hz) or kilohertz QPOs. The low-frequency QPOs (LFQPO) are further divided into three types - A, B, and C depending on their properties and the state of the system they occur in (Casella et al., 2004, 2005). In fact, the presence of absence of one or the other type of QPO has become a defining characteristic of certain states (Section 1.3.5).

### 1.3.4 Spectral components of black-hole binaries

A typical spectrum of a BHB consists of thermal and non-thermal spectral components - a thermal disk, a power law due to Comptonisation, and a reflection component. The origin and different manifestations of each of these components are discussed in the following subsections.

#### 1.3.4.1 Thermal disk

The thermal emission in BHB comes from the the accretion disk and usually peaks in soft X-ray coming from the inner part of the disk. When the matter accretes around the black hole, the strong gravitational potential energy of the black hole is converted into the radiation. The structure of the accretion flow is defined by the balancing between the gravitational heating and cooling. The viscous stress between the adjacent layers of the accretion disk convert the grav-

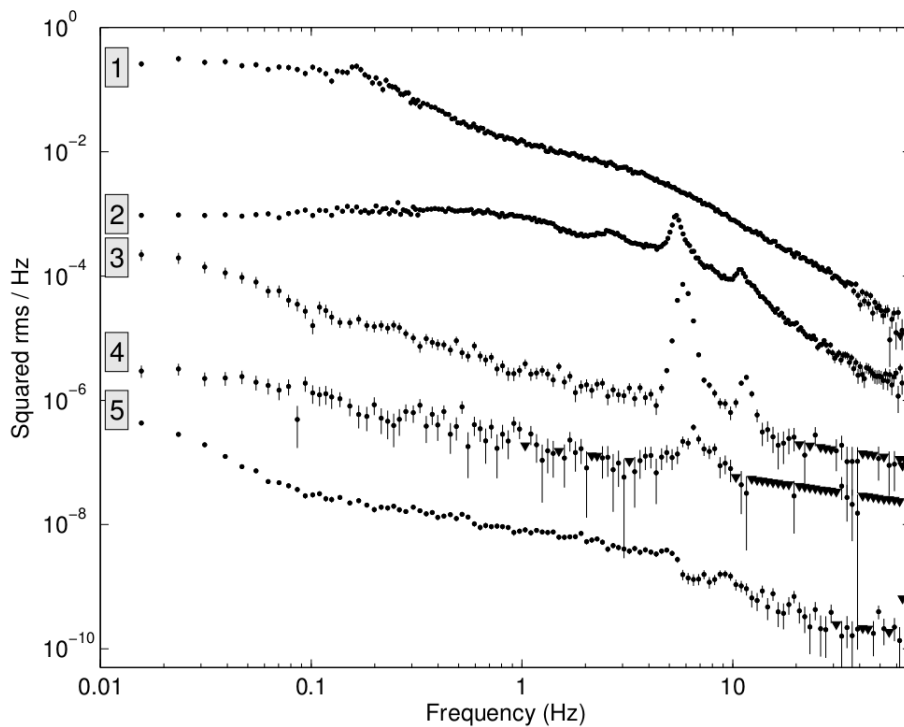


Figure 1.4: The different types of power-density spectra observed in black-hole binaries during various states (Belloni, 2010a).

itational energy into heat (Shakura & Sunyaev, 1973). The cooling happens by the local radiation of this heat. This radiation takes the form of a blackbody if the material in the disk is thermalized and is optically thick. For a blackbody the emission totally depends on the temperature, and the temperature in a disk is a function of the radius. As one moves closer to the black hole, more radiation from stronger potential has to be emitted from a smaller space. So, the temperature increases inward and the disk becomes geometrically thin. The disk formed in this way represents the multi-colour blackbody. Due to the assumption of a thermal disk, the spectrum is independent of the viscosity mechanism at least to the zeroth order. Thus, phenomenological descriptions of the viscosity, such as the  $\alpha$  prescription by Shakura & Sunyaev (1973) are sufficient to describe the emitted spectrum. Their assumption is that the shear viscous stress is proportional to the total pressure with  $\alpha$  serving as the proportionality constant. While the true origin of the viscous stress is a matter of debate, magneto-rotational instability (Balbus & Hawley, 1991) is believed to be a promising candidate.

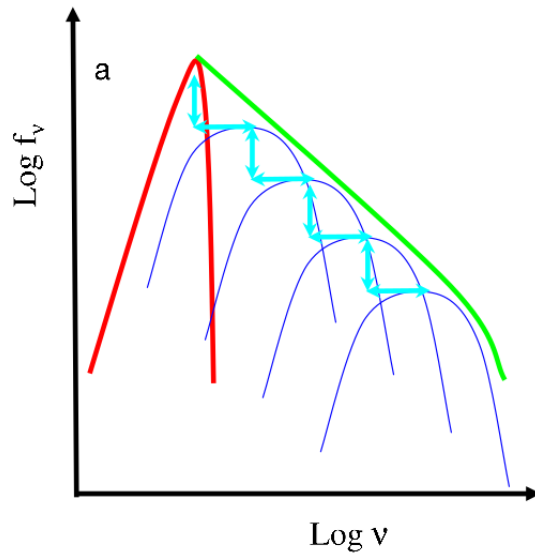


Figure 1.5: The formation of a thermal Comptonisation spectrum by repeated scattering. (Done, 2010)

#### 1.3.4.2 Comptonisation

As discussed in Section 1.2.5, Compton scattering of photons leads to an exchange of energy between photons and electrons upon collision. In the accretion disk of binaries, inverse Compton scattering plays a crucial role as the corona is much hotter than the seed photons originating from the accretion disk. Depending upon the distribution of the electron in the corona, the Compton spectrum will be either thermal or non-thermal.

For a thermal electron distribution, the output energy distribution is the resultant of repeated Compton scattering i.e., thermal Comptonisation till the energy of the output photons reaches the limit of the electron energy after  $N$  scatterings, i.e. when  $\epsilon_{out,N} = (1 + 4\Phi)^N \epsilon_{in} \sim 3\Phi$ . The final spectrum is a power law starting from  $\epsilon_{in}$  to  $3\Phi$ .

Non-thermal Compton scattering happens when electron number density follows a power-law distribution, i.e.,  $n(\gamma) \propto \gamma^{-p}$  from  $\gamma = 1$  to  $\gamma_{max}$ . According to equation 1.12, for  $\gamma \gg 1$  the output photon gets beamed into a conical region of angle  $1/\gamma$  along the electron direction. Assuming an isotropic distribution of electrons and photons the angle averaged output photons energy becomes  $\epsilon_{out} = (4/3\gamma^2 - 1)\epsilon_{in} \approx \gamma^2\epsilon_{in}$ . Thus, non-thermal scattering results in a power-law spectrum extends from  $\epsilon_{in}$  to  $\gamma_{max}^2\epsilon_{in}$  from a single scattering order.

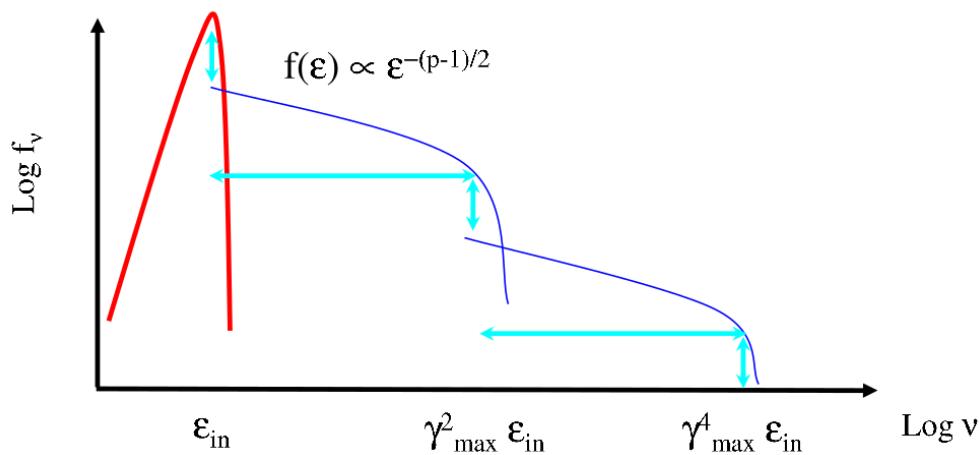


Figure 1.6: The formation of a non-thermal Comptonisation spectrum from a single (or at most two) scattering. (Done, 2010)

Sometimes, the extent of the power-law tail up to 1 MeV in high/soft state (see Section 1.3.5) hints towards the scenario when the electron distribution could be hybrid, i.e., a Maxwellian with a power-law tail. One way to produce this kind of electron distribution is from a single acceleration region, where from the initial non-thermal distribution the low energy electrons thermalize by Coulomb collisions and the high energy electrons preserve the power-law shape by cooling via Compton scattering (Coppi, 1999). Alternatively, instead of one single region there could be two distinct regions above disk or jet, one with a non-thermal distribution, perhaps due to magnetic reconnections, and the other with a thermal distribution from the classical corona or hot inner flow (Done et al., 2007).

### 1.3.4.3 Reflected emission

Out of the Comptonized X-ray photons emanating from the corona, a fraction of them illuminate the geometrically thin and optically thick accretion disk. Some of these photons can get reflect back from the disk along line of sight. The probability of the reflection depends on the relative strength of scattering compared to photoelectric absorption at a particular incident energy (Figure 1.7). The photoelectric absorption dominates over scattering at low energies for neutral disk, therefore, suppressing the reflection fraction. However, the absorption cross-section decreases with energy as  $E^{-3}$  resulting in an enhancement in re-

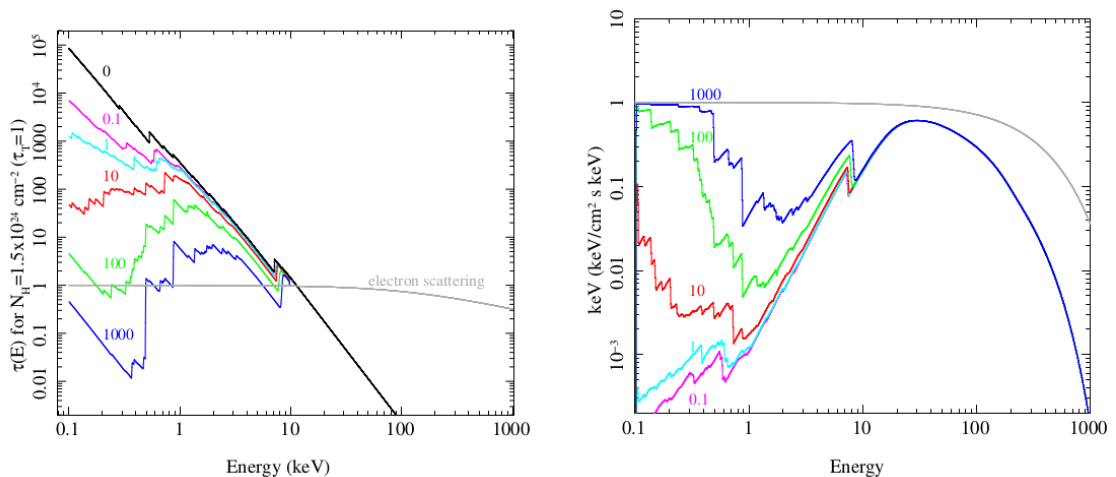


Figure 1.7: Left panel: Dependence of photoelectric absorption and electron scattering cross-sections with energy. Right panel: Reflected spectrum for different ionization states. The different colors represent the different ionization states of the absorbing material (Done, 2010).

reflection fraction. Above 10 keV scattering cross-section begin to dominate for solar abundances causes the steady reflection. For higher incident photon energy ( $\gtrsim 50$  keV) Compton downscattering become significant, so the reflection become inelastic. As the number of photons at higher energies are less and the reflected ones have lower energies, a break appears in the spectrum. This forms a characteristic peak in the 20 - 50 keV range, called as the reflection hump, where the high-energy photons are downscattered and the low-energy photons are photoelectrically absorbed (George & Fabian, 1991).

Photoelectric absorption at low energy excites the atoms and knock out the inner most K ( $n=1$ ) shell electron. These ions instantly de-excite to the ground state either by emitting a fluorescence emission line ( $n=2$  to  $n=1$  transition generate a  $K\alpha$  line,  $n=3$  to  $n=1$  transition generates a  $K\beta$  line, and so on) or by the ejection of an outer-shell electron (known as Auger effect). The low atomic-number elements preferentially de-excite through Auger effect. So, the strongest fluorescent line is from iron owing to its high fluorescence probability and an increased reflection fraction.

The photoelectric absorption cross-section of a material is majorly dependent on its ionization state (Figure 1.7). The reflectivity of a material increases with increasing ionization state as the opacity of the medium decreases.

Therefore, the fluorescent lines from the low atomic number material becomes more prominent over an ionized reflection continuum.

Furthermore, for an ionized material the disk is heated upto Compton temperature by irradiation making Compton upscattering as important as down-scattering. This causes broadening of the lines and edges (Young et al., 2001). For most of the application purpose, the disk is assumed to be either neutral or having constant ionization but the real disk in hydrostatic equilibrium has much more complex structure. Due to strong illumination, the surface of the disk is highly ionized and has much less density. In the disk, density increases while ionization decreases as one go from the surface to the interior. The amount of ionization is also dependent on the hardness of the illuminating flux. A hard spectral illumination gives rise to almost complete ionization of the skin because of high energy photons, while a softer illumination leads incomplete ionization. Therefore, the actual reflected spectrum is a composite of different ionization states.

As discussed above, the fluorescent iron  $K\alpha$  line is a prominent feature of the reflected spectrum. It appears at 6.4 keV for neutral material and  $> 6.4$  keV for an ionized disk. This emission line is intrinsically broadened only upto a few tens of eV depending on the temperature structure of the emitting material. The broadening is increased further (upto several hundreds of eV) due to various special and general relativistic effects. These effects become more pronounced when the line is emitted from the vicinity of the black hole. At distances farther away the disk is mostly non relativistic and the line has a double-horned structure, with the two horns originating from the receding and approaching sides of the disk. It is to be noted that this effect will only be observed for an inclined disk, a face-on disk will not show any Doppler effects. When the emission is from a smaller radius (i.e., closer to the black hole), the orbital velocity of disk is mildly relativistic beaming the blue horn from each radius. Subsequently, transverse Doppler effect and gravitational redshifts move the red horn to lower energies. The combined effect is a highly skewed and broadened line profile. By modeling this line, along with the underlying continuum, accurately the inner radius of the disk and inclination can be obtained.

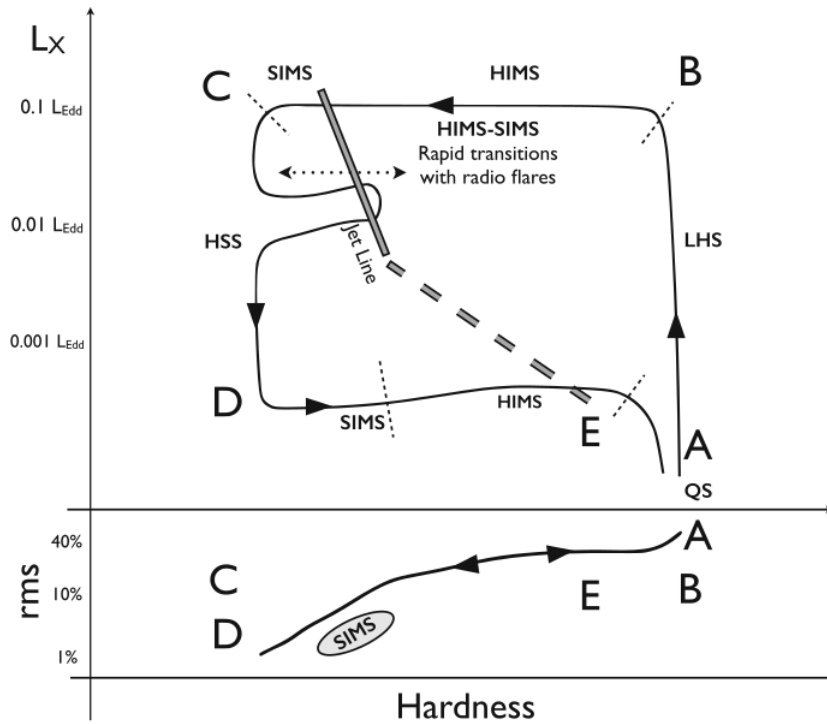


Figure 1.8: Top panel shows the a typical HID from a BHB outburst. Bottom panel shows the HRD. Courtesy: (Belloni & Motta, 2016)

### 1.3.5 State classification

#### 1.3.5.1 X-ray properties

BHB outbursts are classified into different states based on their spectral and timing properties. This classification has been one of the basis for understanding the system and its properties. The first black-hole candidate Cygnus X-1, observed with *Uhuru*, showed the presence of two different states based on changes in flux in different energy range. Since, the instrument had maximum effective area in the soft X-ray band, the states were identified as “high” and “low” states based on the increase and decrease of the flux in these bands. Terrell (1972) showed that the low state was connected with the aperiodic noise while high state was associated with the disappearance of radio counterpart (Tananbaum et al., 1972). In 1975, the first transient black hole source was observed which also showed similar states as in Cygnus X-1 (Elvis et al., 1975). Over the years two more states were added, namely, intermediate state (IMS) and very high state (VHS), both of them had intermediary properties to the high and soft states.

Different states can be mapped simply with the help of hardness-intensity diagram (HID) and hardness-rms diagram (HRD). In the HID, the ratio of the count rate in hard X-ray energy band to the soft X-ray band (hardness ratio) is plotted against total counts rate. HID is very similar to the color-magnitude diagram used in the optical astronomy. The HRD is the variation of fractional rms with hardness ratio. The schematic representation of these two diagrams is shown in Figure 1.8. In this figure, as the ‘q’ shaped curve moves from point A to point E, it describes the evolution of a typical BHB outburst. There are four branches on the curve that can be correlated with the four states described earlier. The two vertical branches AB and CD, and horizontal branches BC and DE correspond to the low, high, VHS and IMS respectively. It was inferred from the extensive spectral and timing study of X-ray binary XTE J1550–564 that IMS and VHS state are associated with the same physical state only occurring at different flux level (Homan et al., 2001). This reduces the total states to three. Unlike HID, the HRD shows a linear correlation between fractional rms variability and hardness. The hardest states show maximum variability ( $> 20\%$ ), the softest ones minimum ( $< 10\%$ ) and the intermediate states show intermediary variability. Other than HID and HRD, a third diagram named as rms-intensity diagram (RID) can also be used to describe the different states (Muñoz-Darias et al., 2011). It maps the variation of rms with intensity resulting in a hysteresis loop similar to the HID (see Figure 1.9). The above description can help in summarize that an outburst can be characterize by four states as described below:

- *Low/hard state (LHS)*: As its name suggests, this state is dominated by hard photons i.e. power-law flux due to Comptonisation dominates over the intrinsic soft flux of the disk. In this case, disk was either relatively cooler or truncated at larger radii. It show high variability ( $\sim 30\%$ ) which is directly correlated with hardness and anti-correlated with the flux. The power spectrum is composed of a number of Lorentzians, one of which can become a type-C QPO. The characteristic frequency of the PDS components increases with flux. In figure 1.8, the vertical line AB represents LHS

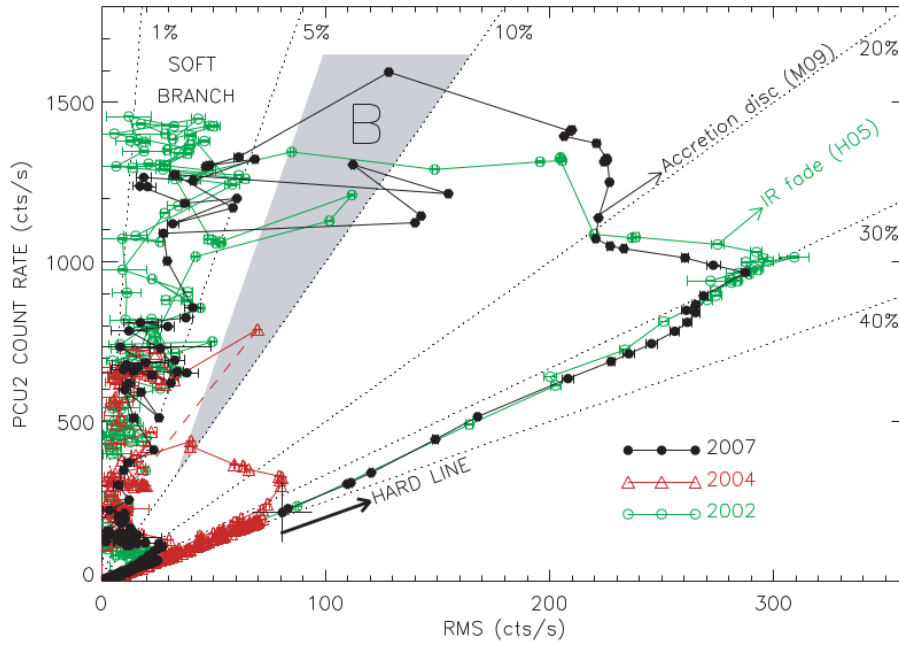


Figure 1.9: The absolute rms-intensity diagram for GX 339-4 observed during three epochs. The fractional rms levels are represented by dotted lines (Muñoz-Darias et al., 2011)

state which indicates that the outburst starts and ends in this state. While in RID the diagonal line at high RMS value represents the LHS.

- *High/soft state (HSS)*: During HSS state, the spectrum is dominated by a thermal disk flux and show very small variability. It is positioned at the left most branches in all the three diagnostic diagrams. Sometimes, type-C QPOs may be detected.
- *Hard-intermediate state (HIMS)*: In this state, contribution from the thermal disk increases resulting in the steepened power law. This translates into a decrease in variability to about 10% level. However, the shape and dependencies of the PDS remain similar to that of the LHS. In the HID, the HIMS covers a major portion of the horizontal branches. Sometimes the sources make occasional transition to the HIMS from the HSS (Figure 1.8).
- *Soft-intermediate state (SIMS)*: The SIMS is marked by low levels of hardness and variability and occurs to the left of the HIMS on the HID and

RID. It is difficult to separate the SIMS and HSS because the variability and hardness are very similar to these two states. However, the SIMS points occupy a small patch below the main track in the HRD. The spectrum, although similar to that of the HIMS, does not show a high-energy cutoff. The PDS makes the identification of the SIMS clear by changing the shape from a band-limited noise to a power law with a type-B QPO.

### 1.3.5.2 Radio properties

Different state classification can also be linked with the properties of relativistic jets as observed in radio bands. The synchrotron emission from the relativistic jet can be studied by the radio emission (Fender, 2010). This depends upon the state of jet in different states. The properties of the radio emission in different states are discussed below and summarised in Figure 1.10.

- *Low/hard state (LHS)*: In this state, a steady compact jet is observed which is difficult to resolve spatially and the observed spectrum is flat or inverted. In this state, there is a correlation of radio flux with the X-ray and IR flux (Coriat et al., 2011). But at the top of the LHS branch, the correlation between X-ray and infrared breaks (Homan & Belloni, 2005)
- *Hard-intermediate state (HIMS)*: When the source is in HIMS and approaches the SIMS a steepening of radio spectrum is observed (Fender & Belloni, 2004).
- *High/soft state (HSS)*: In the HSS state, no nuclear radio emission is observed except a faint radio flux which is believed to be emitted from the ejecta.
- *Soft-intermediate state (SIMS)*: The radio flaring is observed around the time of transition of the source from the HIMS to SIMS state (Fender et al., 2009). It happens at a hardness threshold which is dubbed as "jet line" (see Figure 1.10).

On return transition to HIMS, radio emission is detected but at higher hardness value compared to value where it disappeared earlier, when the

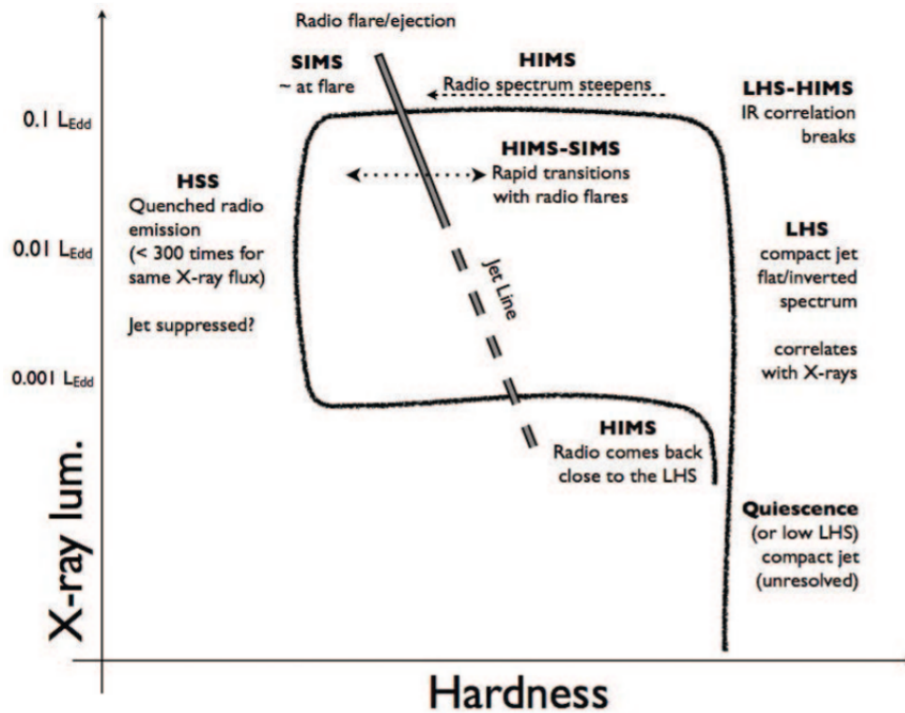


Figure 1.10: Hardness-intensity diagram for a black hole with labels indicating the radio properties (Belloni et al., 2011)

source has already reached the LHS (Kalemci et al., 2006) and radio/X-ray correlation is re-established (Gallo et al., 2006).

## 1.4 X-ray polarisation

The polarisation of electromagnetic radiation is the fundamental property which describes the configuration of electric field. Polarimetry of an electromagnetic wave gives the orientation of its electric field and hence its magnetic component. The radiation is partially polarised if there is orderliness in the orientation of the electric field. The direction of the electric field defines the plane of polarisation, and the fraction of the ordered field with respect to the total field gives the degree of polarisation. It is carried out with an instrument called a polarimeter which can have different designs. The simplest one is to use a filter that allows only the polarised component of the radiation to pass through. But this does not apply to the whole electromagnetic spectrum because at higher energy the construction

of the optical elements, such as filters or wave plates, is problematic. Specific design and more sophisticated techniques are required for the specific purpose.

The study of the linear polarisation has been suggested as a powerful tool in investigating the geometry and emission mechanism of the astrophysical sources (Novick (1975); Rees & Gunn (1974); Meszaros et al. (1988); Weisskopf et al. (2006)). The partially polarised radiation is expected to emerge in all astrophysical sources where a unique direction exists, like asymmetries in the distribution of the matter, the presence of the ordered magnetic field, or some distinct emission process. The polarisation measurements add two parameters, polarisation angle and the polarisation degree, to the current list of the observable quantities, namely energy, time and the direction of the incident photons.

X-ray polarimetry can reveal the signatures of the different emission mechanisms. In the case of bremsstrahlung for the electron-nucleus interaction, the emitted photons are partially polarised and in electron-electron bremsstrahlung it is highly polarised (Haug & Nakel, 2004). Cyclotron radiation emits circularly polarised photons if the system viewed along the magnetic field lines and linearly polarised in the plane of electron motion when viewed edge-on, whereas, synchrotron radiation for the ensemble of electrons is linearly polarised (Lei et al., 1997). If the electrons have power law energy distribution  $n(E) \propto E^{-\tau_e}$ , where  $\tau_e$  is the power law index, then the polarisation fraction ( $p$ ) of the radiation emitted by electrons is given by (Rybicki & Lightman (1985)),

$$p = \frac{\tau_e + 1}{\tau_e + \frac{7}{3}} \quad (1.13)$$

and photons power law spectral index is given by

$$\tau_\gamma = \frac{\tau_e - 1}{2} \quad (1.14)$$

For the  $\tau_e$  in the range of 1.5 – 5.0  $p$  comes out to be 65 - 80% (Lei et al., 1997).

Curvature radiation emit photons linearly polarised parallel to magnetic field (Lei et al., 1997). In the case of scattering, the polarisation signature depends on the scattering angle of the photon in the rest-frame of the electron

(see equation 2.17). For the power law electron energy distribution, the photons spectrum due to inverse Compton scattering has same spectral index as that of synchrotron radiation but the polarisation signature in the two cases will be different, allow to distinguish the two processes.

### 1.4.1 Polarisation in accreting black holes

The black holes are the region of space time from where even light can not escape. To study black hole is extremely challenging as compared to other astrophysical sources because we do not get any radiation directly from the black hole. It is mostly studied through the radiation emitted from the surrounding environment which is under its gravitational influence. Accretion of matter onto black hole gives rise to X-rays along with other wavelengths to study their properties. The typical geometry of accreting environment around the back hole is based on spectroscopic and timing studies. It consists of an optically thick and geometrically thin disk accreting matter from the companion star. The region close to the black hole comprises optically thin and geometrically thick hot cloud of electron called the corona. There is also evidence of bipolar outflows in form of jet that originated from the region. X-ray spectroscopy (photon energy spectrum), and X-ray timing (photon temporal evolution) have been explored most to study black hole binary. The X-rays spectrum of the black hole binary consists of three components: (1) thermal radiation from the disk (2) powerlaw component due to the Comptonisation of the seed photons coming from the disk in the atmosphere of the black hole called corona (3) reflected component due to the reflection of the Comptonized photons from the disk. The variability of the source is studied using the power spectrum which is the Fourier transform of a time series. Apart from the thermal Comptonisation, there is also a non-thermal component which can be produced by the non-thermal Comptonisation (Coppi, 1999) and the synchrotron radiation from the jet (van Paradijs & McClintock, 1995). There are more then one possibilities/models which can explain the timing and spectroscopy observations. Therefore, there is no general consensus over exact geometry of the corona/jet. The spectral models are degenerate as far as

geometry is concerned and to break the degeneracy, some new parameters are required. The photons have one more property i.e., polarization (photons orientation of the electric field vector), remains mostly unexplored due to requirement of relatively longer exposure times and control of systematic uncertainties. The polarisation measurements give two information about the radiation: polarisation angle and polarisation fraction. There are several other aspects which are still remain unclear like contribution of jet in the hard X-ray emission, spin of the black hole, etc. which can be addressed with the X-ray polarimetry. Polarisation with the unison of spectroscopy can give wealth of information about the source geometry and other properties of the black hole.

#### 1.4.1.1 Black hole spin

The mass and spin are two parameters that can be used to describe a BH. The spin is defined by the dimensionless parameter as  $a = J/McR_g$  where  $J$  is the angular momentum and  $R_g = GM/c^2$  is the gravitational radius. It is limited in the range of  $0 \leq a \leq 1$ . A maximally spinning Kerr BH has  $a = 1$ , while a Schwarzschild BH does not rotate and has  $a = 0$ . The event horizon, the distance from which light can not escape, is situated at  $R_g$  for the Schwarzschild black hole and  $2R_g$  for the Kerr black hole, respectively. There is a concept of Innermost Stable Circular Orbit (ISCO), which is the closest distance where the matter can follow a circular orbit. It is  $6R_g$  for the Schwarzschild and  $R_g$  for the Kerr black hole (Shapiro & Teukolsky, 1983). Therefore, in Kerr black hole inner part of the accretion disk suffer stronger gravitational effect in comparison to Schwarzschild black hole. The spin of a black hole is generally measured using the three techniques: thermal continuum emission (McClintock et al., 2011; Zhang et al., 1997) and relativistic reflection (Miller, 2007; Fabian et al., 1989). In continuum fitting method spin is measured indirectly by measuring the inner radius of the accretion disk which is assumed to be equal to ISCO. The inner radius of the disc is measured by fitting the thermal disk continuum with the relativistic disk model (Gierliński et al., 2001; Shafee et al., 2006a; McClintock et al., 2006). It requires other parameters of the black hole like mass of the black hole, distance, inclination, etc. In relativistic reflection technique modeling of

the spectrum originating from the reflection of the coronal emission from the inner disk which consists of Fe- $k\alpha$  emission and Compton hump at around 30 keV. These techniques sometimes give inconsistent results, for example, in case of black hole binary GRO J1655-40 spin parameter is found 0.7 (Shafee et al., 2006b) using continuum fitting method and 0.9 (Reis et al., 2009) using the relativistic reflection method. X-ray polarimetry can be third technique which can measure the spin of the black hole (Connors et al., 1980; Dovčiak et al., 2008; Li et al., 2009; Schnittman & Krolik, 2009). The strong gravity effects can rotate the polarisation angle of the radiation which is depends up on the location of emitting point on the disk. Since, the temperature of the disk decreases with disk radius (see equation 1.2), therefore, the rotation of the polarisation angle with energy is expected.

#### 1.4.1.2 Geometry of the corona

It is not possible to resolve the black hole environment or surrounding geometry spatially with the present instruments, its exact geometry is not known. There are two primary classes of the accretion geometry models (see Figure 1.11): lamp post and extended corona model. In lamp post model (Miniutti & Fabian, 2004) corona is considered as a point source above the black hole whereas in the extended corona model (Zdziarski & Gierliński, 2004), corona is surrounding the black hole and blocking the emission from the inner part of accretion disk. Both the models are able to produce the same X-ray spectrum (see Figure 1.11) though for different set of parameters. Thus, they are degenerate. However, the polarisation from the two models is predicted to be different.

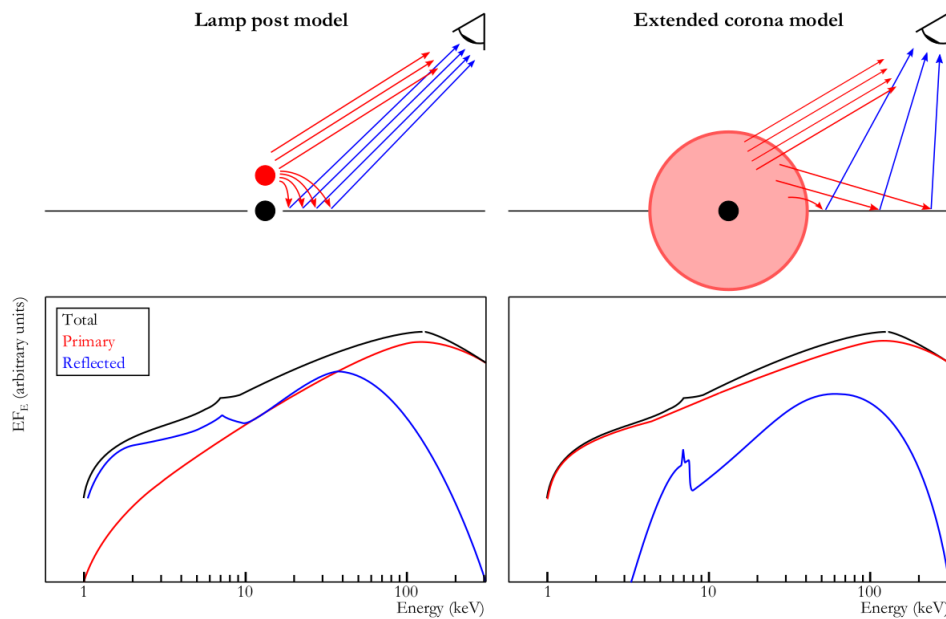


Figure 1.11: Comparison between the lamp post corona and extended corona model. Top panel shows the corona in red, the black hole in black and thin accretion disk (black line). The soft seed photons from the cool disk (not shown) is Compton up scattered and emit the primary component shown in red arrows and the reflected component from the disk is shown in blue arrows. In the lamp post geometry, strong gravity causes the increase in the reflection component and broadening of the iron line due to gravitational and Doppler shift. Credits [Chauvin et al. \(2018\)](#)

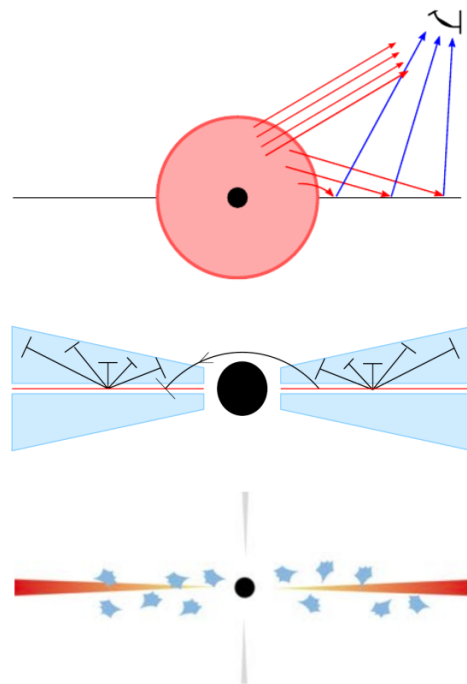


Figure 1.12: Top to bottom: Schematic diagram of spherical, sandwich and clumpy corona geometry. Credits: [Dovčiak et al. \(2012\)](#); [Schnittman & Krolik \(2010\)](#); [Malzac \(2018\)](#)

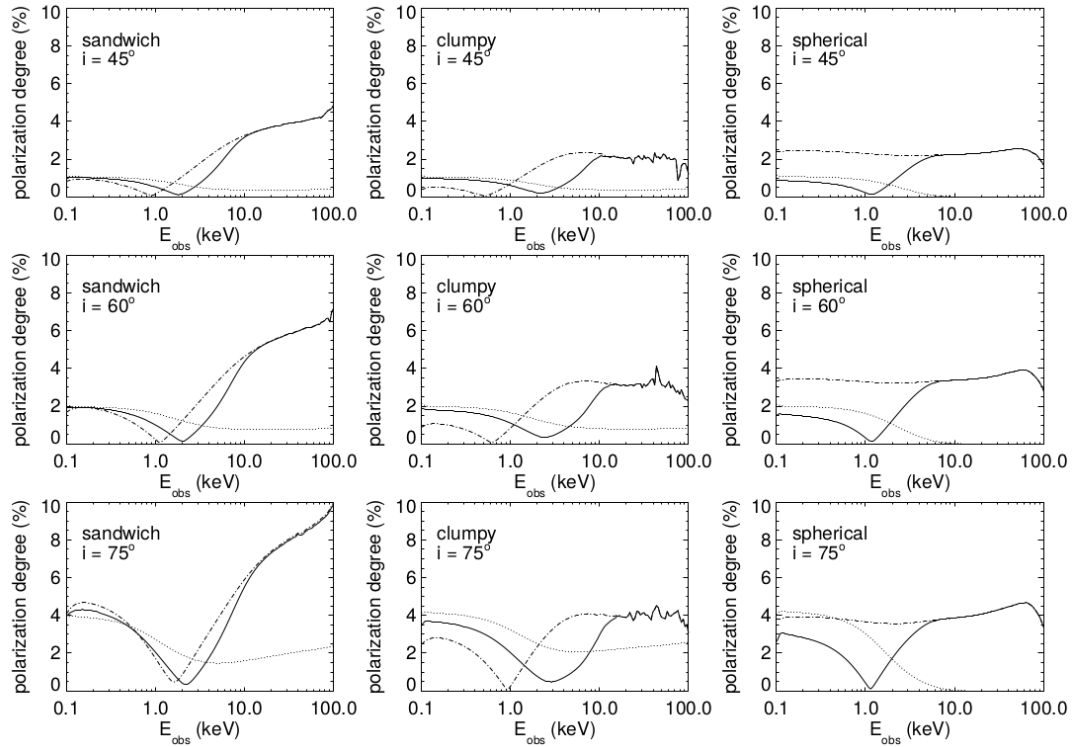


Figure 1.13: Polarisation parameters for different geometry of the extended corona. The solid line is for the total observed flux, dashed lines represents the thermal disk contribution and the dot-dashed lines represents the corona-scattered photons. Credits: [Schnittman & Krolik \(2010\)](#)

The X-rays from the disk are expected to be polarised due to scattering in the corona where polarisation degree depends upon the inclination of the source ([Schnittman & Krolik, 2010](#)). Some of the theoretical models suggest that the polarisation fraction and polarisation degree depend upon the gravitational lensing ([Dovčiak et al., 2008](#)). Photons originated from the vicinity of the black hole are more affected by the relativistic effects. Hence, polarisation studies of these photons can give insight about the inner part of the accretion disk. Observations in the hard X-ray band beyond 10 KeV can give information about the corona geometry because above 10 keV flux is dominated by coronal emission. Emission properties depend on the large number of parameters like black hole mass, spin and coronal properties like homogeneity, temperature, etc. X-ray polarimetry will allow to constrain the coronal models and its geometry. Beyond 100 keV emission is mainly non-thermal and supposed to be of jet origin. From the study of high polarisation measurement of the Cygnus X-1 suggest that it

is jet origin. Polarisation study can provide insight about the origin of the hard X-ray in these sources.

### 1.4.1.3 Lamp post corona model

This kind of coronal geometry was initially proposed by the [Matt et al. \(1991\)](#). According to this model, corona as a point source moves along the axis of the black hole. In this model, there are two free parameters related to geometry of the system, height ( $h$ ) of the corona above the black hole and the inclination ( $\theta$ ) of the accretion disk (i.g.  $\theta = 0$  for a face on observer). For low height of the corona the primary component is more reflected (see [Figure 1.11](#)). Polarisation parameters estimated using the simulation for the different coronal height and the inclination for the Kerr and Schwarzschild black hole are shown in [Figure 1.14,1.15](#) ([Dovčiak et al., 2011, 2012](#)). For the Kerr and Schwarzschild black hole polarisation parameters are significantly different for low lamp post height.

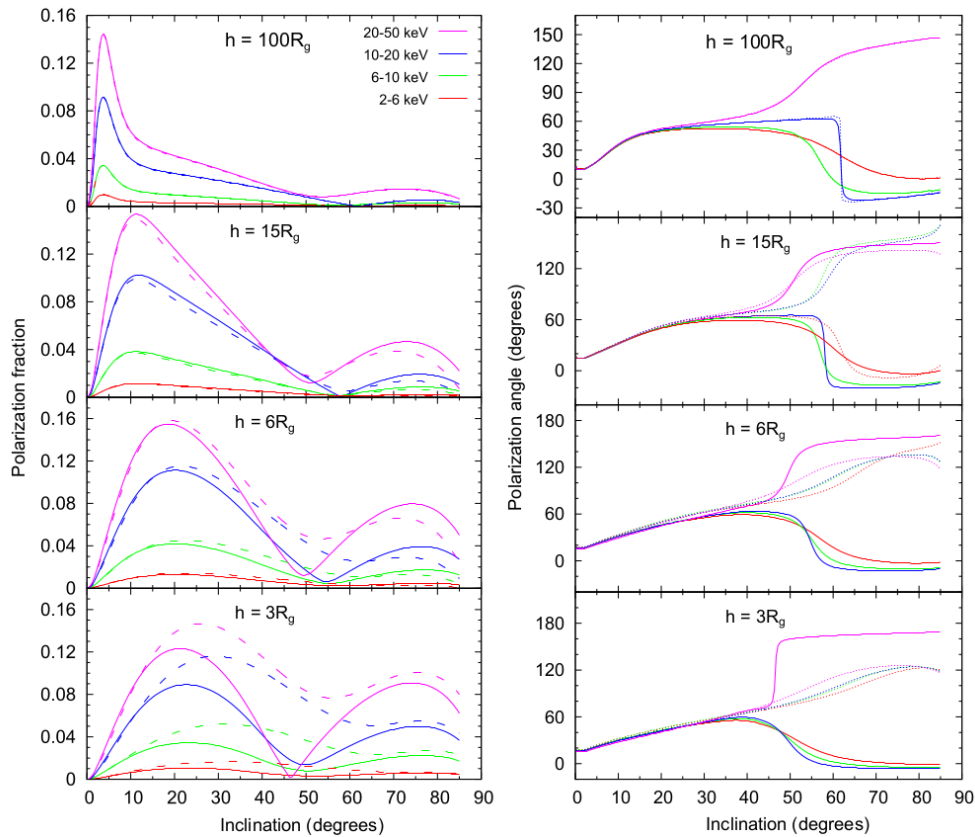


Figure 1.14: Polarisation parameters for the different height of the corona. The solid lines is for the Schwarzschild black hole and the dashed line represents the Kerr black holes. Credits: [Dovčiak et al. \(2011, 2012\)](#)

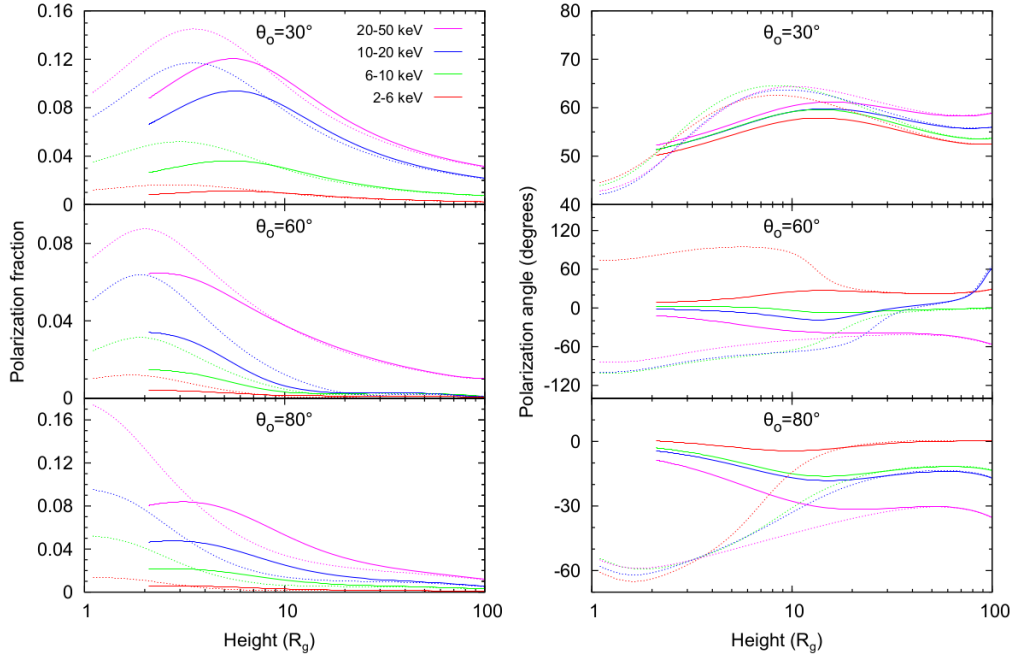


Figure 1.15: Polarisation parameters for the different inclination of the disk. The solid lines is for the Schwarzschild black hole and the dashed line represents the Kerr black holes. For Kerr black hole the lamp post height can be lower because its event horizon is at  $1R_g$  while it is  $2R_g$  for the Schwarzschild black hole. Credits: [Dovčiak et al. \(2011, 2012\)](#)

#### 1.4.1.4 Extended corona model

In the case of extended corona, different coronal geometries are possible: spherical, clumpy and sandwich corona. The shape of the corona affects the polarisation parameters of the X-ray emissions. The polarisation simulation for these geometries has been done by the [Schnittman & Krolik \(2010\)](#) for different inclination angles.

Theoretical and simulation studies ([Dovčiak et al., 2008](#)) suggest that there would be a change in the polarisation angle for photons due to gravitational relativistic (GR) effects. This can lead to depolarisation of the radiation when added up at infinity. The depolarisation effect is more prominent for the radiation emitted from the vicinity of the black hole. Since, the temperature of the inner disk is higher, therefore emits high energy photons. At lower energy, below 0.1 keV, the polarisation is expected to be same as that for Inter stellar medium. However, with increase in energy in 0.1 to 10 keV polarisation decreases possibly due to GR effect. Above 10 keV, the flux of the primary component dominates

over the reflection. For the sandwich corona, at 100 keV and higher inclination, the expected polarisation is about 10% and for lower inclination polarisation decreases. For the inhomogeneous clumpy corona, the polarisation is 3-4% because photons, after the multiple scattering in the spherical clumpy corona, eventually emerge with random electric field orientation leading to low polarisation. For the spherical corona geometry, the expected polarisation is 4% at 100 keV which is independent of inclination angle due to the spherical symmetry. Above 100 keV, the radiation is expected to be dominated by the jet contribution (Vadawale et al., 2001; Markoff et al., 2001) emitted by the synchrotron process, thereby, highly polarised (Romero et al., 2014).

The contribution of the coronal emission in the polarisation degree is significant but not very large (expected to be  $\sim 10\%$ ). However, larger polarisation degrees is expected if the X-ray emission is originated from the jet. For example, Laurent et al. (2011) reported polarisation degree of 67% above 400 keV and suggested it is from the jet by the synchrotron emission.

## 1.5 Cygnus X-1 overview

Cygnus X-1 is a brightest and persistent galactic source in the sky. It was first detected by rocket experiment (Geiger counter on board Aerobee rocket) in 1964 (Bowyer et al., 1965). It was mentioned as Cyg XR-1 in the Aerobee survey and later it is called as Cygnus X-1 as it is located in the constellation of the Cygnus, Swan in the milky way. The 9th magnitude star with a catalogue number HDE 226868 was identified with Cygnus X-1 having a period of  $\sim 5.6$  days (Webster & Murdin, 1972; Bolton, 1972). They observed that the HDE 226868 was located at radio position and optical spectra of the star is Doppler shifted which vary with a period of 5.6 days and correlated with the dip in soft x-rays (0.5-1 keV) intensity with a 5.6 day period.

Initial speculations about its nature were being a neutron star or triple system (Fabian et al., 1974) or a black hole (Bolton, 1972; Webster & Murdin, 1972; Pringle & Rees, 1972). To confirm the compact object in a binary system, dynamical mass measurement is the most accurate method. During the past five

decades many different estimations of the mass of the Cygnus X-1 compact object have been made. [Trimble et al. \(1973\)](#) estimated a mass of  $M < 1$  solar mass based on a model (assuming low luminous secondary) considering the distance  $D \approx 1$  kpc, suggesting a neutron star or a white dwarf, not a black hole as the compact object. But all the conventional binary models which considered O-type secondary exceed the mass of  $3M_{\odot}$  which is the maximum stable mass of the neutron star, hence requiring a black hole. For example, [Paczynski \(1974\)](#) found mass  $M > 3.6M_{\odot}$  considering  $D > 1.4$  kpc. The mass measurement based on the dynamical modeling by [Gies & Bolton \(1986\)](#) estimated  $M > 7M_{\odot}$ , and [Ninkov et al. \(1987\)](#) found  $M = 10M_{\odot}$ . It is concluded that the compact star must be a black hole. However, all the mass measurements were very uncertain due to unsatisfactory estimates of the distance ([Reid et al., 2011](#)). [Orosz et al. \(2011\)](#) found the black hole mass of  $14.8 \pm 1M_{\odot}$  and companion mass of  $19.2 \pm 1.9M_{\odot}$  using the dynamical modelling considering distance of 1.87 kpc from the trigonometric parallax using the Very Long Baseline Array ([Reid et al., 2011](#)). Recently, [Miller et al. 2022](#) refine the distance using radio astrometry and found distance of  $2.22^{+0.18}_{-0.17}$  kpc which leads to most accurate mass measurement of  $\sim 21.2^{+2.2}_{-2.2}M_{\odot}$  and O9.7 supergiant companion with a mass of  $\sim 40.6^{+7.7}_{-7.1}M_{\odot}$  using the dynamical mass measurements. It has inclination of  $27.516^{\circ}$  from the orbital plane and orbital period of 5.6 days ([Miller-Jones et al., 2021](#)).

Due to its brightness and proximity, it is observed by many instruments in wide energy range. The accretion states are mainly classified as: soft, hard and short lived intermediate state joining two main state based on the dominance of flux in different energy band. The typical HID diagram for the Cygnus X-1 is shown in [Figure 1.16](#). While LMXBs trace a 'q'-shaped hysteresis track on the HID, HMXBs do not show any hysteresis. Cyg X-1, in particular, spends most of its life in a hard state and sometimes undergo transition to a softer state through a series of intermediate states. The transitions mostly happen at similar luminosity levels and hence hysteresis effect is not observed ([Grinberg et al., 2013a](#)). It is also observed that the spectral index and flux can vary in same accretion state as shown in [Figure 1.17](#) ([Jourdain et al., 2012b](#)). In the hard state, a radio jet is observed having projection onto the sky plane is  $(158 \pm 5)^{\circ}$

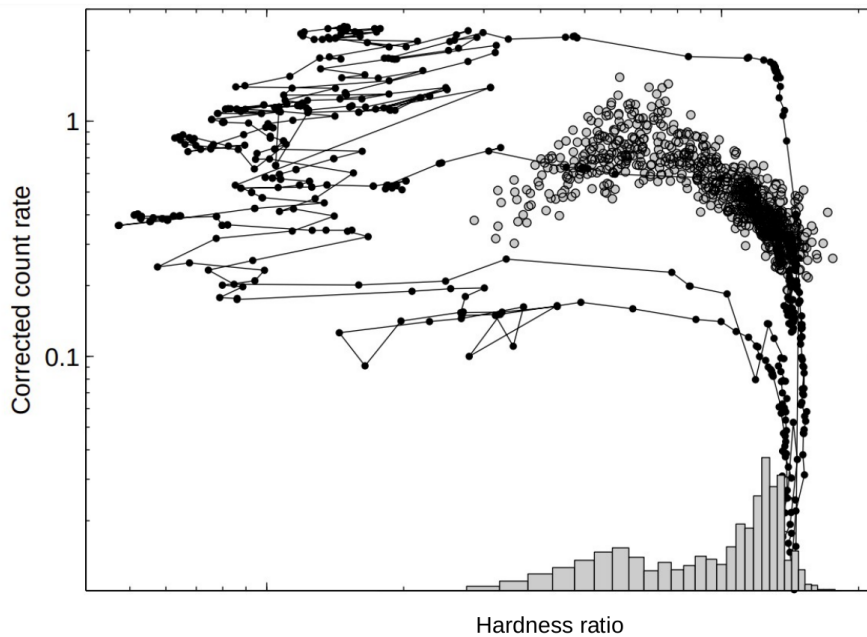


Figure 1.16: HID of Cygnus X-1 (gray circles) for all the RXTE/PCA observations overplotted on the HID of the transient black hole LMXB GX 339-4 (black circle) of the 2002/2003 and 2004/2005 outbursts. The histogram shows the distribution of hardness. Credits: [Belloni \(2010b\)](#)

([Fender et al., 2006](#); [Stirling et al., 2001](#)). The PDS (power density spectra) of Cyg X-1 are also known to be different compared to the LMXBs. The hard and intermediate state PDS of LMXBs consist of a zero-centered Lorentzian often accompanied by a QPO (quasi periodic oscillation) and its harmonics, or a peaked noise. The difference between them is only a reduction in the rms. For Cyg X-1, however, the PDS are fitted by two to four Lorentzians and no QPOs are ever detected ([Pottschmidt et al., 2003a](#); [Axelsson et al., 2005](#)). In soft states, both LMXBs and Cyg X-1 display a power-law shaped PDS.

The spin of the black hole in the Cygnus X-1 is very high. In BHB, the determination of the black hole spin can be done in two ways: continuum spectral fitting ([McClintock et al., 2014](#)) and fitting the profile of the iron line ([Walton et al., 2016](#)). A spin  $a > 0.983$  is inferred in soft state using the continuum fitting method by [Gou et al. \(2014\)](#) and [Walton et al. \(2016\)](#) reported spin between  $0.93 \lesssim a \lesssim 0.96$  fitting the iron line in reflection component in soft state. The spin estimation in continuum fitting depends upon the mass and the distance. Recently, [Miller-Jones et al. \(2021\)](#) found the spin parameter  $a > 0.9985$  close

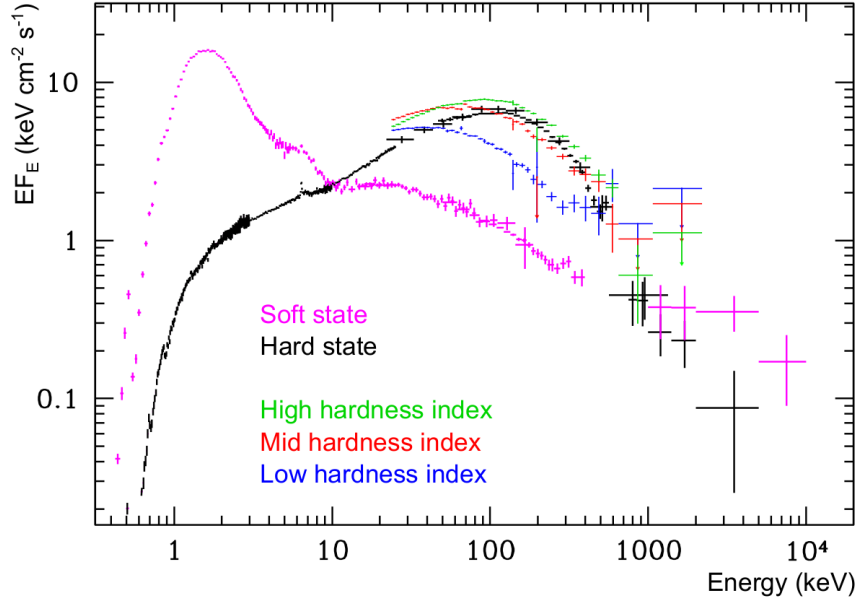


Figure 1.17: Spectrum of Cygnus X-1 for different accretion states. Credits: [McConnell et al. \(2002\)](#); [Jourdain et al. \(2012b\)](#)

to maximum value of 1 using the continuum fitting method considering  $21.2M_{\odot}$  mass black hole at a distance of 2.22 kpc ([Miller-Jones et al., 2021](#)).

### 1.5.1 Accretion

Cygnus X-1 accretes matter from the stellar wind from the companion O type star. The characteristic P Cygni profile observed in the  $H_{\alpha}$  emission from the companion indicates the mass loss in form of stellar wind ([Ninkov et al., 1987](#)). The typical mass loss rate of the O-B type star is  $10^{-6} - 10^{-5} M_{\odot} \text{ year}^{-1}$  ([Puls et al., 2008](#)). Stellar wind from the companion is ejected isotropically but in the presence of the black hole the equipotential surface of the system focus it through the L1 point ([Friend & Castor, 1982](#)). The stellar wind is highly supersonic with velocity  $v_w$  at a distance  $r$  from the center of the companion which is given by,

$$v_w(r) = \left( \frac{2GM_E}{R_E} \right)^{1/2} \quad (1.15)$$

where  $R_E$  and  $M_E$  are the radius and mass of the companion star, respectively. The wind particle pass close to the black hole get captured due to the gravitational potential energy and accreted by it.

## 1.5.2 Previous polarisation measurements

After a few initial attempts back in the 1970s to explore the polarisation properties of the source (e.g. a Bragg polarimeter onboard OSO-8 placed an upper limit of a few percent at 2.6 keV). Later, they estimated polarisation of  $2.4\% \pm 1.1\%$  at 2.6 keV and  $5.3\% \pm 2.5\%$  at 5.2 keV (Long et al., 1980). Lately, there have been some valiant attempts to measure the polarisation of this source in hard X-rays, both in the coronal regime (few 10s of keV to  $\sim 100$  keV) and the suspected jet regime (above 100 keV). The detailed summary of the polarisation measurement results of Cygnus X-1 by various instruments is discussed by Chattopadhyay (2021); Russell et al. (2014). IBIS and SPI, onboard *INTEGRAL* independently estimated high polarisation for this source at  $\sim 67\%$  with sky polarisation angle of 224 degrees (north-east) at energies above 400 keV, while the emission in 250 to 400 keV being weakly polarized or unpolarized (Laurent et al., 2011; Jourdain et al., 2012a). The results were interpreted as jet origin of the photons corroborated by simultaneously observed two distinct spectral components of the source, a thermal Comptonization component at energies below 400 keV and a power law component with a power law of photon index 1.6 beyond 400 keV, primarily due to synchrotron radiation from the jet (Laurent et al., 2011). We note that the polarisation analysis of *INTEGRAL* lacking on-ground polarimetric calibration. Zdziarski et al. (2014) modelled the wide band spectral energy distribution of Cygnus X-1 spanning from radio to MeV and reported negligible contribution of synchrotron jet emission in X-rays for a realistic set of model parameters. They showed that some nonphysical assumptions for efficient particle acceleration and jet magnetic fields above equipartition level are needed to explain the contribution of the jet in the X-ray energy range as reported by *INTEGRAL*, thus questioning the *INTEGRAL* polarization results. *PoGO+*, a dedicated balloon-borne hard X-ray polarimeter (19 - 181 keV) observed the Cygnus X-1 between 12 - 18 July 2016 totalling 123.5 ks observation and given the upper limit of the polarisation in the hard state (Chauvin et al., 2019). They placed an upper limit of 4.8% at a position angle of  $154 \pm 31^\circ$ . They found an upper limit of 11.6%, 2.2%, and 2.9% assuming position angle perpendicular to the accretion

disk ( $\pm 155^\circ$ ), parallel to the disk ( $\pm 330^\circ$ ), and position angle aligned to that of *INTEGRAL* results ( $\pm 222^\circ$ ). These results favour the hard X-ray flux to be originating from an extended corona which has a small fraction of the reflection component in the hard X-ray band (Chauvin et al., 2018, 2019). These results also give an upper limit of polarisation for the jet component around 5 - 10% when the emission from the extended corona was assumed to be accompanied by a synchrotron jet in the energy range  $< 200$  keV. More recently, IXPE, a photoelectric polarimeter, reported the  $4 \pm 0.2\%$  polarisation in the energy range of 2 - 8 keV and the polarisation angle is aligned with the outflowing radio jet. They explained their results by considering the outflowing corona which is extended perpendicular to the jet axis.

## 1.6 Thesis outline

In the X-ray sky, black hole binaries are one of the most peculiar astrophysical sources to understand the physics in the extreme conditions such as high gravity, extreme temperature, and magnetic field. Black hole X-ray binaries are the binary systems in which the compact object is the accreting black hole and a normal companion (donor) star. Accretion of matter onto black hole gives rise to the X-rays along with other wavelengths to study their properties. Because X-rays are produced primarily in extreme conditions, they are important to investigate in order to probe the high gravity, extreme temperature and magnetic field region around black hole. The typical geometry of accreting environment around the black hole is based on spectroscopic and timing studies. It consists of an optically thick and geometrically thin disk accreting matter from the companion star. The region close to the black hole comprises optically thin and geometrically thick hot cloud of electron called the corona. There is also evidence of bipolar outflows in form of jet originating from the central region. X-ray spectroscopic and timing properties of BHBs have been explored abundantly. The X-ray spectrum of the black hole binary consists of three components: (1) thermal radiation from the disk (2) powerlaw component due to the Comptonisation of the seed photons coming from the disk in the hot atmosphere of the black hole

(called corona) (3) reflected component due to the reflection of the Comptonized photons from the disk. The variability of the source is studied using the power spectrum which is the Fourier transform of a time series. Apart from the thermal Comptonisation, there is also a non-thermal component which can be produced by the non-thermal Comptonisation (Coppi, 1999) and the synchrotron radiation from the jet (van Paradijs & McClintock, 1995). There are more than one possibilities/models which can explain the timing and spectroscopy observations. Therefore, there is no general consensus over exact geometry of the corona/jet. To break the degeneracy, some new parameters are required to decipher the fluxes from the different processes. The photons have one more property i.e., polarisation (photons orientation of the electric field vector), remains mostly unexplored due to requirement of relatively longer exposure times and control of systematic uncertainties. The polarisation measurements give two information about the radiation: polarisation angle and polarisation fraction. Polarisation with the unison of spectroscopy can give information about the source geometry and various astrophysical phenomena. Science potential of the polarisation measurement is well known, but the technological and instrumentation advancement in this direction is less compared to spectroscopy, timing, and imaging.

The underlying theme of this thesis is to understand hard X-ray spectro-polarimetric characteristics of Cygnus X-1 using observations with AstroSat-CZTI, and to design a new spectro-polarimeter that can provide better constraints on the observations. In this chapter, a brief overview of the subject matter is presented from describing the various emission processes to the characterization of the BHB Cygnus X-1 and polarisation in X-rays. Rest of the thesis is organized as follows:

### **Chapter 2:** Instrumentation and data analysis

This chapter presents a detailed description of the analysis techniques - polarisation, spectroscopy and timing used in the work along with a brief description of the instruments and telescopes used in the thesis - *AstroSat* , *Swift* , and *NuSTAR* .

**Chapter 3:** Hard X-ray polarisation measurement of Cygnus X-1 with *AstroSat-CZTI*

The results of the polarisation measurements of the galactic HMBH Cygnus X-1 are presented using the *AstroSat*-CZTI data. We found there is an increase in the polarisation with energy which is similar to the INTEGRAL result. This may be due to the increase in the polarised component, which is energy dependent. We can decipher different polarised component with the help of spectroscopy using the same polarisation photons.

**Chapter 4:** Extending the energy range of *AstroSat*-CZTI up to 380 keV with Compton spectroscopy using Crab

This work presents the exploration and extension of the primary spectroscopic energy range of the CZTI using the same photons which are used for the polarisation measurement. The methodology of the background subtraction and selection is developed and at the same time try to constrain the spectral parameters of the Crab.

**Chapter 5:** Dependence of hard X-ray polarization on spectral states in Cygnus X-1

The spectroscopic study of the Cygnus X-1 in the primary spectroscopic range of the CZTI is presented using the 5 years of the CZTI data. We have found out different spectral states based on the spectral index and flux correlation. The extended energy range of the CZTI is also used to do the spectroscopy in broad energy range of 30-380 keV to decipher different spectral components of the polarisation and its dependence on different spectral states of Cygnus X-1. Further, the broad band PDS in 0.1-20 Hz range is fitted with the combination of power law and Lorentzian to trace the power spectral variation in different spectral states. The correlation between different PDS modelled parameters are also explored.

**Chapter 6:** Focal plane hard X-ray Compton spectro-polarimeter

The Conceptual design of the Compton spectro-polarimeter based on the plastic scintillator as the scatterer surrounded by the NaI(Tl) scintillator in circular fashion as the absorber for the scattered photons read out at two ends by the SiPM (Silicon photo-multiplier) arrays. The details of the modulation factor, efficiency and the polarimetric efficiency of the conceptual design is discussed which is done analytically. We have characterised the position-sensitive NaI(Tl)

detector experimentally. The details of the experiments and the simulation are discussed.

**Chapter 7:** Summary and scope for future work

We review all of our results primarily the polarisation measurement of Cygnus X-1 and its spectral state dependence. We have also extended the spectroscopic energy range of the CZTI to see the contribution of the polarisation component above 100 keV. Finally, we explore the implications of these results for understanding the Cygnus X-1 emission mechanism and geometry. The necessity of the Compton Spectro-polarimeter below 100 keV is shown and carried out the experimental and analytical calculation of same. This work's future prospects are also discussed.

# Chapter 2

## Instrumentation and data analysis

### 2.1 Instrumentation

The earth's atmosphere only allows selective wavelength range to pass through it and reach us. While it allows visible, parts of infrared, and radio wavebands, it prevents  $\gamma$ -rays, X-rays, UV, far infrared and very long wavelength radio waves from coming on the earth's surface. The blockage of, particularly, high energy photons due to the atmosphere is beneficial for living creatures on earth but it has thrown challenges for X-ray astronomers. The Earth's atmosphere absorbs X-rays, thereby preventing them from reaching below  $\sim 30$  km altitude (Seward & Charles, 2010). Therefore, to study astrophysical sources in X-rays requires taking the instruments by balloons, sounding rockets, and satellites above the atmosphere, which makes it quite challenging. One such attempt was made in 1949 to study the solar X-rays using the V-2 sounding rocket experiment (Friedman et al., 1951). Consequently, in 1962 a group of scientists led by Riccardo Giacconi launched the Aerobee rocket, which carried Geiger counters to study solar radiation reflected from the surface of the moon. They failed to detect any X-rays from the moon but serendipitously discovered a powerful cosmic X-ray source later named Scorpius X-1 (Giacconi et al., 1962). X-ray astronomy, in a true sense, began with the serendipitous discovery of Scorpius X-1. It was later found to be a neutron star binary system. In such bi-

nary systems, the companion can be a compact object like a black hole, neutron star, and white dwarf. The first dedicated X-ray satellite *Uhuru* was launched by NASA on 12 December 1970 which made many important discoveries and paved the way for several X-ray missions (Giacconi et al., 1971a,b; Tananbaum et al., 1971; Oda et al., 1971; Forman et al., 1978). X-rays were found to be released from different types of astrophysical sources like neutron stars, black holes, supernova remnants, galaxies, and galaxy clusters. In this thesis, we focused our studies on one class of object, namely X-ray binaries, where primarily the origin of high energy photon is through the accretion of matter around the compact object. The release of the gravitational energy due to the accretion of the matter is the main source of the radiation emission (Zeldovich & Guseynov, 1966). The study of such astrophysical sources allows the understanding of the accretion around the compact objects, emission mechanism, the geometry of the sources, and physical processes in extreme conditions like the high magnetic field of the order of  $10^{12}$  Gauss or more in case of magnetars, high temperature of the order of  $10^7$  K, strong gravity, etc.

During the last five decades, high-energy astrophysics saw a huge amount of attention for the physical understanding of the Universe which led to the advancement of technologies. The development of the proportional counter to calorimeters, and collimators to focusing optics has happened. Tremendous feat has been achieved in instrumentation and will be continued to do so with many new missions lined up to be launched in future.

### 2.1.1 X-ray detectors

X-ray detectors work in the photon counting mode where the information of an individual photon like energy, its arrival time, location on the detector and its polarisation state, is stored. Due to higher energy of the X-ray photon a single photon has enough energy to generate sufficient charge to convert into electronic signal which gives all the information of mentioned parameters. But there is often the case where a trade-off between these properties need to be done for precise measurement of the other. Almost all the X-ray detectors do

not differentiate between the real X-ray photon and the other ionizing radiation or charge particle. Therefore, the detector must be designed such that it can return enough information to distinguish the signal coming from the an X-ray photon and other effects mentioned.

Different types of X-ray detectors have been developed depending on the various science goals. Proportional counters can be one of the simplest devices among the X-ray detectors and thus, widely used historically. The PCA and LAXPC onboard *RXTE* and *AstroSat* , respectively, are a couple of examples of proportional counters. A typical proportional counter consists of a grounded box filled with inert gas with a high voltage wire in the middle and a window to allow X-ray radiation. The X-ray photons produces ion pairs (an electron and the ion) in the box. If the energy of the X-ray photon is large enough compared to the energy required to produce an ion pair, remaining energy is used by primary photo-electron to generate secondary ion pairs. As these primary and secondary electrons travel towards the anode wires at high voltage along the electric field, they get accelerated. As a result, they ionize more atoms in the way and create strong electric field near the anode wire reaching an avalanche. This amplifies the original signal which is then stored and transmitted along with information about the time of arrival. In proportional counters, the charged particles are mostly generated by the process of photoelectric effect.

The other most widely used detector, invented in 1969 at Bell laboratories, is Charged Coupled Device (CCD). Their high sensitivity and linear brightness response revolutionized their use in astronomy. In X-ray, *ASCA* was the first satellite with X-ray CCD camera. Since then, CCDs have become ubiquitous in recent past, present and future planned X-ray missions. Many X-ray instruments such as SXT (*AstroSat* ), EPIC (*XMM Newton* ), XRT (*Swift* ) are such examples. A CCD is an array of joint semiconductor where the incoming photon interact and generate electron-hole pairs. The charge carriers are collected with the applied external electric field and stored in pixels. This charge is transferred from one pixel to another pixel in serial mode and digitized at the readout amplifier. Both positional and spectral information can be stored with high level of accuracy using CCDs. Fast timing response can also be achieved

at the cost of positional information. Most CCD-based detectors have special modes where only a part of the CCD, illuminated by the source, is read out to decrease the readout time. However, even with such a trade-off time resolutions much better than 100 ms are difficult to attain.

For detecting X-rays above 10 keV, the standard modern instrument is CZT or CdZnTe. The CZT detectors operate in a similar way as CCDs because both have semiconductor substrate with an exception that in CZT every pixel is read independently unlike CCDs. CZT detectors are preferred over CCDs at higher energies due to the reason of higher cross-section than Si resulting better quantum efficiency. More details about different kinds of detectors and their properties can be found in [Knoll \(2000\)](#) and [Arnaud et al. \(2011\)](#)

## 2.1.2 X-ray observatories

In the following section, a brief introduction of the X-ray observatories used in this thesis work is described:

### 2.1.2.1 *AstroSat*

*AstroSat* is the India's first multi-wavelength satellite working simultaneously the X-ray, UV, and optical wave bands. It was launched on 28 September 2015. It has five primary science instruments - (1) Ultra Violet Imaging Telescope (UVIT; [Tandon et al., 2017](#)), (2) Soft X-ray Telescope (SXT; [Singh et al., 2016, 2017](#)), (3) Large Area X-ray Proportional Counter (LAXPC; [Yadav et al., 2016b,a](#); [Antia et al., 2017](#)), (4) Cadmium Zinc Telluride Imager (CZTI; [Vadawale et al., 2016](#); [Bhalerao et al., 2017a](#)), (5) Scanning Sky Monitor (SSM; [Ramadevi et al., 2017](#)) and a Charge Particle Monitor (CPM). The SSM is equipped with three position sensitive proportional counters and is used to surveys the sky in soft X-ray (2-10 keV) range. It was employed for long term monitoring of X-ray bright sources, and detection of new X-ray outbursts.

The CPM directs the satellite to switch off the detectors in the South Atlantic Anomaly (SAA) region to prevent the damage and ageing. This instrument detects the flux of protons and electrons in SAA. *Astrosat*'s capabilities

can be compared to both Swift and RXTE combined. The SXT, BAT, and UVOT instruments of *Swift* are corresponding to the XRT, CZTI, and UVIT while LAXPC and SSM are similar to the PCA (Proportional Counter Array) and ASM (All Sky Monitor) of RXTE satellite.

The UVIT consists of two telescopes with aperture size of 38 cm each. It has three UV and optical bands : (1) Far-UV (130 - 180 nm), (2) Near-UV (180 - 300 nm), and (3) optical (320 - 530 nm) and each band has its separate detector system. UVIT provides the high angular resolution of around 1.8'' in the UV and 2.5'' in the optical bands and circular FOV with 28' diameter.

The SXT is sensitive to soft X-rays in the energy range of 0.3 - 8 keV. The SXT telescope houses tubular structure of X-ray reflecting mirror and focusing optics. The optics consists of 41 gold-coated conical concentric shells in an approximate Wolter-I configuration which gives a focal length of 20 cm. SXT has a FOV of  $\sim 40'$  diameter with an effective area of 90 cm<sup>2</sup> at 1.5 keV. It provides an energy resolution of 90 eV at 1.5 keV and 136 eV at 5.9 keV. SXT can work either in a full frame or a centered-pixel frame giving time resolution of 2.4 s and 0.278 s, respectively.

The LAXPC is major payload onboard *AstroSat* and consists of three proportional counters with a large effective area of about 6000 cm<sup>2</sup> in 5 - 20 keV. Each LAXPC is filled with high pressure (2 atm) Xenon gas resulting in detection efficiency of  $> 50\%$  in the 30 - 50 keV band and has five anode layers with each layer having 12 anode cells and is surrounded on three sides with Veto cells. LAXPC gives very high time resolution of 10  $\mu$ s making it suitable for exploring rapid variability of different sources. It has a moderate spectral resolution of 12 - 15% in 22 - 60 keV and FOV of  $0.9^\circ \times 0.9^\circ$ .

The CZTI (Cadmium Zinc Telluride Imager) is a hard X-ray coded mask imager and spectrometer onboard India's first dedicated astronomy satellite (Singh et al., 2014; Singh, 2022; Paul, 2013), sensitive in the energy range of 20 - 100 keV. CZTI consists of four identical quadrants with 16 Cadmium Zinc Telluride (CZT) detector modules per quadrant. Each CZT module is 5 mm thick and 39.06 mm  $\times$  39.06 mm in dimension, totaling to a geometric area of 976 cm<sup>2</sup> (Vadawale et al., 2016). The CZT modules are pixelated in 16  $\times$  16

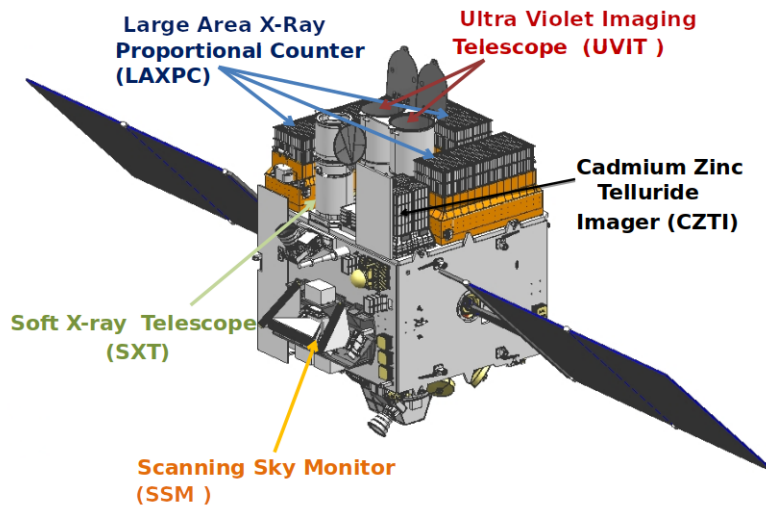


Figure 2.1: The *AstroSat* observatory. Image courtesy: [https://webapps.issdc.gov.in/astro\\$\\_\\$archive/archive/Home.jsp](https://webapps.issdc.gov.in/astro$_$archive/archive/Home.jsp)

array of pixels with a pixel size of  $2.46 \text{ mm} \times 2.46 \text{ mm}$  except for the edge row pixels having slightly smaller dimensions. CZTI is equipped with a 0.5 mm thick Tantalum coded aperture mask (CAM) for simultaneous imaging and background measurement. The CAM is supported by passive collimators and placed at a distance of 478 mm above the detector plane. Below each CZTI quadrant, there is a CsI(Tl) anti-coincidence detector (veto) at around 65 mm from the detector plane. The CsI crystal, with a thickness of 20 mm and cross-section of  $167 \text{ mm} \times 167 \text{ mm}$ , is read out by two Photo-Multiplier Tubes (PMT) from two sides of the crystal. The veto detector acts as the active shielding for the charged particle induced X-ray like signatures and the background gamma-ray radiation at higher energies (above 100 keV). Each detector module has collimated FOV of  $4.6^\circ \times 4.6^\circ$ . It has a spectral resolution of  $\sim 6\%$  at 100 keV and a time resolution of  $20 \mu\text{s}$ . More instrument details are given in [Bhalerao et al. \(2017b\)](#). The collimators and the coded mask become progressively transparent above 100 keV. CZTI acts as an open detector above 100 keV and is sensitive to the polarisation of the incident photons thanks to its large pixelated detector plane ([Chattopadhyay et al., 2014a](#); [Vadawale et al., 2015](#)). Its capability of the polarisation measurement is extensively used in this thesis and it is described in details in the later sections.

### 2.1.2.2 Other X-ray observatories

#### **INTErnational Gamma-Ray Astrophysics Laboratory (INTEGRAL)**

INTEGRAL was launched on 17 October 2002 from Proton-DM2 by European Space Agency to study the gamma-ray emission mechanism in astronomy such as nuclear excitation, positron annihilation and Compton scattering. It is the most sensitive satellite in MeV energy range. It provides the higher sensitivity in the energy range higher than the X-ray instruments such as *XMM Newton*, *NuSTAR* and lower than the gamma-ray instruments like Fermi. It allows the time resolution of milliseconds order, energy resolution of keV order and polarisation measurements. INTEGRAL carries a variety of instruments onboard, namely, a SPectrometer aboard INTEGRAL (SPI), two Joint European X-Ray Monitors (JEM-X1 and JEM-X2), an Imager on Board the INTEGRAL Satellite (IBIS), and an Optical Monitoring Camera (OMC). SPI, JEM-X, and IBIS have coded masks having a wide field-of-view (FoV) and the operating energy range varies from 15 keV to 10 MeV. The JEM-X works in the energy range 3 - 35 keV, whereas SPI and IBIS have energy ranges operating between 18 keV to 8 MeV and 15 keV to 10 MeV, respectively. SPI is ideally-suited for hard X-ray high-resolution spectrometry and gamma-ray up to MeV energies (i.e nuclear lines from radioactive isotopes). Further, the primary capability of IBIS dwells in hard X-ray imaging and gamma-ray range with high angular resolution. In addition, a particle radiation monitor, also known as INTEGRAL Radiation Environment Monitor (IREM), is an essential component which measures the rate of incoming highly-energetic particles that can damage the spacecraft instruments. All the instruments in the INTEGRAL operate simultaneously and it follows a highly elliptical orbit.

In this thesis SPI has been utilized primarily, therefore, only SPI has been described in the following section.

SPI is a spectrometer, working in the energy range 20 keV to 8 MeV (i.e from hard X-ray to soft gamma-ray), with energy resolution of 3 keV at 1.8 MeV ( $\Delta E/E \approx 0.18\%$ ). 19 High Purity Germanium (HPGe) detectors are placed at the core of the instrument, encompassing an anti-coincidence

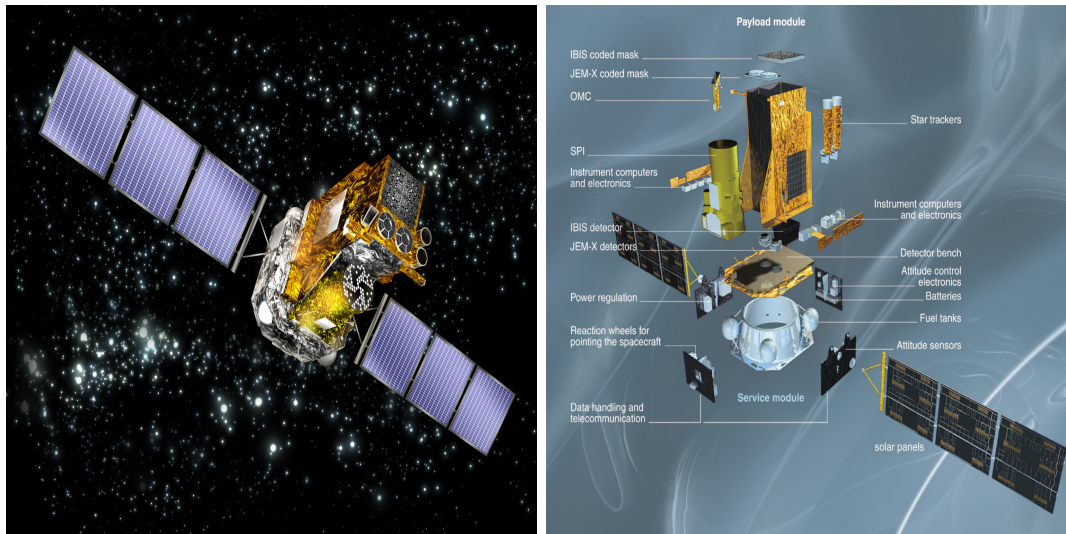


Figure 2.2: The *AstroSat* observatory. Image courtesy: <https://www.cosmos.esa.int/web/integral/mission-overview>

shield (ACS) and cooled at 80 K. The high imaging capabilities of SPI are imparted by a coded mask and the design is such that the configuration of 19 detectors can be accommodated. SPI is able to detect transient gamma-ray sources, for example, gamma-ray bursts. It has capability of time-tagging of detector event with a precision of 50 ns. Apart from spectrometry, SPI can also be used as a polarimeter. The photons having energy above 130 keV undergo Compton scattering in one detector and absorbed by the other one (making a so-called “multiple events” (ME)). During the Compton scattering photons are diffused azimuthally in a plane perpendicular to the electric (or polarisation) vector. Thereby, spatial distribution of “multiple events” embed the information of polarisation of incident photons. Initially, at the start of the mission, SPI provided the effective area between 10-50 cm<sup>2</sup> for the ME but later it degraded to 52 % of the primary area due to the failure of 4 detectors. GRBs (GRB041219A; McGlynn et al., 2007) were the first candidate for the polarimetric studies from SPI and later extended to the pulsars.

**Neil Gehrels Swift Observatory (*Swift*)** The *Swift* observatory (Gehrels et al., 2004) was primarily designed for detecting gamma-ray bursts (GRBs) and their afterglow in multi-wavelength range. It was launched on 20

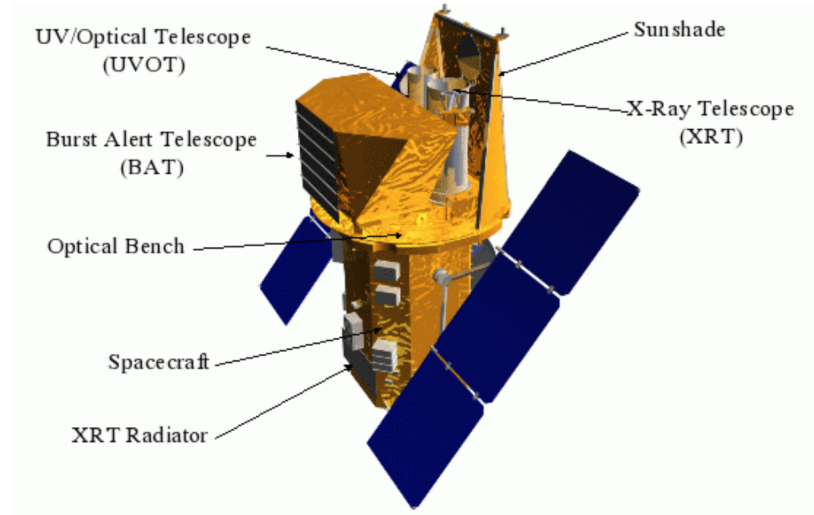


Figure 2.3: The *Swift* observatory. Image courtesy: <https://www.swift.ac.uk/about/instruments.php>

November 2004 and since then it is continuously scanning all kinds of X-ray sources in the sky. *Swift* has three instruments onboard: the Burst Alert Telescope (BAT; Barthelmy et al., 2005) in hard X-ray which quickly detects a source and slew the satellite at the source position, the X-ray Telescope (XRT; Burrows et al., 2005) in soft X-ray (below 10 keV) and the Ultra-violet/Optical Telescope (UVOT; Roming et al., 2005) in UV and optical wavebands. We have used BAT in this work for state classification. BAT is a coded mask imager with field of view of 1.4 steradians that works in 15 - 150 keV. It can measure the position of a GRB with an accuracy of  $\sim 4'$  within a few seconds. After some onboard merit estimation, it sends the position to the spacecraft to slew to the location for pointed follow-up observations. The detector of the BAT is made up of CdZnTe (CZT) with a detector area of 5240 cm<sup>2</sup>. The CZT detector consists of 32500 detector elements that can pin-point the location of sources within 1.4 arcminutes. The BAT has two operation modes : (i) the burst mode, which locates the burst position and (ii) the hard X-ray survey mode that scans the hard X-ray sky.

**Nuclear Spectroscopic Telescope Array (*NuSTAR*)** *NuSTAR* (Harrison et al., 2013) is the first observatory and so far the only one to use focusing optics to observe hard X-rays in the range 3 - 79 keV. It was launched on June 13, 2012 as a Small Explorer satellite mission (SMEX) led by the California Institute of Technology (Caltech) and Jet Propulsion Laboratory (JPL),

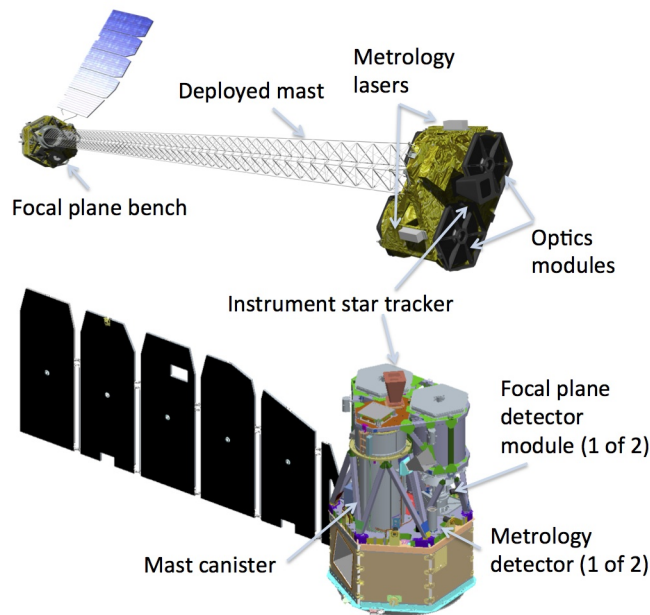


Figure 2.4: Schematic view of the NuSTAR observatory in the stowed (bottom) and deployed (top) configurations. The figure is taken from [Harrison et al. \(2013\)](#)

into a low equatorial earth orbit (with an inclination  $\sim 6^\circ$ ) at an altitude of 600 - 610 km and an orbital period of 97.126 minutes. The telescopes are developed with a Wolter type-I conical approximation with 10.15 m focal length and is separated from the detectors with the help of a long deployable “mast”. To get the exact relative positions of the optics and the focal plane, a laser metrology system is used. A mirror unit consists of 133 concentric shells, each coated with a depth-graded multilayer of high and low density materials (Pt/SiC and W/Si). This arrangement of layers help us to achieve reflectivity upto 78.4 keV. Above this energy, the mirror coating starts absorbing instead of reflecting hard X-ray photons. *NuSTAR* has two Focal Plane Modules A & B (FPM) for each telescope. Each module consists of four ( $2 \times 2$ ) pixelated CdZnTe detectors that result in a FOV of  $\sim 12'$  and an energy resolution of 400 eV at 10 keV. Each pixel of the FPM is individually read-out on X-ray interaction using the smartly designed electronics which ensures that *NuSTAR* observations do not suffer from pile-up until the incoming flux of about  $10^5$  counts  $s^{-1}pixel^{-1}$  is reached.

## 2.2 Spectral analysis

### 2.2.1 X-ray data fitting

In this thesis work, we used the X-ray spectral fitting package **XSPEC** (Arnaud, 1996) to fit the data. **XSPEC** is a command-driven X-ray spectral-fitting program which is available as an integrated part of **HEASoft**. It is independent of the instrument from which the data has been accumulated. The observed spectrum of a source is obtained in terms of instrumental quantities i.e., photon counts ( $C$ ) as a function of instrument channel ( $I$ ). But it is not the actual description of the source properties. This count spectrum is governed by the transfer function of the entire telescope and detector which needs to be decoded. However, what we are interested in is the intrinsic source spectrum ( $S$ ) i.e., count rate per energy bin. The actual spectrum is related to the observed spectrum as follows:

$$C(I) = \int S(E) R(I, E) dE \quad , \quad (2.1)$$

where  $R(I, E)$  is the response matrix of the instrument.  $R(I, E)$  is a product of the redistribution matrix (RMF - Redistribution Matrix File) and the instrument energy dependent effective area (ARF - Auxiliary Response File). The RMF is the response matrix, or probability that a photon with energy  $E$  would be observed in the channel  $I$ . To obtain  $S(E)$ , above equation needs to be inverted. But this is not straightforward because equation 2.1 is not invertible. Rather, an alternative “forward-fitting approach” is to choose a model spectrum  $M(I)$ , that can be described in terms of some parameters and mimic the actual spectrum. This model is convoluted with the instrumental response and effective area to output a spectrum in the same units as the observed spectrum. The folded model and the observed spectrum are then compared using fit statistics. After getting the best fit parameter values, confidence intervals are calculated for the best-fit parameters. The most common statistic, is chi-squared ( $\chi^2$ ) which is defined as:

$$\chi^2 = \sum \frac{(C(I) - C_p(I))^2}{\sigma(I)^2} \quad , \quad (2.2)$$

where  $C_p(I)$  is the count rate calculated from the model and  $\sigma(I)$  is the error for each channel and is estimated as  $\sqrt{C(I)}$ .  $\chi^2$  statistics require that the background subtracted counts in each spectral channel should follow a Gaussian distribution. Thumb rule is, for best-fit, the expected value of “Reduced- $\chi^2 = \chi^2/(\text{dof})$ ” is approximately equal to one for any acceptable model. Here, the number of degrees of freedom (dof) is calculated as the number of channels/bins minus the number of model parameters of the best-fitted model. For the case of low count statistics (or low source counts), it is more appropriate to use C-statistic (CSTAT) for the spectral fitting. Sometimes we encounter a situation while fitting multiple models in one observation that more than one model fit the data well. In such cases the best model is chosen by comparing the physical relevance of the best-fit parameters.

## 2.2.2 Data reduction

The X-ray detectors store three main information of each falling photon (referred as an event) such as arrival time, pulse height amplitude and arrival position on the detector. These three attributes are used to generate science products i.e., light curves (Count/flux vs. time plot), spectra and images. The raw data of each X-ray observation are stored in a Flexible Image Transport System (FITS) (FITS; [Pence et al., 2010](#)) format and are processed to generate a cleaned and filtered “event” file. It is named “event” file because it saves the information of each interaction of the photon or the charged particle with the detector. The primary information that are stored in an event file are the photon (or particle) interaction time, the position of the interaction (X and Y coordinates for a CCD and layers for a proportional counter), the pulse-invariant channel (energy information), and the count rate. Many other auxiliary information is also stored like about the instruments, satellite, etc. The filtering criteria for the raw data varies from instrument to instrument, but mostly it involves the removal of the obvious sources of spurious signals, such as those originating due to bad (hot or flickering) pixels, undershoot and overshoot of the discriminators, afterglows etc. The information about these issues are stored in the Calibration Database of the

instrument (CALDB<sup>\*</sup>). The analysis pipelines of most of the observatories also provide enough flexibility to the users to customize the reduction process as per need. Once the cleaned event file is created, the next task is to extract science products, i.e., spectra, lightcurves and images. Some observatories like *AstroSat* (LAXPC) or *NuSTAR* have their own extractors, others like *NICER* and *Swift* are reduced using the common FTOOL `xselect`<sup>†</sup> for extraction of the science products. The details of the analysis procedure for different instruments used in the thesis will be discussed in the respective chapters.

Once the spectrum is extracted, the next job is to find a suitable model that mimics the source and fit (Section 2.2.1). The fitting is carried out using packages such as `xspec`, `Sherpa`, `ISIS`, etc. In this thesis, `xspec` is used for fitting both the energy and power spectra. `xspec` has a huge repository of empirical and physical models and it also allows to load other local models. In the next subsection, the properties of some of these models used in the thesis are discussed.

### 2.2.3 Spectral models

As discussed in Section 1.3.4 of chapter 1, the X-ray spectrum of a black-hole binary typically consists of three components - a thermal blackbody, a power law for Comptonisation, and a reflection component. Figure 2.5 shows these three components in broad energy band. Several models have been developed over the years trying to compute the spectrum of one or more of these components. In this section, the models used in the thesis will be discussed in detail.

#### 2.2.3.1 Empirical models

Some of the common `xspec` models used in this work are `diskbb`, `powerlaw`, and `gaussian` to account for the thermal emission from an accretion disk, power-law emission due to inverse Comptonisation and synchrotron.

---

<sup>\*</sup>[https://heasarc.gsfc.nasa.gov/docs/heasarc/caldb/caldb\\_intro.html](https://heasarc.gsfc.nasa.gov/docs/heasarc/caldb/caldb_intro.html)

<sup>†</sup><https://heasarc.gsfc.nasa.gov/ftools/xselect/>

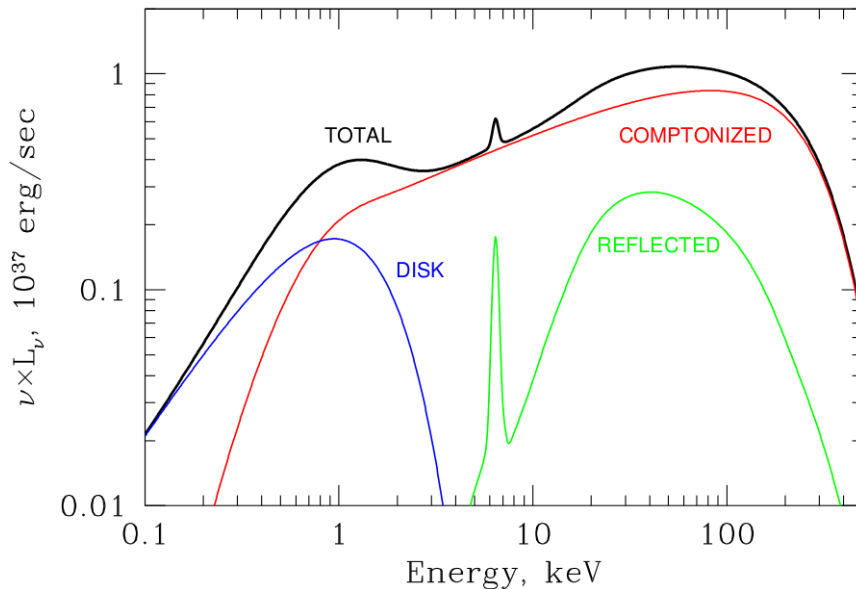


Figure 2.5: The schematic diagram of the X-ray spectrum for a black-hole binary. The blue, red, and green curves represent the thermal disk, Comptonisation, and reflected components respectively. The black curve shows the total spectrum. (Figure courtesy: [Gilfanov, 2010](#))

### 2.2.3.2 Absorption models

The intrinsic continuum emission from the source gets absorbed by our local galactic medium before reaching to the X-ray detectors. This absorption mostly affects the soft X-rays below 10 keV. The spectral model PHABS (i.e., photoelectric absorption model) describes the continuum absorption, and is expressed as:

$$F(E) = \exp[-N_H \sigma(E[1+z])], \quad (2.3)$$

where  $N_H$  is the density of the absorbing material measured in atoms  $\text{cm}^{-2}$  and is normalized to the total hydrogen number density, known as equivalent hydrogen column density,  $\sigma(E)$  represents the cross-section (excluding Thomson scattering) for the absorption of X-ray photon with energy  $E$ . It is mainly derived by considering the individual contribution of three different cross sections of gas, grain and molecules present in the interstellar medium (ISM) (see [Wilms et al., 2000](#) for a detailed discussion). In TBABS model, updated photoionization and gas phase cross sections have been used as a result of updates to the ISM abundances.

### 2.2.3.3 Thermal disk models

The `diskbb` model is the one which is motivated by physical processes occurring in the thin accretion disk. This model was developed by the [Mitsuda et al. \(1984\)](#) considering the [Shakura & Sunyaev \(1973\)](#) thin disk model. It is a multicolor blackbody model based on the Planck's law. The disk is divided into multiple annular segments of radius  $R$ . The temperature profile of the disk varies as  $T(R) \propto R^{-3/4}$ . The model has inner-disk temperature and the norm as the free parameter which is defined as  $(r_{in}/D_{10})^2 \cos \theta$ , where  $D_{10}$  is distance in units of 10 kpc and  $\theta$  is the inclination angle.

### 2.2.3.4 Comptonisation models

The `powerlaw` is the phenomenological model that does not give the physical picture of the X-ray continuum which is the result of Comptonisation of thermal seed photons coming from the disk in the hot electron plasma. The mathematical form `POWERLAW` is given by:

$$A(E) = N[E]^{-\Gamma}, \quad (2.4)$$

where  $N$  is the normalization of the power law, representing the photon flux in Photons  $\text{keV}^{-1} \text{cm}^{-2} \text{s}^{-1}$  units,  $\Gamma$  is the photon index of the power law.

`nthComp` ([Zdziarski et al., 1996](#); [Życki et al., 1999](#)) is one of the common models for thermal Comptonisation. The cutoff at higher energy is parameterized by the electron temperature ( $kT_e$ ). It is sharper than an exponential cutoff of the `cutoffpl` model. At the lower energy also the Comptonised spectrum experiences a rollover which is driven by the seed photon energy. Between these two rollovers the shape of the spectrum is decided by the electron temperature and the scattering optical depth which is approximated by an asymptotic power law with index  $\Gamma$ . A more advanced version of thermal Comptonisation model is `ThComp` ([Niedźwiecki et al., 2019](#)). It calculates the spectrum by Comptonisation of sinusoidally distributed seed photons from a spherical cloud of thermal electrons. `ThComp` can Comptonise both hard and soft seed photons as it is a convolution model. It describes both down-scattering and up-scattering and agrees

more with Comptonised Monte Carlo spectrum than `nthComp` (Zdziarski et al., 2020).

### 2.2.3.5 Reflection models

There are different reflection models available which can be either loaded or embedded in XSPEC such as `pexrav`, `pexriv` (Magdziarz & Zdziarski, 1995), `relxill` (García et al., 2014), `xillver` (Garcia & Kallman, 2010) and `reflkerr` (Niedźwiecki & Zdziarski, 2018) etc. In this thesis work, `pexriv` is used for the reflection component from the accretion disk. This model encompasses the cut-off power law spectrum and the Compton reflected spectrum from the ionized material. By Compton scattering, X-rays emitted by the source impinge on a slab (such as an accretion disk) and re-emerge with a different spectrum which is modified by Compton scattering and bound-free absorption. This resultant reflected spectrum is dependent on the viewing angle of the slab geometry. The dependence on the viewing angle is important in hard X-rays where spectrum hardens with increasing viewing angle of the disk. There are many parameters which characterize this model, one of them is the reflection fraction factor ( $rel_{refl}$ ). It is the ratio of the reflected and the primary component. Only reflected part of the spectrum can be used by considering the negative value for this parameter.

## 2.3 Temporal analysis

The rapid time variability analysis of binaries is primarily performed in the Fourier space. This is because some interesting features, such as QPOs, occur at very high frequencies and have low fractional amplitudes compared to Poisson noise, making them difficult to detect directly in time domain. Only very low frequency oscillations are sometimes studied in the time domain (e.g., Stiele et al., 2016). Fourier analysis requires continuous high-resolution data of sufficiently long segments that exceed the characteristic time scales of the PDS features. The detailed description of Fourier techniques are presented in van der Klis (1989).

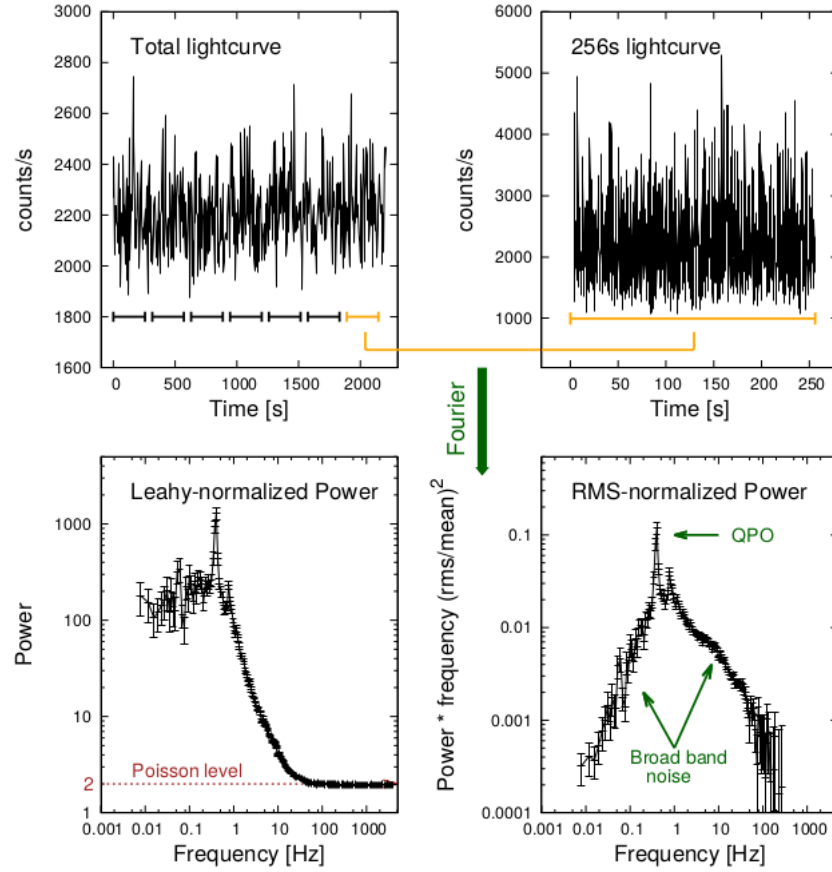


Figure 2.6: The four steps followed during calculation of power spectrum. Courtesy: Stefano Rapisarada

The procedure to generate power spectrum is as follows: First, the time series  $x(t)$ , is divided into a number of adjoining segments of equal length. Each segment is Fourier transformed using the Fast Fourier Transform algorithm (FFT) and converted to the frequency domain ( $x_i(t) \Rightarrow X_i(\nu)$ ). The frequency resolution ( $\delta\nu$ ) and lowest frequency ( $\nu_{min}$ ) are calculated by the length of each segment ( $T$ ), i.e.,  $\delta\nu = 1/T = \nu_{min}$ . The Nyquist frequency ( $\nu_{Ny}$ ), which is the highest detectable frequency, is regulated by the time resolution of the data  $\delta t$ , i.e.,  $\nu_{Ny} = 1/2\delta t$  and this criteria is known as Nyquist-Shannon sampling theorem. The implication of this criteria is that, we need long segments and high time resolution data for analyzing low and high frequency variabilities. The power is computed as the squared modulus of the Fourier amplitudes, i.e.,  $P_i(\nu) = |X_i(\nu)|^2 = X_i^*(\nu)X_i(\nu)$ . This power is then Leahy normalized by dividing a factor  $X_i\nu_0/2$  (Leahy et al., 1983), where  $\nu_0$  equals the number of photons in  $x_i(t)$  and is called the zero-frequency component. In the following step, the Leahy normalized

power spectra of all segments are averaged to produce a single power spectrum  $P(\nu)$  with Poisson noise level of approximately 2. The relative error of the power is given by  $\sigma_P/P = 1/\sqrt{n_p n_f}$  where  $n_p$  and  $n_f$  are the numbers of the power spectra and frequency bins averaged, respectively, where the term  $n_p n_f$  is large enough. Lastly, Leahy normalized and Poisson noise subtracted average power spectrum is normalized to give the fractional root-mean-square (rms) amplitude by dividing again by mean count rate (van der Klis, 1997; Vaughan et al., 2003). With this normalization, the fractional rms of the lightcurve can be computed by integrating the power spectrum over all the frequencies. A typical power spectrum, shown in Figure 1.4 of chapter 1, consists of different features. The peaked features are the QPOs and the broadband features spread over several decades in frequency are the noise. The power spectrum of black-hole binaries can be fitted by a combination of Lorentzians (Nowak, 2000; Belloni et al., 2002).

## 2.4 Polarisation measurement in X-rays

Polarimetry for astrophysical sources at higher energy is very difficult due to its photon hungry nature. The degree of polarisation is definite positive because of the statistical fluctuations; certain polarisation is always measured even if the source is unpolarised. This implies that any realistic polarisation measurement requires a large number of photons or data than the generation of the light curve and measurement of the spectrum. The study of compact sources like a white dwarf, neutron stars, and black holes, which mostly emit in X-rays using X-ray polarimetry, would give a wealth of information about these sources. It can reveal the geometry of the system, for example, the geometry of the corona. It can help in breaking the degeneracy of different possible coronal geometry (discussed in section 1.4.1). It is also a sensitive tool to probe the strong gravity and magnetic field. For example, the degree and plane of polarisation of the radiation which emerges close to the black hole is very sensitive to its magnetic and gravitational fields (Stark & Connors, 1977; Connors et al., 1980).

The first successful measurement of the polarisation in X-rays was done in 1976 by the X-ray polarimeter on-board OSO-8 mission for the Crab nebula

(Weisskopf et al., 1976). Many missions and instruments were developed since the first X-ray observation of celestial object but not a single mission is realized which is capable of doing spectroscopy, imaging, timing and polarisation measurement of the X-ray photons in the hard X-ray regime. But for better understanding of the compact objects we need to have instruments having better spectroscopic and timing sensitivity along with the polarisation measurement of the X-ray photons in the low to higher energy range. Till date no dedicated mission has been sent which is capable of doing spectro-polarimetry, timing and position studies simultaneously in broad energy range. Over the last decade, efforts have been made in this direction by the instruments, originally not designed or optimized for polarimetry such as RHESSI, INTEGRAL/IBIS, and INTEGRAL/SPI. Attempts are made to measure polarisation for some of the bright X-ray sources like Cygnus X-1 and Crab by IBIS and SPI onboard INTEGRAL. Some balloon born missions like POGO+, XL-Caliber, etc. also attempted to measure the polarisation of these sources. But due to low polarimetric sensitivity of these instruments, it was difficult to draw any significant conclusions from these observations except the probable emission mechanism of the radiation. In the recent years, CZTI onboard *AstroSat*, which is primarily designed for the spectroscopy but also calibrated for the polarisation measurements have done polarisation measurement of Crab (Vadawale et al., 2018). Apart from this, recently a dedicated polarimeter, Imaging X-ray Polarimetry Explorer (IXPE) is launched having energy range of 2 - 8 keV and provided the most precise measurements of some of the sources.

The polarisation is not a directly measurable quantity. Some observable is required to measurement of polarisation, typically intensity. X-ray interaction with matter depends upon the polarisation of the photon, giving rise to the variable intensity w.r.t to the polarisation angle of the incident beam. The detector which detects photons at different positions and analyses different angular directions is called polarimeter. The current technology is limited for the measurement of linear polarisation in X-rays. If the radiation is polarised it gives the modulation in the intensity of photons on the detector plane which can be fitted with the  $\cos^2$  function. For example, Compton scattering preferentially happens

in the direction perpendicular to the polarisation of the incident photon which give rise to a sinusoidal distribution of the azimuthal scattering angles (Lei et al., 1997; Kaaret, 2014). In general, modulation function has the form

$$S(\phi) = \bar{S} [1 + a_0 \cos^2(\phi - \phi_0)] \quad (2.5)$$

where  $\phi$  is the angle on the detector plane, perpendicular to the incident direction of photon with respect to the detector reference axis. The polarisation position angle  $\phi_0$  (PA) is the angle at which the maximum intensity is recorded,  $\bar{S}$  describes the unpolarised component (mean number of the events in  $\phi$  bins) of the intensity, and  $a_0$  describes amplitude of the polarized intensity. Both amplitude and phase information is important to know the degree of polarisation and the polarisation position angle, respectively.

Once the modulation curve is obtained by fitting the azimuthal distribution of the photons, conventionally the polarisation fraction,  $P$ , is measured by normalising the modulation amplitude ( $\mu$ ) obtained from the modulation curve with the modulation amplitude for 100% polarized source ( $\mu_{100}$ ), which is estimated experimentally or by simulation.

$$\mu = \frac{C_{max} - C_{min}}{C_{max} + C_{min}} \quad (2.6)$$

where  $C_{max}$  and  $C_{min}$  are the maximum and minimum number of counts in the modulation curve.

$$P = \frac{\mu}{\mu_{100}} \quad (2.7)$$

The probability of measurement of polarisation amplitude  $a$  and phase  $\phi$  in the presence of noise (assume to be Poisson distribution) when the true amplitude is  $a_0$  and phase is  $\phi_0$ , given by,

$$p(a, \phi) = \frac{Na}{4\pi} \exp \left[ -\frac{N}{4} [a^2 + a_0^2 - 2aa_0 \cos(\phi - \phi_0)] \right] \quad (2.8)$$

where  $N$  is the number of total detected photons. Since the measure-

ment of polarisation is definite positive quantity, therefore, even for the unpolarised source there is always a finite probability to measure an amplitude  $a$  (i.e.  $P(a) \neq 0$ ). After integrating and modifying the equation 2.8 to determine the amplitude ( $a_{1\%}$ ) having the 1% probability of being exceeded by chance when the source is unpolarised ( $a_0 = 0$ ).

$$\frac{N}{2} \int_{a_{1\%}}^{\infty} a \exp \left[ -\frac{Na^2}{4} \right] da = 0.01 \quad (2.9)$$

Solution of equation 2.9 gives

$$a_{1\%} = \frac{4.29}{\sqrt{N}} \quad (2.10)$$

The modulation amplitude as a fraction of the detected signal is given by:

$$a_s = a_{1\%} \times \frac{(R_{src} + R_{bkg})}{R_{src}} \quad (2.11)$$

here,  $R_{src}$  and  $R_{bkg}$  are source and background count rate.

equation 2.11 leads to the Minimum detectable Polarisation (MDP) in terms of the source , background rates and the modulation amplitude for the 100% polarised radiation ( $\mu_{100}$ )

$$MDP_{99\%} = \frac{4.29}{\mu_{100} R_{src}} \sqrt{\frac{R_{src} + R_{bkg}}{T}} \quad (2.12)$$

where T is the source observation time. The minimum detectable polarisation is the polarisation corresponding to the amplitude of modulation which would not be observed by chance, with 99% confidence.

### 2.4.1 X-ray polarisation measurement techniques

There are number of techniques of polarisation measurements in X-rays based on the type of photon interaction used in the measurement like photoelectric, Compton scattering, Rayleigh scattering, etc. The probability of photon interaction (efficiency) determines which process is the most effective for the polarisation analysis in different energy range: photoelectric below few tens of KeV

and Compton interaction at higher energy (shown in Figure 2.7)

The interaction probability of photon undergoing different physical processes is energy dependent quantity. The efficiency of the interaction of the photons in 5 mm silicon with different physical processes is illustrated in Figure 2.7. The data for the interaction cross section at different energies for the different interaction processes is taken from the National Institute of Standards and Technology (NIST) <sup>‡</sup>.

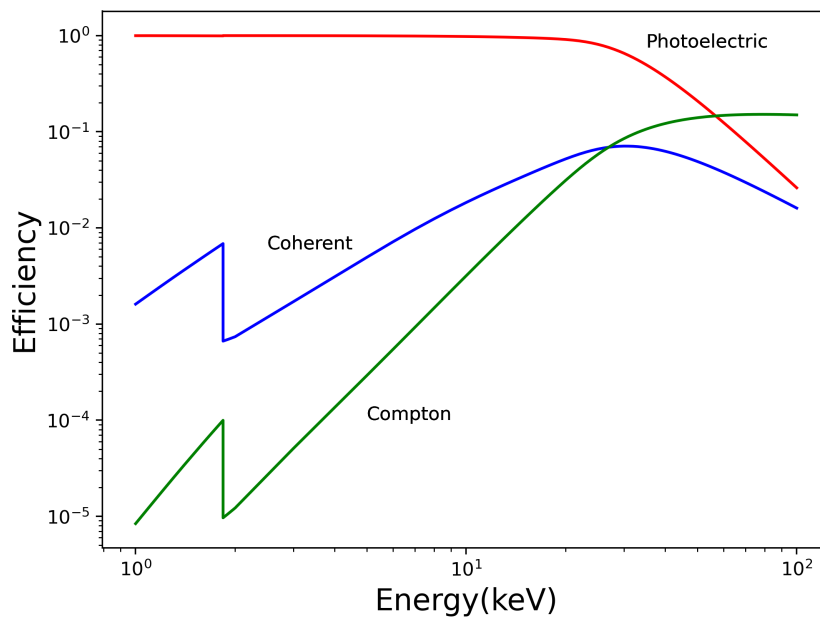


Figure 2.7: The photon interaction probability at different energy for 5 mm thick Silicon. Different colors represent different interactions as mentioned in the figure

Following are the X-ray polarimeters based on the different physical processes:

#### 2.4.1.1 Bragg reflection polarimetry

The polarisation measurement using the Bragg crystal polarimeter (Toraskar (1975); Silver et al. (1990)) relies on the reflection of the photons at nearly  $45^\circ$  because the diffraction of the radiation polarised parallel to the incidence plane is close to zero at Brewster angle which is nearly  $45^\circ$  for the X-rays. The radiation component, which is polarised perpendicular to the plane of diffraction, gets

<sup>‡</sup><https://physics.nist.gov/cgi-bin/Xcom/xcom2><https://physics.nist.gov/cgi-bin/Xcom/xcom2>

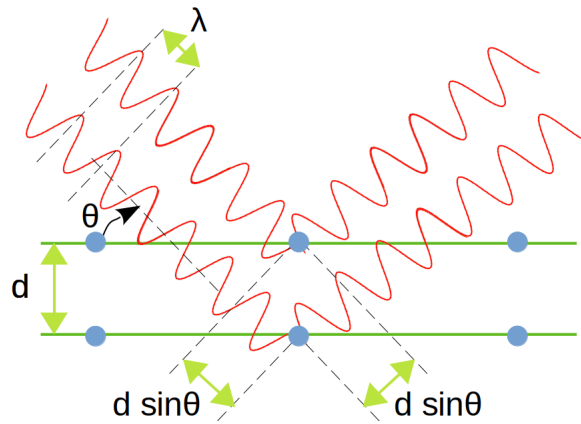


Figure 2.8: Bragg reflection.  $d \sin \theta$  is the difference in path length between two waves,  $d$  is the crystal plane spacing,  $\theta$  is angle of incidence and  $\lambda$  is photons wavelength.

reflected efficiently, and the azimuthal distribution in output flux is observed by rotating the instrument about the incident photon direction. The polarimetric efficiency of the Bragg polarimeter is very low because of the very low energy band. According to the Bragg diffraction condition: the difference between the path length for the diffraction from the two adjacent crystal planes,  $2d \sin \theta$ , should be integer multiple,  $n$ , of the wavelength,  $\lambda$  (see equation 2.13)

$$n\lambda = 2d \sin \theta \quad (2.13)$$

Where  $d$  is the crystal planes spacing, and  $\theta$  is the angle between the scattering plane and the incident ray.

The Bragg polarimetry for X-rays require the diffraction at  $45^\circ$  results in very low energy bandwidth (a small fraction of an eV), hence, low polarimetric efficiency. However, the imperfect crystals, which are the mosaic of numerous perfect crystals with random orientations, can provide a higher bandwidth (a few tens of eV). The first precise polarisation measurement of Crab was done using the Bragg polarimeter onboard OSO-8 having mosaic parabolic graphite reflector (Novick, 1975). The measured polarisation at 2.6, and 5.2 keV are  $15.7\% \pm 1.5\%$  at  $161.1 \pm 2.8$  deg and  $18.3\% \pm 4.2\%$  at  $155.5 \pm 6.6$  deg, respectively (Weisskopf et al., 1976)

### 2.4.1.2 Photo-electric polarimetry

The dominant process by which the interaction of low-energy photons ( $h\nu \ll m_e c^2$ ) takes place with matter is photoelectric absorption. If the incident energy of a photon,  $\epsilon = h\nu$ , is greater than the atomic energy level  $E_1$  then the electron from that level can be ejected with kinetic energy  $h\nu - E_1$ . Thus, it is also called as bound-free emission as the electron is bound to the atom before the interaction and becomes free afterward. The spectrum has an absorption edge at the energy level where  $h\nu = E_1$  as the photons with lower energy cannot displace any electron.

For the linearly polarised photon, the cross-section of the photoelectric absorption is given by (Heitler, 1954)

$$\frac{d\sigma}{d\Omega} = \frac{r_e^2 Z^5}{137^4} \left( \frac{mc^2}{E} \right)^{7/2} \frac{4\sqrt{2} \sin^2 \theta \cos^2 \phi}{(1 - \beta \cos \theta)^4} \quad (2.14)$$

where  $\theta$  is the photo-electron ejection angle relative to the incident photon direction,  $\phi$  is the azimuthal angle relative to the incident photon electric field vector, and  $\beta$  is the speed of the photo-electron as a fraction of the speed of light. The ejection of the photo-electron is preferentially parallel to the incident photon's electric field vector i.e., distribution peaks at  $\phi = 0$ . Therefore, by measuring the initial direction of the photo-electron, it is possible to determine the linear polarisation of the incident photon. At low energy,  $\beta \ll 1$ , the photo-electron is emitted at  $\theta = 90^\circ$  (see equation 2.14), therefore, the modulation amplitude is anticipated to be higher. Furthermore, at lower energy, the photoelectric cross section is high. Therefore, the polarimetric efficiency is high at soft X-rays compared to scattering polarimeters.

The photo-electron makes the electron-ion pair trail tracing its path from the initial ejection to the final stopping point by losing energy in between. This trail is called a photo-electron track. Tsunemi et al. (1992), Llopert et al. (2007), and Michel & Durst (2008) discussed the methods to trace the path of the photo-electron track in a pixelated semiconductor detector. The track length of the photo-electron in semiconductor detectors is very small ( $\sim 1\mu m$  for 10 keV electron) (Ashley et al., 1976). The size of the pixels required to trace the electron

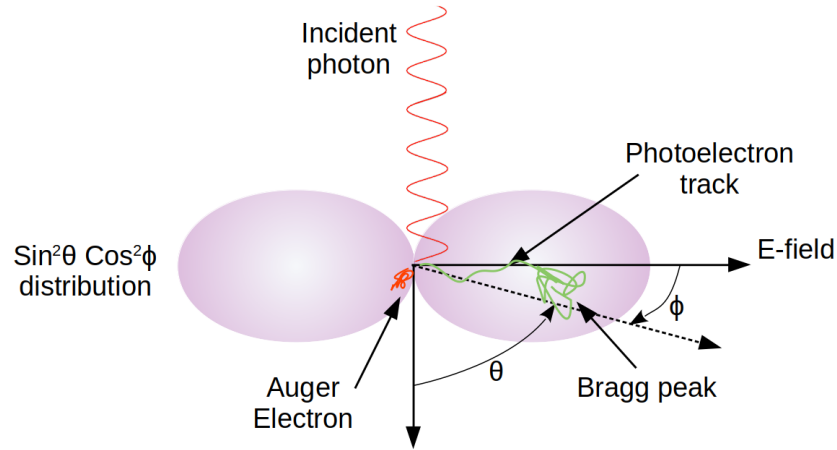


Figure 2.9: Photo-electron angular distribution due to interaction of linearly polarised photon with the atom. Photo-electron preferentially ejected along the direction of the electric field vector of the incident photon.  $\theta$  is the emission angle with respect to the incident direction of the photon and  $\phi$  is the angle relative to the electric field vector of the photon.

trail should be smaller than the photo-electron track length. The present solid-state detector's smallest pixel size is of the order of a few  $\mu m$ . Therefore, mapping the electron path with these detectors is very difficult makes them insensitive to the polarisation measurement. However, in the gases, photo-electron trail length is of the order of a few mm. The Gas Electron Multiplier (GEM) based detectors like Gas Pixel Detector (GPD) (Costa et al., 2001; Bellazzini et al., 2007) with two end readout or the Time Projection Chamber (TPC) (Black et al., 2007) with one end readout, where the second dimension is obtained from the electron drift time are more sensitive to trace the photo-electron track.

### 2.4.1.3 Scattering polarimetry

The polarimetry based on scattering uses Compton scattering and the Rayleigh scattering, where the photon imparts some energy to the electron (Compton scattering) or travels with the same energy (Rayleigh scattering), respectively. Compton scattering is the dominant process at energies above a few tens of KeV where the energy of the incident photon is more than the rest mass energy of the electron. The change in wavelength of incident photon due to Compton scattering is given by

$$\frac{\Delta\lambda}{\lambda} = \frac{h\nu}{m_e c^2} (1 - \cos\theta) \quad , \quad (2.15)$$

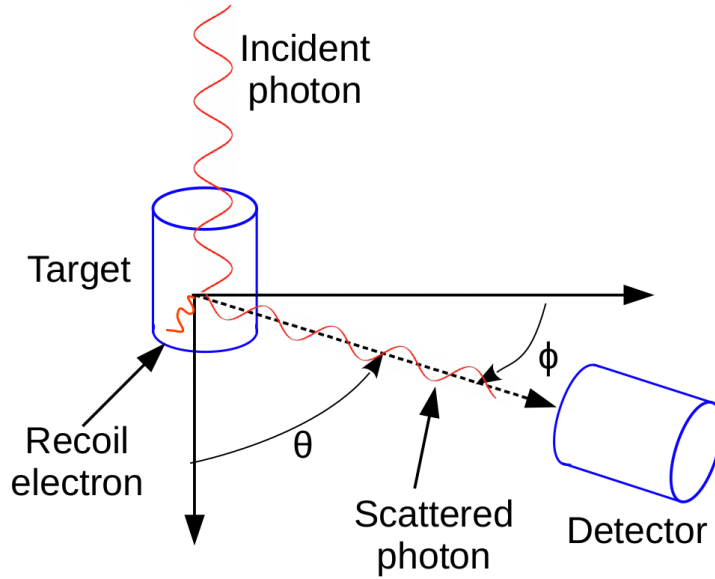


Figure 2.10: The schematic diagram of a Compton polarimeter.

where  $\theta$  is the scattering angle.

The Compton scattering cross section of a polarised X-ray source is given by Klein-Nishina formula

$$\frac{d\sigma}{d\Omega} = \frac{r_e^2}{2} \left( \frac{E'}{E} \right)^2 \left( \frac{E'}{E} + \frac{E}{E'} - 2 \sin^2 \theta \cos^2 \phi \right) \quad (2.16)$$

For a given incident photon having energy  $E$ , the modulation factor as a function of  $\theta$  is give by (Krawczynski et al., 2011)

$$\mu(\theta) = \frac{\sin^2 \theta}{E/E' + E'/E - \sin^2 \theta} \quad (2.17)$$

where  $E'$  and  $E$  are the energies of the scattered photon and incident photons which are related as

$$\frac{E'}{E} = \frac{1}{1 + \frac{E}{m_e c^2} (1 - \cos \theta)} \quad (2.18)$$

where  $r_e$  is the classical electron radius, and  $\theta$  is the angle relative to the photons incident direction, the scattered photon direction, and  $\phi$  is the angle between the electric field vector of the photon and the scattering plane. If the incident energy  $E$  is much less than the rest mass of the electron,  $\frac{E}{m_e c^2} \sim 1$  then:

$$\frac{d\sigma}{d\Omega} = r_e^2 (1 - \sin^2 \theta \cos^2 \phi) \quad r_e = \frac{1}{4\pi\epsilon} \frac{e^2}{mc^2}, \quad E \ll m_e c^2 \quad (2.19)$$

for  $\theta = \frac{\pi}{2}$ , equation 2.19 becomes:

$$\frac{d\sigma}{d\Omega} = r_e^2 (1 - \cos^2 \phi) \quad (2.20)$$

From equation 2.19 & 2.16 the scattered flux is modulated as a function of  $\cos^2 \phi$ , minimum in the direction of polarisation. Therefore the modulation factor is low or moderate compared to the photoelectric and Bragg polarimeter.

The polarimeters based on the scattering record the photons scattered at various azimuthal angles. The basic design of a scattering polarimeter consists of the scatterer to scatter the incident photons and the surrounding absorber, which detects the scattered photons. In the case of the Compton polarimeter, the scatterer is active (deposition of energy) to record the photons only in temporal coincidence. Therefore, the background is very low in comparison to the Thomson polarimeter, where the scatterer is passive. Since the Compton cross section dominates at higher energy, the Compton polarimeter works at higher energy. On the other hand, coincidence is not required in Thomson polarimeters. Hence, these are sensitive to the lower energy, where lower energy limit is decided by the cross over between the photoelectric and Thomson scattering probability.

### 2.4.2 Hard X-ray polarimetry using AstroSat/CZTI

CZTI is also works as a Compton polarimeter for bright X-ray sources at higher energies. The 5 mm thick CZT detector provide sufficient Compton cross section to detect photons above 100 keV where a significant fraction of interaction occurs by the Compton scattering. CZTI is a pixelated detector where the scattered photon can be detected in the adjacent pixel. It has a feature of recording each photon interaction as time tagged event with a resolution of 20  $\mu$ s. The 2-pixel events can be used to measure the polarisation of the incident photon. The direction of the scattered photon depends up on the polarisation of the

incident photon and give rise to the sinusoidal modulation in the distribution of the azimuthal scattering angles as discussed in the previous section. The polarisation measurement capability of the CZTI is shown through the detailed experiments and simulation on ground (Chattopadhyay et al., 2014a; Vadawale et al., 2015). This has been also successfully utilized for polarisation analysis of Crab pulsar and nebula (and transients like Gamma-ray bursts) in 100 - 380 keV (Vadawale et al., 2018; Chattopadhyay et al., 2019). The method of the polarisation analysis using CZTI data is discussed below.

#### 2.4.2.1 Compton event selection

First, we remove the high background regions during the passage of South Atlantic Anomaly (SAA) and also all the bad or noisy pixels (pixels having counts more than 5-sigma above the mean count rate in the detector) events from the data to increase the signal to noise ratio. To identify the Compton events, first, we select the events occurring in a coincidence time window of 40  $\mu$ s such that events must be recorded within 40  $\mu$ s of each other in two separate pixels. The standard CZTI pipeline generates an event file with the list of the 2-pixel events. The actual Compton events (CS) are identified from the chance 2-pixel events by applying two other criteria: (1) spatial proximity of pixels – events with only the adjacent pixels are considered, and (2) the sum and ratio of deposited energies must be consistent with the Compton kinematics (ratio of the energy deposited in the two pixels should be between 1 and 6) (Chattopadhyay et al., 2019). We estimate the scattering angle from the energies deposited in the two individual pixels. From the pixel geometry (2.5 mm pixel pitch and 5 mm in depth), we impose that the estimated scattering angle should be within 26 to 154 degrees. Apart from applying the above mentioned criterion, events with the sum of two energies between 100 and 380 keV are considered for analysis.

#### 2.4.2.2 Background selection

Appropriate selection of blank sky observation is vital for the polarisation analysis. The CZTI mask, collimators, and other support structures become increas-

ingly transparent above 100 keV. Therefore, the actual blank sky background observation can be affected due to the presence of bright X-ray sources within 80 - 90 degrees of the pointing direction of CZTI. Special care should be taken, so that bright sources like Crab and Cygnus X-1 are outside the 80 - 90 degrees of the pointing direction during the background observation. Declination of the blank sky background observation should be within the  $\pm 5$  degrees to the declination of the source observation. Because earth's X-ray albedo also contributes to the background and it comes from the one side of the spacecraft so it may lead to the asymmetry in the azimuthal distribution of the background. Another important consideration is the time exposure of the blank sky observation which should be greater than 30 ks (same as source) to get a statistically significant number of Compton counts. Further, to select the appropriate blank sky observation for each source observation, the longitudinal variation of spectral hardness in background data with the spectral hardness in source data is compared. The best matched blank sky observation from the sample of background observations is selected for background subtraction for that particular source observation.

### 2.4.2.3 Background subtraction

X-ray background consists of multiple sources such as cosmic background radiation, induced radioactivity, trapped particles near the SAA, earth albedo, etc. (Campana, 2022) and small fraction being due to the chance coincidence events within the  $40\mu s$  coincidence time window. It is difficult to predict the particle background for an orbit in -135 to 45 degrees of longitude because of multiple complex factors like the exact time span of satellite in the SAA regions, which is different for different orbits, depth in SAA regions, induced radioactivity in the detector, etc. Thus, in our analysis, we have excluded the duration's from the GTI both for the source and blank sky background observations when the satellite is in the longitudinal range of -135 to 45 degrees. We also use counts in the CsI anti-coincidence (veto) detector (CsI detector seated below the CZT detector) as a proxy to identify high background regions. We ignore the time intervals where the counts in the veto detector of each quadrant are above these threshold values to remove the high particle background events anywhere in orbit

away from the SAA.

Background also show quasi-diurnal variation due to earth rotation (Antia et al., 2022) which is corrected using the ‘phase match method’ In this method, first, we fit the source and background light curves with the higher degree polynomials (here, 5th degree). Then the source polynomial is shifted over the background polynomial every 10 seconds to compare and calculate the chi-square. The region with the minimum chi-square value is where the phases of the source and background match. The ratio of the total background count rate and the background count rate in the phase-matched region gives a correction factor (see equation 2.21) to the background exposure, which is then used to scale the background count rate for subtraction.

$$S_{cr} = \frac{N_{s+b}}{T_{s+b}} - \frac{N_b}{T_b a} \quad (2.21)$$

where  $N_{s+b}$  is number of source count,  $T_{s+b}$  is source exposure time,  $N_b$  number of background counts,  $T_b$  is background exposure. where  $a$  is the effective exposure scaling factor.

The detailed discussion over the background selection and subtraction is given in chapter 4.

#### 2.4.2.4 Geometric correction

Background events are not polarised so in principle it should not show any modulation in the azimuthal distribution. However, because of the non-uniformity in the solid angles subtended by the surrounding edge and corner pixels to the central scattering pixel, we see unequal count rates in the edge and corner pixels, which is first corrected by normalizing it with an ASAD for 100 % unpolarized X-rays in the same energy range. For Gamma-ray bursts, this is typically obtained from the Geant4 Monte Carlo simulation (Chattopadhyay et al., 2019). However, for ON-axis sources, the unpolarized ASAD is obtained from the observed source azimuthal distribution by averaging the edge and corner pixels separately (Vadawale et al., 2015, 2018).

$$N_{i,corrected} = \frac{N_{i,pol}}{M_{i,unpol}} M_{unpol}^- \quad (2.22)$$

Where  $N_{i,corrected}$  is the corrected counts,  $N_{i,pol}$  counts for 100 percent polarised radiation,  $M_{i,unpol}$  is the counts for the unpolarised radiation,  $M_{unpol}^-$  is the mean counts in each bin.

#### 2.4.2.5 Polarisation estimation

Geometric corrected azimuthal distribution of the counts is fitted with a sinusoidal function to get the polarisation angle (PA) and polarisation fraction (P) as described in section 2.4. The modulation fitting gives the polarisation angle in the detector plane which can be converted to the celestial/sky reference frame by taking into account the satellite orientation at time of observation.



# Chapter 3

## Hard X-ray polarisation measurement of Cygnus X-1 with *AstroSat-CZTI*

### 3.1 Introduction

Cygnus X-1, a Galactic black hole binary source, has been extensively studied across almost the entire electromagnetic spectrum over the last five decades. The source displays state transitions between thermal disk dominated soft state and hard state with power law dominant spectrum. It is also studied in radio wavelengths where the emission is attributed to the relativistic jets. During hard states, this source could be as bright as Crab, and the hard X-ray emission is mainly attributed to Compton scattering from the hot corona. Hard X-ray polarisation measurements offer the unique possibility to distinguish emission from corona and jet, however, observationally the X-ray polarisation measurements are extremely difficult to carry out, and so far, there is only a faint hint of polarisation measurement.

*AstroSat /CZTI* is a moderately sensitive hard X-ray polarimeter at energies beyond 100 keV. The polarisation information is obtained by accurately identifying the Compton scattering events in the CZTI, and the azimuthal angle distribution of these events would be modulated if the incident radiation is

polarized. The capability of CZTI as a polarimeter has been demonstrated both in the laboratory before the launch of *AstroSat* (Vadawale et al., 2015; Chattopadhyay et al., 2014a) and in space by the measurement of phase resolved polarisation of Crab (Vadawale et al., 2018) and prompt phase of Gamma Ray bursts (Chattopadhyay et al., 2019). CZTI polarimetry range (100 - 380 keV) bridges the *PoGO+* (19 - 181 keV energy band) and *INTEGRAL* regions ( $> 250$  keV energy band) and, therefore, can contribute significantly to understanding the emission mechanism in this energy range. If there is indeed a transition in the emission mechanism from corona to jet, that can be effectively probed by studying the energy resolved polarisation properties of the source with CZTI. We have carried out polarization analysis of Cygnus X-1 using the selected observations from the 5 years CZTI data to probe the emission mechanism and polarisation behaviour. In section 3.2, we briefly discuss the observations and in section 3.3 the polarisation analysis techniques, followed by the polarisation results in section 3.4. We summarize the results and conclusions in section 3.5.

## 3.2 Observations

Cygnus X-1 has been observed by *AstroSat* multiple times. Many of them, however, is of short exposure, and some were in the soft state with very low hard X-ray flux. During the last few cycles of observations, when the source made a transition from the soft state to the hard state, two long ( $> 200$  ks) targeted observations of Cygnus X-1 (ID 2992 and ID 4646, see Table 5.2) were made. We did a detailed polarisation analysis for all CZTI observations of Cygnus X-1 having enough Compton counts, including these two observations.

We selected 9 observations of Cygnus X-1 for this study based on the Burst Alert Telescope (BAT; Barthelmy et al., 2005) flux in the 15 - 50 keV and the exposure of the observation. Observations having the BAT flux  $> 500$  mCrab and CZTI exposure  $> 50$  ks are selected so that sufficient Compton counts are available above 100 keV to carry out polarisation measurement. Out of the 9 observations, one has data dominated by noisy pixels. In the noisy pixels when the number of events reaches its limit, it does not record subsequent events,

making the data not useful for scientific purposes. Therefore, finally we have 8 observations (hereafter ID 426, ID 436, ID 456, ID 2992, ID 4492, ID 4638, ID 4646, and ID 4678).

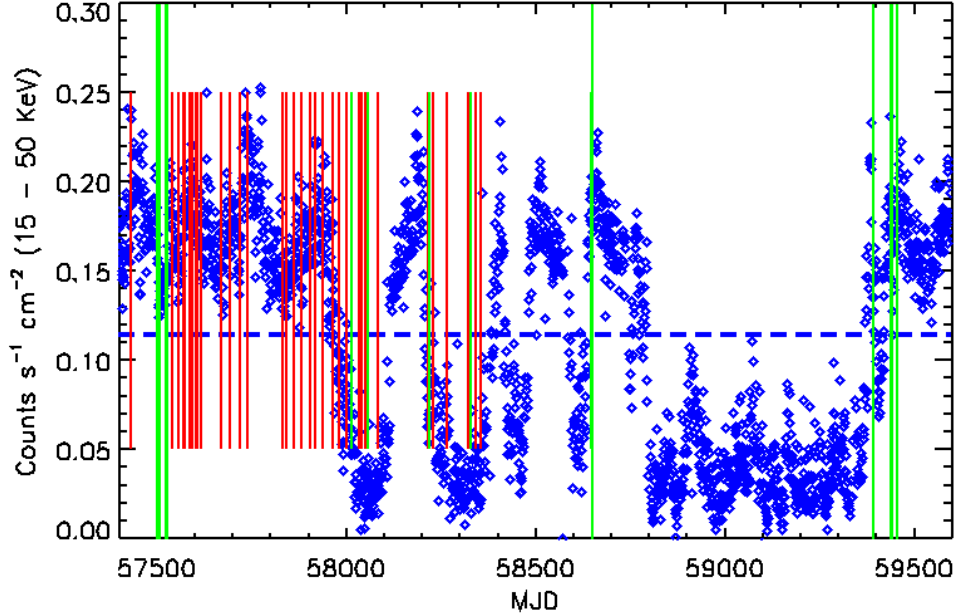


Figure 3.1: Cygnus X-1 all the observations overplotted on the BAT light curve in 15 - 50 keV. Blue horizontal dashed line represents BAT count rate ( $0.11 \text{ Counts s}^{-1} \text{ cm}^{-2}$ ) which corresponds to  $\sim 500 \text{ mCrab}$ . The green vertical lines represents the observations having exposure greater than 50 ks and the red color vertical lines shows the observations having exposure below 50 ks. The green full vertical lines represents all the observations selected for the analysis having exposure greater than 50 ks and BAT flux  $> 500 \text{ mCrab}$ .

The blank sky observation is selected for the background subtraction which are taken avoiding the bright sources like Crab and the Cygnus X-1 in the pointing direction of observation. Further details on the selection of background observations is given in next section. Details of the Cygnus X-1 observations and the corresponding background observations selected for the present analysis are given in Table 5.2.

Table 3.1: Details of the Cygnus X-1 and blank sky observations. The last four digits of the full observation ID (ObsID) will be used to identify the observation in the rest of the chapter. Cygnus RA: 299.59° and DEC: 35.20°

Cygnus X-1			Blank Sky				
ObsID	Date (yyyy/mm/dd)	Exposure (ks)	ObsID	Date (yyyy/mm/dd)	Exposure (ks)	RA (deg)	DEC (deg)
9000000426	2016/04/22	104	9000000464	19/05/2016	68	185.34	30.17
9000000436	2016/04/29	58	9000000464	19/05/2016	68	185.34	30.17
9000000456	2016/05/15	138	9000000464	19/05/2016	68	185.34	30.17
9000002992	2019/06/15	333	9000002210	03/07/2018	207	203.65	37.91
9000004492	2021/06/27	178	9000002210	03/07/2018	207	203.65	37.91
9000004638	2021/08/13	55	9000002210	03/07/2018	207	203.65	37.91
9000004646	2021/08/16	228	9000002210	03/07/2018	207	203.65	37.91
9000004678	2021/08/29	118	9000002210	03/07/2018	207	203.65	37.91

## 3.3 Analysis method

### 3.3.1 Estimation of polarisation fraction and polarisation angle

In order to estimate the polarisation fraction and polarisation angle, we use two methods: 1. Modulation curve fitting method where the geometry corrected histogram is fitted with the sinusoidal function, and 2. using the Markov Chain Monte Carlo (MCMC) simulations.

#### 3.3.1.1 Modulation curve fitting method

CZTI onboard AstroSat is primarily designed for the hard X-ray spectroscopy and imaging which is also sensitive to the polarisation due to its pixelated detector plane. It is well calibrated on the ground as well as in space for the polarisation measurements [Chattopadhyay et al. \(2014a\)](#); [Vadawale et al. \(2015\)](#). In CZTI, polarisation is estimated from the azimuthal scattering angle distribution (hereafter ASAD) of the Compton scattered photons, which lie preferentially in a direction orthogonal to the electric field vector (see [Bernard et al., 2022](#); [Chattopadhyay, 2021](#); [Lei et al., 1997](#), for the Compton scattering technique details). Polarisation analysis of Cygnus X-1 follows the same steps used for Crab pulsar and nebula and is also described in great detail in the methods section of [Vadawale et al. \(2018\)](#) as well as see section 2.4.2 of Chapter 2. Here we briefly cover these steps.

- The first step of the polarisation analysis is to select valid Compton events after doing the necessary filtering which are then used to obtain the source ASAD.
- The second step is to consider an appropriate blank sky observation after avoiding the bright sources in the sky such as Crab and Cygnus X-1 are out of the open field of view of CZTI. Further, to minimize the earth's X-ray albedo effect, the blank sky observations were selected such that the relative orientation of the spacecraft during the background measurement

is the same ( $\pm 5^\circ$ ) as that during the source measurement. The details of the background observation selected for the subtraction are given in Table 5.2. The same data cleaning process and Compton criteria are implemented to generate the background ASAD.

- Before the background ASAD subtraction from the source ASAD, an important point to consider is that the background count rate changes within the duration of observation with a stable periodic nature. This results from the inclined orbit of *AstroSat* (Kumar et al., 2021, 2022; Antia et al., 2022). To correct for this effect, we try to match the phases of the orbital variation of the total rate for background and source observations using a cross-correlation method described (Kumar et al., 2021, 2022) and select the common or phase-matched region of the background for subtraction (see Figure 3.2). We used the phase-matched regions to obtain a multiplication factor which is then applied to the ASAD for the full background duration subtraction.
- In the next step, we fit the ASAD to obtain the polarisation fraction and angle. Because of the non-uniformity in the solid angles subtended by the surrounding edge and corner pixels to the central scattering pixel, we see unequal count rates in the edge and corner pixels, which is corrected by normalizing it with an unpolarized ASAD which is obtained from the observed source azimuthal distribution by averaging the edge and corner pixels separately (Vadawale et al., 2015, 2018).

The geometry-corrected modulation curves were fitted by a sinusoidal function,  $A \cos 2(\phi - \phi_0 + \pi/2) + B$ , to estimate the polarisation angle in the detector plane ( $\phi_0$ ) and the modulation amplitude ( $\mu = A/B$ ). The polarisation fractions for each of these observations were estimated by normalizing  $\mu$  by the modulation factor expected for 100 % polarized radiation ( $\mu_{100}$ ), which was obtained by using Geant4 simulations in the same range (100 - 380 keV) where an identical process for the selection of Compton events was followed. Uncertainties on the estimated polarisation fraction values and angles were obtained using the standard error propagation method where

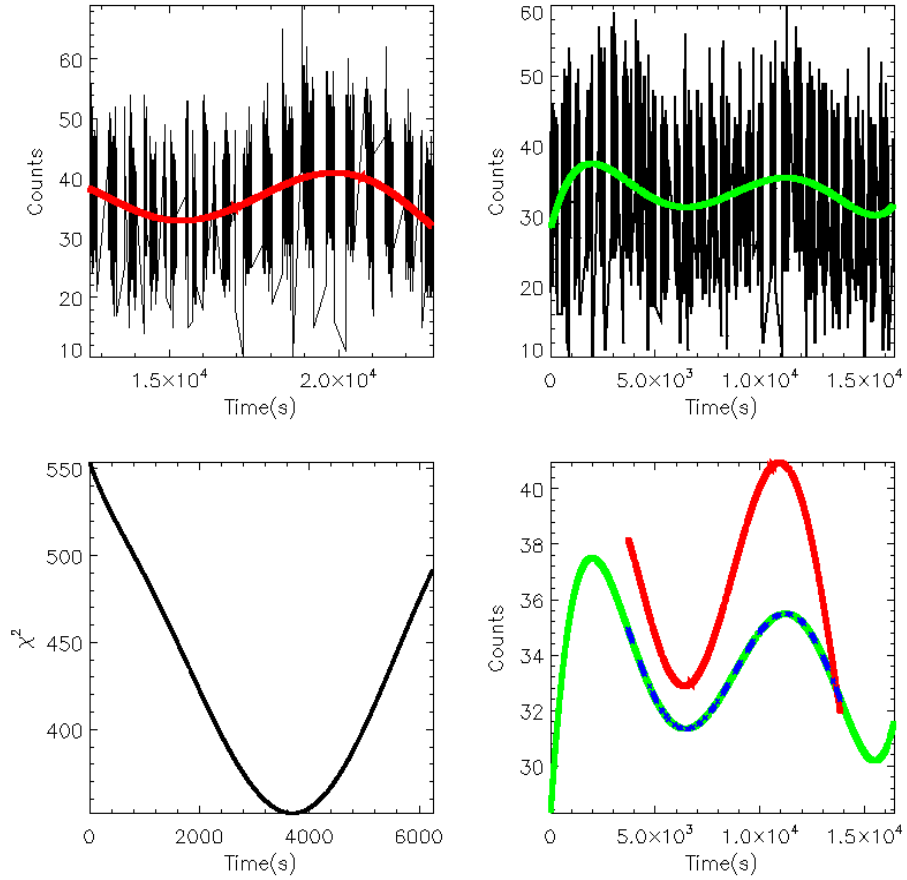


Figure 3.2: Top panel shows the light curves of Cygnus X-1 (ObsId 4646, one of the segment of the full observation) on the left and background (ObsId 2210) on the right, both fitted with fifth degree polynomials (red curve for Crab and green curve for background). Bottom left figure shows the variation of  $\chi^2$  as a function of shift in the Cygnus X-1 light curve with respect to the background, to determine the time for ‘phase matching’. Bottom right figure shows the ‘phase matched’ background and Cygnus X-1 polynomials, in the green curve and red, respectively. The blue curve represents the background where Cygnus X-1 observation is available.

errors on the raw ASAD of source and background observations were computed individually based on counting statistics and propagated to calculate the errors on the background-subtracted ASAD.

### 3.3.1.2 Polarisation estimation using MCMC simulations

This method is more robust to estimate the uncertainties on the polarisation parameters compared to  $\chi^2$  analysis, mainly for the observations having low Compton counts. It also allows the exploration of Bayesian model comparison

which helps in achieving the confirmation of the detection of polarisation. The fitted parameters and the associated errors are estimated by performing Markov Chain Monte Carlo (MCMC) simulations (Geyer, 2011) based on the Metropolis-Hastings algorithm (Hastings, 1970; Chib & Greenberg, 1995) for a large number (1 million) of iterations for the observations for which we are able to constrain the polarisation. For each iteration, the posterior probability is estimated based on the random sampling of the model (equation 3.3) parameter (A, B and  $\phi_0$ ) values. A set of parameter values for a given iteration is accepted or rejected by comparing the posterior probability with the previous iteration (ratio of the posterior probability should be greater than 1 for accepting the parameter values). The iteration for which the ratio of the posterior probability is less than unity is further compared to a random number to finally accept or reject the parameter values. Finally the modulation factor and the polarisation angle are estimated from the best fitted value of the parameters. The uncertainties on A, B and  $\phi_0$  are estimated by integrating the probability distribution function for the 68% confidence level (1 sigma uncertainty). The uncertainty on modulation factor is estimated by error propagation on A and B.

### Systematic uncertainties

The measurement of the polarisation are sensitive to the systematic uncertainties which make it important to account for all the sources of uncertainties for the final error estimations. Here we are going to describe the possible systematics involved in the polarisation measurement.

- There is a possibility of systematics in the background selection for the subtraction. We have investigated this effect by estimating the modulation factor and the polarisation angle considering two different blank sky observations for the background subtraction. It is found that the estimated parameters are within the error bar of each other.
- We also investigate the systematics in the modulation amplitude due to the unequal quantum efficiency of the CZTI pixels. The relative efficiency of the pixels varies about 5% which induces negligible false modulation.

Since we search for the Compton events throughout the CZTI plane, the relative quantum efficiency of the pixels is expected to be averaged out.

- Polarisation analysis using CZTI requires the geometric corrections to correct for the intrinsic asymmetry in the detector as well as asymmetry in the scattering geometry induced because of the presence of other instruments on one side of the CZTI and the one-sided albedo background. The background events are expected to be unpolarized and therefore, should not, in principle, show any modulation in the azimuthal angle distribution but it reflects a small but definite  $\sim 2\%$  modulation in the azimuthal angle distribution. Initially, we use to normalize the histogram by the simulated unpolarised histogram to correct this asymmetry. Now, we have normalized the polarised histogram by the observed average counts in the corner and the edge pixels which reduce the systematic almost negligible.

The contribution of each of these sources is taken into account while estimating the final uncertainties on the parameters but the effect of these systematics is found to be negligible.

### 3.3.2 Estimation of polarisation upper limit

The upper limit of polarization is estimated for the cases where we are not able to constrain the polarisation. We follow the method prescribed in [Kashyap et al. \(2010\)](#) (also used in [Chattopadhyay et al. \(2019\)](#) for GRB polarization analysis) which is done in two steps. First, we estimate the polarization detection threshold which is determined by limiting the probability of false detection, i.e.

$$Pr(\mu > \mu_\alpha \mid P = 0, N_{Compt}, N_{bkg}, BF > 3) \leq \alpha, \quad (3.1)$$

where,  $\alpha$  is the maximum allowed probability of false detection,  $P$  is the fraction of polarization,  $N_{Compt}$  and  $N_{bkg}$  are the observed number of Compton events and background events respectively and  $BF$  is the Bayes factor, minimum value of which should be equal to 3 according to our chosen criteria. The false probability is estimated simulating unpolarized incident radiation in Geant4 using

the *AstroSat* mass model for the observed Compton and background events. The modulation amplitude,  $\mu_\alpha$  for the maximum allowed probability of a false detection ( $\alpha$ ) is called the  $\alpha$ -level detection threshold. The next step involves calculation of probability of detection of polarization such that

$$Pr(\mu > \mu_\alpha \mid P > 0, N_{Compt}, N_{bkg}, BF > 3) \geq \beta, \quad (3.2)$$

where,  $\beta$  is the minimum probability of detection. For the given number of source and background events, simulation is done with varying polarization fractions (from 0 to 100%) and estimate  $Pr(\mu > \mu_\alpha)$  as a function of polarization fraction. We simulate the polarized photons in Geant4 at a polarization angle of  $22.5^\circ$  which corresponds to a  $\mu_{100}$  averaged over 0 to  $90^\circ$  polarization angles. The polarization fraction ( $P$ ) for which  $Pr(\mu > \mu_\alpha)$  exceeds  $\beta$  gives the upper limit of polarization. We use values of  $\beta = 0.5$  in conjunction with  $\alpha = 0.01$  for the upper limit estimations. It is to be noted that  $\beta = 0.5$  actually corresponds to the  $\alpha$ -level detection threshold if we assume the sampling distribution of the estimated modulation amplitude follows smooth Gaussian statistics with median equal to  $P$  (Kashyap et al., 2010).

### 3.4 Results and discussions

For polarisation analysis, the Compton events in the energy range of 100 - 380 keV are used. The analysis methodology where the azimuthal distribution of the Compton count is fitted with a sinusoidal function (equation 3.3) after the background subtraction and the geometric correction as discussed in Sec.3.3.

$$C(\phi) = A \cos(2(\phi - \phi_0 + \pi/2)) + B \quad (3.3)$$

where A, B and  $\phi_0$  are the fitting parameters. The modulation factor ( $\mu$ ) is given by the ratio of A and B which is directly proportional to the polarisation of the photon. The polarisation angle in the detector plane is given by  $\phi_0$ . For example, The modulation factor for ID 2992 is  $0.0746 \pm 0.0148$  and polarisation

angle in the detector plane,  $\phi_0$  is  $-6.53 \pm 11.81$ . The fitted parameters and the associated errors are also estimated by performing Markov Chain Monte Carlo (MCMC) simulations (see Section 3.3.1.2) In Figure 3.3 the posterior probability distribution for  $\mu$  (top left plot) and polarisation angle in the detector plane,  $\phi_0$  (bottom right plot) is shown for ID 2992. The best fit value from the MCMC for ID 2992 for the modulation factor and polarisation angle are  $0.0747 \pm 0.0148$  and  $-6.73 \pm 11.0$ , respectively. We find that the polarisation fraction and the polarisation angle by the modulation fitting and MCMC are similar.

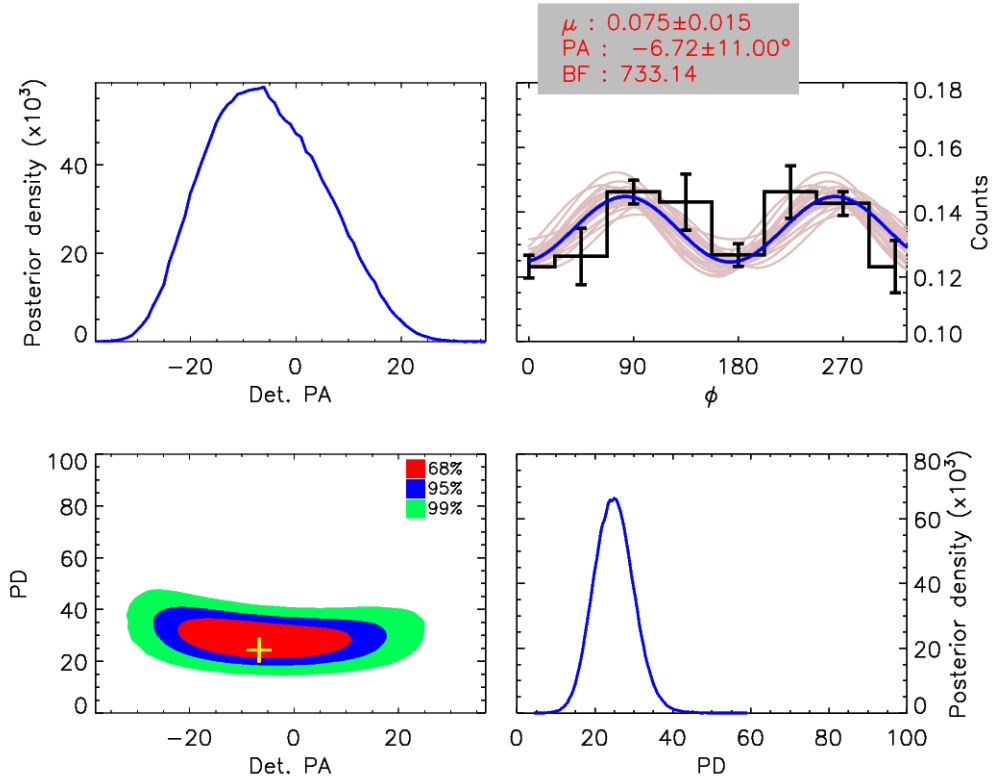


Figure 3.3: Modulation curve for ID 2992. Top left: posterior probability distribution for polarisation degree from MCMC iterations. Top right: the modulation curve and the sinusoidal fit shown in solid blue line, along with 100 random MCMC iterations. Bottom left: the contour plot for polarisation angle and degree for 68, 95 and 99% confidence levels. Bottom right: posterior probability distribution for polarisation angle from MCMC iterations.

The 8-bin modulation curve after background subtraction and geometry correction, along with the sinusoidal fit (solid blue line), is shown in the top right plot. We also show a distribution of the sinusoidal fits for 100 random iterations in solid pink lines. The 68%, 95% and 99% contours for polarisation fraction and

angle are shown in the bottom left plot in red, blue and green respectively. We have done the similar analysis for all remaining observations. The polarisation modulation curves and the contour plots are given in Figure 3.4, and 3.5. Since, the modulation amplitude is a positive definite quantity further investigation is required to claim the polarisation measurements. In order to claim confidently that the particular observation is truly polarized we have also estimated the Bayes factor, which is the ratio of the marginal likelihoods (likelihood function computed by integrating the posterior probability over the parameter space) of two function here the sinusoidal model (M1, for polarized photons) and a constant model (M2, unpolarized photons) to fit a function (for more details, see Chattopadhyay et al. (2019)). We have considered the observation polarised if the Bayes factor greater than 3 is obtained. The value of the Bayes factor above which the polarised model is favoured above unpolarised is subjective and sometimes  $>3.2$  is considered (Kass & Raftery, 1995). All the polarisation results of 8 observations is summarized in Table 3.2. The estimated Bayes factors are given in the fourth column of the table. We see that except ID 2992 all have Bayes factor below 3. The number of selected Compton events in 100 - 380 keV for the full observation is also given. It is to be noted that the uncertainties quoted in Table 3.2 on polarisation fraction and angle are obtained at 68% confidence level. From Table 3.2, based on the Bayes factor value only ID 2992 is polarised and in remaining observations we are unable to constrain the polarisation due to low exposure except ID 4646. In ID 4646, we do not see any polarisation even after sufficiently long exposure and low MDP value, only  $< 10\%$ , leads to the conclusion that this observation is unpolarised (see Figure 3.4 and 3.5). We have estimated the upper limit of the polarisation for the observations where we are unable to constrain it (see Table 3.2).

Table 3.2: Measured polarisation fractions (PF) and position angles (PA) for the Cygnus X-1 observations in (100 - 380 keV) energy range.

Observation ID	Effective Exposure (ks)	$N_{\text{compt}}$	Bayes Factor	PF(%) <sup>a</sup>	CZTI PA (°) <sup>b</sup>	sky PA (°)	MDP (%)	Count rate
9000000426	86	45048	0.72	<14	-	-	23	0.52
9000000436	48	26974	1.37	<16	-	-	29.67	0.56
9000000456	106	75430	0.82	<12	-	-	16.	0.71
9000002992	257	277662	733.14	$23 \pm 4$	$-6.53 \pm 11$	$236 \pm 11$	7.4	1.07
9000004492	139	103721	1.22	<15	-	-	14.41	0.75
9000004638	42	27182	1.51	<21	-	-	30.5	0.64
9000004646	170	137047	0.89	<7	-	-	10	0.81
9000004678	118	83782	0.71	<13	-	-	16	0.71

ID 2992 have sufficiently large exposure and statistically significant results. The analysis of this long observation confirms the hard X-ray polarisation in Cygnus X-1 in the 100 - 380 keV band. The modulation curve and the contour plot are shown in Figure 3.3. The source exhibits a clear polarisation signature with an estimated degree of polarisation of  $23\pm 4\%$ , greater than 5-sigma detection for 1 parameter of interest at 68% confidence level. The CZTI PA is  $-6.53\pm 11$  which when converted to the Sky PA, as discussed in chapter 2, results in the sky PA of  $236^\circ$  (from local North towards East in the anti-clockwise direction). The observed polarisation angle projected in the sky plane is in agreement with the *INTEGRAL* results ( $224^\circ\pm 15^\circ$ ). The contour plot, shown on the right side of the figure, shows that the polarisation degree and the angle are well constrained in 68, 95, and 99% confidence levels. The estimated Bayes factor is very high ( $\sim 734$ ), confirming very high statistical significance. With such high significance of detection, the energy dependence of the polarisation can also be explored. Figure 3.6 top panel shows the polarisation for ID 2992 in 100 - 175, 175 - 230, and 230 - 380 keV regions.

The bottom panel shows the polarisation angle of Cygnus X-1 in the hard state for all energy ranges. We see that the 100-175 keV signal is unmodulated (Bayes factor of only  $< 1.5$ ). The higher energies are polarized at  $> 3\sigma$  level (Bayes factor of 120 and 54, respectively). This resolves a long-standing puzzle in the X-ray polarisation measurements of Cygnus X-1. The low level of polarisation measured at low energies (OSO-8, *PoGO+*), consistent with the level of polarisation expected from a putative Compton cloud, was in apparent contradiction with the high level of polarisation measured by *INTEGRAL* above 250 keV, thus, in fact, making the *INTEGRAL* measurements viewed with scepticism in the community. The CZTI measurements smoothly bridge this gap, confirming the presence of a separate highly polarised component above 100 keV. Such high polarisation fraction very strongly suggests synchrotron emission and indicates the presence of an ordered magnetic field, very strongly indicating the dominance of a separate jet component close to the black hole. We could not constrain the polarisation in some observations probably due to low exposure observations. However, in some observations we do not see any modulation in signal even after

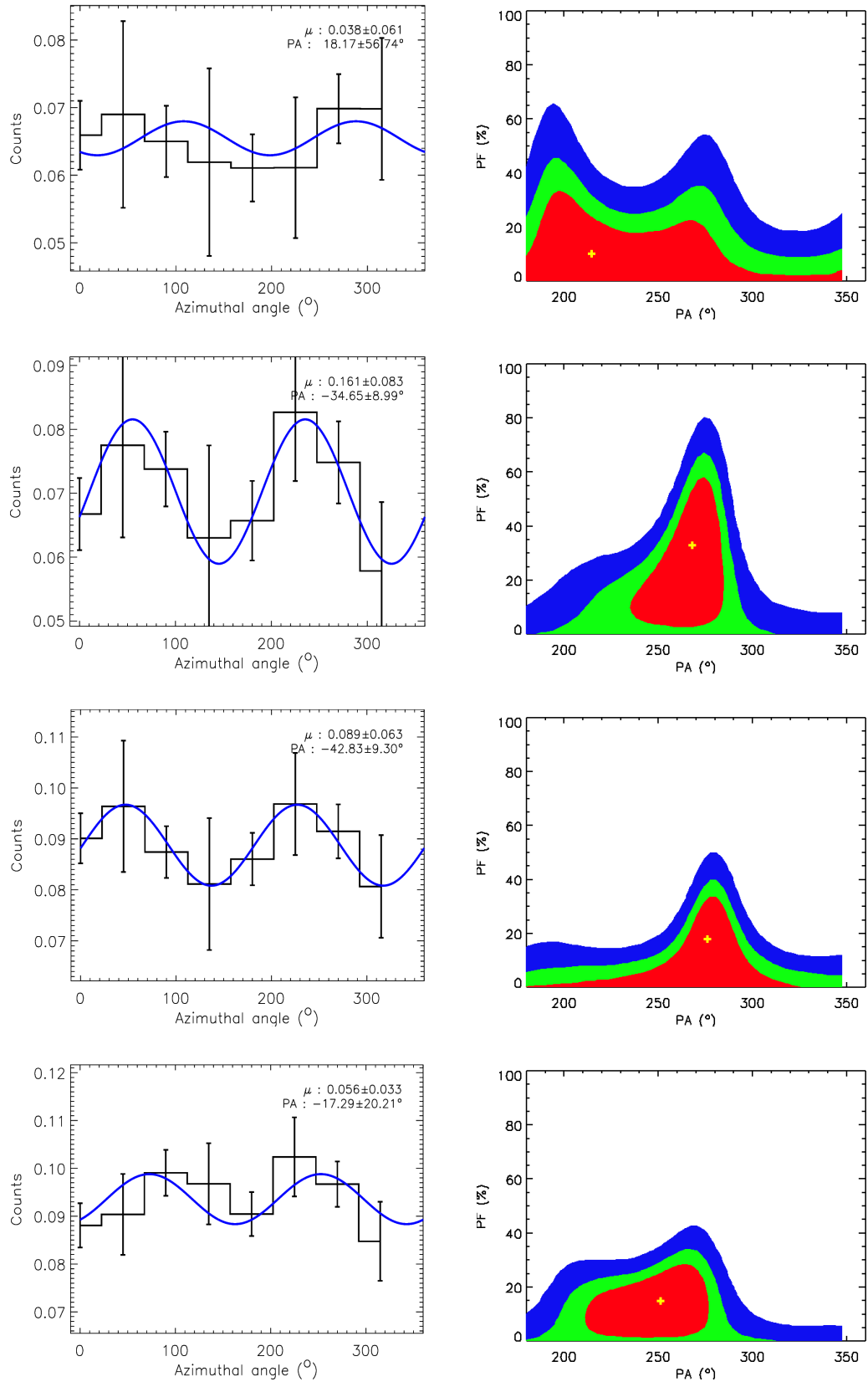


Figure 3.4: Top to bottom: Cygnus X-1 polarisation results for ID 0426, ID 0436, ID 0456, ID 4492 in 110 - 380 keV energy band. The left figure shows the modulation curve and the right figure shows the contour plot.

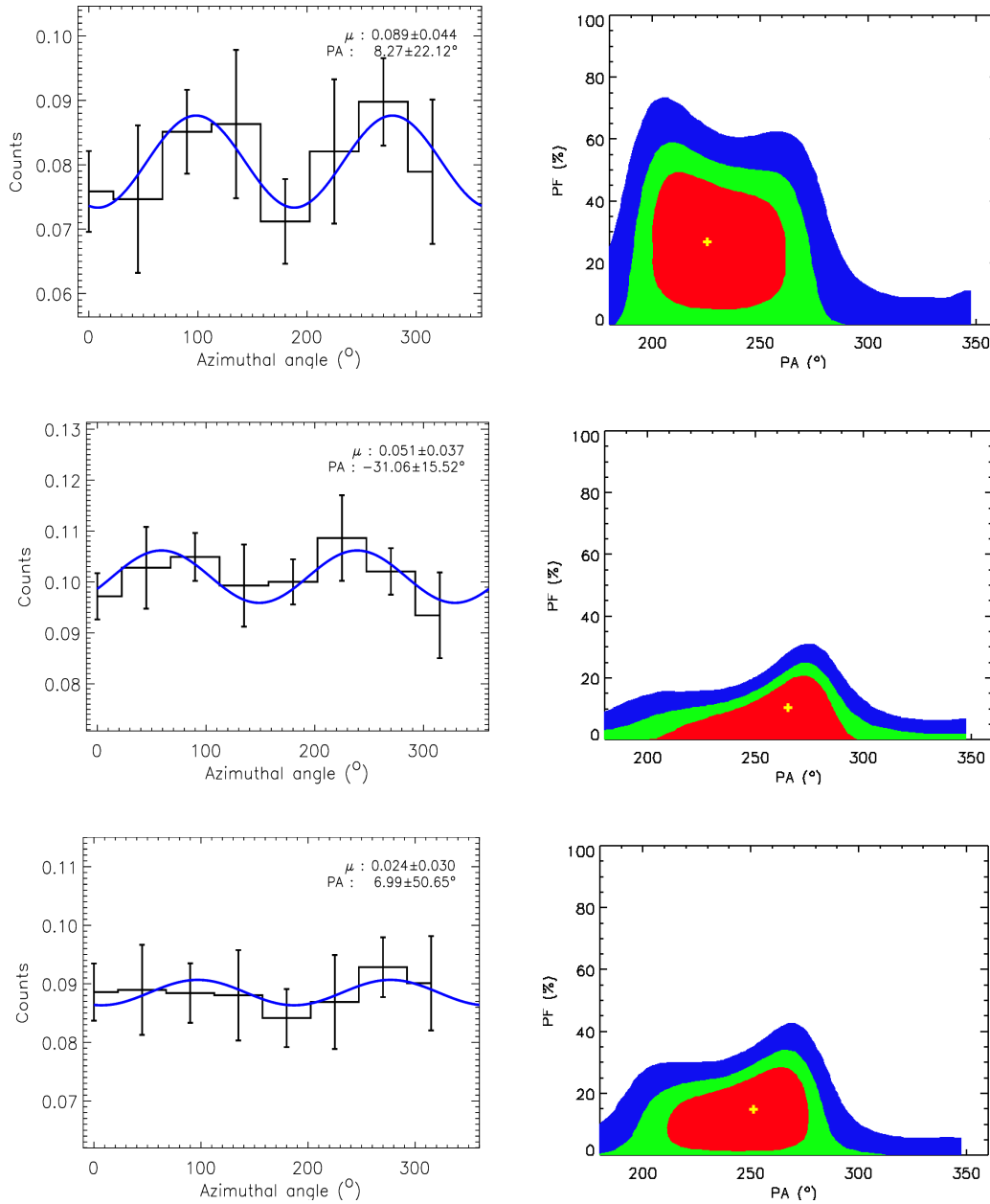


Figure 3.5: Top to bottom: Cygnus X-1 polarisation results for ID 4638, ID 4646, and ID 4678 in 100 - 380 keV energy range. The left figure shows the modulation curve and the right figure shows the contour plot.

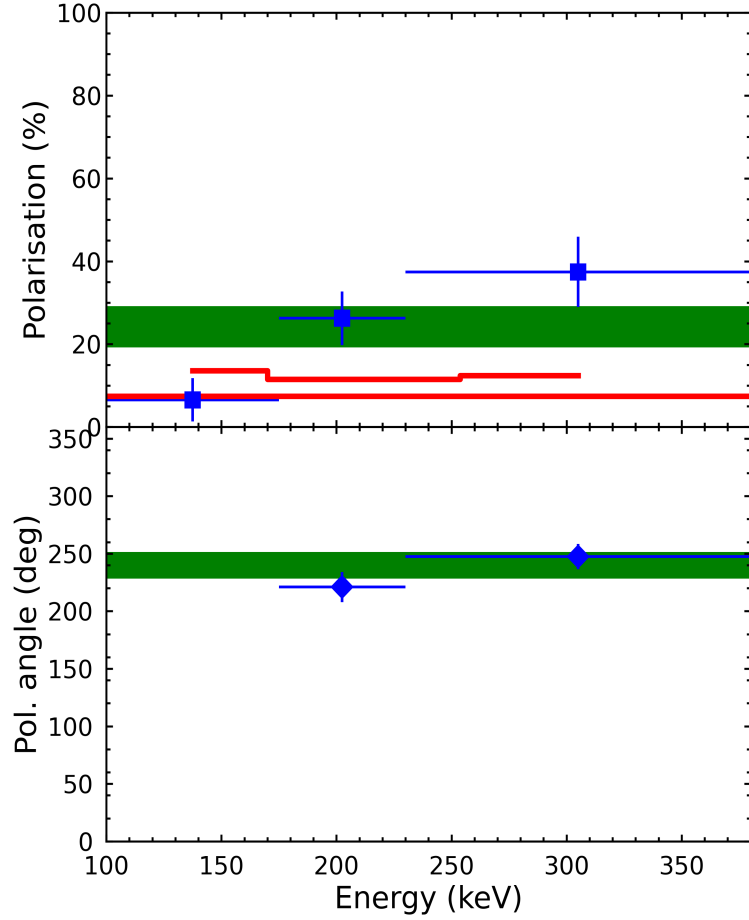


Figure 3.6: Top panel: Cygnus X-1 polarisation results for ID 2992 for the full energy range of 100 - 380 keV (shown in green band), 100 - 175 keV (PF < 15%), 175 - 230 keV (PF- $26 \pm 6\%$ , PA- $228 \pm 12^\circ$ ) and 230 - 380 keV (PF- $39 \pm 9\%$ , PA- $239 \pm 11^\circ$ ). The red line shows the respective MDP values. The bottom panel shows the polarisation angle in sky (North to East in an anti-clockwise direction)

having sufficiently long exposure, for example, ID 4646 having MDP  $\sim 10\%$ . Cygnus X-1 show polarisation in some observations and unpolarised in others, it is not constant in observation to observation. The possible explanation for this could be the different spectral states of the Cygnus X-1. [Lubiński et al. \(2020\)](#) showed there is a correlation in the radio flux in different spectral states of the Cygnus X-1. It is observed that the radio flux variation is highest in the hard state and low in the soft state. We need to determine the spectral states of the these observations to see if there is any dependence of polarisation on spectral states. The trend of gradual increase in PF with energy above 170 keV and PF 39% at higher energies (see Figure 3.6) suggest that the net polarisation could be

due to the mixing of two separate components with one component being highly polarized synchrotron radiation from jet whereas the other component is unpolarised, possibly from thermal Comptonisation from the corona. To decipher the contribution from the two components, spectroscopy in the higher energy is required.

### 3.5 Summary

We have performed the polarisation analysis of the eight observations which are selected based on the flux and the exposure. Most of these observations are unpolarised (Bayes factor  $< 3$ ) or unconstrained due to the low exposure giving statistically insignificant Compton counts. Despite having sufficient exposure time, observation ID 4646 still gives unpolarised flux. Observation ID 2992 is found to be polarised having 23% polarisation with 5 sigma level detection in 100 - 380 keV. Polarisation show increasing trend with energy with 39% polarised in the highest energy bin. MDP is very high below 200 keV because of low count rate, hence difficult to constrain the polarisation fraction in 100 - 200 keV. Such a high polarisation with increasing trend with energy in one observation and no modulation in the signal in ID 4646 is possibly due to different spectral states. (Lubiński et al., 2020) showed the correlation between the variation in the radio flux and the spectra state of the Cygnus X-1. It is highest in the hard intermediate state and intermediate level in other hard state and very low variation in the soft state. Therefore, getting such high polarisation in ID 2992 is possibly due to synchrotron emission from the jet. We got different polarisation in different observations and (Lubiński et al., 2020) suggest there is correlation between the spectral state and the radio flux variation. To see the spectral state of the different IDs of the Cygnus X-1 and decipher the contribution of the polarisation component in the signal spectroscopy in the higher energy is required. We will try to explore and extend the spectral energy range of the CZTI using the polarisation events in the next chapter.

# Chapter 4

## Extending the energy range of AstroSat-CZTI up to 380 keV with Compton spectroscopy using Crab

In the previous chapter, we have shown the need of Compton spectroscopy at higher energy to decipher the contribution of the polarisation component at higher energy. In this chapter, we have discussed the methodology to extended the energy range of the CZTI using the polarisation events upto 380 keV. In the first section of the chapter, exploration of the compton sensitivity of the CZTI upto 500 keV using the good and low gain pixels. In the later section we have discussed about the technique for the background selection and subtraction developed to finally extend the energy range and validated the same using the 5 years data of Crab observations.

### 4.1 Exploring sub-MeV sensitivity

After the launch of *AstroSat*, about 20% of the CZTI pixels (therefore  $\sim 20\%$  of the total  $976 \text{ cm}^2$  geometric area) were found to have a relatively lower gain than that of the spectroscopically good pixels, which makes these pixels sensitive to

higher energy photons ( $\sim 70 - 1000$  keV). The 5 mm thick CZT detector provides sufficient detection efficiency up to 1 MeV. Motivated by this, we tried to explore the possibility of including these low gain pixels in the analysis to enhance the spectroscopic sensitivity of CZTI up to the sub-MeV region.

The Coded mask spectrum generated using the standard pipeline is restricted up to 100 keV, where the background is simultaneously obtained from the coded mask imaging. Above 100 keV, the 0.5 mm thick Tantalum mask becomes increasingly transparent, along with the collimators and CZTI support structures. To obtain the high energy spectra above 100 keV in the absence of simultaneous background measurements requires a careful selection of blank sky observations. Background flux depends on multiple factors like the spacecraft's geometric location in orbit, orbital precession of the satellite, and the time spent within the high background South Atlantic Anomaly (SAA) region in an orbit. These contribute to a systematic modulation in the flux along the satellite's orbit, making the background subtraction quite challenging.

Another challenge is to calibrate these pixels in the absence of any mono energetic lines at energies above 100 keV to estimate their gains. A careful calibration of these pixels have been attempted by [Chattopadhyay et al. \(2021\)](#) and spectroscopy up to 900 keV is explored for Gamma Ray Bursts (GRBs). Compared to the ON-axis sources, spectroscopy of GRBs is relatively easy because of the availability of background (from the immediate pre-GRB and post-GRB observations) and the significantly higher signal to noise ratio for the GRBs. The ON-axis bright astrophysical sources are fainter, and hence longer exposure observations are required for sufficient detection, which leads to more instrumental, charged particle, and cosmic X-ray background contributions.

This chapter outlines the methodology of sub-MeV spectroscopy with CZTI for bright ON-axis sources. We utilize the same Compton events, which are used to extract polarimetry information of the X-ray photons ([Chattopadhyay et al. 2014, 2019](#); [Vadawale et al. 2015, 2018](#)) to enhance the spectroscopic capability. The selection of background observations and the background subtraction used for polarimetric measurements is described in detail here, with an emphasis on spectroscopy. We utilize the low gain pixels to extend the spectro-

scopic energy range of the instrument well beyond the standard limit. With the inclusion of the low gain pixels, Compton spectroscopy was also extended to 500 keV. We use the *AstroSat* mass model in GEANT4 (Agostinelli *et al.* 2003) to generate the spectral response.

To extend the spectroscopic range, a standard calibration source is required with known spectral parameters. It should be bright, relatively stable, and have simple spectrum in the broad energy range. In X-rays, Crab (pulsar+nebula) is the primary astrophysical calibration source which is bright, stable and have simple power law spectrum with photon index  $\sim 2.1$  (Kirsch *et al.*, 2005) and above 100 keV reported a softer index of  $\sim 2.2-2.25$  Jourdain & Roques (2020); Kuiper *et al.* (2001). The Crab is observed many times since the launch of the *AstroSat*. Therefore, we have used the CZTI observations of the Crab for the broad band spectral analysis.

Here we carry out broadband spectroscopy of Crab using standard spectroscopic events (30 - 100 keV), 2-pixel Compton events including low gain pixels (100 - 500 keV), and also explored the 1-pixel events including low gain pixels (100 - 700 keV) to establish the sub-MeV spectroscopy methods and at the same time try to constrain the spectral parameters of Crab at higher energies.

In section 4.2.1.2, a brief description of the observations and analysis procedure is given. The results obtained are presented in section 4.2.3. Finally, in section 4.2.4, we discuss the sub-MeV sensitivity of CZTI.

### 4.1.1 Observations and analysis procedure

There are many observations of Crab over the past seven years of operation of *AstroSat*. We have selected those observations with sufficient exposure ( $>30$  ks to get the statistically significant Compton counts) and also having a suitable background observation. The selection of appropriate background observation and subtraction is an important part of the analysis. The CZTI support structure becomes increasingly transparent above 100 keV. Therefore, background measurements can be affected due to the presence of bright X-ray sources within  $70^\circ$  of the pointing direction of CZTI. The Crab and Cygnus X-1 are two bright

sources which should be avoided during the background observation. Since both the sources are located almost opposite to each other in the sky, it is possible to find a good region, away from these two sources, for the background observations. The background observation should also be close to the source observation time to avoid the error in some long-term secular variations in the background behavior. There are a few such observations that satisfy the criterion of the background selection. Based on these considerations, we have finally selected five observations for further analysis. Details of the Crab observations and the corresponding background observations selected for the present analysis are given in Table 4.3.

Table 4.1: Summary of Crab and blank sky observations. Crab RA: 83.63° and DEC: 22.01°

ObsID	Crab			Blank Sky			RA (deg)	DEC (deg)
	Date (yyyy/mm/dd)	Exposure (ks)	ObsID	Date (yyyy/mm/dd)	Exposure (ks)	ObsID		
9000000096	2015/11/12	41	9000000276	2016/01/16	64	9000000276	183.48	22.8
9000000252	2016/01/07	60	9000000276	2016/01/16	64	9000000276	183.48	22.8
9000000406	2016/03/31	114	9000000404	2016/03/29	64	9000000404	228.21	-9.09
9000000964	2017/01/14	78	9000000974	2017/01/22	51	9000000974	183.48	22.8
9000000970	2017/01/18	123	9000000974	2017/01/22	51	9000000974	183.48	22.8

#### 4.1.1.1 Single and Compton event selection

CZTI is a pixelated detector. The scientific data analysis of CZTI is done with two types of CZTI events: 1-pixel or single pixel events and 2-pixel events. The single pixel events registered in the CZTI are considered as the true 1-pixel events if there is no event registered within 100  $\mu\text{s}$  time window on either side of the single event. The events in the CZTI are time stamped at every 20  $\mu\text{s}$  (Bhalerao *et al.* 2017) and any two events occurring within 40  $\mu\text{s}$  coincidence time window in two pixels are considered as true 2-pixel event (Chattopadhyay *et al.* 2014). The standard single pixel mask-weighted spectra in 30 - 100 keV (hereafter PE (Photo-Electric events)) is generated following standard pipeline software available at the AstroSat science support cell (ASSC) \*.

Above 100 keV, the 5 mm thick CZTs have sufficient efficiency for Compton interactions. Polarisation analysis in the 100 - 380 keV range depends upon such Compton events (Chattopadhyay *et al.* 2014; Vadawale *et al.* 2015). These Compton events are used here to do spectroscopy in the 100 - 380 keV range. After incorporating the low gain pixels, Compton spectroscopy can be further extended to 500 keV. For the Compton event selection, we follow the 2-pixel Compton event selection criteria, as discussed in Chattopadhyay *et al.* 2014. The readout logic in the CZTI is such that it reads events from one module at a time. If two events are registered in two different pixels in the same module, then it is possible that two events would get two different time stamps. Hence, all the events occurring within the coincidence time window of 40  $\mu\text{s}$  are selected for the analysis. These events are further filtered through Compton kinematics criteria: 1) events must be in adjacent pixels and 2) sum and ratio of the deposited energies must be consistent with those expected for true Compton events for the scattering geometry of CZTI (ratio of the energies deposited in two adjacent pixels is between 1 and 6). After the selection of the Compton events, the sum of the energy deposited in the scattering and the absorption pixel is used to generate the 2-pixel Compton events spectrum including low gain pixels in the 100 - 500 keV (hereafter CS (Compton Scattered events)). We have binned the

---

\*<http://astrosat-ssc.iucaa.in/>

data at 10 keV energy bin size in the 40 channels ranging from 100 keV to 500 keV.

#### 4.1.1.2 Background subtraction: Phase match method

The primary sources of background in the CZT detector are the Cosmic X-ray background, the Earth's X-ray albedo, and the locally produced X-rays due to Cosmic ray interactions. The Compton background in the detector is due to the Compton scattering of these background X-rays. In addition to this, a small part of the Compton background consists of chance coincidence events within 40  $\mu$ s coincidence time window.

The background events from the blank sky observations are filtered through the same selection criteria as the source, as discussed in section 4.1.1.1. The observed background counts show a prominent orbital variation as well as a diurnal variation (Antia *et al.*, 2022) depending on the geometric location of the spacecraft in the orbit, orbital precession, and the location and duration of the SAA region in orbit. All these contribute to a systematic modulation (see the top panel of Figure 4.1) in the flux along the orbit of the satellite within the duration of the observation. Because of the modulating flux, it is important to select similar portions of the Crab and background orbits based on the spacecraft's ground tracks (latitude and longitude) and use them for further analysis. But this puts a strict condition on the selection of the orbits and leaves a short usable exposure of Crab and background observations. An alternate method developed for background subtraction is to match the phase of the background and Crab light curves (the 'phase match method'), used for the polarisation measurements of Crab (Vadawale *et al.* 2018). In the phase match method, first, the Crab and background light curves are fitted with an appropriate higher-order (here 5<sup>th</sup> order) polynomial. Then the Crab and background light curves are matched by sliding the Crab polynomial over the background polynomial every 10 seconds and estimating the best match by minimising the  $\chi^2$ . Within the matched region of the two polynomials, the background is taken only for those time regions for which there is a source observation (see bottom right of Figure 4.1). From the background's phase-matched region, we calculate the ratio of the average back-

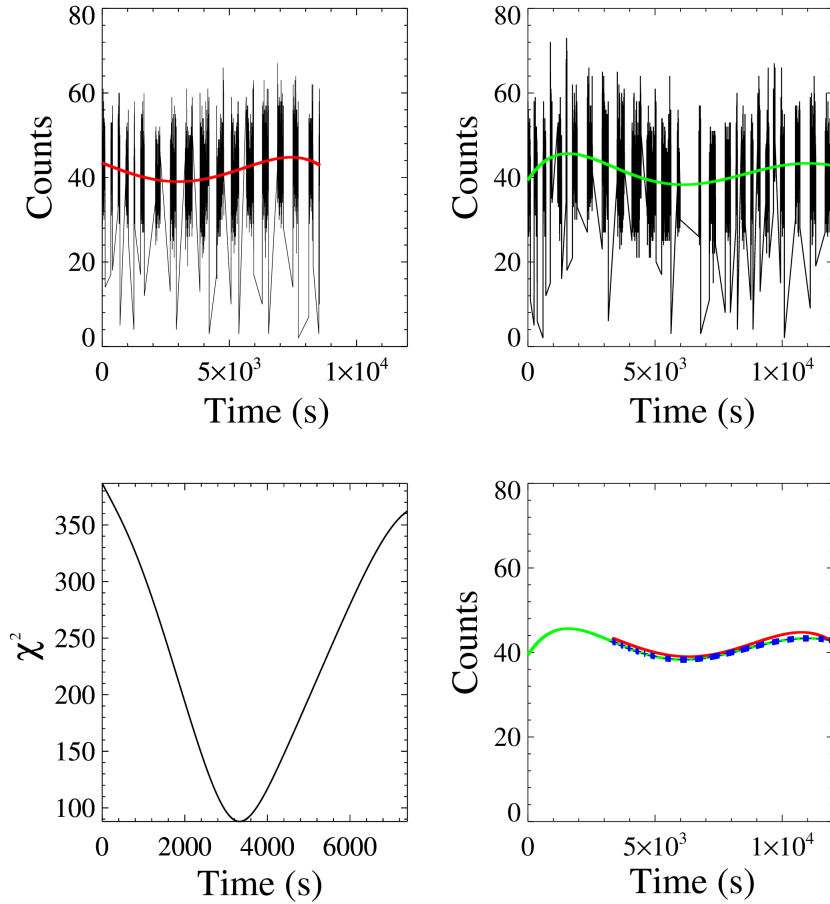


Figure 4.1: Top panel shows the light curves of Crab (ObsId 96) on the left and background (ObsId 276) on the right, both fitted with fifth degree polynomials (red curve for Crab and green curve for background). Bottom left figure shows the variation of  $\chi^2$  as a function of shift in the Crab light curve with respect to the background, to determine the time for ‘phase matching’. Bottom right figure shows the ‘phase matched’ background and Crab polynomials, in the green curve and red, respectively. The blue curve represents the background where Crab observation is available.

ground count rate to the count rate in the phase matched region (‘correction factor’) and multiply that to the total background exposure to calculate an effective background exposure. The use of effective exposure automatically takes care of the different phases of source and background observations. For example, if the source and backgrounds are observed in the same phase, the multiplication factor will be close to 1. For longer source observations (exposure  $\gg$  background exposure), it is divided into multiple parts and for each part of the source observations, we calculate the correction factor in the way described above and then the final correction factor is calculated as the weighted average.

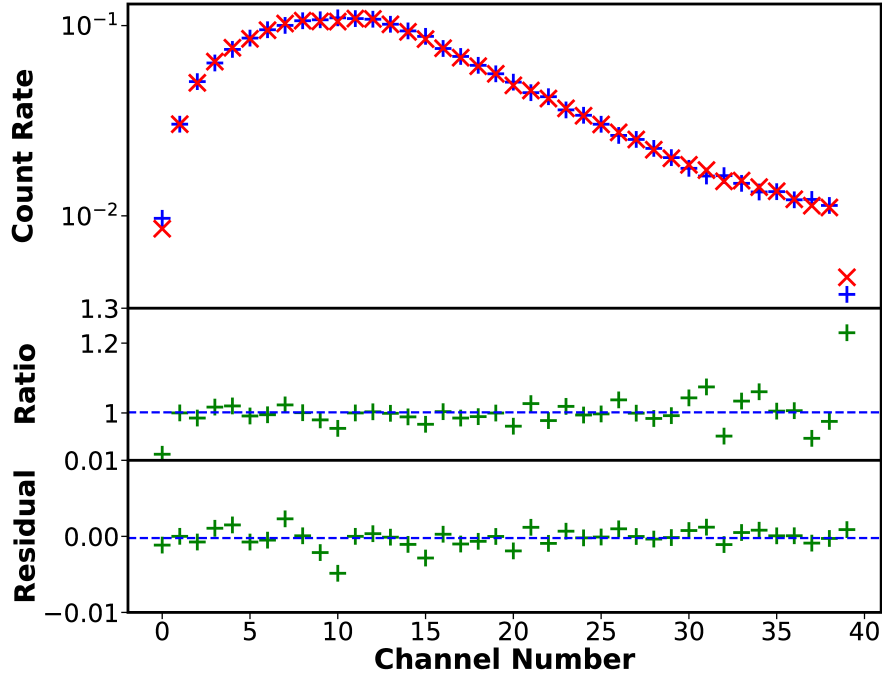


Figure 4.2: The top figure shows the phase matched 2-event Compton spectra (CS) of the blank sky observation UB (red) and background CB (blue) from 100 keV to 500 keV. The ratio of the two spectra is shown in the middle panel and the residuals of the two are shown in the bottom panel.

It is to be noted that the phase match method only ensures that the source (Crab in this case) and blank sky background data are taken for the same orbital phase (spacecraft orbit). It is not for the background spectral modeling. The background scaling is done to the phase matched background region to best mimic the actual background during the source observation. Because the background spectra are obtained from observations of “blank sky” with no other hard X-ray sources in the FOV (confirmed from BAT catalog), the spectra for the used backgrounds are expected to be the same. To demonstrate this, we selected a CZTI observation from UVIT catalog (ObsID 1008) such that there are no other bright X-ray sources in the FOV of CZTI (hereafter ‘UB’ (UVIT catalog Background)). We then used the polynomial method to do phase match between UB and background data ObsID 974 (here after ‘CB’ (CZTI catalog Background)), which is used in the analysis and correct for total flux in CB for the phase of UB. Because UB is essentially a blank sky background for CZTI, similar flux and spectra for both CB and UB after phase correction is expected.

We found identical flux for both CB and UB (see Figure 4.2), signi-

fyng that the polynomial method is capable of finding the common phase and scale the flux accordingly. The spectra are also found to be identical, justifying the underlying assumption that the blank sky observations for CZTI with the predefined selection criteria yield a similar photon energy distribution.

#### 4.1.1.3 Spectral response

The response for PE is generated using the standard pipeline of the *AstroSat* whereas for CS using the GEANT4 simulation of the *AstroSat* mass model. Details of the *AstroSat* mass model and its validation has been discussed in Chattopadhyay *et al.* 2019 and Mate *et al.* 2020. We simulated the mass model for 56 mono-energies ranging from 100 keV to 2 MeV (at every 20 keV up to 1 MeV and 200 keV till 2 MeV) for  $10^9$  photons. For each energy, the distribution of deposited energy in CZTI pixels is computed at 1 keV binning for each pixel. The CZTI pixel-level LLD (Lower Level Discriminator), the ULDs (Upper Level Discriminator), list of noisy and dead pixels obtained from the actual observational data are applied to the simulation data. For 2-pixel Compton events, the sums of the energies in the corresponding two pixels are used to obtain the total deposited energy, while for single event response, total absorbed energy for a given incident photon is used. We applied the same criterion of event selection, as discussed in section 4.1.1.1. We then convolve the 1 keV bins by a Gaussian of 8 keV Full Width at Half Maximum (FWHM). We have not noticed any significant increase in FWHM with energy for CZTI pixels during ground calibration. Therefore, FWHM is kept constant across the energy. It is to be noted that the response for PE is generated using  $\mu\tau$  and charge diffusion based line profile model (Chattopadhyay *et al.* 2016).

Table 4.2: Comparison of fitted parameters between *INTEGRAL/SPI* and *AstroSat* for broken power law. The errors are reported for 90% confidence interval. The mean value of the parameters of all the observations for different combinations of data is mentioned in the bottom row of each block.

Instrument	Spectra	ObsID	<i>PhoIdx1</i>	<i>PhoIdx2</i>	$E_{break}$ (keV)	<i>Norm</i>	$Flux(30 - 100keV)$ $10^{-8}(\text{erg}/\text{cm}^2\text{s})$	$\chi^2/\text{dof}$
INTEGRAL			$2.08^{+0.01}_{-0.01}$	$2.23^{+0.05}_{-0.05}$	100*	$9.3^{+0.14}_{-0.14}$	1.30	
CZTI	<i>PE&amp;CS</i>	96	$2.18^{+0.05}_{-0.05}$	$1.80^{+0.48}_{-0.47}$	100*	$5.98^{+1.27}_{-1.04}$	$0.56^{+0.10}_{-0.09}$	232/175
		252	$2.08^{+0.03}_{-0.03}$	$1.72^{+0.44}_{-0.48}$	100*	$6.00^{+0.84}_{-0.73}$	$0.85^{+0.12}_{-0.10}$	238/172
		406	$2.12^{+0.03}_{-0.03}$	$1.63^{+0.39}_{-0.36}$	100*	$7.5^{+0.78}_{-0.70}$	$0.89^{+0.09}_{-0.08}$	288/175
		964	$2.08^{+0.04}_{-0.04}$	$2.65^{+0.90}_{-0.74}$	100*	$5.73^{+0.90}_{-0.77}$	$0.82^{+0.11}_{-0.12}$	244/172
		970	$2.10^{+0.03}_{-0.03}$	$1.98^{+0.48}_{-0.44}$	100*	$6.44^{+0.72}_{-0.64}$	$0.82^{+0.09}_{-0.08}$	328/172
		mean	$2.11^{+0.02}_{-0.02}$	$1.95^{+0.18}_{-0.18}$	100*	$6.33^{+0.32}_{-0.32}$	$0.79^{+0.06}_{-0.06}$	

### 4.1.2 Results: Single and Compton event spectra (PE and CS)

We use the broken power law model to fit the Crab curved spectra in 30 - 500 keV. It has been long used to explain the Crab spectra with break energy at 100 keV (Strickman *et al.* 1979; Ling & Wheaton 2003 ). *INTEGRAL/SPI* has also shown the spectral fitting using broken power law up to sub-MeV region (20 keV - 1 MeV) (Jourdain & Roques 2008). We have analysed all the selected observations and then fitted the resultant spectra (PE and CS) simultaneously using `const×bknpower` in *XSPEC* (Arnaud 1996) freezing break energy at 100 keV while the other parameters (photon indices) are tied across the spectra. To account for the cross calibration and differences between the different spectra, a constant was multiplied to the model. It was fixed to one for PE and left free to vary for others. The PE below 30 keV and above 100 keV is ignored due to calibration issues. No systematic has been added to the PE and CS. Spectral fitting for one of the five observations (ObsID 406, 114 ks) is shown in Figure 4.3. The values of the fitted parameters for all the five observations along with the *INTEGRAL/SPI* results are given in Table 4.5. The low energy slope (*PhoIndx1*) and the higher energy slope (*PhoIndx2*) are well constrained and consistent with the *INTEGRAL/SPI* (Jourdain E., Roques J. P. 2008) values within errors (see Figure 4.4). The contour plots of *PhoIndx2* versus *Norm* for all the five observations are shown in Figure 4.5. The inputs for the contour plot are generated using the chain command in *XSPEC* after getting the best fit parameters, and the corner plots are generated using the python corner module (Foreman-Mackey 2017). The corner plots show that the value of *PhoIndx2* is  $2.04^{+0.48}_{-0.44}$  and that of *Norm* is  $6.39^{+0.71}_{-0.63}$ , which is  $\sim 31\%$  smaller than the *Norm* for *INTEGRAL/SPI*.

CZTI sensitivity is also studied by looking at the flux variation of Crab with time. Figure 4.6 compares the Crab flux covering the period between 2015 Nov 12 and 2017 Jan 18. Each data point corresponds to the flux obtained in each observation, and the dotted line represents the flux measured by *INTEGRAL/SPI*. The flux from ObsID 96 is much lower than the values found for the

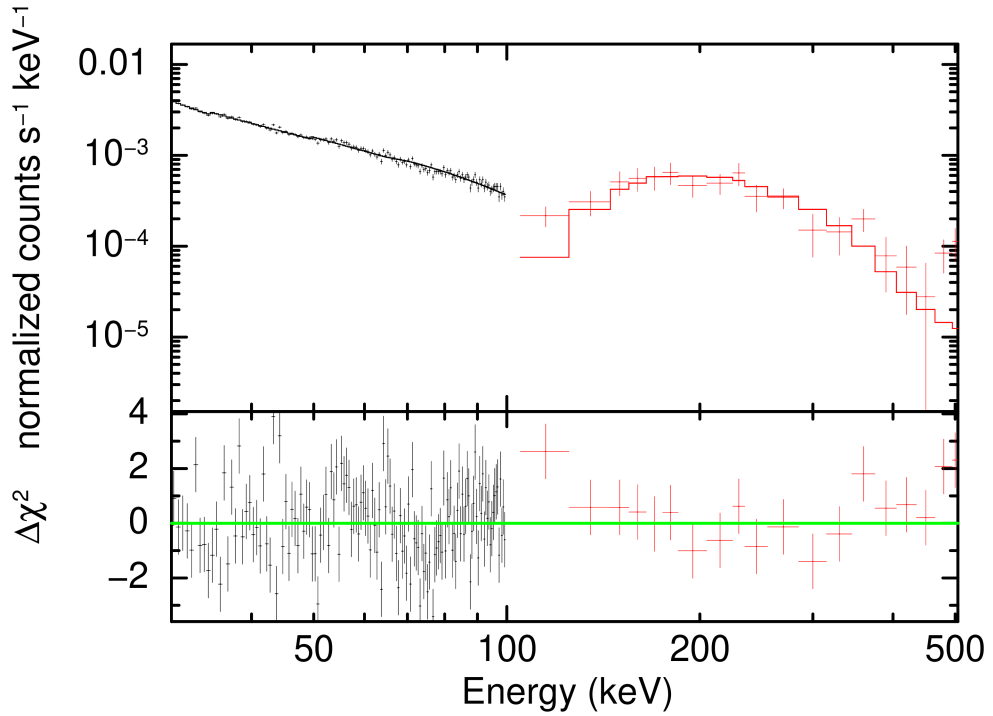


Figure 4.3: Broadband spectra of Crab (ObsID 406, 114 ks) fitted with a broken power law. The black, red colors are used for PE, and CS respectively.

other ObsIDs. If we exclude the data from ObsID 96, the remaining four measurements are within 5% of the mean value. We note here that the background for this ObsID is measured more than two months before the Crab observation, whereas for all the other ObsIDs, the background is measured within ten days of the respective Crab observation. The effect of secular variations in the background on the flux measurements needs to be investigated further.

### 4.1.3 Discussion

In this article, we have attempted to explore the sensitivity of CZTI in the sub-MeV region and have outlined a methodology of sub-MeV spectroscopy using Crab observations. For this purpose, we have used the single pixel mask-weighted spectral data in the 30 - 100 keV energy range (PE) and 2-pixel Compton events including low gain pixels in the 100 - 500 keV energy range (CS). For this work, we used the calibration parameters obtained by [Chattopadhyay et al. \(2021\)](#) for similar work to explore the sub-MeV spectroscopic sensitivity for Gamma ray Bursts (GRBs). The advantage in the case of GRBs is the higher signal

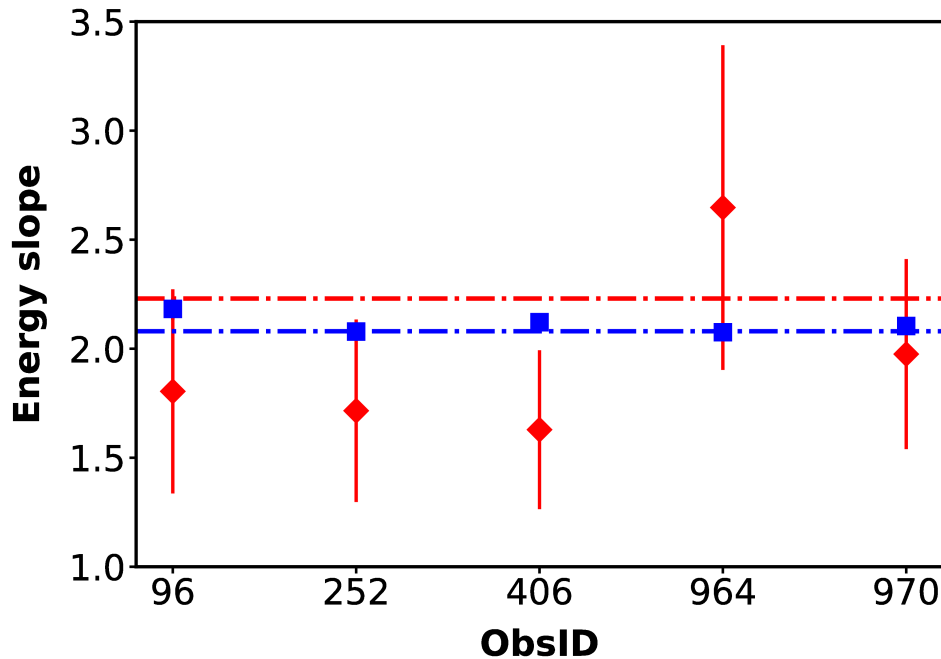


Figure 4.4: Best fit parameter of all the selected observations obtained after simultaneous fitting of PE and CS using broken power law model. Red diamonds represent higher energy slope (*PhoIndx2*) and the blue squares represent low energy slope (*PhoIndx1*). The dashed-dot horizontal lines represent the INTEGRAL value of *PhoIndx1* (blue) and *PhoIndx2* (red) in the corresponding energy regime.

strength and, in particular, the availability of simultaneous background events before and after the burst. In the case of persistent sources, the unavailability of simultaneous background spectra makes the selection of proper blank sky flux and its subtraction extremely important (section 4.1.1.2), particularly when the signal to noise ratio is relatively low. For this work, the spectral response was generated using a simple Gaussian energy distribution for simplicity (section 4.2.2.5), which we plan to improve later with the use of a more physical line profile model based on charge trapping and diffusion (Chattopadhyay *et al.* 2016).

We applied these techniques for spectral analysis of the Crab, where we used a broken power law (`bknpower` in `XSPEC`) for the spectral fitting. The spectral fits show sufficient flux sensitivity of CZTI to carry out spectroscopy for ON-axis bright sources (see Table 4.5) up to 500 keV. For the single event and Compton event spectra in 30 - 500 keV (PE and CS) for the individual observations, the low energy slope (*PhoIndx1*) agree reasonably with the INTE-

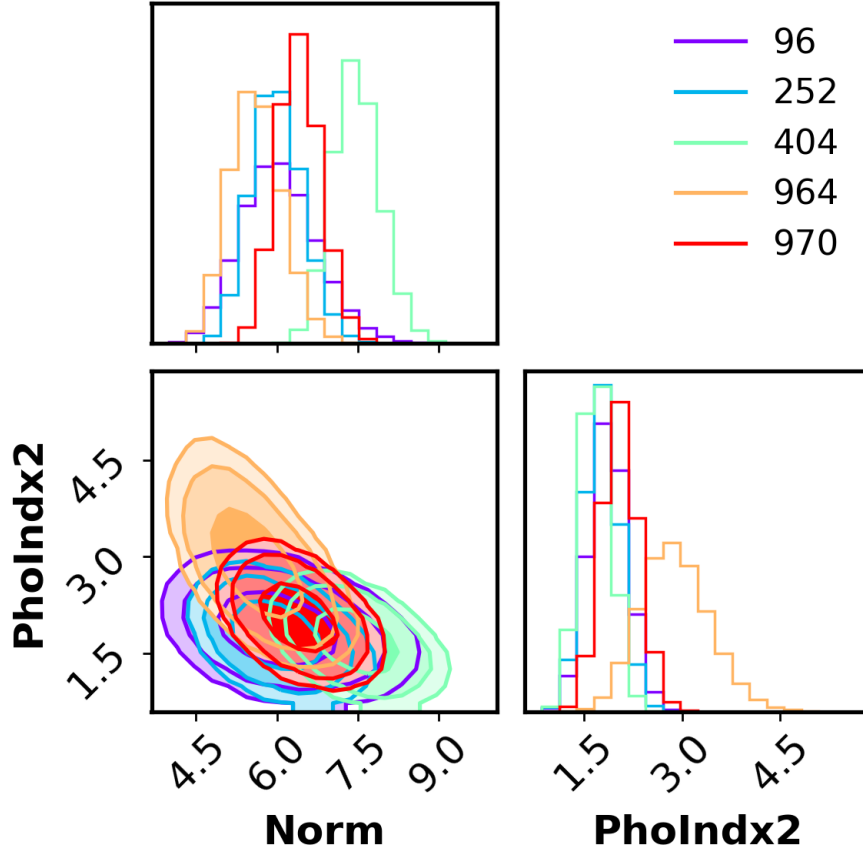


Figure 4.5: Corner plot of the  $phoIdx2$  versus  $Norm$  for all the five ObsIDs plotted together for PE and CS. Different colors of contours represents different observations as shown in legend. The peak value of the  $PhoIdx2$  is  $2.04^{+0.48}_{-0.44}$  and the  $Norm$  is  $6.39^{+0.71}_{-0.63}$

GRAL/SPI result but high energy slope ( $PhoIdx2$ ) showing a possible flattening. We note that the measured flux by CZTI is lower by  $\sim 31\%$  than that estimated by *INTEGRAL/SPI*. However, it should also be noted that in general, it is quite difficult to make a comparison of flux measurements of the two instruments, particularly in hard X-rays, due to the difficulty in measurement of the absolute effective areas of various instruments. Considering the errors in our flux measurements ( $\sim 15\%$ ) and the 5% accuracy claimed for Crab flux measurements (Jourdain & Roques 2020), there appears to be a  $\sim 2$  sigma difference in the flux measurements of Crab made by CZTI as compared to *INTEGRAL/SPI*.

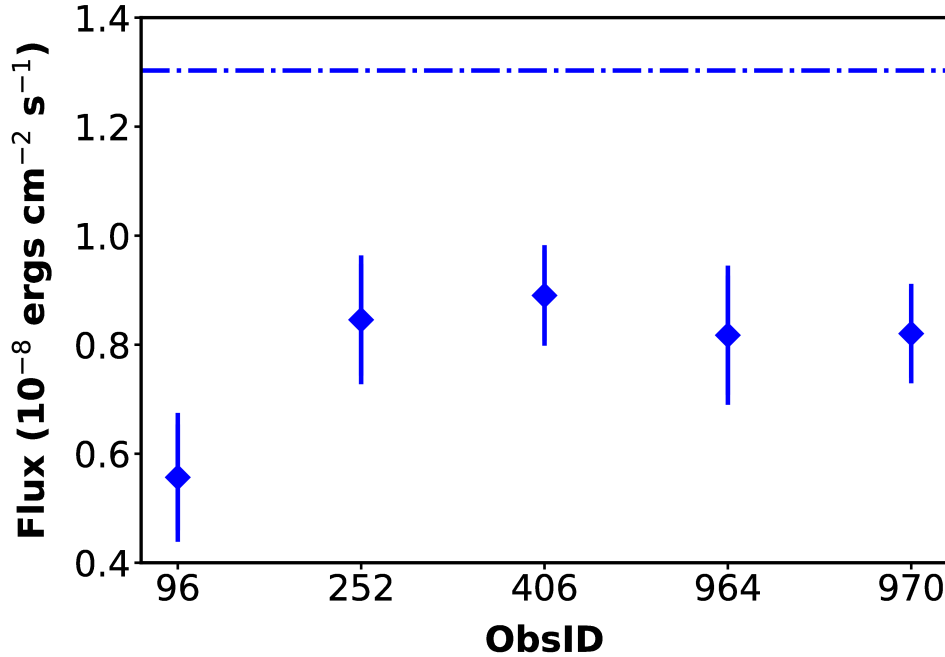


Figure 4.6: Estimated flux of the selected observations after fitting PE and CS simultaneously using broken power law. The blue diamond represents the CZTI value of the Crab flux. The dashed-dot horizontal line represent the INTEGRAL value of the Crab flux in the corresponding energy band.

SPI.

## 4.2 Compton spectroscopy excluding low gain pixels

In the previous section we have explored the Compton sensitivity of the CZTI up to 500 keV by the spectral fitting using the Crab observations. It is found out that the CZTI have sufficient flux sensitivity up to 500 keV and the low energy spectral index is consistent with the INTEGRAL/SPI. However, we find higher energy spectral index shows possible flattening compared to the INTEGRAL/SPI. The flattening could be due to the incorrect background subtraction and the incorrect gain calibration of the low gain pixels. To reduce the uncertainty of possible reason of the flattening of the spectral index we have excluded the low gain pixels in the further analysis. We have attempted the Compton spectroscopy up to the energy of 380 keV, which is determined by the upper limit of the Compton event

between two adjacent good pixels. Here we jointly analyse the Compton spectra obtained with the new background selection and subtraction methods along with the single event spectra to cover the wide energy range of 30 - 380 keV. We use all available clean Crab observations with CZTI having exposure greater than 30 ks, to establish the background selection and subtraction methods for the Compton spectroscopy.

We compared our results with those obtained by the *INTEGRAL/SPI* satellite (Jourdain & Roques, 2009) and found them quite consistent with each other. This technique enables the spectroscopic study of Crab like bright sources. There are many transient sources that reach such brightness levels; therefore, CZTI can be used for the extended spectroscopy of such sources.

This section is structured as follows: in subsection 4.2.1.2 and 4.2.2, observations and analysis procedure are briefly described, respectively. The results obtained are presented in subsection 4.2.3. Finally, in section 4.2.4, we discuss the Compton spectroscopy capability of CZTI and future plans. It is to be noted that this chapter is primarily intended to describe the methods for Compton spectroscopy. The coded mask spectroscopy, which is available by default from the CZTI data pipeline, is the standard CZTI spectroscopy method and therefore has not been discussed in detail in this chapter. However, some of the data cleaning procedures (described in sub-section 4.2.2.2) are applied on both Compton and coded mask spectra.

## 4.2.1 Observations

### 4.2.1.1 Crab observations

The Crab has been observed multiple times by *AstroSat* over the past six years, including in the Performance and Verification (PV) stage of CZTI. Figure 4.7 shows all the available Crab observations by CZTI. We have selected Crab observations having exposure greater than 30 ks to get a statistically significant number of Compton counts. For the present analysis, the observations with exposures below 30 ks (shown in red bars) are ignored because, during GTI (Good Time Interval) selection, almost half of the exposure is lost to filter out the

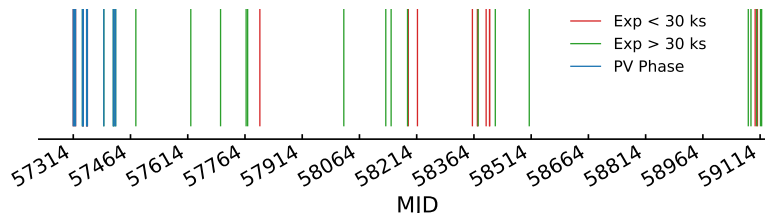


Figure 4.7: Crab observation times are plotted against MJD. Blue, red and green color represents PV phase observations, observations having exposure less than 30 ks and above 30 ks, respectively.

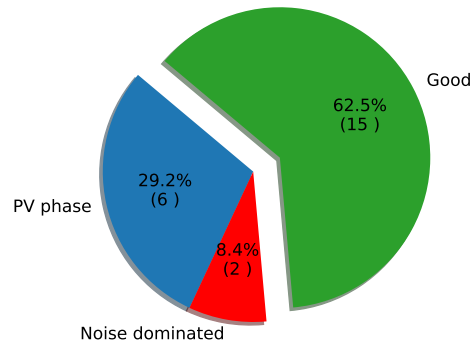


Figure 4.8: Crab observations distribution having exposure greater than 30 ks. 'Good' observations (15) are those after excluding the PV phase (6) and noise dominated observations (2).

charge particle background (more detail in section 4.2.2.3) which results in an insufficient number of Compton events. Apart from this, we have excluded the PV phase observations (shown in blue bars) of the *AstroSat* i.e., September 2015 to March 2016 while the instrument configurations was being optimized. These considerations resulted in 17 observations between 2016 and 2020 for further analysis. Out of the 17 observations, two were found to be dominated by events from noisy pixels. When the number of events recorded by the instrument per second reaches its limit, subsequent events, including those from the source, are not recorded for the remaining fraction of the second. This happens on occasions when very noisy pixels are present making the data not very useful for scientific analysis. Therefore, we proceed with further analysis for the 15 observations (see Figure 4.8). Details of the Crab observations (CZTI observation ID, date of observation, and time exposures) are given in Table 4.3.

Table 4.3: Summary of Crab and blank sky observations.

ObsID	Crab			Blank Sky			
	Date (yyyy/mm/dd)	Exposure (ks)	ObsID	Date (yyyy/mm/dd)	Exposure (ks)	RA (deg)	DEC (deg)
9000000406	2016/03/31	114	9000004016	2020/11/16	75	174.81	17.14
9000000620	2016/08/22	84	9000000956	2017/01/10	81	183.48	22.80
9000000778	2016/11/8	61	9000000956	2017/01/10	81	183.48	22.80
9000000964	2017/01/14	78	9000000956	2017/01/10	81	183.48	22.80
9000000970	2017/01/18	123	9000000956	2017/01/10	81	183.48	22.80
9000001850	2018/01/15	193	9000002710	2019/02/07	60	186.22	21.38
9000001876	2018/01/29	234	9000002712	2019/02/08	49	186.66	19.75
9000001976	2018/03/13	41	9000002046	2018/04/22	45	174.79	19.65
9000002368	2018/09/14	49	9000002712	2019/02/08	49	186.66	19.75
9000002472	2018/10/29	74	9000002712	2019/02/08	49	186.66	19.75
9000002678	2019/01/26	130	9000002710	2019/02/07	60	186.22	21.38
9000003836	2020/08/22	60	9000000996	2017/01/31	37	176.15	19.83
9000003848	2020/08/29	290	9000002712	2019/02/08	49	186.66	19.75
9000003900	2020/09/23	136	9000000996	2017/01/31	37	176.15	19.83
9000003904	2020/09/26	164	9000002710	2019/02/07	60	186.22	21.38

### 4.2.1.2 Background observations

As already discussed in section, the bright sources like Crab and the Cygnus X-1 must be avoided and should be outside the 80 - 90 degrees of the pointing direction during the background observation. Apart from right ascension (RA), we have considered some new criterion for the background selection. We have considered declination (DEC) of the background observation and try to maintain the DEC within 5 degrees of the source observation to minimize any possible latitudinal variation of the background. Another important consideration is the time exposure of the blank sky observation which should be greater than 30 ks (same as source) to get a statistically significant number of Compton counts. Further, we have filtered out the observations which are having BAT sources with flux level  $>1.5$  mCrab (Oh et al., 2018) in the field of view to avoid any possible contamination in the background.

After applying these criteria, we have selected 16 blank sky observations out of a total of 2025 observations to measure background. In Figure 4.9, we show the different considerations behind the selection of sixteen blank sky observations in a flow chart. In Table 4.3, we give the details of the selected blank sky observations, e.g., the CZTI observation ID, time exposures, and date of observation.

## 4.2.2 Analysis procedure

In this section, we discuss the methodology of Compton spectroscopy for Crab. The analysis steps are summarized in a flow chart in Figure 4.10. We discuss these steps in the following subsections.

### 4.2.2.1 Selection of single-pixel and 2-pixel Compton events

In this study, spectroscopic analysis of Crab is attempted in a broad energy range of 30 - 380 keV using two types of CZTI events – the single-pixel events in 30 - 100 keV (PE) and the 2-pixel Compton scattering events in 100 - 380 keV (hereafter ‘CS’) As described in the section 4.1.1.1, we remove events from noisy pixels and spectroscopically bad pixels to reduce the instrumental systematic. This

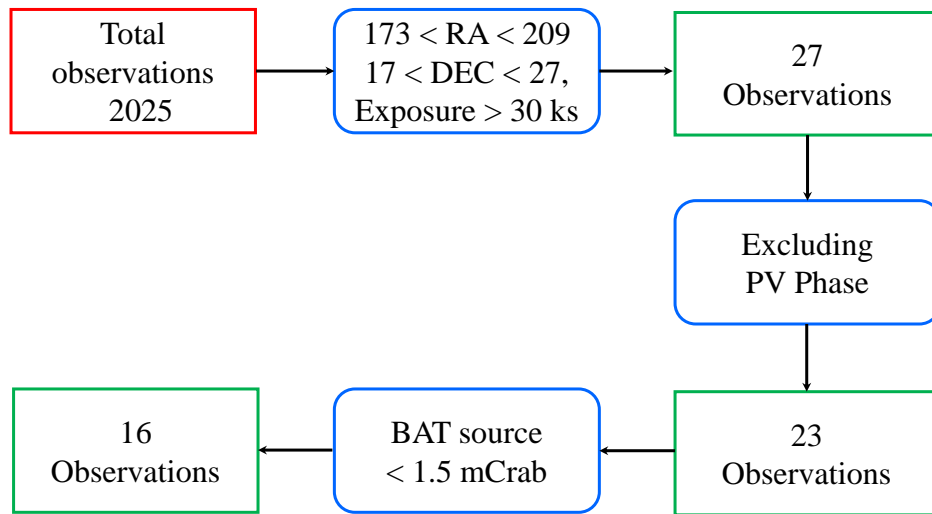


Figure 4.9: Background selection flow chart. Total CZTI observations till 2020 is 2025 (shown in red). After applying the RA, DEC and exposure conditions, 27 are selected (shown in the 3rd box). Further, excluding PV phase observations resulted in 23 observations (shown in the 5th box). Finally, after applying the BAT flux criterion gives 16 blank sky observations as shown in the last box.

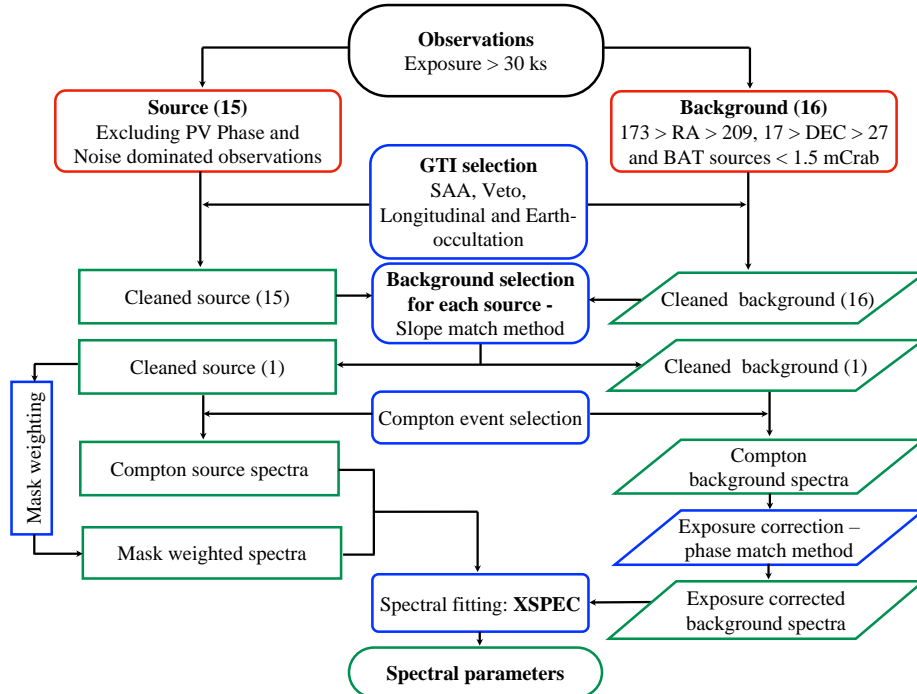


Figure 4.10: Crab spectral analysis flow chart. The red box shows the initial conditions for selecting 15 source regions and 16 background regions. The blue box is for the process, the green rectangular box represents the source outputs, and the green parallelograms represent the background outputs.

is done for both the PE and CS events. The event selection criteria discussed in section 4.1.1.1 are applied to both the Crab and the blank sky background observations.

The actual Compton events (CS) are identified from the chance 2-pixel events by applying Compton kinetic criteria as discussed in the section 4.1.1.1. Only those events with the sum of two energies between 100 and 380 keV are considered for analysis. The selection of Compton events has been discussed in the CZTI polarimetry chapters in more detail – [Chattopadhyay et al. \(2014a\)](#); [Vadawale et al. \(2015, 2018\)](#); [Chattopadhyay et al. \(2019\)](#). Compton event analysis is done outside the standard pipeline, and we have used algorithms written in Interactive Data Language (IDL).

#### 4.2.2.2 Data cleaning for short-term variation in data

Because of the interaction of charged particles with the spacecraft and the payload structure during the SAA passages, the background increases and decreases immediately upon the entrance and exit of the SAA ([Campana, 2022](#)), which leads to short-term temporal variation in data. This can be seen in the individual orbital segments of the 1-s light curve (shown in the solid blue line in the top plot of Figure 4.11 and the inset plot) of Crab single-pixel events. Apart from the short-term variations, we also see a long-term quasi-diurnal variation in the data due to periodic variation in ground traces of the satellite because of earth rotation. More details of the long-term variations and their correction are discussed in subsection 4.1.1.2. Here we describe the method to correct the short-term variation in the data. It is difficult to predict the particle background for an orbit in  $-135^\circ$  to  $45^\circ$  degree of longitude because of multiple complex factors like the exact time span of satellite in the SAA regions, which is different for different orbits, depth in SAA regions, induced radioactivity in the detector, etc. Because of the unpredictable nature of the particle background, subtraction of blank sky from the source is impossible without correcting for this short-term variation in the data. Since the geomagnetic field in this longitudinal range ( $-135^\circ$  to  $45^\circ$ ) is relatively weak, it leads to the high concentration of particle background ([Ye et al., 2017](#)). Thus, in our analysis, we have excluded the duration's from the

Table 4.4: Predefined Veto cut threshold values.

Quadrant	Threshold (counts-s <sup>-1</sup> )
Q1	450
Q2	500
Q3	500
Q4	480

GTI both for the Crab and blank sky background observations when the satellite is in the longitudinal range of -135 to 45 degree . We also use counts in the CsI anti-coincidence (veto) detector as a proxy to identify high background regions. Using data from several long observations, we obtain histograms of veto count rates for each quadrant. It was seen that the distributions are asymmetric with a tail towards the higher count rate side corresponding to the observations near SAA or any other duration's of high background in orbit away from the SAA. We determine upper threshold for veto count rates of each quadrant such that they ignore typically 15% of the time corresponding to highest background levels while the background rates does not vary significantly during the remaining intervals. The thresholds for each quadrant are listed in Table 6.1. We ignore the time intervals where the counts in the veto detector of each quadrant are above these threshold values to remove the high particle background events anywhere in orbit away from the SAA.

With these selection criteria, the regions of high charged particle background yielding the short-term variations in the light curve are removed. This is shown in the light curve in the solid red line in the bottom plot of Figure 4.11. It is to be noted that we lose 40 - 50% of the original exposure in this process. We use the identical final GTI for data filtering in the single and 2-pixel Compton events for Crab and blank sky observations.

#### 4.2.2.3 Selection of background for Compton spectroscopy

In mask weighted single-pixel spectroscopy, the background is simultaneously measured during the source observation. However, because the mask weighting is effective up to 100 keV, measurement of Compton background (100 - 380 keV) requires a separate blank sky observation for each Crab observation.

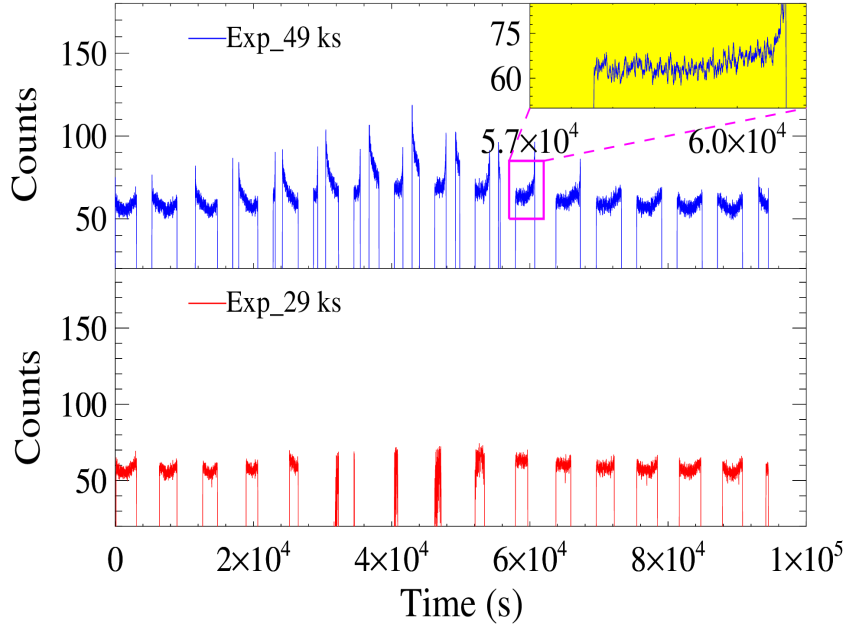


Figure 4.11: Light curve of the blank sky observation for Crab background (obsId: 2712). From top to bottom, the blue color represents raw light curve with SAA and earth-occultation cuts. The yellow box at the top right corner shows the zoom-in view of one of the orbits. The red light curve is after applying the longitudinal cuts and veto cuts.

Since a significant fraction of the observed counts in the source data consists of cosmic background, we can assume that variation of counts with the orbital position should be similar in the source and the blank sky observations. We also do not expect any variation in the source observation for Crab, which is known to be a steady source. To select the appropriate blank sky observation for each source observation, we compared the longitudinal variation of spectral hardness in background data with the spectral hardness in source data. The source and background observations are divided into six longitudinal bins starting from  $45^\circ$  to  $-135^\circ$  longitude, with 30 degrees binning avoiding the SAA regions. The spectrum for each longitudinal bin is generated in 70 - 190 keV. The spectrum of each longitudinal bin is then fitted with a straight line where the fitted slope represents the hardness of the spectrum (see Figure 4.12). This is done for all the 15 Crab and 16 blank sky observations.

In figure 4.13, we show the longitudinal variation of the spectral hardness of the Crab (observation ID 2472) and blank sky observations (observation

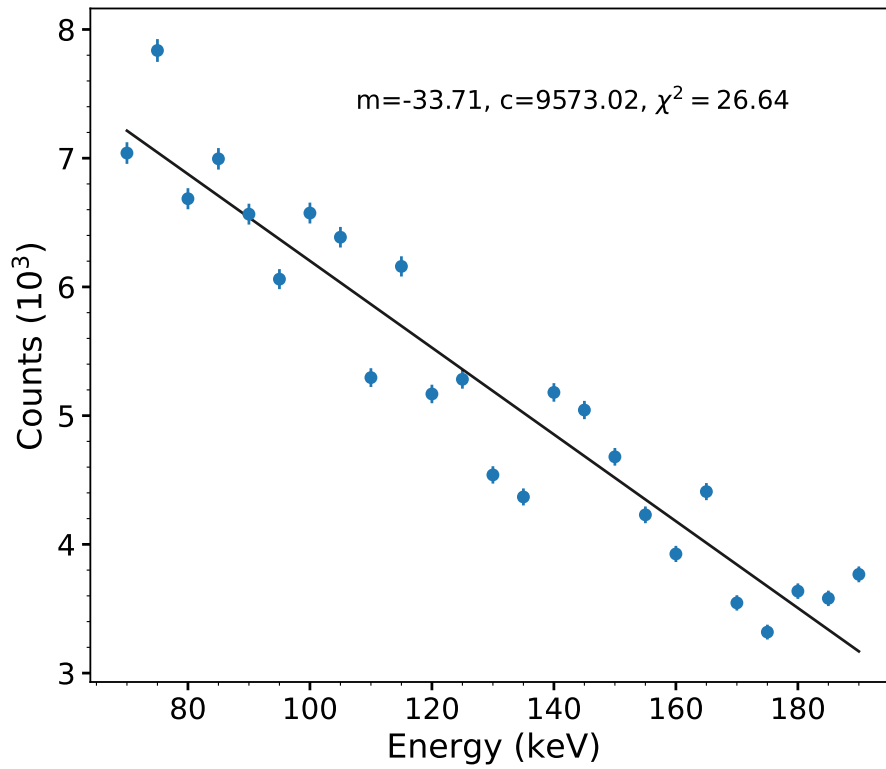


Figure 4.12: Spectral hardness using a straight line fit in 70 to 190 keV .

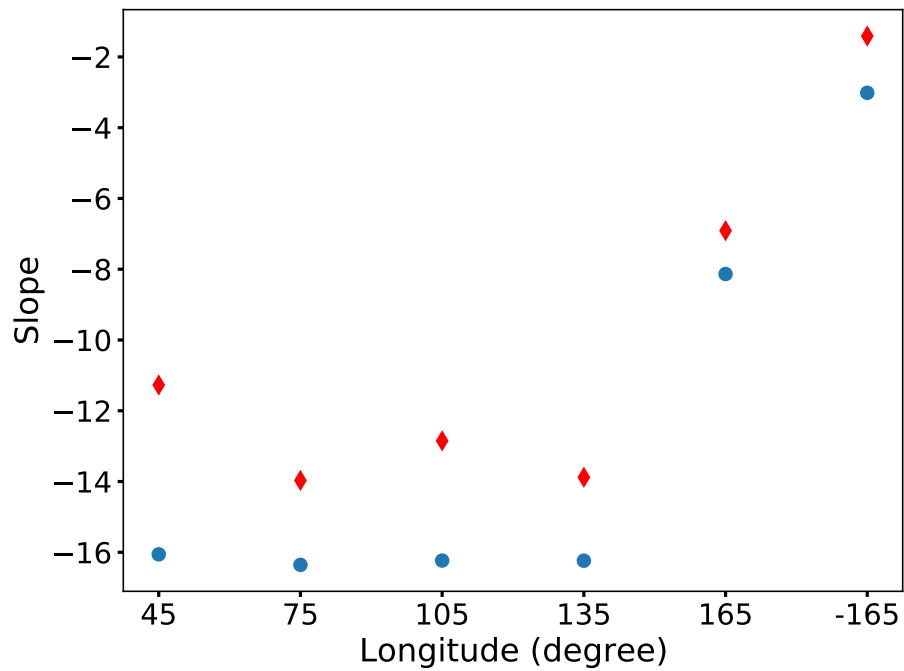


Figure 4.13: Longitudinal variation of the hardness of the Crab and background. Blue is Crab (obsId: 2472) and red is blank sky observation (obsId: 2712)

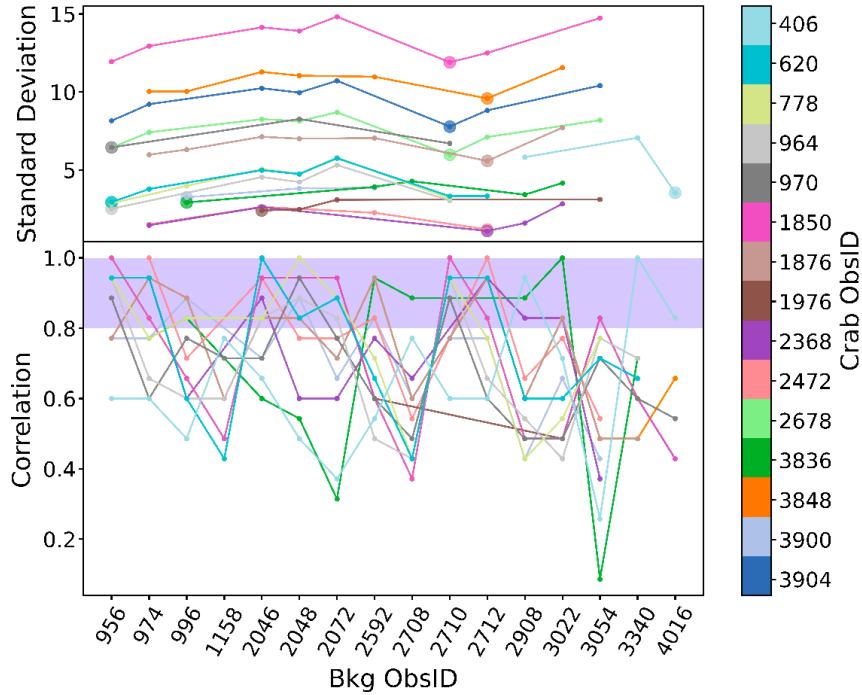


Figure 4.14: Bottom panel: correlation between the source and background longitudinal hardness variation for different Crab and blank sky background observations. Top panel: standard deviation of the difference in the longitudinal hardness of the source and blank sky backgrounds having a correlation above 0.8. Each colour in the colour bar represents a different source observation.

ID 2712). We expect the longitudinal variation of spectral hardness to be similar in the source and blank sky data for the correct blank sky for a given source observation. This is done in two steps: first, we calculated the correlation in longitudinal hardness variation between each source and all the background observations. All the backgrounds having a correlation greater than 0.8 for a given source observation are selected (see the bottom panel of Figure 4.14). We then calculate the standard deviation of the difference between the source and background slopes for the selected blank sky observations (see the upper panel of Figure 4.14). The variation of the difference should be minimum if the background embedded in the source is similar to the blank sky observation. Therefore, the blank sky observation for which the standard deviation is minimum is selected for background subtraction for that particular source observation. It is to be noted that at the beginning, we filter out the backgrounds for which the difference between the background and source slope in one or more longitudinal bins is negative. The final background is selected from the remaining background

observations using the correlation and standard deviation algorithm.

#### 4.2.2.4 Exposure correction in background due to long-term variation in data

Here we describe methods to correct the long-term variation in the selected background data. An example of the long-term variation is shown in Figure 4.11 where we see a systematic modulation in the flux along the orbit of the satellite, arising because of the earth rotation (Antia et al., 2022). Since the phases of such modulations in source and background are always different, subtraction of background without correcting for this will lead to incorrect net source flux. One way to address this issue is to obtain similar portions of the Crab and background orbits based on the spacecraft's ground tracks (latitude and longitude) for further analysis. However, this puts a stringent condition on orbital selection, resulting in a short usable exposure of Crab and background observations. An alternate method (the 'phase match method') developed for background subtraction is to match the phase of the background and Crab light curves. The phase match method has been discussed and validated in detail in section 4.1.1.2.

In the previous subsections, we explained the selection of blank sky observation for the measurement of Compton background and methods to correct for the short-term and long-term variation in the data. To validate the measured Compton background (100-380 keV) and its variation with time, we compared it with the low energy background (30-100 keV) obtained by the mask weighting technique. We generated low energy background spectra (30 - 100 keV) for each observation by subtracting the source spectrum obtained by mask weighting from the total spectrum (source + background). Background count rates obtained from these spectra are shown with black data points in Figure 4.15. The Compton background rates computed for each observation are shown in blue data points. Both the background rates are seen to be well correlated. The observed long-term secular variation in the background closely follows the trend of the number of Galactic Cosmic rays, anti-correlated with the Sunspot number that is decreasing towards its minimum in 2019/20 (Wang et al., 2022). There are also additional short-term variations between observations that are also found to

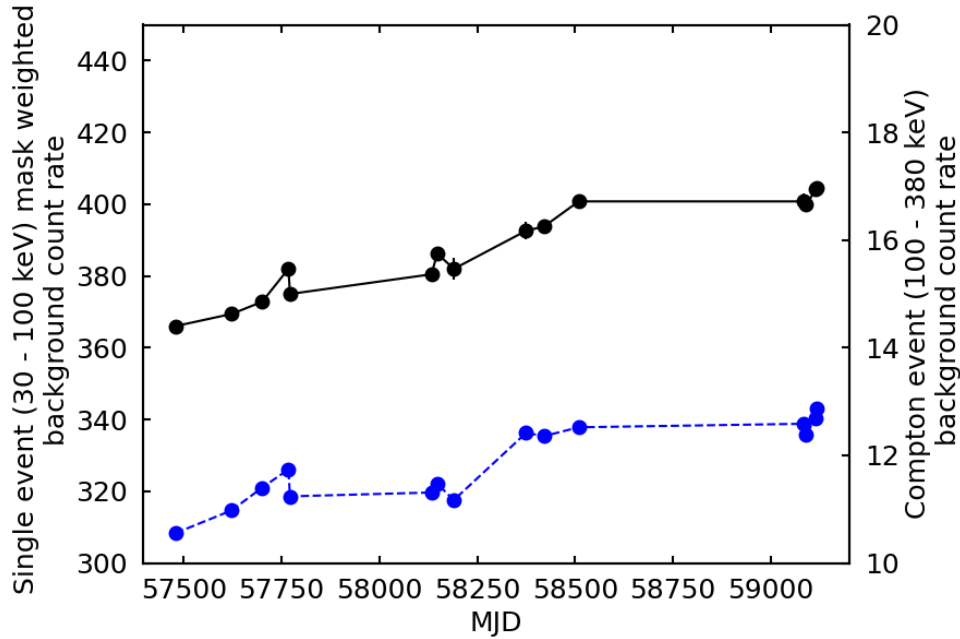


Figure 4.15: Mask weighted and Compton background count rate variation with MJD. The blue line with filled circles represents the Compton background (right hand side scale). The black line with filled circles represents the mask weighted background (left hand side scale).

be correlated. The similar behavior of the estimated Compton event background and the low energy background strongly validates the background measurement method presented here.

#### 4.2.2.5 Generation of the Compton spectra

Once the blank sky data for background measurement is selected for a given source observation and the background (and source) data are corrected for the long term variation, the next step is to generate the spectral and response files.

For each of the observations, the single event spectrum (30 - 100 keV) is generated using `cztbindata` module in the CZTI data analysis pipeline<sup>†</sup>. Clean event files with the GTI selection as described in previous sections are used as the input. For each event, the module assigns a mask-weight based on the open fraction of the respective pixel and the event energies are binned with respective weights to obtain background subtracted source spectrum (Mithun et al in prep). Spectra are generated with a bin size of 0.5 keV and corresponding response for

<sup>†</sup>[http://astrosat-ssc.iucaa.in/uploads/czti/CZTI\\_level2\\_software\\_userguide\\_V2.1.pdf](http://astrosat-ssc.iucaa.in/uploads/czti/CZTI_level2_software_userguide_V2.1.pdf)

spectral analysis is generated by using `cztrspgen` module of the pipeline, which takes into account the spectral redistribution of CZT detectors based on  $\mu\tau$  charge sharing model (Vadawale et al., 2012; Chattopadhyay et al., 2016).

The 2-pixel Compton events are used to get the Compton scattering events spectrum in the 100 - 380 keV (CS) as discussed in section 4.2.2.5

### 4.2.3 Results

We use an XSPEC (Arnaud, 1996) model, broken power-law, to fit the Crab curved spectra in 30 - 380 keV. It has long been used to explain Crab spectra with 100 keV break energy. (Strickman et al., 1979; Ling & Wheaton, 2003). Ling & Wheaton (2003) reported using BATSE earth-occultation observations that the emission from the Crab in 35 - 300 keV can be described by a broken power-law with a break at 100 keV. Later, *INTEGRAL/SPI* has also shown the spectral fitting using broken power law in the energy range of 23.5 keV - 1 MeV (Jourdain & Roques, 2009) with freezing break energy at 100 keV.

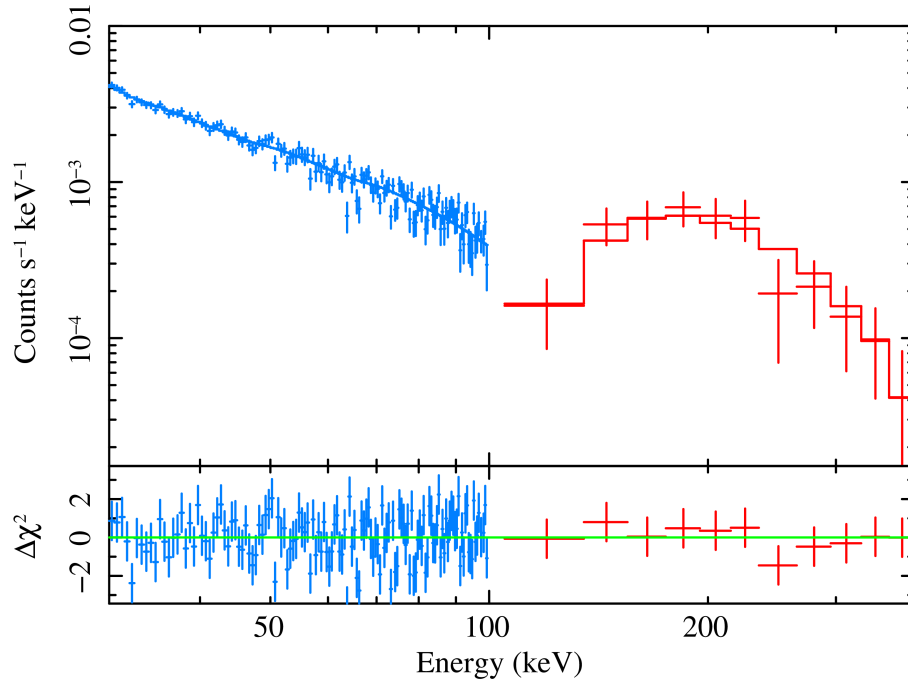


Figure 4.16: Broadband spectra of Crab (ObsID 2368, 49 ks) fitted with a broken power law. Blue and red colors are used for PE and CS, respectively.

In the case of CZTI, since the energy range is limited to 380 keV, we also considered freezing break energy at 100 keV for spectral fitting, as most

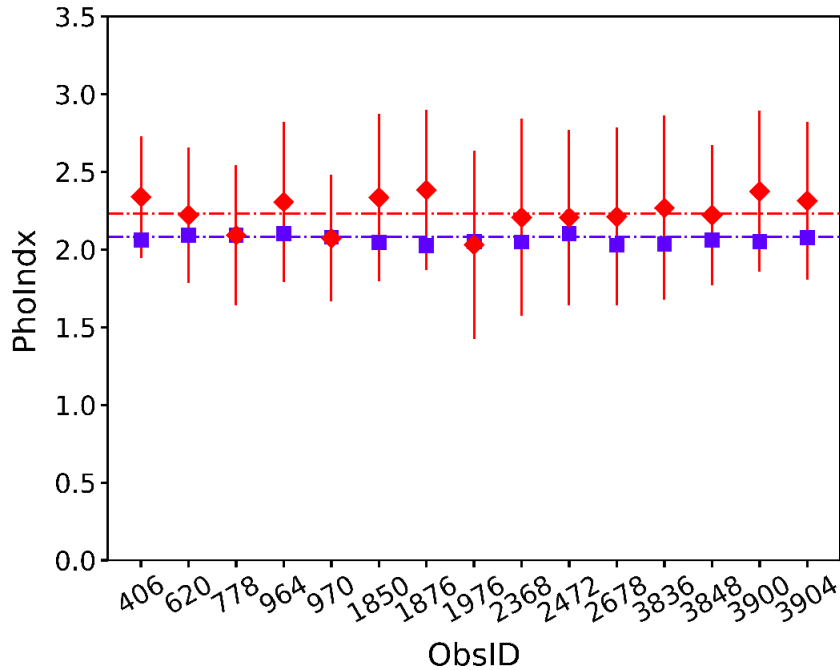


Figure 4.17: PhoIndx vs ObsID plot. Blue and red colors are used for PhoIndx1 and PhoIndx2, respectively, and the dashed line represents the *INTEGRAL/SPI* reported values.

of the instruments have considered. We fitted the CZTI PE and CS spectra simultaneously using  $\text{const} \times \text{bknpower}$  in *XSPEC* freezing break energy at 100 keV (same as *INTEGRAL/SPI*). At the same time, the other parameters (photon indices) are tied across the spectra.

A constant was multiplied to the model to account for the cross-calibration and differences between the different spectra. It was fixed to one for PE and left free to vary for CS. We have added a 4% systematic while fitting the observations having effective exposure  $>65$  ks so that the reduced chi-square becomes less than 1.5. Spectral fitting for one of the 15 observations (ObsID 2368, 49 ks) is shown in Figure 4.16. The residual plots of the remaining observations are shown in Figure 4.19. The fitted parameters for all the 15 observations along with the *INTEGRAL/SPI* results are given in Table 4.5. The low-energy slope (*PhoIndx1*) and the high energy slope (*PhoIndx2*) are well constrained and consistent with the *INTEGRAL/SPI* (Jourdain & Roques, 2009) results within error bars (see Figure 4.17). The norm reported in Table 4.5 correspond to PE. The value of the fitted normalisation constant for CS is consistently half compared to that for PE (see Figure 4.18), which may be due to the inaccurate

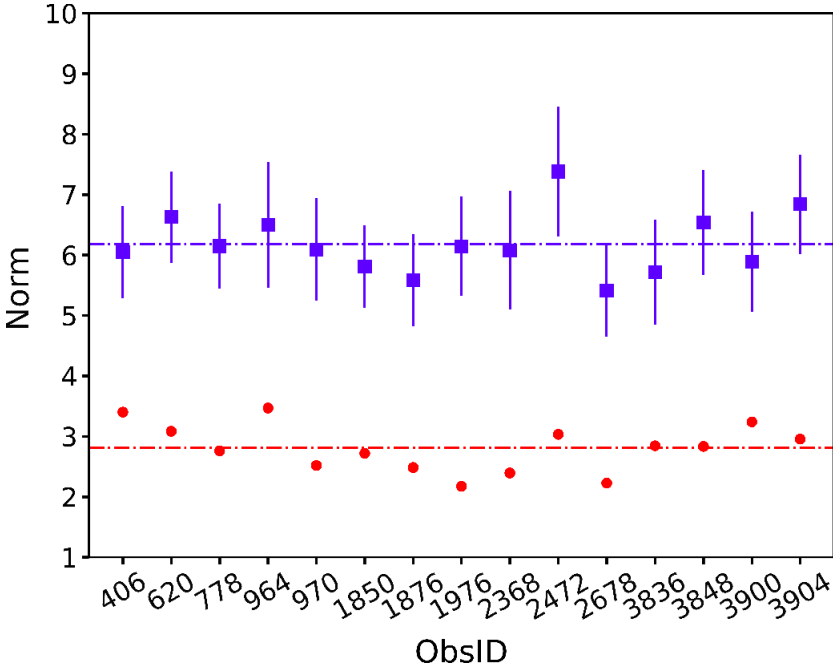


Figure 4.18: Norm vs ObsId. Blue and red colors are used for PE and CS, respectively. The dashed lines represent the mean values.

consideration of the effective area of the CZTI for the Compton response.

Table 4.5: Comparison of fitted parameters between *INTEGRAL/SPI* and *AstroSat* for broken power law. The errors are estimated for 90% confidence interval. \* represents a frozen parameter.

Instrument	ObsID	Exposure	Effective Exposure	<i>PhoIdx1</i>	<i>PhoIdx2</i>	$E_{break}$	<i>Norm</i> (keV)	$\chi^2/dof$
NTEGRAL/SPI			~400 ks	$2.07^{+0.01}_{-0.01}$	$2.23^{+0.03}_{-0.03}$	100*		
AstroSat/CZTI	406	114	68	$2.06^{+0.03}_{-0.03}$	$2.34^{+0.40}_{-0.39}$	100*	$6.05^{+0.89}_{-0.76}$	188/163
	620	84	53	$2.09^{+0.03}_{-0.03}$	$2.22^{+0.44}_{-0.44}$	100*	$6.63^{+0.87}_{-0.75}$	209/163
	778	61	37	$2.09^{+0.03}_{-0.03}$	$2.09^{+0.48}_{-0.45}$	100*	$6.15^{+0.81}_{-0.71}$	228/161
	964	78	44	$2.10^{+0.05}_{-0.04}$	$2.31^{+0.54}_{-0.52}$	100*	$6.50^{+1.26}_{-1.04}$	205/163
	970	123	72	$2.08^{+0.04}_{-0.04}$	$2.07^{+0.41}_{-0.41}$	100*	$6.09^{+1.00}_{-0.85}$	184/163
	1850	193	105	$2.05^{+0.03}_{-0.03}$	$2.33^{+0.56}_{-0.54}$	100*	$5.81^{+0.81}_{-0.68}$	232/163
	1876	234	112	$2.03^{+0.04}_{-0.04}$	$2.38^{+0.52}_{-0.51}$	100*	$5.58^{+0.93}_{-0.77}$	243/163
	1976	41	24	$2.05^{+0.04}_{-0.04}$	$2.04^{+0.62}_{-0.61}$	100*	$6.14^{+1.01}_{-0.82}$	205/163
	2368	49	28	$2.05^{+0.05}_{-0.05}$	$2.21^{+0.65}_{-0.63}$	100*	$6.08^{+1.20}_{-0.98}$	207/163
	2472	74	33	$2.10^{+0.04}_{-0.04}$	$2.21^{+0.60}_{-0.56}$	100*	$7.38^{+1.28}_{-1.07}$	203/163
	2678	130	34	$2.03^{+0.04}_{-0.04}$	$2.21^{+0.60}_{-0.57}$	100*	$5.41^{+0.92}_{-0.77}$	230/161
	3836	60	29	$2.03^{+0.04}_{-0.04}$	$2.27^{+0.61}_{-0.59}$	100*	$5.72^{+1.05}_{-0.87}$	202/161
	3848	290	157	$2.06^{+0.04}_{-0.04}$	$2.22^{+0.47}_{-0.45}$	100*	$6.54^{+1.04}_{-0.87}$	216/161
	3900	136	40	$2.05^{+0.04}_{-0.04}$	$2.37^{+0.54}_{-0.52}$	100*	$5.89^{+1.00}_{-0.82}$	205/161
	3904	164	64	$2.08^{+0.03}_{-0.03}$	$2.31^{+0.54}_{-0.51}$	100*	$6.84^{+0.95}_{-0.82}$	221/161

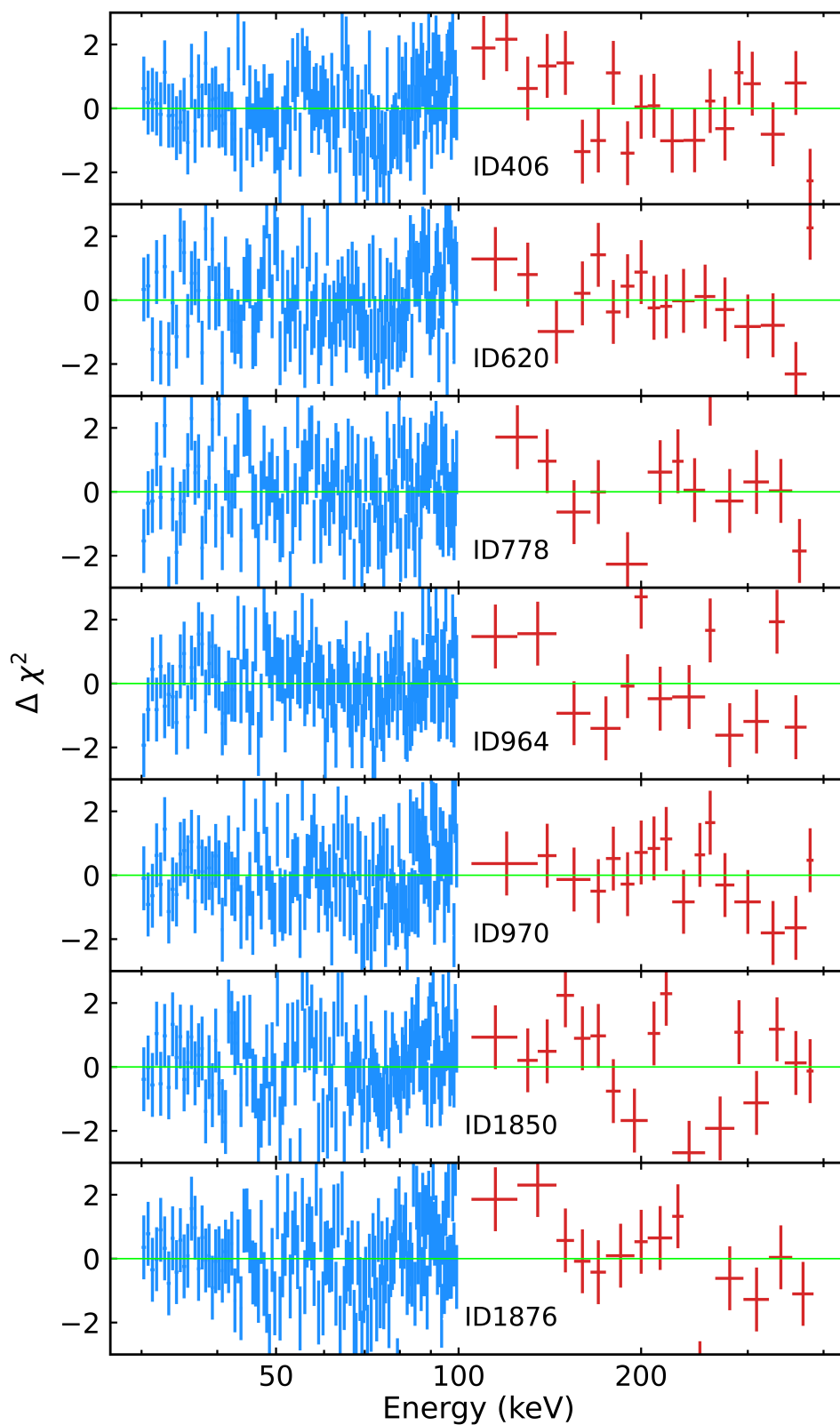
### 4.2.3.1 Spectroscopic sensitivity of CZTI in 100 - 380 keV

We have estimated the Compton flux sensitivity of CZTI in 100 - 380 keV. For the  $3\sigma$  detection of the source, limiting incident flux value is estimated. To calculate this, we have simulated the flat spectra in the XSPEC and used one of the exposure corrected blank sky observation for the background. Then the required flux level is calculated for the given exposure and energy for the  $3\sigma$  detection in the CZTI. The sensitivity at lower energy is low (see Figure 4.20) because photoelectric absorption dominates over Compton interaction in this energy range. However, at lower energy no. of interactions are large but mostly its photoelectric, Compton interaction starts to dominate at high energy, hence, the sensitivity. We can do Compton spectroscopy in the energy range of 100-380 keV for the source having flux of 700 mCrab for the effective exposure of  $> 200$  ks.

### 4.2.4 Discussion

In this section, we have outlined methods for Compton spectroscopy using *AstroSat*-CZTI. We use the single-pixel mask-weighted spectral data in the 30 - 100 keV energy range (PE) and 2-pixel Compton events in the 100 - 380 keV energy range (CS) for a joint 30 - 380 keV broadband spectroscopy. As a proof of concept, we applied this analysis for Crab and compared the spectral parameters with the *INTEGRAL/SPI* reports which were found to be consistent.

In the case of on-axis sources, the unavailability of simultaneous background measurement for Compton spectroscopy makes the estimation of accurate blank sky flux and its subtraction essential, mainly when the signal-to-noise ratio is relatively low. The selection of blank sky data is done by comparing the longitudinal variation of the spectral hardness of the source and blank sky data (subsection 4.2.2.3). However, the presence of short-term and long-term temporal variation in the observed count rates due to high charge particle concentration in the SAA regions and earth rotation, respectively, make the subtraction of background non-trivial and complicated. To exclude the short-term variation, we ignore the data from  $-135^\circ$  to  $45^\circ$  longitude, where the earth's magnetic field is relatively weak compared to other regions (subsection 4.2.2.2). The long-term



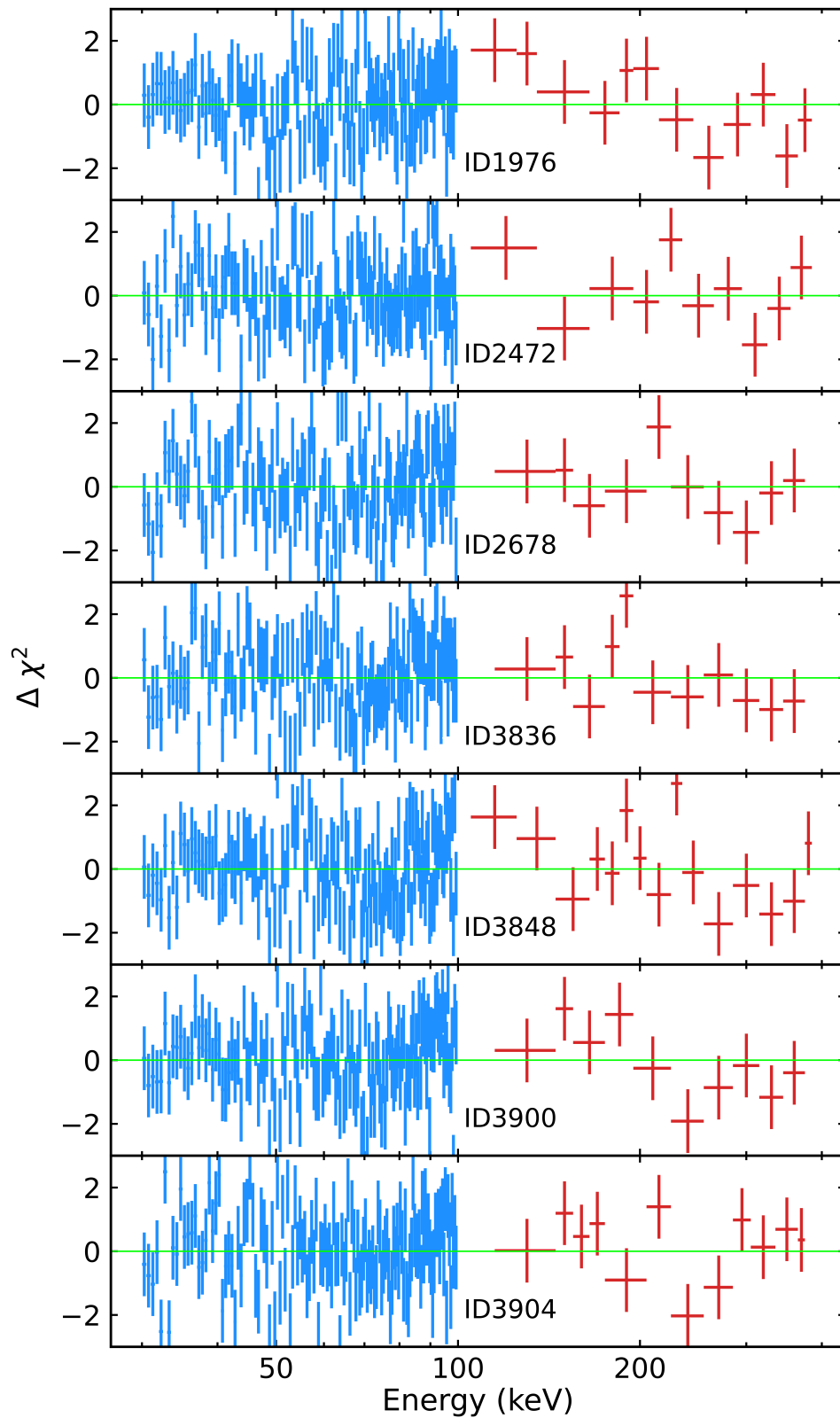


Figure 4.19: Residual plots of remaining observations (14). The blue and red colours are used for PE, and CS residuals, respectively. The ObsID is shown at the center of each panel.

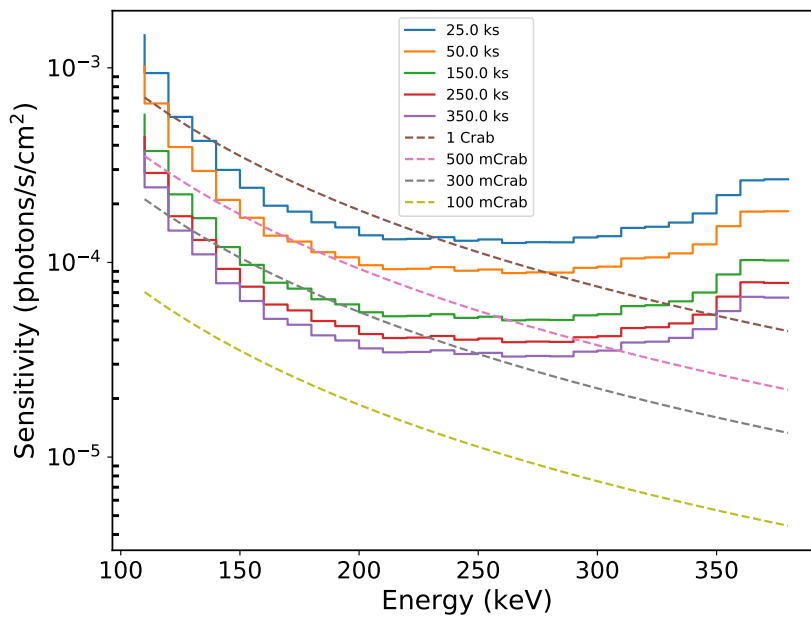


Figure 4.20: CZTI Compton sensitivity for  $3\sigma$  detection of any source with a flux level above a particular value. Different colors represent different exposures, and dashed lines represent different crab flux levels.

variation, on the other hand, is corrected by comparing the phases of the Crab and the selected background and scaling the overall background count rate according to the count rate observed in the matched phase (subsection 4.1.1.2). While this method ensures correct estimation of background (and source) flux, the background selection procedure makes sure that the selected blank sky background and the original background embedded in the source observation follow the same spectral energy distribution.

For this work, the Compton spectral response was generated by simulating the *AstroSat* mass model in Geant4. The estimated energy distributions were convolved with a Gaussian kernel for simplicity (section 4.2.2.5), which we intend to improve with the use of a physical line profile model based on charge trapping and diffusion (Chattopadhyay et al., 2016). In the future, we would also include the charge sharing effect in Compton response for improved spectral analysis. For CZTI like pixelated detectors, charge sharing between the adjacent pixels is expected to give rise to 2-pixel events that mimic the Compton events. This effect has been seen in the polarimetry data analysis of GRBs with CZTI (Chattopadhyay et al., 2022) as well as in polarimetry experiments with CZT

detectors identical to those used in CZTI (Vaishnava et al., 2022). Inclusion of charge sharing in the response will help in better estimation of the relative norm (and source flux in 100 - 380 keV) for the Compton spectra.

We have done the spectral analysis of the Crab using these techniques, where we used a broken power-law (bknpower in XSPEC) for the spectral fitting. The spectral fits showed that CZTI has sufficient flux sensitivity to perform spectroscopy for on-axis bright sources up to 380 keV (see Table 4.5). For the single event and Compton event spectra in 30 - 380 keV (PE and CS), the low-energy slope (*PhoIndx1*) and higher energy slope (*PhoIndx2*) agree reasonably with the *INTEGRAL/SPI* result.

### 4.3 Summary

To summarize, we find that CZTI has sufficient spectral sensitivity in the sub-MeV region up to 500 keV for the ON-axis sources.

With the background selection and subtraction methods, described in this chapter, we find that CZTI has the capability to do spectroscopy for on-axis sources in 30 - 380 keV. This will provide sensitive spectroscopic information for various bright ( $\sim 1$  Crab) hard X-ray sources such as Cygnus X-1 and other transient sources, which will help in better understanding of the emission mechanisms in these sources. CZTI is also a sensitive polarimeter; hence, simultaneous spectroscopy and polarisation measurements can give a wealth of information about these sources. For example, for bright black hole binaries like Cygnus X-1, a detailed spectro-polarimetry study will help us understand the putative jet's emission mechanism, geometry, and magnetic field structure.



# Chapter 5

## Dependence of hard X-ray polarization on spectral states in Cygnus X-1

### 5.1 Introduction

Cygnus X-1 spectral states are mostly studied based on the RXTE data [Cui et al. \(1997a\)](#); [Gierliński et al. \(1999\)](#), mainly in the 3 - 35 keV band. The emission in this energy range is thought to be a mixture of the primary emission coming from the disk, hot plasma, and the reflection component from the disk due to the Compton reflection of the corona or plasma photons from the disk. Therefore, interpreting these results in terms of complex physical models is normally very challenging. However, the emission in the energy range of 20 - 100 keV is mainly from the Comptonised continuum ([Filothodoros et al., 2018](#)), therefore allowing to be the direct probe to the plasma properties. There have been various spectral studies in hard X-rays ([Gleissner et al., 2004](#); [Zdziarski et al., 2011](#)). It is generally believed that these states are related to the various arrangements of the accretion disk, plasma regions(s) or corona, and outflowing material, considered to be in the form of jet or winds (e.g.,([Fender & Muñoz-Darias, 2016](#))). Recently, [Lubiński et al. \(2020\)](#) have done the extensive spectral analysis in 22 - 100 keV using the 15 years INTEGRAL/ISGRI data ([Winkler et al., 2003](#))

in science window mode typically lasts for 0.2-2 hr uninterrupted which is ideal to study short-term (hourly scale) spectral variation. They have shown the six plasma spectral states in the Cygnus X-1 based on the flux and spectral index correlation (discussed in section 5.3.1).

In Chapter 3., We have done the polarisation analysis for a sample of 8 observations from different epochs having statistically significant counts. It is found that most of the observations polarisation properties are unconstrained due to low exposure, but observation dated 15 June 2019 (ID 2992, see Table 5.1) is  $\sim 23\%$  polarised, and the observation taken on 16 August 2021 (ID 4646) is unpolarised in the 100 - 380 keV energy range. This suggests that the polarization properties of the Cygnus X-1 may be dependent on its spectral states. The spectral and timing analysis using the long term data of Cygnus X-1 can provide useful insights into the spectral states and dependence of polarisation properties on it. Apart from this, broadband spectral analysis using the LAXPC, SXT and CZTI, including the extended energy range of the CZTI using the polarisation events as discussed in chapter 4 can help in understanding the source geometry and the emission mechanism in different spectral states.

In this work, we have used eight *AstroSat* observations of Cyg X-1 (used for the polarisation analysis in chapter 4.) made between 22 April 2016 and 29 August 2021 for the spectral and timing analysis. We carried out spectral and timing analysis to understand the coronal geometry and the corona-jet contribution in the polarisation in different spectral states and also try to identify the jet or coronal emission contribution in the polarisation component. In section 5.3 we describe the identification of different spectral states along with the details of data reduction and analysis and present the spectral and the timing results. In section 5.5 we present the broadband spectroscopy in the energy range of 1 to 380 keV for the ID 2992. In section 5.6 we conclude by discussing the implications of our results. Lastly, in section 5.7 we summarize the results obtained using the spectro-polarimetry along with the timing studies of the Cygnus X-1.

## 5.2 Observations

Cygnus X-1 has been observed many times since the launch of the *AstroSat* . However, for the present work, we have used the eight observations for which polarisation analysis is carried out in chapter 4. The details of the observations are given in Table 5.1.

Table 5.1: List of all the observations used in this work. In the rest of the chapter, only the last four digits of the ObsIDs are mentioned for simplicity with ID as prefix. RA: 299.59° and DEC: 35.20°.

ObsID	Date (yyyy/mm/dd)	Exposure (ks)
9000000426	2016/04/22	104
9000000436	2016/04/29	58
9000000456	2016/05/15	138
9000002992	2019/06/15	333
9000004492	2021/06/27	178
9000004638	2021/08/13	55
9000004646	2021/08/16	228
9000004678	2021/08/29	118

## 5.3 Spectral state determination

We have attempted to see the spectral states of the eight observations based on the timing and spectral analysis.

### 5.3.1 Spectral analysis

We looked into the 30 - 100 keV spectrum of these observations to determine what subclass of hard and soft spectral states they belong to. First, we have attempted to see the spectral index and flux variation using the full observation data of AstroSat-CZTI. For each of the observations, the single event spectrum (30 - 100

keV) is generated using `cztbinding` module in the CZTI data analysis pipeline\*. Clean event files with the GTI selection are used as the input. Spectra are generated with a bin size of 0.5 keV and the corresponding response for spectral analysis is generated by using the `cztrspgen` module of the pipeline. The spectra is extracted in the energy range of 30 - 100 keV. The spectral analysis is carried out using the `xspec` (Arnaud, 1996). The spectrum for all the observations is fitted with an `powerlaw` model. The spectral index in 30 - 100 keV and the flux in 22 - 100 keV is obtained from the spectral fitting is shown in Figure 5.1. There is a distribution in flux and spectral index.

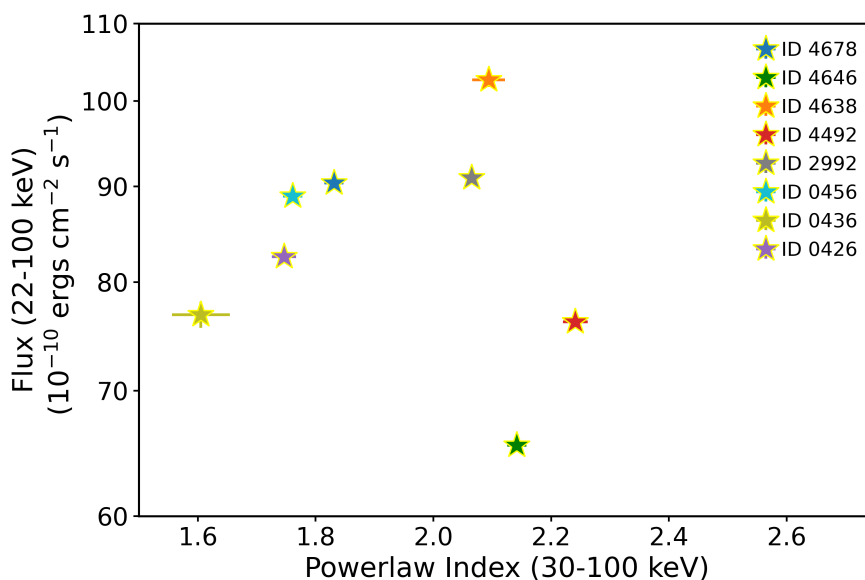


Figure 5.1: Cygnus X-1 flux and spectral index distribution for the eight observations obtained from the spectral fitting of CZTI observation.

Lubiński et al. (2020), categorised the states into hard and soft regimes based on the hard X-ray flux in 22 - 100 keV, above  $75 \times 10^{-10}$  erg  $\text{cm}^{-2}$   $\text{s}^{-1}$  flux it is categorised as hard and below it as soft regimes. Each regime is further categorised into pure, transitional and intermediate, totaling six states – pure hard (PH), transitional hard (TH), hard intermediate (HI), soft intermediate (SI), transitional soft (TS), and pure soft (PS) states based on the clustering of the data in spectral index and flux density diagram (see Figure 5.2). Assuming that the Comptonisation process is the primary source of the hard X-ray flux

\*[http://astrosat-ssc.iucaa.in/uploads/czti/CZTI\\_level2\\_software\\_userguide\\_V2.1.pdf](http://astrosat-ssc.iucaa.in/uploads/czti/CZTI_level2_software_userguide_V2.1.pdf)

in 22 - 100 keV they have interpreted six states in terms of the six different geometries of the plasma region in Cyg X-1. The pure hard and the pure soft states do not show any hour scale flux and spectral index correlation which suggest the absence of plasma and accretion disk interaction. The remaining four states exhibit strong correlation where flux is slowly decreasing with increasing spectral index, possibly due to the decrease in the inner radius of the disk.

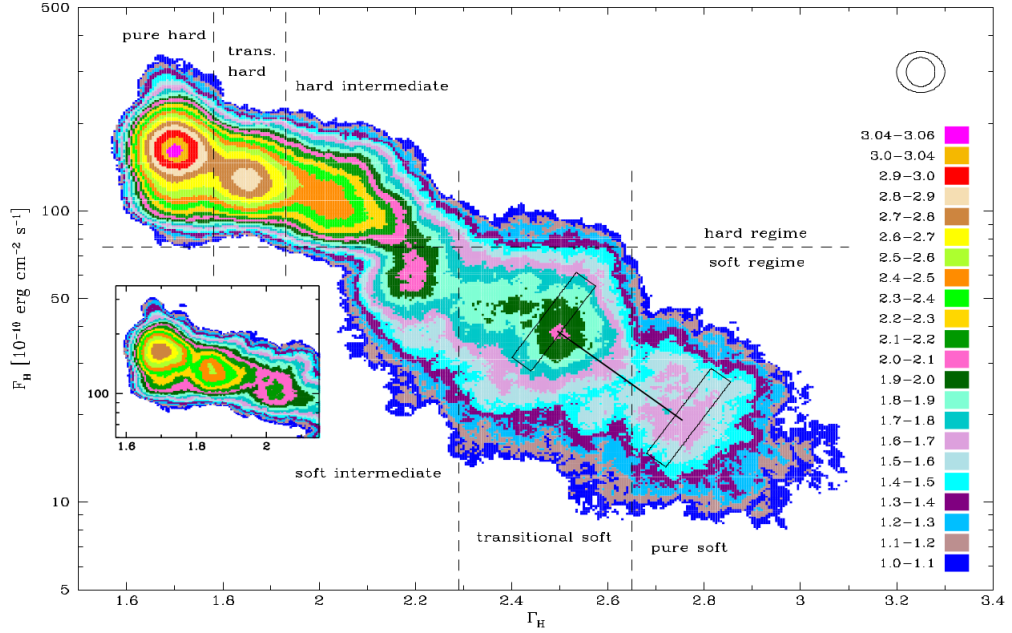


Figure 5.2: Density map of the spectral index vs flux. The color coding represents the logarithm of number of the data points within an area (ellipse shown above the color bar) around a given pixel. The horizontal dashed line represents the separation between the hard and soft regime. The vertical dashed lines separates the six plasma states. Rectangular regions: The two examples of the estimation of the density gradient within the soft state using the rectangular regions (for details see [Lubiński et al. \(2020\)](#)). This figure is taken from the [Lubiński et al. \(2020\)](#)

Comparing our results with the [Lubiński et al. \(2020\)](#), it is found that the ID 0426, ID 0436, ID 0456 are in pure hard, ID 2992, ID 4638 and ID 4492 in hard intermediate, ID 4646 in soft intermediate and ID 4678 in transitional hard (see [Table 5.2](#)).

Further, correlation between the radio flux and the spectral index is shown (see Figure 1 in [Lubiński et al. \(2020\)](#)) using radio data taken by the Ryle Telescope (RT) and the Arcminute Microkelvin Imager (AMI) at 15 GHz. The radio emission in the pure hard state varies relatively in narrow radio flux

Table 5.2: Flux and photon index obtained after the fitting of CZTI observation. *INTEGRAL* /ISGRI (Lubiński et al., 2020) values are shown for comparison. The errors are estimated for 90% confidence interval. Flux is in the units of  $10^{-10}$  erg cm $^{-2}$  s $^{-1}$ .

INTEGRAL/ISGRI			AstroSat/CZTI		
Spectral state	$\Gamma$	Flux	ObsID	$\Gamma$	Flux
PH	$\leq 1.78$	$\geq 75$	ID 0426	$1.75 \pm 0.02$	$82.56 \pm 0.60$
			ID 0436	$1.60 \pm 0.05$	$76.86 \pm 1.24$
			ID 0456	$1.76 \pm 0.02$	$88.94 \pm 0.52$
TH	$1.78 < \Gamma \leq 1.98$	$\geq 75$	ID 4678	$1.83 \pm 0.02$	$90.39 \pm 0.51$
HI	$1.98 < \Gamma \leq 2.29$	$\geq 75$	ID 2992	$2.06 \pm 0.01$	$90.96 \pm 0.37$
			ID 4638	$2.09 \pm 0.03$	$102.64 \pm 0.92$
			ID 4492	$2.24 \pm 0.02$	$76.19 \pm 0.50$
SI	$1.98 < \Gamma \leq 2.29$	$< 75$	ID 4646	$2.14 \pm 0.02$	$65.47 \pm 0.36$
TS	$2.29 < \Gamma \leq 2.65$	$< 75$			
PS	$> 2.65$	$< 75$			

band of 6 - 13 mJy. In transitional hard state it varies around two times higher compared to the pure hard state while in the hard intermediate state highest radio emission is reported. However, the average value of the radio emission in the hard intermediate state is similar to the transitional hard state but shows the largest flux variability (see Figure 5.3)

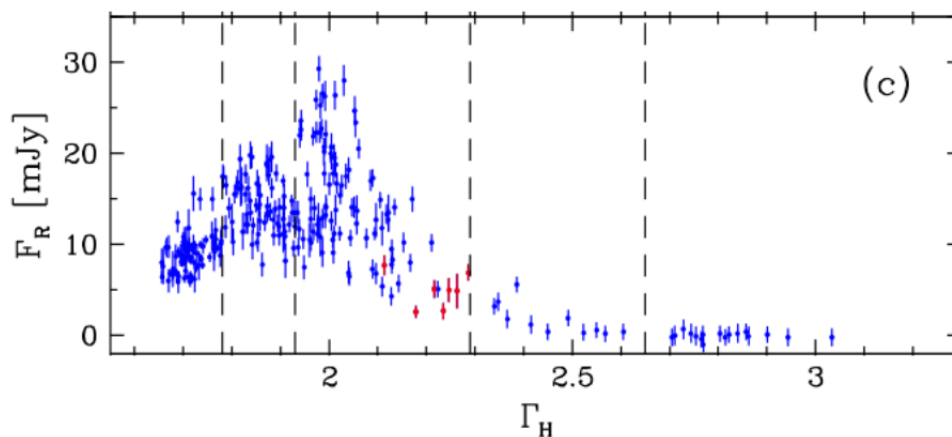


Figure 5.3: Radio flux vs spectral index variation for the six different plasma states (for details see text). This figure is taken from the Lubiński et al. (2020)

For further confirmation, spectral analysis similar to the (Lubiński et al., 2020) is required using the hourly or sub-hourly data (0.5 - 2 hr). This is possible for the CZTI as well. Each orbit of the AstroSat lasts for  $\sim 96$  min-

utes, so using the orbitwise data spectral analysis is possible. Each observation is divided into a separate orbitwise cleaned event file by applying the orbitwise GTI, which is obtained using a program written in IDL. Each orbit is considered to be equal to the time elapsed by the satellite reaching a reference longitude after starting from the same. The reference starting value of the longitude is assumed inside the SAA region to reduce the possibility of any data loss during GTI selection and in the final GTI the actual SAA region is excluded. This is done outside the pipeline using the IDL program. Orbitwise event file is further used to get the spectra and the response running the standard pipeline of the CZTI. Finally, after the spectral fitting using *xspec* as described above, we get the spectral index and the flux in 22 - 100 keV. The orbitwise spectral index versus flux correlation is shown in Figure 5.4.

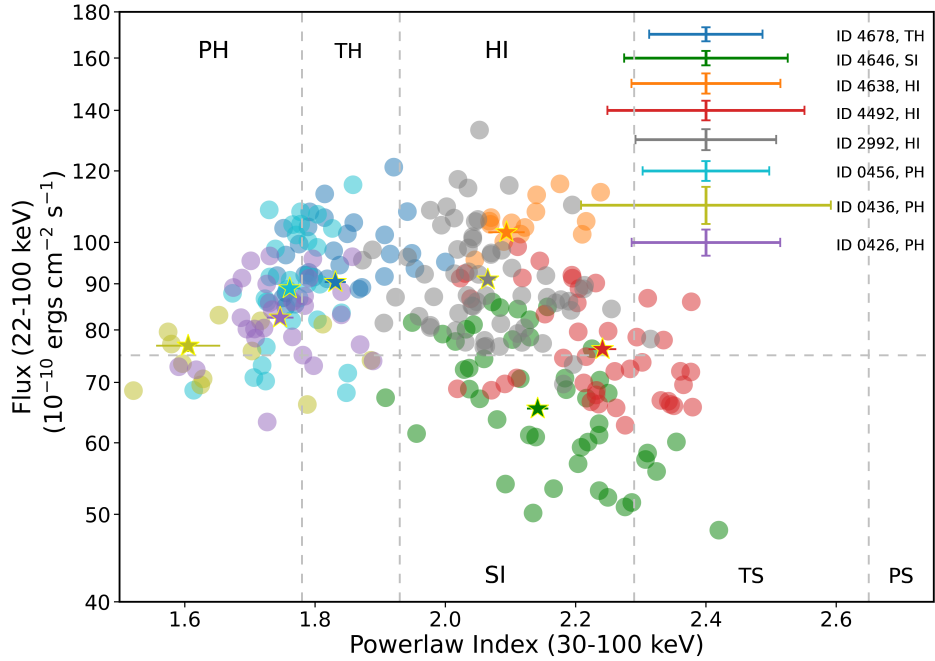


Figure 5.4: Cygnus X-1 spectral states based on power law index and flux correlation. Identified spectral state is mentioned following observation ID in the legend

According to the classifications given in [Lubiński et al. \(2020\)](#) the spectral states of all the eight CZTI observations of Cyg X-1 is confirmed by comparing the hourly flux versus spectral index correlation obtained after the orbitwise analysis. The observation ID 0426, ID 0436, ID 0456 are in PH, ID 2992, ID 4638 in HI and ID 4678 lies in TH (See Figure 5.4). We found that ID 4492 and 4646

lie in both the states- HI and SI (see Table 5.2). Further, we have checked the temporal evolution of the spectral index of these observations (see Figure 5.5). It is found that in both cases, the spectral index is varying from the 2.2 to  $\sim 2$  with the increase in the flux (see Figure 5.4). The state transition is occurring from the soft intermediate state to the hard intermediate state. It is interesting to see the state transition within the observation .

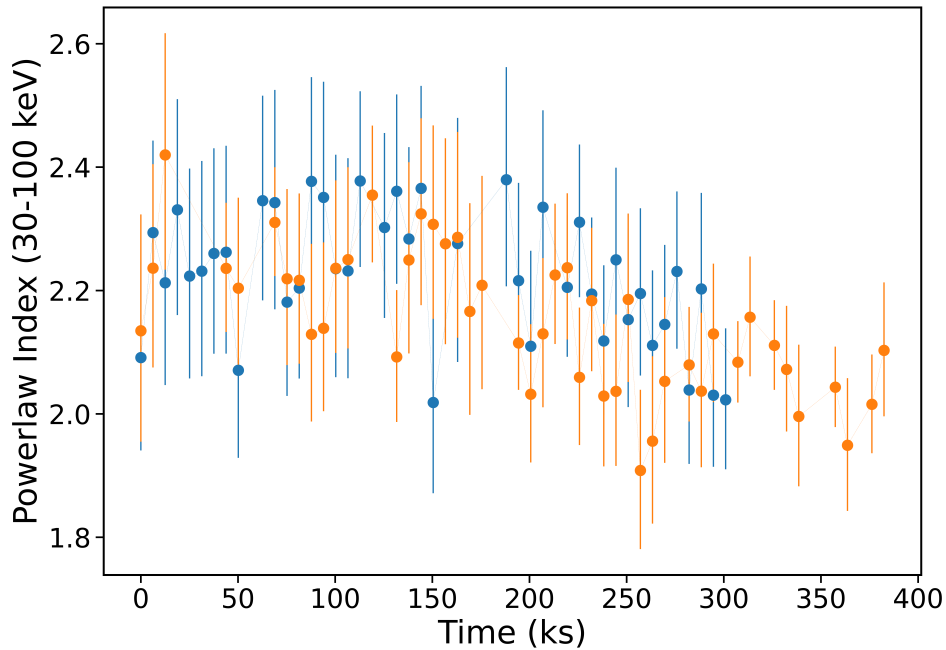


Figure 5.5: The spectral index variation with time for observation ID 4492 (blue color) and ID 4646 (orange color).

The intermediate hard state of Cygnus X-1 (like ID 2992) has also been seen in strong correlation with the increase in radio flux (Lubiński et al., 2020) whereas, in the case of the pure hard and transitional hard states (like ID 4678), the correlation is not very clear.

### 5.3.2 Timing analysis

Rapid time variability is studied using the LAXPC instrument (Chapter 2) in the broad energy band of 3 - 80 keV. The analysis was done using the LAXPC (Yadav et al., 2016b,a; Agrawal et al., 2017) Format A - LAXPCsoftware.Aug4 - package<sup>†</sup>. LAXPC30 module is affected by the gas leakage leading to the con-

<sup>†</sup><http://astrosat-ssc-iucaa.in/>

tinuous gain instability (Antia et al., 2017). Hence, LAXPC10 and LAXPC20 data is used for the timing analysis in this work. All the layers are used to maximize the signal. Level 2 event files are generated using the `laxpc_make_event` and `laxpc_make_stdgti` for the generation of the GTI file. Finally, the `laxpc_find_freqflag` tool is used to generate the power density spectrum ascii file, which is used to make the `xspec` compatible data and response files using the `laxpc_rebin_power` tool. PDS is generated in the frequency range of 0.1 to 20 Hz to keep the uniformity in the frequency range because orbitwise data is not statistically good to go up to higher frequency ranges in some cases. The PDS is then fitted with a combination of Lorentzian and the cutoff power law (`lorentz` and `cutoffpl` in XSPEC, (Axelsson et al., 2005)).

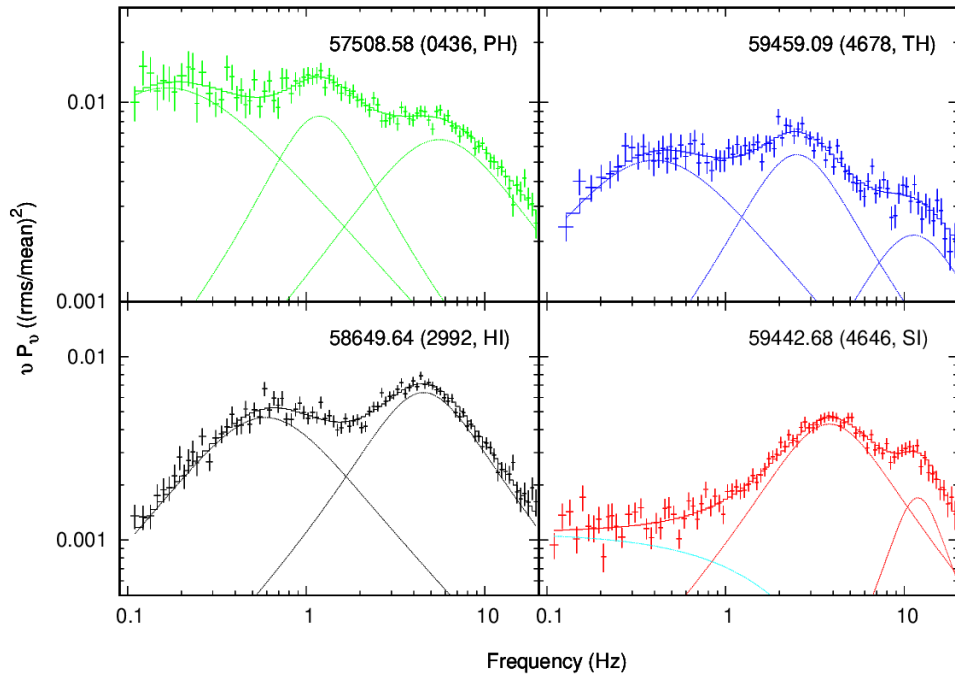


Figure 5.6: PDS for four representative cases are shown. The observation ID, spectral state and MJD of the observation are given at the top right corner of each panel.

The first three observations (ID 0426, ID 0436, ID 0456, ID 4678) required three Lorentzian components in 0.1 to 20 Hz similar to that obtained by the Pottschmidt et al. (2003b) for the hard state. For ID 4678, the centroid frequency of the Lorentzian is slightly shifted to higher values. Pottschmidt et al. (2003c) shows that with the softening of the spectrum, there is an increase in

the centroid frequency and a decrease in the average rms amplitude within the hard state. For ID 2992 and ID 4638, two Lorentzian are required, similar to the obtained by the [Pottschmidt et al. \(2003b\)](#) in the intermediate state. The two observations (ID 4646 and ID 4492) required one cutoff power law and two Lorentzian in soft state as shown by [Cui et al. \(1997c\)](#). The example PDS for above discussed observations for one orbit is shown in Figure 5.6.

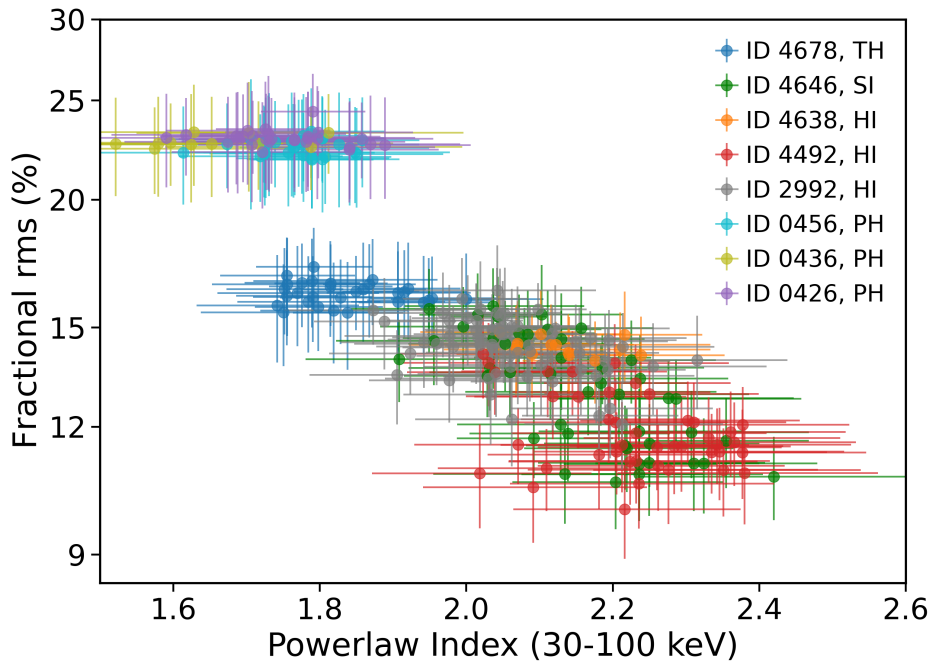


Figure 5.7: Cygnus X-1 spectral index (30 - 100 keV) vs fractional rms in 0.1 to 20 Hz (3 - 80 keV) using LAXPC data are shown. Each color represents different observations and spectral states as shown in the legend.

According to the requirement of different components (`lorentz` and `cutoffpl`) to fit PDS in different observations indicates that these are different states which are also found by the spectral analysis. Further, total root mean square (rms) variability is estimated by taking the square root of the flux obtained from the PDS fitting and then rms variation with the spectral index is investigated. Figure 5.7 shows the dependence of the total rms between the 0.1 and 20 Hz in different spectral states. The timing and spectral index show a strong correlation in time scales of the hour across the spectral states. This is also a good proxy for the source state. [Grinberg et al. \(2013b\)](#) shows a similar correlation in the energy range of 9.4 - 14.8 keV and 4.5 - 5.7 KeV.

Based on the spectral and timing analysis, it is clear that the Cygnus X-1 spectral states can be classified into six spectral states.

## 5.4 Spectral state dependence of polarisation

In chapter 3. we have shown the polarisation results where it is found that polarisation varies from observation to observation. After carrying out the spectral and timing studies, it is found that these observations belong to different spectral states ranging from the pure hard to soft intermediate states. The observation ID 2992 is clearly polarised, which belong to the hard intermediate state, and ID 4646, which is clearly unpolarised, lies in the soft intermediate state. Apart from this, we found that other observations also lie in different spectral states, as shown in Table 5.2. But for those observations, we are not able to constrain the polarisation results due to low exposure. The two observations for which polarization is well constrained, belong to two different states, which suggests that there is some dependence of polarization properties on spectral states in Cygnus X-1. The observation ID 2992 shows the strong polarisation and it increases with the energy as discussed in chapter 3. The trend of gradual increase in PF with energy above 170 keV and PF >39% at higher energies suggest that the net polarisation could be due to the mixing of two separate components, with one component being highly polarized synchrotron radiation from jet, whereas the other component is unpolarized, possibly from thermal Comptonisation from the corona. If we assume the CZTI highest energy measurement is due to 100% of synchrotron flux from the jet in a partially ordered field, then the CZTI PF results can be reproduced if the Comptonisation and the jet component intersection should occur at around 200 keV. We attempt to verify this hypothesis using a broad-band X-ray spectroscopy of this observation.

## 5.5 Broad band spectroscopy

We have selected observation ID 2992 out of eight observations for the broad band spectroscopy. It has sufficient exposure (333 keV) to do Compton spectroscopy in

100 - 380 keV based on the Compton sensitivity of the AstroSat-CZTI (discussed in chapter 4). We have done the broadband spectroscopy in 1 - 380 keV using the SXT (Singh et al., 2016, 2017), LAXPC (Yadav et al., 2016b,a) and CZTI mask weighted, and the Compton spectrum obtained using the method discussed in chapter 4.

The reduction of *AstroSat* data is carried out using the standard procedure. SXT data is analysed using the standard software and other tools provided by the Payload Operation Center (POC †). The cleaned and GTI filtered event file is used to generate the final data products using the Ftool `xselect`. The SXT observation is expected to be piled up if the count rate is  $\sim > 30$  counts/s in Photon Counting (PC) mode. During spectral fitting, an additional gain correction is done using the command `gain fit` in `xspec` as suggested by the SXT team. The average best-fit offset is found to be  $\sim 47$  eV for a unit slope. In the Cygnus X-1 observations we analysed, ID 2992 is piled up. To remove the pileup, we typically extract an annular region. We used an inner radius of 4 arcmins and an outer radius of 14 arcmins to remove the pileup. The change in the effective area due to annular region selection is corrected by scaling the default ARF (Auxiliary Response File) using the script `sxtARFModule`. The response and the background spectrum is provided by the POC.

The LAXPC data analysis is done using the software package as discussed in the section 5.3. The Level 2 event files are generated using the tool `laxpc_make_event` which is followed by the usage of `laxpc_make_spectra` and `laxpc_make_backspectra` to extract the source and the background spectra. We have used only LAXPC20 spectral files in this analysis.

The standard spectrum of CZTI in the energy range of 30 - 100 keV is obtained by the `cztipipeline`. The CZTI level 1 file to level 2 reduction and the extraction of the final product is carried out using the `cztipipeline`. The Quadrant 0 spectral files are used because other quadrants are affected by the higher systematics.

The Compton spectra, background spectra, and response in the energy range of 100 - 380 keV are generated using the method we have developed, which

---

†[www.tifr.res.in/~astrosat\\_sxt](http://www.tifr.res.in/~astrosat_sxt)

is discussed in detail in chapter 4.

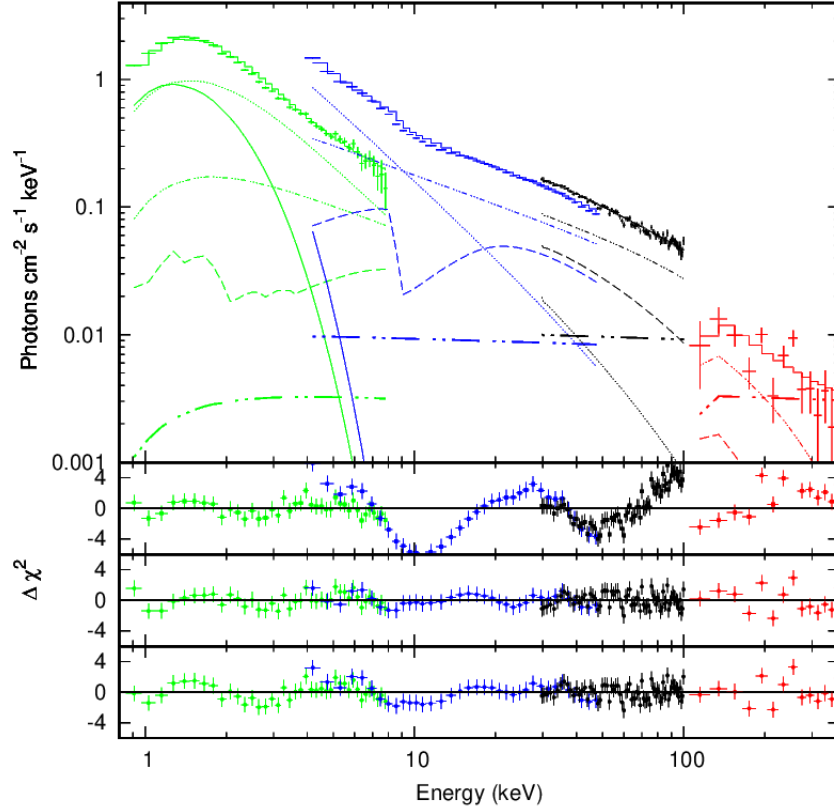


Figure 5.8: Broad band spectral fitting of the ID 2992 using the LAXPC, SXT, and CZTI data. Top panel: The unfolded spectrum along with the individual model components. The dotted, solid, threedotdash, dashed, and twodotdash, respectively, the soft Comptonisation, thermal-disk, hard Comptonisation, reflection and powerlaw components (Model 3 below). Residuals for the models are shown in the second to fourth panel: Model 1 - `const*TBabs*(diskbb + pexriv+ nthComp)`; Model 2 - `const*TBabs (diskbb + pexriv + nthComp + powerlaw)`; Model 3 - `const*TBabs*(diskbb + pexriv + nthComp + nthComp + powerlaw)`.

The broadband spectral analysis is carried out by jointly fitting the SXT, LAXPC20, CZTI mask weighted (30 to 100 keV) and the Compton spectra (100 to 380 keV) in `xspec` (Arnaud, 1996). The energy ranges of SXT and LAXPC spectra are restricted to 1 to 7 keV and 4 - 50 keV (to avoid the background dominated data), respectively. Thus, the combination of the four spectra resulted in a wide energy range starting from 1 to 380 keV. along with `TBabs`, that accounts for absorption due to neutral hydrogen. The thermal disk is accounted by `diskbb`, the thermal Comptonisation by `nthComp`, and the reflection part is fitted by `pexriv`. The ionization parameter ( $\log \xi$ ) and Fe abundance

( $A_{Fe}$  in solar units) are let free. The ratio of flux in the reflected component to that in the primary source (i.e., the reflection fraction *rel\_refl*) is frozen to a negative value since the *nthComp* accounts for the thermal Comptonisation. The final model in *xspec* is `constant*TBabs*(diskbb+nthComp+pexriv)`. The seed photon temperature in *nthComp* was tied to the inner-disk temperature ( $T_{in}$ ) in *diskbb*. The photon index (*PhoIndex*) of *pexriv* is tied to the respective parameter in *nthComp*. The *foldE* of *pexriv* is tied to 3 times the  $kT_e$  of *nthComp*. The spectral fitting shows the bad fit having the  $\chi^2_\nu$  is close to 7 (see Figure 5.8, second panel). We tried keeping free and freezing the  $kT_e$  at 60, which lies between 60 - 80 keV (Wilms et al., 2004), still, the spectral fitting does not improve. Further, we tried adding a powerlaw component in the model as suggested by the polarisation and radio correlation with the spectral state (as discussed in chapter 3). The model becomes `constant*TBabs*(diskbb+nthComp+pexriv+pow)`. The fit is good with a  $\chi^2_\nu$  is close to 1 but unable to constrain the  $kT_e$ . In this model, the powerlaw starts dominating over the Comptonisation above 100 keV, which do not support the polarisation results.

The polarisation results suggest the power law should dominate over Comptonisation above 200 keV because we got higher polarisation above 200 keV and shows increasing trend with energy. The broad band spectra (2-500 keV) of the Cygnus X-1 can be well fitted with the two Comptonisation components (Chitnis et al., 1998; Gierlinski et al., 1997), one at low energy and other one at higher energy. Therefore, we added another Comptonisation model to the previous model which results in model 3: `constant*TBabs*(diskbb+pexriv+nthComp+nthComp+pow)`. The spectral fit is acceptable ( $\chi^2_\nu=1.03$ ) however the power law index is not consistent with the polarisation results. According to the polarisation results the crossover between the Comptonisation and the powerlaw component should be at 200 keV. This is possibly due to the low counts in the data at higher energy which makes it difficult to constrain the photon index. Further, we have frozen the powerlaw spectral index and norm such that the spectral fit remains consistent with the polarisation results. The spectral index is frozen at 1.06 and the norms of the *nthComp* at  $7.45 \times 10^{-3}$  keeping  $kT_e$  free. The spectral fitting for the third model

Table 5.3: Best fit parameter of Model 3.

Model components	Parameters	Model 3
TBabs	nH (cm <sup>-2</sup> )	0.37 <sup>+0.03</sup> <sub>-0.03</sub>
diskbb	T <sub>in</sub> (keV)	0.46 <sup>+0.02</sup> <sub>-0.02</sub>
	norm (×10 <sup>4</sup> )	1.95 <sup>+0.58</sup> <sub>-0.42</sub>
powerlaw	Index	1.07*
	norm	7.45* × 10 <sup>-03</sup>
nthComp	Γ	1.78 <sup>+0.02</sup> <sub>-0.01</sub>
	kT <sub>e</sub> (keV)	95.3 <sup>+93.04</sup> <sub>-32.29</sub>
	kT <sub>bb</sub> (keV)	0.46 <sup>+0.02</sup> <sub>-0.02</sub>
	norm	0.8 *
nthComp	Γ	2.89 <sup>+0.07</sup> <sub>-0.07</sub>
	kT <sub>e</sub> (keV)	104.39 <sup>+52.86</sup> <sub>-26.36</sub>
	kT <sub>bb</sub> (keV)	0.46 <sup>+0.02</sup> <sub>-0.02</sub>
	norm	5.4*
pexriv	PhoIndex	1.78
	foldE	285.89
	rel_refl	-0.9*
	Fe_abund	1.02*
	cosIncl	0.76*
	T_disk (K)	10 <sup>*6</sup>
	xi (erg cm/s)	1205*
	norm	0.85
χ <sup>2</sup> (dof)	...	159.35(125)
χ <sub>ν</sub> <sup>2</sup>	...	1.27

[1] The asterisk superscript (★) represents that the parameter frozen to that value while fitting.

is acceptable ( $\chi^2_{\nu}=1.27$ ). The parameters obtained after the spectral fittings are presented in Table 5.3. The contribution of the powerlaw flux at higher energy is calculated by taking the ratio of the powerlaw flux to the total of powerlaw and nthcomp flux in the three energy ranges: 100 - 175 keV, 175 - 230 keV, and 230 - 380 keV (see Table 5.4). The obtained powerlaw flux contribution is consi-

tent with our polarisation results as expected. The final model, containing two Comptonisation model suggests that there are two Comptonising regions at same average temperature but having different optical depth (Sunyaev & Truemper, 1979; Sunyaev & Titarchuk, 1980). This could be possible if there is different length of the Comptonising region. The slab geometry of the corona is one such possible scenario.

Table 5.4: Flux value for the power law and the nthcomp in the different energy ranges for the broadband fit.

Energy range (keV)	power-law flux ( $\times 10^{-10}$ erg cm $^{-2}$ s $^{-1}$ )	nthcomp flux ( $\times 10^{-10}$ erg cm $^{-2}$ s $^{-1}$ )	Ratio
100 - 175	$6.46^{+0.35}_{-0.45}$	$19.9^{+0.20}_{-0.10}$	$0.24 \pm 0.01$
175 - 230	$4.68^{+0.18}_{-0.33}$	$7.94^{+0.46}_{-0.56}$	$0.37 \pm 0.02$
230 - 380	$12.3^{+0.58}_{-0.77}$	$8.32^{+0.08}_{-0.19}$	$0.60 \pm 0.01$

## 5.6 Discussion

We attempted spectral state determination based on the spectroscopy and timing to investigate the polarisation results obtained in chapter 3. The spectral and timing analysis suggests that there is a dependence of the polarisation on the different spectral states. The observation ID 2992, which belongs to hard intermediate state is highly polarised, while the ID 4646 is unpolarised, which belongs to the soft intermediate state, while polarisation for the others is unconstrained, but they also belong to different spectral states. Further, it is shown by the (Lubiński et al., 2020) that the radio flux is correlated with the HI state. Therefore, this high polarisation possibly comes from the synchrotron emission at the base of the jet in a partially ordered magnetic field, contribution of which increases with energy. The broadband spectroscopy of ID 2992 is carried out which suggests that we need an additional powerlaw component at higher energies to fit the broadband spectra (see Figure 5.8). These results complement the observed polarisation results seen for these observations and support that there is a separate polarized jet component in some of the hard spectral states of Cygnus X-1. The spectral model which fits the data required two Comptonising models

which suggest there are more than one Comptonising medium at two different optical depths. This can be possible in the slab geometry of the corona. The polarisation results suggests the contribution of the synchrotron emission from the jet should be  $\sim 17\%$  at 100 keV if we consider the 100% contribution from the synchrotron at 380 keV. The simulation and the theoretical studies suggest that the most probable geometry of the corona for which the maximum possible polarisation can be obtained at 100 keV by scattering is sandwich corona (Schnittman & Krolik, 2010) which is  $\sim 11\%$ . If the mixing of the two components is the possible region of low polarisation at lower energy then the slab geometry is one of the possible geometry of the corona in the HI state like ID 2992. But actual parameterization of the Comptonisation and power law components and their intersections are not possible with the current data, particularly at higher energies. It requires continuous and sensitive data extending deep into the sub-MeV region. Also the more sensitive polarisation measurements are required in broad energy range to decipher the two contribution and constraining the coronal geometry.

## 5.7 Summary

We carried out the orbitwise simultaneous spectral analysis of 5 years *AstroSat*-CZTI and LAXPC data of Cygnus X-1 and obtained consistent results with the INTEGRAL (Lubiński et al., 2020). We found different spectral states based on the spectral index and flux correlation. Further to study the spectral index correlation with the rapid variability in system the power density spectrum (PDS) is generated using *AstroSat*-LAXPC data. A power spectrum represents the variation of the power with the temporal frequency. The 3 - 80 keV power spectrum using LAXPC data required three Lorentzian in the hard state, two Lorentzian in the intermediate state, and finally a single powerlaw and two Lorentzian during the soft state while fitting. The extended energy range of the CZTI is also used to do the spectroscopy in broad energy range of 1 to 380 keV to decipher different spectral components of the polarisation and its dependence on different spectral states of Cygnus X-1. The parameters of the Comptonisation and power

low components are difficult to constrain with the present data, particularly at higher energies. It requires continuous and sensitive data extending deep into the sub-MeV region. Further, to separate the two polarisation components: corona and jet the polarisation measurements below 100 are required. For this, we have developed the conceptual design of the Compton spectro-polarimeter and the related instrumentation, which is discussed in the next chapter.

# Chapter 6

## Focal plane hard X-ray Compton spectro-polarimeter

### 6.1 Introduction

As discussed in chapter 5 that to decipher the contribution of the coronal and jet emission in the polarisation, the measurement of the polarisation in the broad energy range is required. The synchrotron emission surpasses Comptonised emission at higher energy, the actual cross over and the contribution of the different processes in total polarised emission is difficult to decipher with the present polarisation measurements using the existing polarimeters. There is no existing polarimeter that works in a broad energy range. Further, the spectroscopic study is required to obtain the contribution of the flux of the different processes in the total polarised emission and cross over of different spectral components like Comptonisation, power law, etc. Recently, Imaging X-ray Polarimeter Explorer (IXPE) reported the measurement of the polarisation of the Cygnus X-1 in the small energy range of 2 - 8 keV and proposed the emission from the extended corona (Krawczynski et al., 2022). However, there is no existing space-borne polarimeter that works in the energy range of 10 - 100 keV. The sensitivity of the X-ray detectors is limited due to low photon flux above 10 keV. However, with the development of hard X-ray optics (e.g., *NuSTAR* mission), which can focus photons in 3 - 80 keV. *NuSTAR* is the only mission so far with hard X-ray optics

and has improved X-ray spectroscopic sensitivity in the energy range of 3 - 80 keV by orders of magnitude. An X-ray polarimeter working in the similar energy range at the focal plane of such optics is expected to have similar improvement in the sensitivity for hard X-ray polarimetry. The feasibility of such polarimeter based on the Compton scattering (CXPOL) is explored by [Chattopadhyay et al. \(2014b\)](#) (details are given in the next section). Further, by adding the spectroscopic capabilities to this polarimeter, the spectro-polarimetric study can be carried out using such a polarimeter which can be further improved significantly with the focusing optics. We can do the spectro-polarimetry in 20 - 80 keV which can be further extended above 100 keV with the simultaneous measurement with the instruments like AstroSat-CZTI and INTEGRAL. In this way, we can study the corona-jet coupling in black hole binary, geometry of Corona, accreting pulsars, isolated pulsars like Crab, and other bright astrophysical sources in the broad energy range.

In this context, we have explored the feasibility of a focal plane hard X-ray spectro-polarimeter based on Compton scattering similar to the CXPOL. The conceptual design of the Compton spectro-polarimeter is described in Section [6.3.1](#). Semi-analytical calculations for some of the polarimeter parameters like efficiency, modulation factor, and spectroscopic sensitivity are given in Section [6.3.2](#). Characterisation of the detectors surrounding the absorber is described in Section [6.4](#). Finally, we have summarized the chapter and discussed the future plans.

## 6.2 Compton polarimeter

The Compton polarimeter work on the principle of Compton scattering, where the azimuthal distribution of the scattered photons from the scatterer is measured. The scatterer should be active, which can detect the deposited energy in the scatterer by the incident photon. The detection limit of the scatterer (low energy threshold) determines the lower energy limit of the polarimeter, and polarimetric sensitivity also depends on it. The decrease of the energy threshold increases the number of lower energy photons, which increases the polarimetric

sensitivity (see equation 6.17). The deposited energy in the scatterer depends on the incident photon's energy and the scattering angle (see Figure 6.3). The scattered photon is recorded by the surrounding absorber in coincidence with the interaction of the incident photon in the scatterer within a coincidence time window. The scatterer and the absorbing detector can be scintillating detectors emitting optical light when an X-ray photon deposits some energy. The criteria for selecting the scintillator are determined by the purpose of the scintillator for which it is required. Conditions like radiation length or absorption coefficient, decay constant, light output per unit energy deposition, etc., are important. The scatterer should be such that the Compton scattered photon can easily escape from it after the scattering and the probability of Compton scattering in the energy range of interest should be higher than that for the photo-electric interaction. It is possible only if the scatterer is a low  $Z$  element or large radiation length and of low density. The plastic (C and H are the constituents) scintillator is the appropriate choice for scatterers having low  $z$  constituent along with small decay constant and high light output. The scattering element should also be of optimum diameter so that the photon after a single scattering can escape easily from the scatterer and have a sufficient length so that the incident photon can undergo Compton scattering instead of pass through without interaction. The absorber should be a high  $Z$  absorbing detector to maximize the photoelectric absorption (see equation 2.14). A scintillator detector with low radiation length, high light yield, and low decay constant is required (e.g., CsI(Tl), NaI(Tl), etc.).

[Chattopadhyay et al. \(2014b\)](#) explored the feasibility of the focal plane hard X-ray polarimeter based on the Compton scattering (named CXPOL, Compton X-ray polarimeter). The conceptual design of the Compton polarimeter consists of the thin plastic scatterer surrounded by the CsI(Tl) scintillator in a circular fashion. Compton polarimeter is considered as the focal plane detector with hard X-ray optics based on the above mentioned configuration. The configuration has a cylindrical plastic scintillator (BC404) at its center having 5 mm diameter and 100 mm height surrounded by the 16 CsI(Tl) scintillator (each 15 cm long and 5 mm  $\times$  5 mm cross section) to record the azimuthal dependence of the scattered X-ray photons. The plastic scatterer integrated with the photo-

multiplier tube (PMT - Hamamatsu R6095 with photocathode of bialkali and maximum quantum efficiency of  $\sim 25\%$  at 420 nm) readout was procured from the Saint-Gobain. Scatterer is kept inside the 1 mm thick Aluminium cylinder with 0.5 mm thick Aluminium entrance window. The CsI(Tl) crystals, readout by the single Silicon Photomultiplier (SiPM) (procured from the KETEK, Germany (SiPM PM3350), active area of  $3 \times 3 \text{ mm}^2$ ) at one end of scintillator, which absorbs the scattered photons. SiPM is an array of semiconductor photodiodes which works in the Gieger mode (bias voltage  $>$  breakdown voltage). The details of the SiPM working principle can be found in [Buzhan et al. \(2002, 2003\)](#); [Otte \(2006\)](#). Each CsI(Tl) scintillator is kept inside an aluminum case that encloses the crystal from all sides except the side facing the scatterer and the lower end for readout.

### 6.3 Compton spectro-polarimeter

Compton spectro-polarimeter can measure the polarisation and the energy of the incident photons. The polarisation measurements can be done using the same technique as the ([Chattopadhyay et al., 2014b](#)). Energy of the incident photon can be estimated by the sum of the energy deposited in the scatterer and the absorber. Another way is using Compton kinematics, where the scattering angle and the energy deposited in the absorber are required (see equation 6.1). For the measurement of scattering angle, the position of interaction in the absorber and the scatterer is required. The scattering angle can be estimated by simple geometry, knowing the interaction position of the photon in absorber and scatterer. The position sensitive absorber and scatterer can provide the position of interaction and the energy of the scattered photon from the surrounding absorber, hence the energy of the incident photon.

$$\Delta E = E - \frac{E}{1 + \frac{E}{m_e c^2} (1 - \cos \theta)} \quad (6.1)$$

### 6.3.1 Proposed detector configuration

As discussed in the previous section, apart from the energy deposited in the absorber, scattering angle or energy deposited in the scatterer is required to get the energy of the incident photon. Therefore, the position sensitive absorber and scatterer are required.

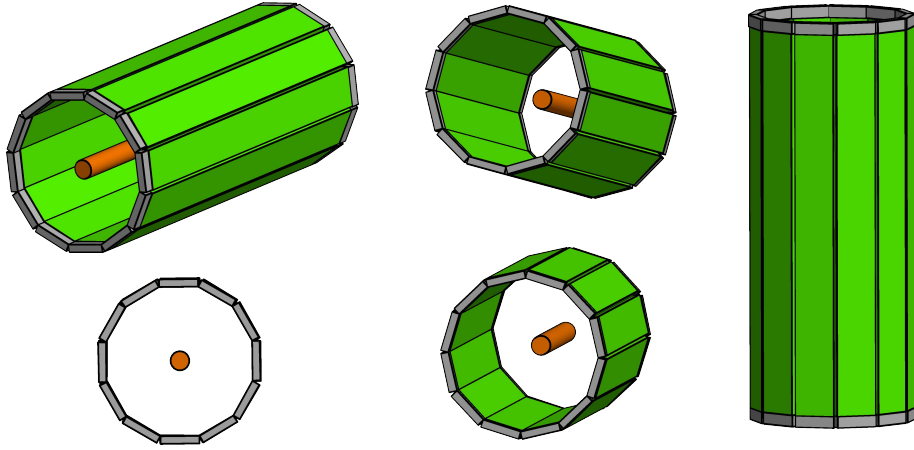


Figure 6.1: Conceptual design of the spectro-polarimeter. NaI(Tl) scintillators are shown in green, SiPM array in grey and scatterer in orange color. Here 12 absorbers are shown, but for CXPOL like geometry, only 8 are required.

Also the modulation factor and the detection efficiency of the polarimeter should be optimized accordingly to maximize polarimetric sensitivity. These two factors are dependent on the shape and material of the detectors. The scattering element should be a low atomic number ( $Z$ ) element to obtain the high Compton efficiency (because photoelectric interaction cross section is proportional to  $Z^5$ ) and its diameter and length must be such that incident photon sees a large depth while passing through the scatterer (so that it have significant probability of Compton scattering) and sees smaller depth perpendicular to the incident photon so that the scattered photon can escape easily from the scatterer. A narrow cylindrical position sensitive scatterer surrounded by the cylindrical array of position sensitive absorbers would be the feasible design of the Compton spectro-polarimeter. Compton spectro-polarimeter is considered as the focal plane detector with hard X-ray optics based on the above mentioned configuration.

One way to determine position of the incident photon in the scatterer is to use segmented scatterer as shown in Figure 6.2 where each segment is read out separately. Another possibility to determine the position of interaction in the scatterer by two end readout of the scatterer by the SiPM array, and then the ratio of the charge at both ends can give the position of interaction. Here we are proposing to readout the scatterer by the single or array of SiPMs instead of PMT as done in CXPOL depending upon the diameter of the scatterer. SiPMs have high photon detection efficiency, comparable to or larger than that of PMTs, comparable gain and output signal, the capability of detecting single photons, insensitive to magnetic fields, minimal weight, and small size, low bias voltage, and low power consumption than PMTs (Wonders, Marc A. et al., 2018). Various companies produce SiPMs like the Hamamatsu, Sensl and KETEK (used in the CXPOL, KETEK, Germany (SiPM PM3350)). The properties of different SiPMs are shown in Table 6.2). The SiPM from the Sensl has low background, high gain, and low operating voltage. Therefore we will use SensL SiPMs procured from Advatech, UK. However, the two end readouts would degrade the energy threshold of the scatterer due to absorption in the SiPM. Hence, the energy threshold of the overall polarimeter. The active scatterer's lower energy threshold determines the polarimeter's lower energy limit and the polarimetric sensitivity. The total number of source photons increases by decreasing the lower energy threshold, which improves the polarimeter's sensitivity (see equation 6.17). Another possible configuration is the SiPM readout along the length of the scatterer. For now, we consider scatterer readout only at one end using conventional PMT and hence no position estimation within scatterer. This will lead to some uncertainty in polar scattering angle and consequently energy measurement. In future we plan to conduct experiments for threshold and position measurements in the scatterer using SiPM readout. In further discussion we will assume the CXPOL like scatterer (plastic scatterer having 5 mm diameter and 100 mm length) readout by the PMT.

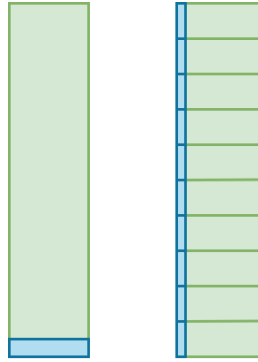


Figure 6.2: Schematic of the plastic scintillator scatterer readout by the SiPM array: One end readout is shown on left and readout along the length for the segmented or non-segmented scatterer on the right.

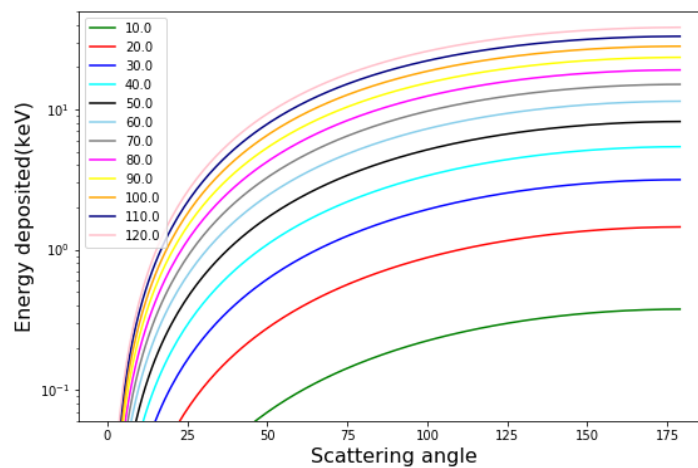


Figure 6.3: Energy deposition in the scatterer vs scattering angle for different incident energy photon.

For the absorber, low radiation length, high light yield, and low decay constant are required. One way to determine position of the incident scintillator is required. NaI(Tl) has a significantly lower decay constant (230 ns) (Shionoya et al., 2018) than CsI(Tl) and is comparable to the other parameters. Shorter scintillation time helps in higher count rate applications and reduces background collection per unit time, which results in increase in the absorber's sensitivity. LYSO:Ce<sup>3+</sup> (Cerium-doped Lutetium-Yttrium Oxyorthosilicate) have better light output, low decay constant, low radiation length (Shionoya et al., 2018) but requires fast readout electronics to avoid the pile up and also difficult to find in the required size. Therefore, we have used NaI(Tl) scintillator as the absorbing detector surrounding the scatterer.

Table 6.1: Details of the scatterer and absorber along with scattering geometry.

<b>Scatterer</b>	
Shape and material	Cylindrical, segmented plastic
Height	100 mm
Diameter	5 mm
Cover	0.2 mm thick Aluminium
<b>Absorber</b>	
Shape and material	Cylindrical array of 8 NaI scintillator
Dimension	5 mm x 20 mm x 100 mm
Dead space between absorbers	0.2 mm Al
Distance between center of scatterer and front of scintillator	42.5 mm
Al thickness between the scatterer and absorber	0.2 mm
Front cover	0.2 mm epoxy
remaining sides	0.2 mm Al

NaI scintillator with two end readout by an array of SiPMs (array of 3 silicon photo multiplier on each end) is used as an absorber for the scattered photons having dimensions of 5 mm  $\times$  20 mm  $\times$  100 mm. The length of the NaI(Tl) scintillator is 10 cm because in CXPOL for 59.5 keV incident photon the sensitivity degrades significantly after 4 cm (15 cm CsI(Tl) scintillator readout by SiPM at one end). Therefore, we considered 10 cm long NaI(Tl) scintillator will be the better for two end readout. In future, we will optimise the dimensions with the experimentation and simulation. In the present conceptual design there are 8 NaI absorbers circularly placed around the plastic scatterer for CXPOL like spectro-polarimeter. The conceptual model of the configuration is shown in Figure 6.1, which also includes the thin Aluminium housing structure. The detailed specifications of the configuration are given in Table 6.1.

The deposited energy ( $\Delta E$ ) in the absorber by photoelectric interaction along with the position of the interaction of the scattered photon can be estimated using the two end readout of the NaI(Tl) scintillator using the SiPM array. The two end readout can provide the position of interaction from the ratio of pulse heights recorded at the two ends of the absorber by the SiPM. The energy resolution of the polarimeter depends upon the position resolution of scatterer, absorber and the energy resolution of the absorber.

Table 6.2: Some important characteristics of the SensL (now OnSemi) MicroJ-series, KETEK and Hamamatsu SiPM at  $V_{br} + \sim 2.5V$ 

Parameters	SensL [1]		KETEK [2]	Hamamatsu [3]
	6 mm (60035)	3 mm (30035)		
Active area ( $mm^2$ )	$6.07 \times 6.07$	$3.07 \times 3.07$	$3 \times 3$	$3 \times 3$
$V_{br}$ (V)	24.7(max)	24.7(max)	25	54
Microcell size ( $\mu m$ )	35	35	50	50
No. of microcells	22,292	5676	3472	3600
Peak PDE (%)	38	38	28	40
Peak wavelength (nm)	420	420	430	500
Dark count rate (kHz/ $mm^2$ )	50	50	250	1.7
Gain ( $\times 10^6$ )	2.9	2.9	3.6	150
Recovery (ns)	50	45	130	

[1] <https://www.onsemi.com/pdf/datasheet/microj-series-d.pdf>[2] <https://www.ketek.net/wp-content/uploads/2017/01/KETEK-PM3325-EB-PM3350-EB-Datasheet.pdf>[3] [https://www.hamamatsu.com/content/dam/hamamatsu-photonics/sites/documents/99\\_SALES\\_LIBRARY/ssd/s13360\\_series\\_kapd1052e.pdf](https://www.hamamatsu.com/content/dam/hamamatsu-photonics/sites/documents/99_SALES_LIBRARY/ssd/s13360_series_kapd1052e.pdf)

### 6.3.2 Analytical calculation of modulation factor, efficiency and spectroscopic sensitivity

Here, we presents the analytical calculation of the different parameters of the polarimeter. Analytical calculation is one of the ways to quickly check the effect of the different configuration over the different parameters of the polarimeter. It helps to find out the best possible configuration to start with before performing the actual experiment and the simulation studies. We have done a similar analytical calculation as done by the [Chattopadhyay et al. \(2013\)](#) for the modulation factor and efficiency of the proposed configuration at different energies to optimize the geometry of the configuration (see Figure 6.5). The modulation factor is calculated using the equation 6.2 where  $C_{\max}$  and  $C_{\min}$  are number of photons scattered by scatterer at polar angle  $\theta$  and azimuthal angle is  $\phi = \pi/2$  and  $\phi = 0$  respectively.

$$\mu(E) = \frac{C_{\max} - C_{\min}}{C_{\max} + C_{\min}} \quad (6.2)$$

To calculate the modulation factor first, we calculate the  $C_{\max}$  and  $C_{\min}$  in each segment of the scatterer and add them. The transmission probability of the photons from one segment to another, which is  $e^{-\mu\tau\rho n}$  is considered. The ratio of the cross-sections (see equation 2.16 of chapter 2) and equation 6.3 gives the fraction of photons scattered at angle  $\theta$ .

$$\sigma_t = \int_0^\pi \frac{r_0^2}{2} \left(\frac{E'}{E_0}\right)^2 \left(\frac{E'}{E_0} + \frac{E_0}{E'} - \sin^2 \theta\right) 2\pi \sin \theta d\theta \quad (6.3)$$

The possible maximum and minimum scattering angles are required to get the fraction of photons absorbed in the absorber after scattering from each segment. The  $\theta_{\min}$  and  $\theta_{\max}$  depend upon the geometry and position sensitivity of the plastic scatterer. The  $\theta_{\max}$  and  $\theta_{\min}$  (equation 6.4 and 6.5) are calculated for each segment using the scattering geometry as shown in Figure 6.4.

$$\theta_{\max} = \pi/2 + \sin^{-1} \frac{10 - x' + x}{\sqrt{(10 - x' + x)^2 + (z)^2}} \quad (6.4)$$

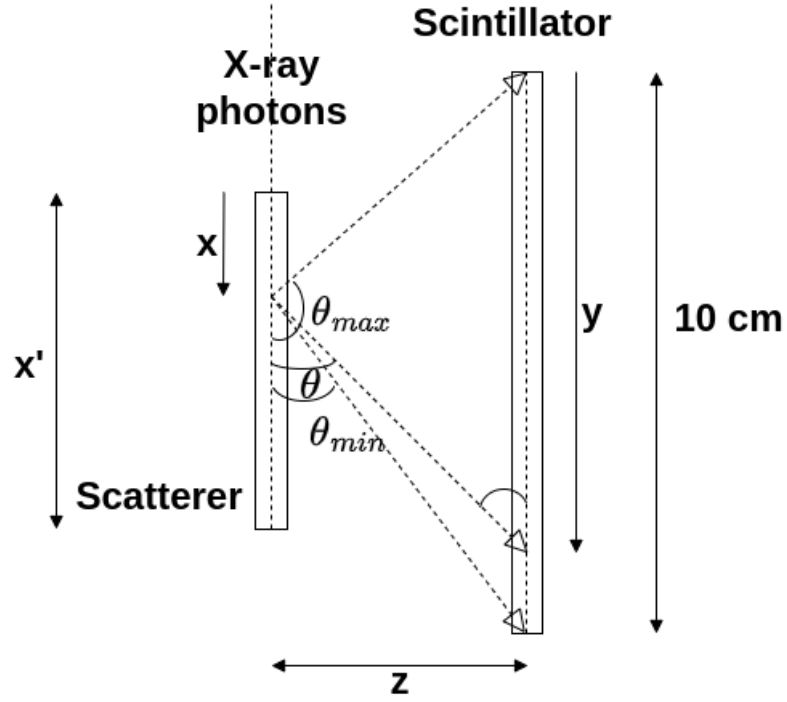


Figure 6.4: Scattering geometry of the proposed spectro-polarimeter

$$\theta_{\min} = \sin^{-1} \frac{z}{\sqrt{(x' - x)^2 + (z)^2}} \quad (6.5)$$

The  $\theta_{\min}$  also depends on the energy threshold of the scatterer and is given by the equation 6.6, the  $E$  is the incident energy of the scatterer, and  $E_{\text{thres}}$  is the threshold energy of the scatterer. To count all the photons scattered towards the absorber, the  $\theta_{\min}$ , which is the lower limit of the integration, is taken as the maximum of the two values (sine or cosine).

$$\theta_{\min} = \cos^{-1} \left( 1 - \frac{E_{\text{thres}} m_e c^2}{E(E - E_{\text{thres}})} \right) \quad (6.6)$$

Finally, the contribution of each segment is summed up to get the total scattered photons detected in the absorber considering the 100% detection efficiency of the absorber. Put the values of equation 6.7 and 6.8 give the modulation factor.

$$C_{\max} = \sum_{i=0}^{i=n-1} N e^{-\mu_t \rho_i n} \left( \frac{\mu_c}{\mu_t} \right) (1 - e^{-\mu_t \rho_n}) \left( \frac{\int_{\theta_{\min}}^{\theta_{\max}} \left( \frac{d\sigma}{d\Omega} \right)_{\phi=\frac{\pi}{2}} \sin \theta d\theta d\phi}{\sigma_t} \right) \quad (6.7)$$

$$C_{\min} = \sum_{i=0}^{i=n-1} N e^{-\mu_t \rho i n} \left( \frac{\mu_c}{\mu_t} \right) (1 - e^{-\mu_t \rho n}) \left( \frac{\int_{\theta_{\min}}^{\theta_{\max}} \left( \frac{d\sigma}{d\Omega} \right)_{\phi=0} \sin \theta d\theta d\phi}{\sigma_t} \right) \quad (6.8)$$

The efficiency of the spectro-polarimeter is calculated by estimating the total number of the scattered photons from the scatterer detected in the absorber considering the 100 % detection efficiency of the absorber (see equation 6.9). The dead space between the consecutive absorber due to the aluminium shielding is also considered by multiplying the efficiency by a multiplicative factor given by  $1 - \frac{8 \times 0.02}{2\pi \times 2.65}$

$$\epsilon = \sum_{i=0}^{i=n-1} e^{-\mu_t \rho i n} \left( \frac{\mu_c}{\mu_t} \right) (1 - e^{-\mu_t \rho n}) \left( \frac{\int_{\theta_{\min}}^{\theta_{\max}} \left( \frac{d\sigma}{d\Omega} \right) \sin \theta d\theta d\phi}{\sigma_t} \right) \quad (6.9)$$

**Spectroscopic sensitivity** Absorber should be position sensitive for the measurement of the scattering angle of the incident photon. The measurement of the scattering angle and the energy of the scattered photons finally give the energy of the incident photon (see equation 6.12). Position sensitivity of the absorber limits the configuration's angular resolution, which affects the energy resolution.

The proposed configuration is discussed in the above section. We want to measure the energy and polarisation simultaneously with the proposed configuration. The analytic calculation is done for the energy resolution of the proposed configuration. Let suppose length of the scatterer is  $x'$  and the length of the absorber is already fixed i.e 10 cm, distance between scatterer and absorber is  $z$ . Now x-ray photon undergoes Compton interaction at position  $x$  in the incident direction and gets absorber at position  $y$  in the absorber.

Scattering angle will be given by

$$\cos \theta = \frac{(y + x' - x - 10)}{\sqrt{(y + x' - x - 10)^2 + z^2}} \quad (6.10)$$

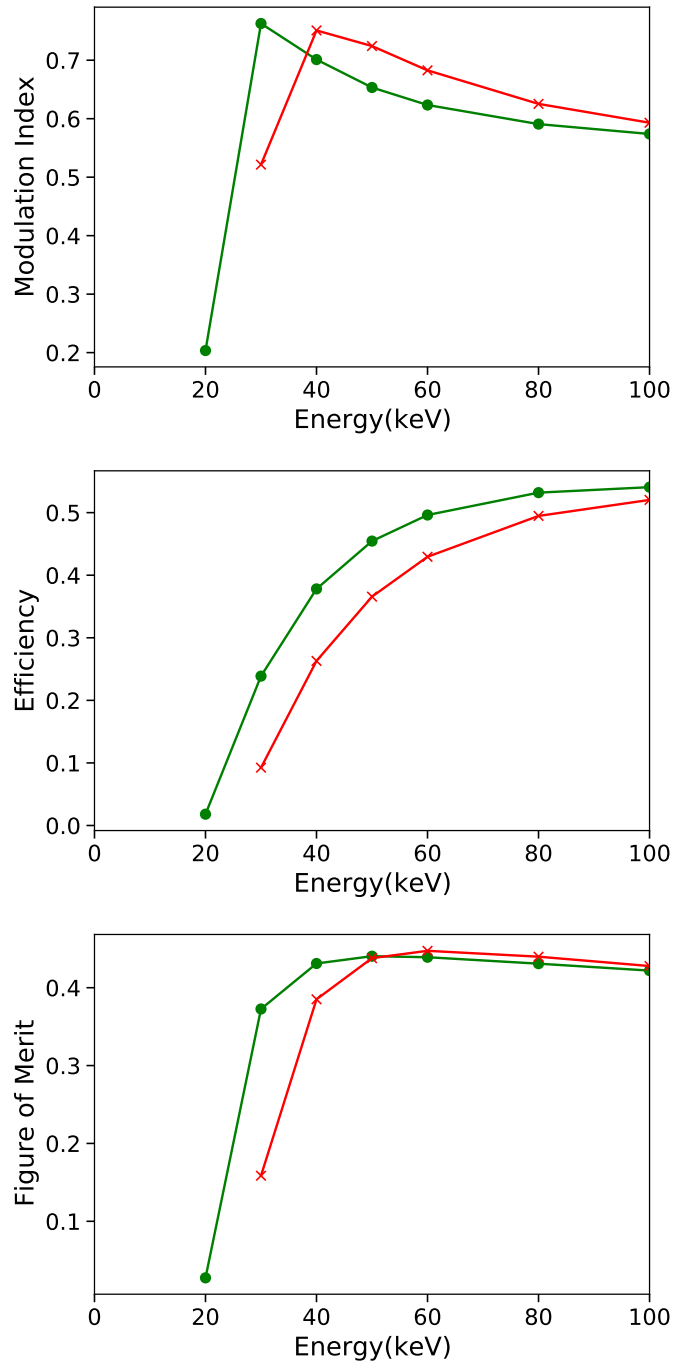


Figure 6.5: Top to bottom: Modulation factor, efficiency and figure of merit for the CXPOL like conceptual design. The green and red color represents values corresponding to the 1 keV and 2 keV threshold of the scatterer, respectively.

Error in scattering angle or the angular resolution is given by

$$\Delta\theta = \frac{\Delta y + \Delta x}{z} \left[ 1 + \left[ 1 - \frac{(E - E')mc^2}{EE'} \right]^2 \right] \quad (6.11)$$

Where  $E$  is the incident energy and  $E'$  is the scattered photon energy

We know from the Compton scattering phenomenon i.e

$$E = E' \left[ 1 - \frac{E'(1 - \cos \theta)}{mc^2} \right]^{-1} \quad (6.12)$$

Energy resolution will be given by

$$\frac{\Delta E}{E} = \left[ \frac{\Delta E'}{E'} + \frac{\Delta E'(E - E')mc^2 + E' \Delta \theta mc^2 (E - E') [2EE' - (E - E')mc^2]}{EE' mc^2 \left[ 1 - \frac{E'}{mc^2} + \frac{(E - E')mc^2}{EE'} \right]} \right] \quad (6.13)$$

We have plotted energy resolution variation with the incident energy for different scattering angles assuming  $z$  is equal to 2.65 cm (for CXPOL like configuration), the experimental value of energy resolution of the absorber is  $\sim 20$  KeV for 59.5 KeV  $\text{Am}^{241}$  (average energy resolution, see section 6.4.4.1), position resolution of the scatterer is assumed to be 5 mm (for segmented scatterer) and position resolution of the absorber is 1.6 cm (average position resolution, see section 6.4.4.2). This is the worst case scenario which will improve significantly with the improvement in the position and energy resolution of the absorber. Energy deposition in the scatterer depends upon the energy of the incident photon and the angle of scattering (Figure 6.3). From Figure 6.6, we can see that energy resolution improves at higher incident energy for the same scattering angle.

Angular resolution in terms of scattering angle using geometry (see Figure 6.4),

$$\Delta \theta = \frac{\Delta y + \Delta x}{z} \left[ 1 + \cos^2 \theta \right] \quad (6.14)$$

Therefore, energy resolution in terms of scattering angle can be given by,

$$\frac{\Delta E}{E} = \left[ \frac{\Delta E'}{E'} + \frac{\Delta E'(1 - \cos \theta) + E' \Delta \theta \sin \theta}{mc^2 \left[ 1 - \frac{E'(1 - \cos \theta)}{mc^2} \right]} \right] \quad (6.15)$$

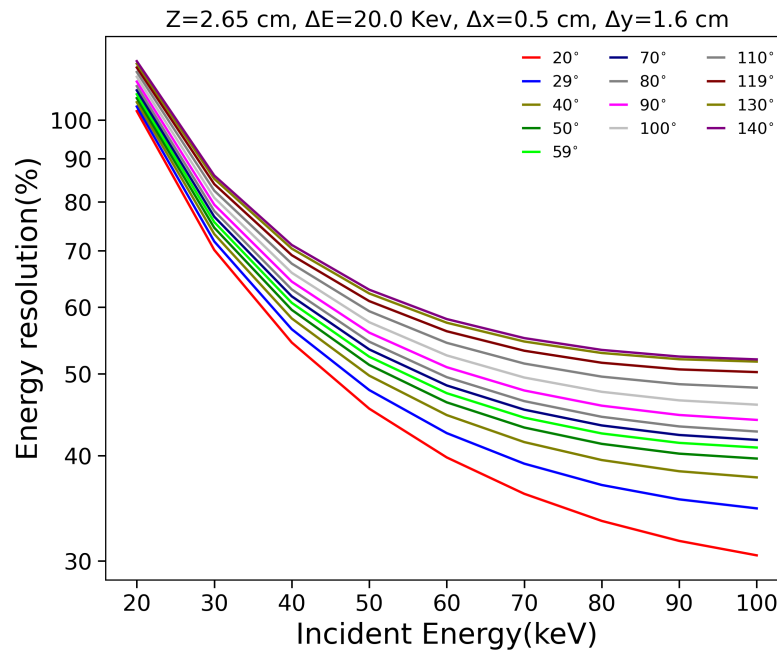


Figure 6.6: Energy resolution of the CXPOL like conceptual design. Different color represents different scattering angle. The value for the position and energy resolution of absorber is taken from the experiment. The scatterer position resolution is assumed to be equal to the size of the each segment of the scatterer.

## 6.4 Characterisation of position sensitive absorber - based on the NaI(Tl) - scintillator and SiPM arrays

In scintillation detectors, a considerable number of visible light photons is generated during the interaction of X-rays with crystal scintillators, here NaI(Tl), and the following de-excitation process. These photons are converted into electrons by means of a photo-detector, here SiPM array. In comparison to the gas detectors, the scintillation detectors are based on a higher Z material with a higher density and often, they have a larger thickness. This means that they have a high probability of detecting photons in a wider X-ray energy range. However, the energy resolution offered by this detector is the poorest among X-ray detectors, especially in the low energy range. Pulse-height measurement of signals of the two end SiPMs of the scintillator can be used to determine the position of the

interaction of the X-ray photons. The NaI(Tl) scintillator having a dimension of  $10 \times 2 \times 0.5$  cm is used as the absorber for the X-rays coming from the scatterer after the scattering. We have done the experimental measurement of the position resolution of the NaI(Tl) absorber readout by the array of 3 SiPMs from both sides. The details of the SensL (now OnSemi) SiPMs used is given in Table 6.2 (procured from the Advatech, UK). The optical photon count in the SiPM is measured for nine different positions (1 cm apart) by illuminating the absorber with the X-ray source placed in front it. The position of the interaction can be determined by the gradient in the light intensity with the function of the source location.

### 6.4.1 Characterisation setup

The experimental arrangement is set up inside the light-tight dark box at room temperature. The scintillator, light source, and the SiPM arrays coupled at both the ends of the scintillator are kept inside the box along with the readout electronics (see Figure 6.7). NaI(Tl) scintillation crystal with  $10 \times 2 \times 0.5$  cm<sup>3</sup> dimension is used. It is hygroscopic in nature so we have procured the enclosed package containing the NaI(Tl) scintillator coupled with SensL SiPM (procured from the Advatech, UK) which are fast and have low background than other available SiPMs (see Table 6.2). The scintillator is coupled with the array of three SiPMs of  $6 \times 6$  mm<sup>2</sup> each at both ends for the readout of optical photons and sealed by the aluminum cap to minimize the stray light background (see Figure 6.7). SiPM of 6 mm size is used instead of 3 mm to reduce the dead area between the SiPMs in the array to get the better sensitivity of the detector. The SensL SiPM gives two signal outputs: Standard and fast. Fast output is generally used to get the ultra fast timing measurements and allow higher count rates but gives poor energy information due to the insufficient electric charge integration. Here, Standard output is used because we are more interested in charge deposited by the scintillation photons to get the energy and position of interaction of the incident X-ray photon. Radiation source of Am<sup>241</sup>, which emits 59.5 keV line, is placed head-on on the surface of scintillator crystal. For data

acquisition, the labview software is used where the time of the event and the ADC value is stored in a file for further analysis in python and idl. The events are recorded with a coincidence time window of  $4.25 \mu\text{s}$ .

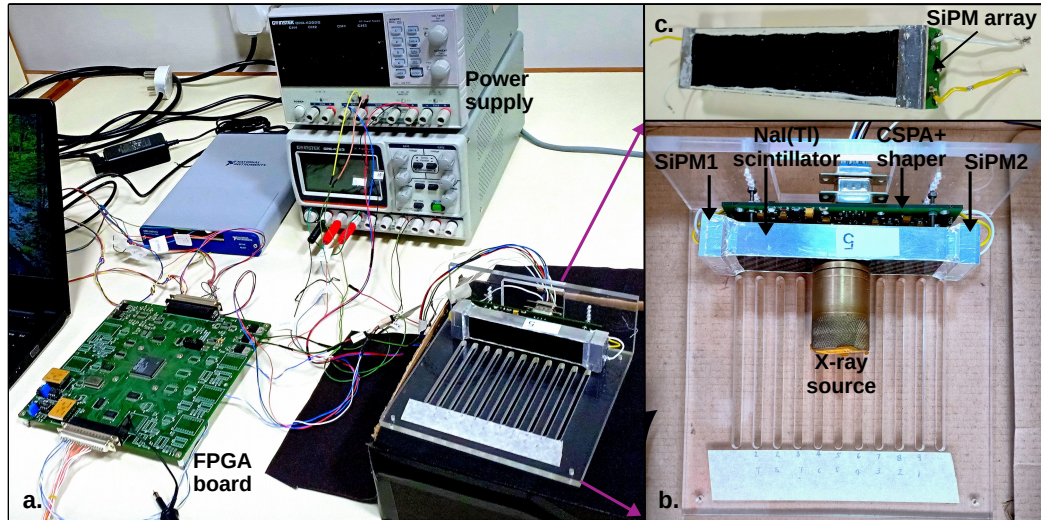


Figure 6.7: Experimental setup for the position measurement

### 6.4.2 Readout electronics

The light produced in the NaI(Tl) scintillator due to interaction of the incident X-ray photons is collected using the array of 3 SiPMs at both the end of the scintillator. A charge sensitive pre-amplifier (CSPA) amplifies the signal obtained from the SiPM array, which is then fed to the shaper having  $4 \mu\text{s}$  shaping time to shape it in a gaussian peak. The gaussian peak is then fed to the peak detector for the measurement of the peak of the pulse distribution. Peak detector holds the peak for  $1.25 \mu\text{s}$  and discharge in  $1 \mu\text{s}$ . The analog signal is then converted to a digital signal using 12-bit ADC. Finally, the ADC value and the time of the event are stored in the data acquiring software LABVIEW (see Figure 6.8) The events are recorded in coincidence with  $1 \mu\text{s}$  time resolution, which is done in the FPGA. The shapers trigger the comparator having the reference voltage of  $50 \text{ mV}$ , which in turn triggers the FPGA to acquire the data if there is a signal from the second comparator within a coincidence time window of  $4.25 \mu\text{s}$ . The dead time of the electronics is  $9.25 \mu\text{s}$ .

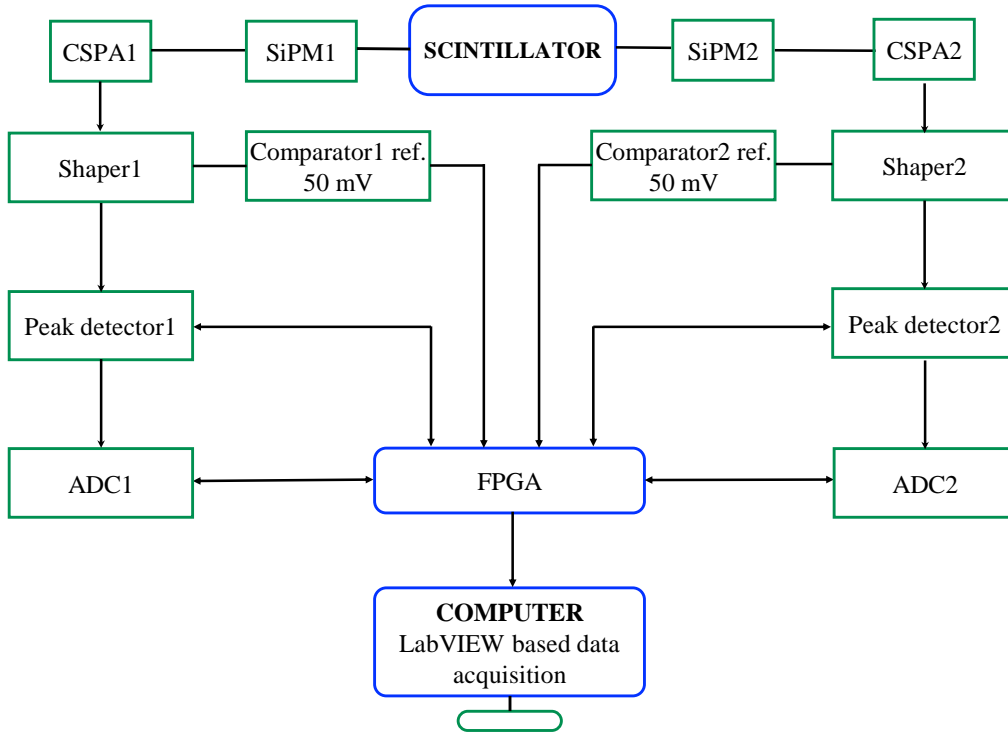


Figure 6.8: Readout electronics schematic

### 6.4.3 Data analysis

The ratio of the pulse height is used to describe the radiation source location in front of the scintillator. For each event, the ratio of  $ADC1/(ADC1+ADC2)$  gives the axial location of the interaction of the incident X-ray photon. The histogram of the ratio at each location is fitted with a gaussian function to determine the peak value and the FWHM. The axial-position resolution of the scintillator detector is the FWHM of the gaussian fitted to the ratio histogram. The measured position resolution at the center of the absorber for 59.5 KeV  $Am^{241}$  source is 1.86 cm. The true position resolution will be obtained using the following relation.

$$R_m^2 = R_t^2 + R_o^2 \quad (6.16)$$

where,  $R_m^2$  is the measured position resolution,  $R_t^2$  is the true position

resolution and the  $R_b^2$  is the beam size. Considering the beam size of 0.2 mm the true position resolution does not change much, it is still 1.89 cm.

The energy spectrum for each position is obtained by summing up the two SiPM signals (ADC1+ADC2). The energy resolution is calculated as the FWHM of the 59.5 KeV photopeak for each summed spectrum fitted with a gaussian function.

## 6.4.4 Results

### 6.4.4.1 Measurement of the position of individual X-ray photons

In case of CXPOL, the estimation of the position of the interaction of photon in the absorber was not possible due to the one end readout of the CsI(Tl) scintillator. The position can be estimated by the two end readout of the scintillator by the ratio of the charge at both the end of the scintillator. The ratio of the two SiPM arrays signals  $ADC1/(ADC1+ADC2)$  (charge in digital unit) at nine different irradiation positions of the scintillator is histogrammed to see the distribution of the ratio of the charge at each position. The ratio is multiplied with a constant number of 1024 to make the plot more appealing. The two end readout of the NaI(Tl) scintillator two end readout gives the position of the photon throughout the length of the scintillator. The distribution of the ratio signal at nine different positions is plotted (see Figure 6.9). Further, full width at half maxima (FWHM) of each histogram at nine irradiation positions is estimated (see Figure 6.9). The axial position resolution ranges from 1.16 cm at one end to 1.06 cm at the other end and 1.86 cm at the center, with an average of 1.6 cm.

### 6.4.4.2 Measurement of energy

The sensitivity of the CsI(Tl) absorber was up to  $\sim 5$  cm along the length of the absorber [Chattopadhyay et al. \(2014b\)](#). We are able to detect X-ray photon throughout the length of the absorber (see Figure 6.9) with two end readout of the NaI(Tl) scintillator. The energy of the photon can be measured by the summation of the charge generated in SiPM array due to interaction of optical photons generated in the scintillator due to X-rays interaction. The charge can

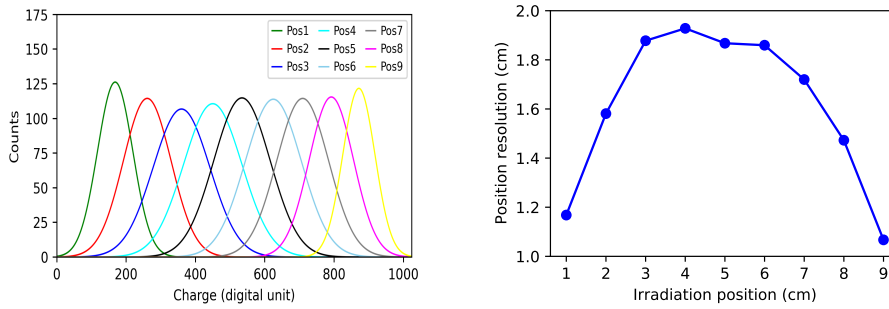


Figure 6.9: Gaussian fitted to the position histogram at different irradiation position and the FWHM of the same.

be written in terms of digital units (ADC1 and ADC2 at both the ends) and summation of which  $ADC1+ADC2$  gives the energy of the incident photon. We have measured the ADC1 and ADC2 values at both the ends of the scintillator by illuminating the scintillator by 59.5 keV  $Am^{241}$  source. The sum of the two SiPM array signals  $ADC1+ADC2$  at nine different irradiation positions of the scintillator is histogram to see the peak value and the distribution of the signal at each position. We will characterise each position with multiple X-ray sources to get the relation between the absorbed energy and the incident energy to get the energy of the any unknown incident photon by this relation.

Further, we have obtained the energy resolution at each position for 59.5 keV incident energy for the two end readout of the scintillator where each event at both the ends is recorded in co-incidence with other. First, the histogram of the  $ADC1+ADC2$  at each position is fitted with two gaussian (see Figure 6.10) where the first peak corresponds to background and second corresponds to the 59.5 keV line. We have separately measured the NaI(Tl) background spectrum where events are recorded in coincidence without illuminating the scintillator with the X-ray source. The background is over plotted as dotted Gaussian (see Figure 6.10). Further, energy resolution of the scintillator at different irradiation position is obtained by dividing the FWHM of the 59.5 keV Gaussian with the centroid value of the gaussian. The average value of the energy resolution is  $\sim 34\%$  and it degrades towards the center from either ends (see Figure 6.10). In figure 6.10 the 59.5 KeV photopeak position of the scintillator as a function of the irradiation position is shown. The peak channel is lowest at the center of

the scintillator (see Figure 6.10) because the light collection is low at the center position. Therefore, the energy resolution is poor at the center of the scintillator as shown in Figure 6.10. The background peak channel value is shown by red dotted line.

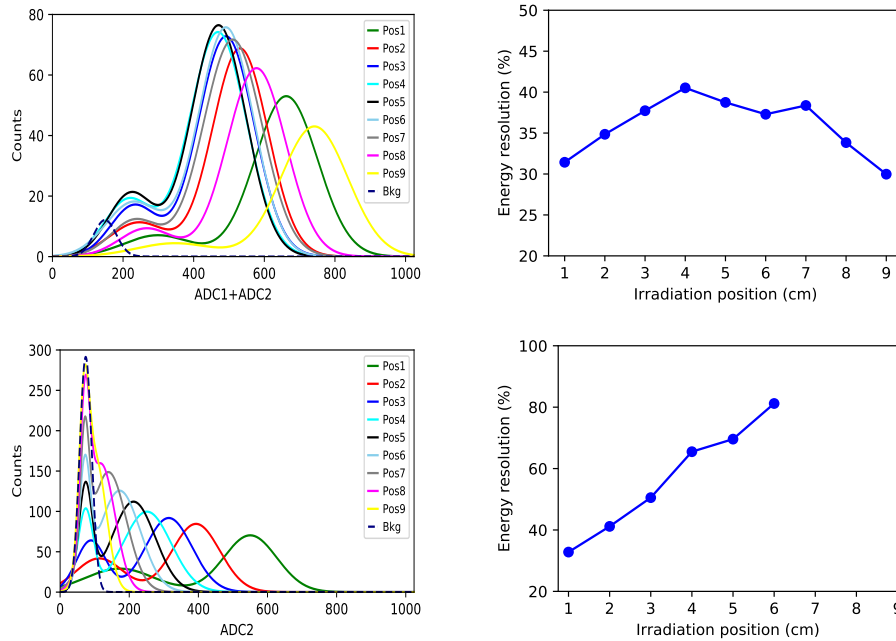


Figure 6.10: Gaussian fitted to ADC1+ADC2 histogram at different irradiation position and the energy resolution. Top panel represents two end readout plots and one end readout plots are shown in bottom panel.

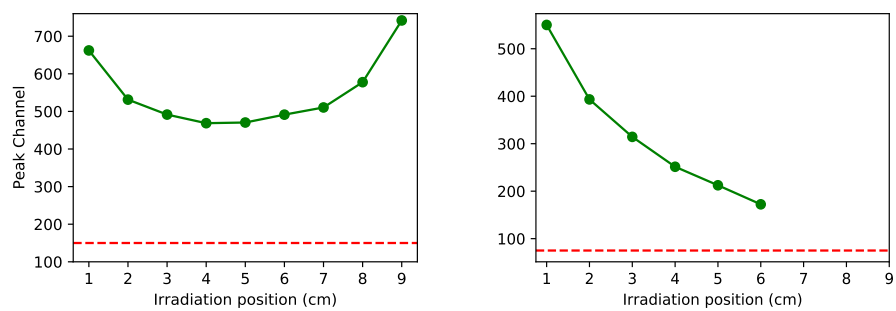


Figure 6.11: Peak channel vs irradiation position. The right figure represents one end readout and the left figure represents two end readout

We have done the similar measurements for the one end readout of the NaI(Tl) scintillator. The histogram of the ADC values is obtained for one of the end and then fitted with the two gaussians and obtained the peak value and the FWHM for the 59.5 keV line at nine irradiation positions. We have also

obtained the background spectrum for the same end (over plotted with dashed line, see Figure 6.11). The first peak (background) starts dominating after 6 cm in total counts results in the sensitive of the NaI(Tl) scintillator up to  $\sim 6$  cm (see Figure 6.11) which is slightly better than CXPOL. It is possibly due to the large width of the scintillator and light collecting area at both the ends of the scintillator. In CXPOL, CsI(Tl) scintillator was readout by the single SiPM while NaI(Tl) is readout by the array of 3 SiPMs. However, we are not able to detect photons throughout the length of the scintillator in one end readout of the scintillator. In Figure 6.10, 59.5 KeV line photopeak position of the scintillator as a function of the irradiation position is shown. The red dotted line represents the peak value of the background spectrum. The peak channel drops along the length of the scintillator (see Figure 6.10) because the light collection decreases as go far from the readout end of the scintillator and becomes very small after 6 cm. Therefore, the energy resolution is poorest at the far end of the scintillator, as shown in Figure 6.10.

#### 6.4.4.3 NaI(Tl) background

We recorded the events at both the ends of the scintillator without illuminating it with the radiation source. The background is measured at both ends in two ways. First, background counts are measured without the coincidence for 5 minute exposure. Second, background is measured in coincidence mode, with a coincidence time window of  $4.5 \mu s$ . It is found that the background at one of the ends is more in non-coincidence mode, which may be due to the gain difference of the SiPM array and leakage in the light shielding at two ends. In coincidence mode background is reduced by a factor of  $\sim 10$  (see Figure 6.12).

The polarimetric sensitivity of the polarimeter is defined in terms of MDP (Minimum Detectable Polarisation, discussed in chapter 2) which is given by,

$$MDP_{99\%} = \frac{4.29}{\mu_{100} R_{src}} \left[ \frac{R_{src} + R_{bkg}}{T} \right] \quad (6.17)$$

From the above equation it can be seen that the MDP is directly pro-

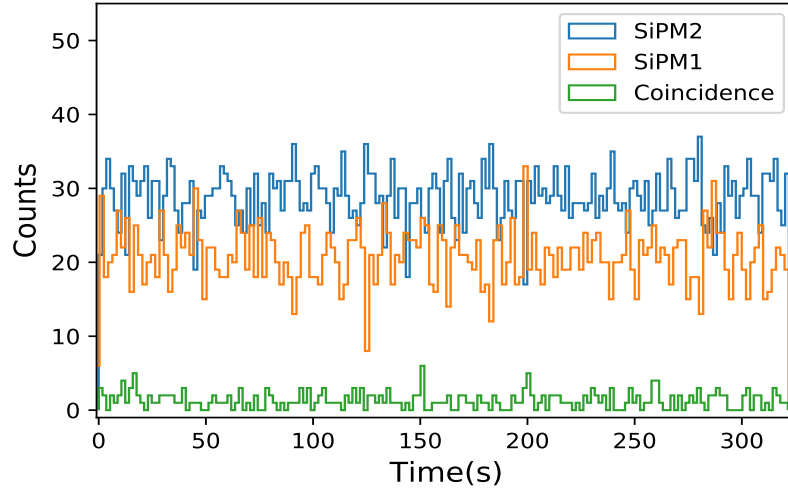


Figure 6.12: Background counts per bin (binsize-2s) in SiPM array 1 (SiPM1) represented in orange color. Blue color represents other end of the scintillator (SiPM2) and green color represents the background in coincidence mode

portional to the root of the background rate. For the CXPOL simulation results suggests the 1% MDP for the 100 mCrab source for 1Ms exposure. This can be improved by the factor of  $\sqrt[2]{10}$  due to the reduction in background in coincidence in case of two end readout. It will be further improved by the reduction in the background when the photons will be recorded in the coincidence with the scatterer also. This will improve the polarimetric sensitivity significantly.

## 6.5 Comparison with the other upcoming missions

There are number of proposed and under development missions which works above 10 keV like XL-Caliber (balloon-borne) [Abarr et al. \(2021\)](#), POLAR-2 [Kole \(2019\)](#), PING-P [Kotov et al. \(2016\)](#), PolariS [Hayashida et al. \(2014\)](#) out of which only XL-Caliber and PolariS are with focusing optics. POLAR-2 is an open GRB detector and hence, can not be directly comparable. PING-P is a hard X-ray polarimeter on the PING-M experiment, which is a satellite based mission proposed for Solar flare studies in 20 - 150 keV. Unlike our configuration, it includes three plastic scatterers surrounded by the six CsI(Tl) absorbers, hence, it can not be compared. Our configuration closely matches the XL-caliber.

It is a hard X-ray balloon-borne mission in the energy range of 15 - 80 keV. It consists of a beryllium rod as the active scatterer surrounded by the CZT pixelated detectors from the four sides. The asymmetry in the geometry is likely to introduce artificial modulation due to the inherent preferred plane for azimuthal distribution of scattered photons. However, geometric effects can be resolved by rotating the instrument with respect to the optical axis, but this requirement leads to additional complications in the realisation of the instrument. In the case of cylindrical geometry proposed here, this additional requirement is not needed due to intrinsic symmetry. Furthermore, the position of interaction in Be scatterer can not be determined due to the poor resolution of the scintillators. Therefore, position sensitive CZT detectors add further complexity in the readout system, which is not required in our case.

Unlike XL-Caliber, PolariS (Polarimetry Satellite) is a focal plane satellite based mission in the energy range of 10 - 80 keV. Here, the block ( $8 \times 8$  pillars each) of the plastic scintillator is used as the scatterer, which is read out by the multi-anode photo-multiplier tube (MAPMT). Scatterer is surrounded by eight GSO (cerium-doped gadolinium orthosilicate:  $\text{Gd}_2\text{SiO}_5:\text{Ce}$ ) scintillator block ( $4 \times 4$  pillars each) to absorb the scattered photons coming from the scatterer. The trigger logic to consider the event is when any GSO channel yields a signal. The whole configuration is installed on a motor stage to rotate (0.033 RPM) the whole configuration to minimize any geometric effect, which leads to the addition of artificial modulation. The rotation of the whole geometry and the array of several blocks of scintillators made this configuration readout and selection of events very complex. Our proposed configuration is cylindrical with position sensitive scatterer and absorber which reduces the background and gives the energy of the incident photons. It is very simple in terms of the readout and the event selection. The only complexity might come due to the asymmetry in the photon scattering due to the readout of the segmented scatterer along the length which will require the rotation of the configuration to minimize the geometric effects. Therefore, the proposed configuration is better in terms of feasibility, and in addition to that it gives simultaneous spectroscopic and polarisation information, which no other configuration provides.

## 6.6 Discussion and summary

In this work, we have given the conceptual design of the Compton spectropolarimeter where the energy of the photon is measured by knowing the scattering angle and the energy of the scattered photon. Scattering angle can be estimated by knowing the interaction position of the photon in the scatterer and the absorber. We have done the analytical calculations of the modulation factor, efficiency, and spectroscopic sensitivity of the design and characterised the one dimensional position and energy sensitivity of absorber-NaI(Tl) scintillator readout by the SiPM array at the two ends. In case of CXPOL the surrounding detectors were readout by SiPM at one end. Using the two end readout angle of scattering can be measured and the background is reduced. The two end readout of NaI(Tl) scintillator improved the following things:

- Scintillator background is reduced by 8-10 times in two end readout.
- Position of interaction can be measured within  $\sim 1.9$  cm accuracy while it is not possible in case of one end readout.
- Use of two SiPMs at two ends of a scintillator will give a better energy threshold and also give the position of interaction from the ratio of pulse heights.

In the future, we will optimize our configuration and improve the electronics to get the best possible position and energy resolution in the detector for the proposed spectro-polarimeter.



# Chapter 7

## Summary and scope for future work

### 7.1 Summary

In order to understand the geometry of the corona/jet and break the degeneracy of the multiple models in the black hole binaries, we have studied the galactic black hole binary Cygnus X-1 which is a persistent and variable source. It displays state transitions between thermal disk dominated soft state and hard state with power law dominant spectrum. It is also detected in radio wavelengths where the emission is attributed to emission from relativistic jets. During hard states, this source could be as bright as Crab, and the hard X-ray emission is mainly attributed to Compton scattering from hot corona. But there are studies that suggest a significant contribution from the jet to hard X-ray/soft gamma emission in other black hole sources ([Vadawale et al., 2001](#); [Markoff et al., 2001](#)). Polarisation signatures expected from jet and coronal emissions are different, which makes the measurement of polarisation important in probing the jet contribution in hard X-rays. We have carried out polarisation analysis for all the observations having sufficient flux and exposure in 100 - 380 keV. Polarisation results suggest that it varies based on the spectral state of the source. We have carried out the spectral analysis using the CZTI data to see any spectral dependence of polarisation. We found that the primary spectral states of Cygnus

X-1, i.e. hard and soft state are further classified into pure, transitional, and intermediate states based on the flux and spectral index correlation. In 100 - 380 keV energy range, only hard-intermediate state was found to be polarised. The polarisation components in the different spectral states can be delineated using the spectroscopy in 100 - 380 keV. We attempted to extend the spectroscopic energy range of CZTI upto 700 keV including the 20% pixels of the CZTI detector which are sensitive to higher energies due to gain shift. However, it was not possible to accurately constrain the spectral parameters, mainly because of the difficulty in estimating the correct background. Therefore, we decided to exclude the low-gain pixels and attempted the spectroscopy up to the energy of 380 keV using the polarisation events. The spectroscopy in broad energy range 30 - 380 keV suggests that there is a polarised spectral component which is state dependent. The increasing trend of the polarisation fraction with energy suggest that the contribution from the emission component having higher polarisation is dominating at higher energies. In this scenario possibly there is mixing of photons from the jet and the corona in which jet component dominates at higher energy leading to higher polarisation. All these results hint towards that the favourable geometry of the corona is sandwich corona above the thin disk and there is a bipolar jet originated from the same region. Further to delineate the polarisation contribution from the corona below 100 keV, we need the polarisation measurement of low energy Comptonised photons. However, this is not possible due to the unavailability of the dedicated polarimeter in this energy range at the moment. To find out the exact contribution of the disk, corona and jet in the polarisation, we show the need of a polarimeter below 100 keV. In this context, we have explored the feasibility of a focal plane hard X-ray spectro-polarimeter based on Compton scattering with a thin segmented plastic scatterer surrounded by the cylindrical array of Sodium Iodide (NaI) scintillator absorber. We performed the theoretical calculations for the sensitivity estimation, efficiency and characterisation of the absorber. The exhaustive results and their consequences from the work of previous chapters are described below.

In Chapter 3, a detailed analysis of polarisation measurement of black hole binary Cygnus X-1 using *AstroSat*-CZTI has been described. The estimated

polarisation is for one of the observation (ObsID 2992) when the source was in hard intermediat state is 24 %, another observation (ObsID 4646) is found to be unpolarised and polarisation estimation of remaining observations are difficult to constrain in 100 - 380 keV. Further, energy dependent polarisation measurements suggest the mixing of the corona and the jet components. It can be delineated by the broad band spectroscopy in low to high (polarisation) energy range.

In chapter 4, we have extended the spectroscopic range of CZTI using polarisation events upto 380 keV which is described in chapter 4. We have presented the method of Compton spectroscopy using *AstroSat* -CZTI beyond 100 keV. The CZTI is a coded mask imager and spectrometer having primary energy range of 20 - 100 keV. For the spectroscopy in primary energy range background measurement is done simultaneously using the mask weighting technique. Above 100 keV, the dominance of Compton scattering cross-section in CZTI results in a significant number of 2-pixel Compton events and these have been successfully utilized for polarisation analysis of Crab pulsar and nebula (and transients like Gamma-ray bursts) in 100 - 380 keV. These 2-pixel Compton events can also be used to extend the spectroscopic energy range of CZTI up to 380 keV for bright sources. However, unlike the spectroscopy in the primary energy range, where simultaneous background measurement is available from masked pixels, Compton spectroscopy requires blank sky observation for background measurement. We have described the background selection and subtraction techniques and validated them using spectroscopy of Crab in the extended energy range of 30 - 380 keV region and compare the obtained spectral parameters with the *INTEGRAL* results (Jourdain & Roques, 2009). This methodology is used to carry out broad band spectroscopy in 1 - 380 keV including the polarisation data which is discussed in next chapter (Chapter 5).

Chapter 5, presents the orbitwise spectral analysis of the observations for which polarisation analysis is done using *AstroSat*-CZTI data of Cygnus X-1 and compared it with the *INTEGRAL* (Lubiński et al., 2020). We found different spectral states based on the spectral index and flux correlation. Further to study the spectral index correlation with the rapid variability in system the power density spectrum (PDS) is generated using *AstroSat*-LAXPC data. The

3 - 80 keV power spectrum using LAXPC data required four Lorentzians in the hard state, two Lorentzians and a powerlaw in the intermediate state, and finally a single powerlaw during the soft state while fitting. We have also estimated the hard X-ray normalized fractional variability amplitude in 22 to 80 keV using the LAXPC data. We found out a decrease in the fractional variability with spectral index from hard state to hard intermediate state and again increase as moved towards the soft state. The broad band spectroscopy in the energy range of 1 - 380 keV is carried out using the SXT, LAXPC and the CZTI extended energy range (30 - 380 keV) to do the spectroscopy in broad energy range of 1 to 380 keV to decipher different spectral components of the polarisation and its dependence on different spectral states of Cygnus X-1.

Finally, in Chapter 6 we presents the conceptual design of Compton spectro-polarimeter. Since polarisation is an energy dependent quantity, therefore, to decipher the emission mechanism and region of emission of photons from the source, a polarimeter is required, which can give polarimetric and spectroscopic information simultaneously. The feasibility of Compton polarimeter in 14 to 80 keV is already established by [Chattopadhyay et al. \(2014b\)](#) using plastic scatterer and CsI absorber. Furthermore, to get a better sensitivity NaI scintillator is used in place of CsI(TI) because NaI scintillator, which has a comparatively smaller decay time constant(of the order of nanoseconds) and higher light output, can give better sensitivity. In this context, we have explored the feasibility of a focal plane hard X-ray spectro-polarimeter based on Compton scattering with a thin segmented plastic scatterer surrounded by the cylindrical array of NaI scintillator absorber. We have performed the semi-analytical calculation for the MDP, efficiency and characterization of the NaI absorber.

## 7.2 Future work

The polarisation studies along with the theoretical modelling of the black hole provides valuable insights about the geometry of the corona/jet and the strength and orientation of the magnetic field. In future, we will continue to explore the spectroscopic and polarisation studies of Cygnus X-1. We plan to expand

the spectroscopic energy range from X-rays to multi-wavelength along with the theoretical modelling. The broad band spectro-polarimetry can give insights about the coronal emission mechanism and the exact geometry of the corona. We have shown the need of Compton spectro-polarimeter in low energy range and discussed the conceptual design of it in chapter 6. Below, we have listed three projects that will be considered in the immediate future.

- *Spectro-polarimeter development*

Spectro-polarimetry of Cyg X-1 above 100 keV, predict that variable X-ray polarisation from synchrotron emitting jets and the Comptonized corona can be detected from accreting BHs by future X-ray polarimeters below 100 keV. The feasibility of Compton spectro-polarimeter is discussed in this thesis. Analytical calculations and characterisation of the absorber is done. We will continue to work on the development of the Compton spectro-polarimeter. We will characterise the absorber using different energies to get the gain calibration function so that the energy and position of any unknown energy incident photon can be known using gain calibration. Further, the characterisation of the scatterer will be done. The initial experimental setup for the energy threshold measurements of the scatterer is done in the lab. The focal plane Compton polarimeter uses long thin low-Z scatterer, typically plastic scintillator, to maximize the probability of Compton scattering. Scatterer shape, size, detection efficiency, and minimum energy measurement capability are important in deciding the polarimeter's sensitivity. The Lower energy threshold value improves the MDP (minimum detectable polarisation) by decreasing the low energy detection limit, which results in increase in the source count. The MDP scales with source count; hence, polarimetric sensitivity will improve.

$$\Delta E = E - \frac{E}{1 + \frac{E}{m_e c^2} (1 - \cos \theta)} \quad (7.1)$$

In order to have a better understanding of the behavior of the scatterer for very low energy deposition, we will carry out a controlled Compton

scattering experiment with the plastic scatterer. It can be done by measuring the energy of Compton scattered photons by the plastic scintillator for different scattering angles. Energy deposition depends upon the incident photon energy and the angle of scattering (see equation 7.1). Energy deposition will be least for a particular scattering angle. The precise energy measurement of the scattered photon can be done by the standard X-123CdTe system from Amptek. By comparing the energy of the incident photon and scattered photon, we can estimate the energy deposition in the plastic scintillator. Thus we can get the detection threshold of the plastic scintillator. This method is well established by [Chattopadhyay et al. \(2014b\)](#).

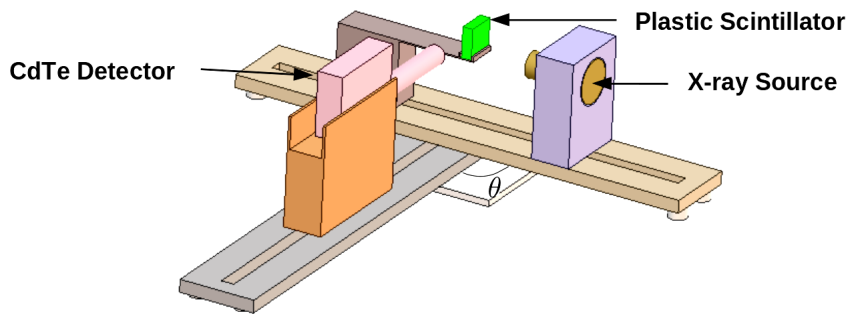


Figure 7.1: Scatterer energy threshold measurement mechanical setup CAD model.

We have done the initial experimental setup for measuring the energy threshold of the square shape plastic scintillator readout by the SiPM array. The final experiment still needs to be done. We have used SiPM instead of PMT or MAPMT due to its compactness and is not affected by the external magnetic field, unlike the PMT and MAPMT. The electronics will be complicated, and the SiPM higher background can affect the low energy detection limit of the plastic scatterer. There is a trade-off between the two. The experimental setup and the related electronics is described below.

The experimental setup consists of X-ray source, Plastic scintillator (24x24x5 mm), SiPM array (6x1), AMPTEK X123 CdTe detector to measure the energy of the scattered photon (see Figure 7.1). It is a complete

package of MCA along with DPP (Digital pulse processor). The axis of the CdTe is hinged on the axis of the scintillator and X-ray source so that it can rotate to vary the detection angle. The axis of hing should pass through the middle of the scintillator. The line of intersection of the plane passing through the CdTe, X-ray source, and hing should pass through the middle of the scintillator for better alignment. A similar experiment is done earlier by [Fabiani et al. \(2013\)](#). Angular degree of freedom is introduced by [Chattopadhyay et al. \(2014b\)](#) to measure the scattered photon energy at different angles. We have developed a similar setup.

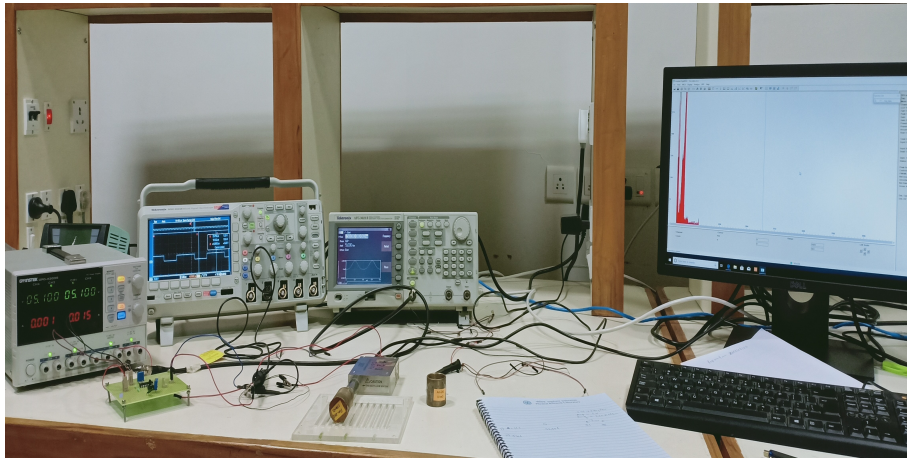


Figure 7.2: Coincidence between the CdTe and the pulse generator experimental setup

The SiPM reads out the plastic scintillator, and the PRE-AMP pre-amplifies the output signal because it is a weak signal for further analysis. The output of PRE-AMP is not a well-shaped signal to detect the peak. It is fed to the CR-RC shaper to make it a gaussian pulse to reduce the dead time and to get the required information. AMPTEK X123 CdTe has a different dead time. Its pulse width is approx.  $3 \mu s$ , so any input signal less than this will be ignored. We need a coincident unit between the shaper and CdTe detector to measure the energy of the Compton scattered photon, not the other source photons. A monostable multivibrator is connected between the comparator and CdTe detector Gate input for the coincidence. The output pulse width of the multivibrator can vary from  $1 \mu s$  to  $20 \mu s$ . We can optimize it according to the CdTe's dead time and

the count rate of the scattered photons. The actual experiment with the cylindrical plastic scatterer will be done in future.

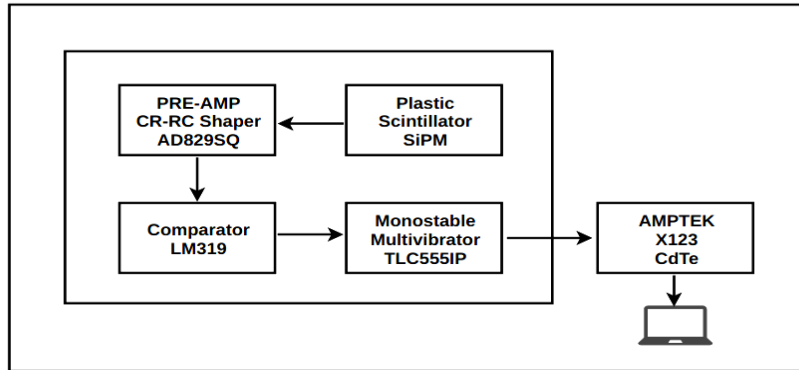


Figure 7.3: Readout electronics

- *Long-term spectro-polarimetry of Cygnus X-1*

The long-term spectro-polarimetry of Cygnus X-1 using the seven years of AstroSat data could help understand the system's emission mechanism and geometry in detail. It will help identify the long-term variation of the polarisation and polarisation angle as well as any correlation between the different states and geometry of the system. We have already discussed the polarisation results and its spectral state dependence in Chapter 3 and 5. We observed very high polarisation in IMH with maximum radio flux variation while in PH and IMS spectral states, on the other hand, there is no evidence of polarization from the jet component ( $\sim 10\%$  upper limit), though steady radio emission is seen in these states. In the PH state of Cygnus X-1, the radio flux and its variation, in general, are found to be low (Lubiński et al., 2020). On the other hand, the radio flux decreases as the source transitions from IMH to IMS state. One can, therefore, assume that the X-ray emission is primarily dominated by the coronal emission even at very high energies in these states, unlike in the IMH state which is dominated by the jet emission. Observationally, a detailed time-resolved polarimetry of Cygnus X-1 would be instrumental in understanding long term behaviour of the polarisation in different states. By our theory, we

expect maximum polarisation in the intermediate hard state, low in the hard state, and lowest in the soft state due to low or no jet contribution (see Figure 7.4). We will use 7 years CZTI data of Cygnus X-1 for the detailed polarisation analysis using Stokes parameter method.

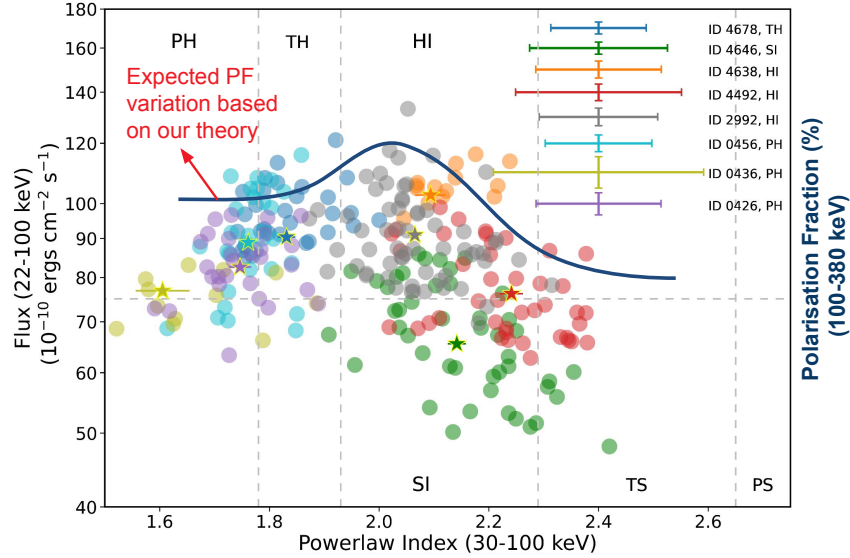
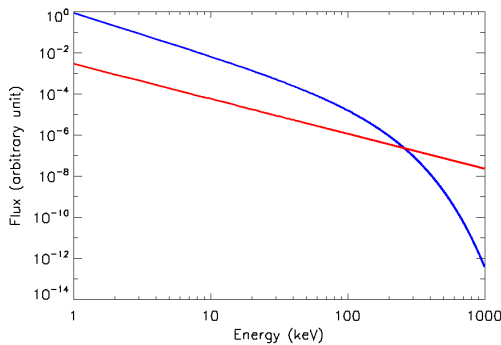


Figure 7.4: Flux and spectral index correlation overplotted with the expected polarisation fraction (blue solid line) variation in Cygnus X-1

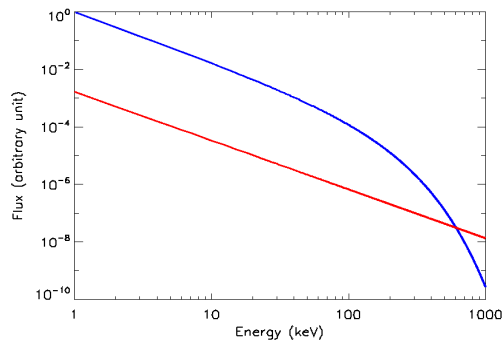
- *Jet modelling: Cygnus X-1*

The polarised synchrotron emission from the jet depends upon the orientation and strength of the magnetic field in the jet (Russell et al., 2014). The theoretical modelling of the jet emission is important to understand the magnetic field structure and strength at different energies that can explain the synchrotron polarisation from the jet. This may help to understand the overall geometry and contribution of the jet in the polarised emission. We have tried modelling the polarisation using the AstroSat, IXPE, and POGO+ polarisation measurements in X-rays. The contribution of the jet (Synchrotron emission) in the total flux is defined by powerlaw and the coronal emission by the cutoff powerlaw. The maximum possible polarisation from the Synchrotron jet is 70% and polarisation from the Comptonised emission from the Corona is considered varying linearly starting from 1% up to 8% (Krawczynski et al., 2022). The polarisation angle for

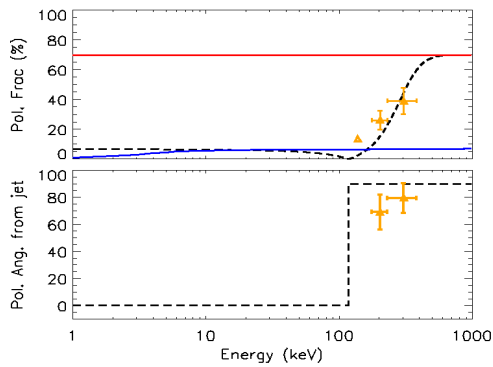
the Corona is parallel to radio jet (Krawczynski et al., 2022) and angle for the Synchrotron jet is perpendicular to the radio jet (Jourdain et al., 2012a). Therefore, PA in both cases are considered orthogonal to each other in the modelling. The mixing of the two emission at each energy gives the final spectrum. The modulation curves for both the spectra are calculated and finally the polarisation fraction and polarisation angle are obtained by sinusoidal curve fitting of the summation of the two modulation curves.



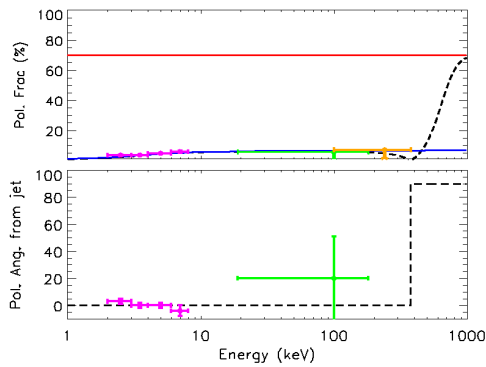
(a) Corona and jet spectrum in IMH state shown by blue and red color respectively.



(b) Corona and jet spectrum in PH state shown by blue and red color respectively.



(c) IMH state-top panel shows the PF with energy. Blue and red solid line represents the Corona (scattering) and jet (synchrotron) polarisation fraction. Dashed black line represents the modelled polarisation fraction. Bottom panel: shows the polarisation angle with energy. Dashed black line represents the modelled polarisation angle. The PF and PA measured using CZTI are shown in orange color.



(d) PH state-top panel shows the PF with energy. Blue and red solid line represents the Corona (scattering) and jet (synchrotron) polarisation fraction. Dashed black line represents the modelled polarisation fraction. Bottom panel: shows the polarisation angle with energy. Dashed black line represents the modelled polarisation angle. The pink and green color shows the IXPE and POGO+ measurements respectively. CZTI upperlimit is shown in orange.

We are able to model both Intermediate hard state AstroSat measurements as well as IXPE and POGO+ results (see Figure 7.5d) in Pure hard state

Table 7.1: Model parameter values.

State	Parameter	Value	
		Corona	Jet
IMH	Powerlaw index	2.06	1.7
	Efold (keV)	70	-
	Norm	1	1/300
	PF (%) (max)	8	70
PH	Powerlaw index	1.75	1.7
	Efold (keV)	100	-
	Norm	0.87	0.87/600
	PF (%) (max)	8 )	70

except except slight difference in the polarisation angle (see Figure 7.5c). The parameters and the values are given in Table 7.1. In future, we will try to include radio, optical, IR, and gamma rays polarisation measurements in the broad band modelling.

- *Simultaneous spectro-polarimetry of Cygnus X-1 in different spectral states*

The simultaneous spectro-polarimetry in different spectral states using multi-wavelength observations can help in understanding how accretion onto the BHs can result in the launching of relativistic jets, different corona geometry, and the magnetic field structure of the jet. The polarisation modeling using the existing observational results predicts the highly ordered magnetic field of the jet of the Cygnus X-1, unlike the other BHBs and AGNs having predominantly tangled magnetic field (Russell et al., 2014).

We plan to simultaneously observe the source using existing X-ray polarimeters like IXPE, CZTI, and INTEGRAL and the upcoming Indian facility, POLIX, along with ground-based telescopes, including radio observations. This will help in understanding the relative contribution of the disk, corona, and jet in polarisation in different energy ranges. It will also help in understanding the geometry of the corona in different spectral states of the source.



# Bibliography

- Abarr, Q., Awaki, H., Baring, M. G., et al. 2021, *Astroparticle Physics*, 126, 102529 [Cited on page 173.]
- Abramowicz, M. A., & Fragile, P. C. 2013, *Living Reviews in Relativity*, 16, 1 [Cited on page 8.]
- Agrawal, P. C., Yadav, J. S., Antia, H. M., et al. 2017, *Journal of Astrophysics and Astronomy*, 38, 30 [Cited on page 140.]
- Antia, H. M., Agrawal, P. C., Katoch, T., et al. 2022, arXiv e-prints, arXiv:2205.03136 [Cited on pages 74, 82, 101, and 121.]
- Antia, H. M., Yadav, J. S., Agrawal, P. C., et al. 2017, *The Astrophysical Journal Supplement Series*, 231, 10 [Cited on pages 48 and 141.]
- Arnaud, K. 1996, in *Astronomical Data Analysis Software and Systems V*, Vol. 101, 17 [Cited on pages 123, 136, and 145.]
- Arnaud, K., Smith, R., & Siemiginowska, A. 2011, *Handbook of X-ray Astronomy* [Cited on page 48.]
- Arnaud, K. A. 1996, in *Astronomical Society of the Pacific Conference Series*, Vol. 101, *Astronomical Data Analysis Software and Systems V*, ed. G. H. Jacoby & J. Barnes, 17 [Cited on page 55.]
- Ashley, J. C., Tung, C. J., Ritchie, R. H., & Anderson, V. E. 1976, *IEEE Transactions on Nuclear Science*, 23, 1833 [Cited on page 68.]
- Axelsson, M., Borgonovo, L., & Larsson, S. 2005, *Astronomy & Astrophysics*, 438, 999 [Cited on pages 38 and 141.]

- Baade, W., & Zwicky, F. 1934, *Physical Review*, 46, 76 [Cited on page 7.]
- Balbus, S. A., & Hawley, J. F. 1991, *The Astrophysical Journal*, 376, 214 [Cited on pages 3 and 18.]
- Bambi, C. 2018, *Annalen der Physik*, 530, 1700430 [Cited on page 8.]
- Bambi, C., Cárdenas-Avendaño, A., Dauser, T., García, J. A., & Nampalliwar, S. 2017, *The Astrophysical Journal*, 842, 76 [Cited on page 8.]
- Bambi, C., Jiang, J., & Steiner, J. F. 2016, *Classical and Quantum Gravity*, 33, 064001 [Cited on page 8.]
- Barthelmy, S. D., Barbier, L. M., Cummings, J. R., et al. 2005, *Space Science Reviews*, 120, 143 [Cited on pages 53 and 78.]
- Bellazzini, R., Spandre, G., Minuti, M., et al. 2007, *Nuclear Instruments and Methods in Physics Research A*, 579, 853 [Cited on page 69.]
- Belloni, T., Klein-Wolt, M., Méndez, M., van der Klis, M., & van Paradijs, J. 2000, *Astronomy & Astrophysics*, 355, 271 [Cited on page 14.]
- Belloni, T., Psaltis, D., & van der Klis, M. 2002, *The Astrophysical Journal*, 572, 392 [Cited on page 62.]
- Belloni, T. M. 2010a, *States and Transitions in Black Hole Binaries*, ed. T. Belloni, Vol. 794, 53 [Cited on pages xv and 18.]
- . 2010b, in *Lecture Notes in Physics*, Berlin Springer Verlag, ed. T. Belloni, Vol. 794, 53 [Cited on pages xvi and 38.]
- Belloni, T. M., & Motta, S. E. 2016, *Transient Black Hole Binaries*, ed. C. Bambi, Vol. 440 (Springer), 61 [Cited on pages xv and 23.]
- Belloni, T. M., Motta, S. E., & Muñoz-Darias, T. 2011, *Bulletin of the Astronomical Society of India*, 39, 409 [Cited on pages xvi and 27.]
- Bernard, D., Chattopadhyay, T., Kislak, F., & Prodit, N. 2022, arXiv e-prints, arXiv:2205.02072 [Cited on page 81.]

- Bhalerao, V., Bhattacharya, D., Vibhute, A., et al. 2017a, *Journal of Astrophysics and Astronomy*, 38, 31 [Cited on page 48.]
- . 2017b, *Journal of Astrophysics and Astronomy*, 38, 31 [Cited on page 50.]
- Black, J. K., Baker, R. G., Deines-Jones, P., Hill, J. E., & Jahoda, K. 2007, *Nuclear Instruments and Methods in Physics Research A*, 581, 755 [Cited on page 69.]
- Bolton, C. T. 1972, *Nature*, 235, 271 [Cited on pages 8 and 36.]
- Bombaci, I. 1996, *Astronomy & Astrophysics*, 305, 871 [Cited on page 7.]
- Bowyer, S., Byram, E. T., Chubb, T. A., & Friedman, H. 1965, *Science*, 147, 394 [Cited on page 36.]
- Burrows, D. N., Hill, J. E., Nousek, J. A., et al. 2005, *Space Science Reviews*, 120, 165 [Cited on page 53.]
- Buzhan, P., Dolgoshein, B., Ilyin, A., et al. 2002, in *Advanced Technology - Particle Physics*, ed. M. Barone, E. Borchini, J. Huston, C. Leroy, P. G. Rancoita, P. Riboni, & R. Ruchti, 717–728 [Cited on page 154.]
- Buzhan, P., Dolgoshein, B., Filatov, L., et al. 2003, *Nuclear Instruments and Methods in Physics Research A*, 504, 48 [Cited on page 154.]
- Campana, R. 2022, arXiv e-prints, arXiv:2205.09359 [Cited on pages 73 and 116.]
- Casella, P., Belloni, T., Homan, J., & Stella, L. 2004, *Astronomy & Astrophysics*, 426, 587 [Cited on page 17.]
- Casella, P., Belloni, T., & Stella, L. 2005, *The Astrophysical Journal*, 629, 403 [Cited on page 17.]
- Celotti, A., Miller, J. C., & Sciama, D. W. 1999, *Classical and Quantum Gravity*, 16, A3 [Cited on page 8.]
- Chandrasekhar, S. 1931, *The Astrophysical Journal*, 74, 81 [Cited on page 7.]

- Chattopadhyay, T. 2021, *Journal of Astrophysics and Astronomy*, 42, 106 [Cited on pages 40 and 81.]
- Chattopadhyay, T., Vadawale, S. V., & Pendharkar, J. 2013, *Experimental Astronomy*, 35, 391 [Cited on page 160.]
- Chattopadhyay, T., Vadawale, S. V., Rao, A. R., et al. 2016, in *Society of Photo-Optical Instrumentation Engineers (SPIE) Conference Series*, Vol. 9905, *Space Telescopes and Instrumentation 2016: Ultraviolet to Gamma Ray*, ed. J.-W. A. den Herder, T. Takahashi, & M. Bautz, 99054D [Cited on pages 123 and 130.]
- Chattopadhyay, T., Vadawale, S. V., Rao, A. R., Sreekumar, S., & Bhattacharya, D. 2014a, *Experimental Astronomy*, 37, 555 [Cited on pages 50, 72, 78, 81, and 116.]
- Chattopadhyay, T., Vadawale, S. V., Shanmugam, M., & Goyal, S. K. 2014b, *Astrophysical Journal Supplement*, 212, 12 [Cited on pages 152, 153, 154, 169, 180, 182, and 183.]
- Chattopadhyay, T., Vadawale, S. V., Aarthy, E., et al. 2019, *The Astrophysical Journal*, 884, 123 [Cited on pages 72, 74, 78, 85, 88, and 116.]
- Chattopadhyay, T., Gupta, S., Sharma, V., et al. 2021, *Journal of Astrophysics and Astronomy*, 42, 82 [Cited on pages 96 and 107.]
- Chattopadhyay, T., Gupta, S., Iyyani, S., et al. 2022, *The Astrophysical Journal*, 936, 12 [Cited on page 130.]
- Chauvin, M., Florén, H. G., Friis, M., et al. 2018, *Nature Astronomy*, 2, 652 [Cited on pages 32 and 41.]
- Chauvin, M., Florén, H.-G., Jackson, M., et al. 2019, *Monthly Notices of Royal Astronomical Society*, 483, L138 [Cited on pages 40 and 41.]
- Chib, S., & Greenberg, E. 1995, *The American Statistician*, 49, 327 [Cited on page 84.]

- Chitnis, V. R., Rao, A. R., & Agrawal, P. C. 1998, *Astronomy & Astrophysics*, 331, 251 [Cited on page 146.]
- Connors, P. A., Piran, T., & Stark, R. F. 1980, *The Astrophysical Journal*, 235, 224 [Cited on pages 31 and 62.]
- Coppi, P. S. 1999, in *Astronomical Society of the Pacific Conference Series*, Vol. 161, *High Energy Processes in Accreting Black Holes*, ed. J. Poutanen & R. Svensson, 375 [Cited on pages 20, 29, and 42.]
- Coriat, M., Corbel, S., Prat, L., et al. 2011, *Monthly Notices of Royal Astronomical Society*, 414, 677 [Cited on page 26.]
- Costa, E., Soffitta, P., Bellazzini, R., et al. 2001, *Nature*, 411, 662 [Cited on page 69.]
- Cui, W., Heindl, W. A., Rothschild, R. E., et al. 1997a, *The Astrophysical Journal Letters*, 474, L57 [Cited on pages 17 and 133.]
- Cui, W., Heindl, W. A., Swank, J. H., et al. 1997b, *The Astrophysical Journal Letters*, 487, L73 [Cited on page 17.]
- Cui, W., Zhang, S. N., Focke, W., & Swank, J. H. 1997c, *The Astrophysical Journal*, 484, 383 [Cited on pages 17 and 142.]
- Cunningham, C. 1976, *The Astrophysical Journal*, 208, 534 [Cited on page 8.]
- Done, C. 2010, arXiv e-prints, arXiv:1008.2287 [Cited on pages xv, 19, 20, and 21.]
- Done, C., Gierliński, M., & Kubota, A. 2007, *The Astronomy and Astrophysics Review*, 15, 1 [Cited on pages 8 and 20.]
- Dovčiak, M., Muleri, F., Goosmann, R. W., Karas, V., & Matt, G. 2008, *Monthly Notices of Royal Astronomical Society*, 391, 32 [Cited on pages 31, 33, and 35.]
- . 2011, *The Astrophysical Journal*, 731, 75 [Cited on pages xvi, 34, and 35.]

- Dovčiak, M., Muleri, F., Goosmann, R. W., Karas, V., & Matt, G. 2012, in *Journal of Physics Conference Series*, Vol. 372, *Journal of Physics Conference Series*, 012056 [Cited on pages xvi, 32, 34, and 35.]
- Dubus, G., Hameury, J. M., & Lasota, J. P. 2001, *Astronomy & Astrophysics*, 373, 251 [Cited on page 15.]
- Eddington, A. S. 1924, *Nature*, 113, 192 [Cited on page 7.]
- Elvis, M., Page, C. G., Pounds, K. A., Ricketts, M. J., & Turner, M. J. L. 1975, *Nature*, 257, 656 [Cited on page 23.]
- Fabian, A., Pringle, J., & Whelan, J. 1974, *Nature*, 247, 351 [Cited on page 36.]
- Fabian, A. C., Iwasawa, K., Reynolds, C. S., & Young, A. J. 2000, *Publications of the Astronomical Society of the Pacific*, 112, 1145 [Cited on page 8.]
- Fabian, A. C., Rees, M. J., Stella, L., & White, N. E. 1989, *Monthly Notices of Royal Astronomical Society*, 238, 729 [Cited on pages 8 and 30.]
- Fabiani, S., Campana, R., Costa, E., et al. 2013, *Astroparticle Physics*, 44, 91 [Cited on page 183.]
- Fender, R. 2010, in *Lecture Notes in Physics*, Berlin Springer Verlag, ed. T. Belloni, Vol. 794, 115 [Cited on page 26.]
- Fender, R., & Belloni, T. 2004, *Annual Review of Astronomy and Astrophysics*, 42, 317 [Cited on page 26.]
- Fender, R., & Muñoz-Darias, T. 2016, in *Lecture Notes in Physics*, Berlin Springer Verlag, ed. F. Haardt, V. Gorini, U. Moschella, A. Treves, & M. Colpi, Vol. 905, 65 [Cited on page 133.]
- Fender, R. P., Homan, J., & Belloni, T. M. 2009, *Monthly Notices of Royal Astronomical Society*, 396, 1370 [Cited on page 26.]
- Fender, R. P., Stirling, A. M., Spencer, R. E., et al. 2006, *Monthly Notices of Royal Astronomical Society*, 369, 603 [Cited on page 38.]

- Filothodoros, A., Lubiński, P., & Zdziarski, A. A. 2018, in XXXVIII Polish Astronomical Society Meeting, ed. A. Ró&zańska, Vol. 7, 326–329 [Cited on page 133.]
- Finkelstein, D. 1958, *Physical Review*, 110, 965 [Cited on page 7.]
- Forman, W., Jones, C., Cominsky, L., et al. 1978, *The Astrophysical Journal Supplement Series*, 38, 357 [Cited on pages 1 and 46.]
- Frank, J., King, A., & Raine, D. J. 2002, *Accretion Power in Astrophysics: Third Edition* (Cambridge University Press, Cambridge, UK) [Cited on pages 2 and 14.]
- Friedman, H., Lichtman, S. W., & Byram, E. T. 1951, *Physical Review*, 83, 1025 [Cited on page 45.]
- Friend, D. B., & Castor, J. I. 1982, *The Astrophysical Journal*, 261, 293 [Cited on page 39.]
- Gallo, E., Fender, R. P., Miller-Jones, J. C. A., et al. 2006, *Monthly Notices of Royal Astronomical Society*, 370, 1351 [Cited on page 27.]
- Garcia, J., & Kallman, T. R. 2010, *The Astrophysical Journal*, 718, 695 [Cited on page 60.]
- García, J., Dauser, T., Lohfink, A., et al. 2014, *The Astrophysical Journal*, 782, 76 [Cited on page 60.]
- Gehrels, N., Chincarini, G., Giommi, P., et al. 2004, *The Astrophysical Journal*, 611, 1005 [Cited on page 52.]
- George, I. M., & Fabian, A. C. 1991, *Monthly Notices of Royal Astronomical Society*, 249, 352 [Cited on page 21.]
- Geyer, C. J. 2011, In *Handbook of Markov Chain Monte Carlo*. Chapman & Hall/CRC [Cited on page 84.]
- Giacconi, R., Gorenstein, P., Gursky, H., & Waters, J. R. 1967, *The Astrophysical Journal Letters*, 148, L119 [Cited on page 8.]

- Giacconi, R., Gursky, H., Kellogg, E., Schreier, E., & Tananbaum, H. 1971a, *The Astrophysical Journal Letters*, 167, L67 [Cited on page 46.]
- Giacconi, R., Gursky, H., Paolini, F. R., & Rossi, B. B. 1962, *Physical Review Letters*, 9, 439 [Cited on pages 8 and 45.]
- Giacconi, R., Kellogg, E., Gorenstein, P., Gursky, H., & Tananbaum, H. 1971b, *The Astrophysical Journal Letters*, 165, L27 [Cited on page 46.]
- Gierliński, M., Done, C., & Page, K. 2008, *Monthly Notices of Royal Astronomical Society*, 388, 753 [Cited on page 5.]
- Gierliński, M., Maciołek-Niedźwiecki, A., & Ebisawa, K. 2001, *Monthly Notices of Royal Astronomical Society*, 325, 1253 [Cited on page 30.]
- Gierlinski, M., Zdziarski, A. A., Done, C., et al. 1997, *Monthly Notices of Royal Astronomical Society*, 288, 958 [Cited on page 146.]
- Gierliński, M., Zdziarski, A. A., Poutanen, J., et al. 1999, *Monthly Notices of Royal Astronomical Society*, 309, 496 [Cited on page 133.]
- Gies, D. R., & Bolton, C. T. 1986, *The Astrophysical Journal*, 304, 371 [Cited on page 37.]
- Gilfanov, M. 2010, X-Ray Emission from Black-Hole Binaries, ed. T. Belloni, Vol. 794, 17 [Cited on pages xvii and 58.]
- Gleissner, T., Wilms, J., Pooley, G. G., et al. 2004, *Astronomy & Astrophysics*, 425, 1061 [Cited on page 133.]
- Gou, L., McClintock, J. E., Remillard, R. A., et al. 2014, *The Astrophysical Journal*, 790, 29 [Cited on page 38.]
- Greenstein, J. L. 1963, *Nature*, 197, 1041 [Cited on page 7.]
- Greenstein, J. L., & Schmidt, M. 1964, *The Astrophysical Journal*, 140, 1 [Cited on page 7.]

- Grinberg, V., Hell, N., Pottschmidt, K., et al. 2013a, *Astronomy & Astrophysics*, 554, A88 [Cited on page 37.]
- . 2013b, *Astronomy & Astrophysics*, 554, A88 [Cited on page 142.]
- Harrison, F. A., Craig, W. W., Christensen, F. E., et al. 2013, *The Astrophysical Journal*, 770, 103 [Cited on pages xvii, 53, and 54.]
- Hastings, W. K. 1970, *Biometrika*, 57, 97 [Cited on page 84.]
- Haug, E., & Nakel, W. 2004, The Elementary Process of Bremsstrahlung, doi:10.1142/5371 [Cited on page 28.]
- Hayashida, K., Yonetoku, D., Gunji, S., et al. 2014, in Society of Photo-Optical Instrumentation Engineers (SPIE) Conference Series, Vol. 9144, Society of Photo-Optical Instrumentation Engineers (SPIE) Conference Series, 0 [Cited on page 173.]
- Heitler, W. 1954, Quantum theory of radiation [Cited on page 68.]
- Hewish, A., Bell, S. J., Pilkington, J. D. H., Scott, P. F., & Collins, R. A. 1968, *Nature*, 217, 709 [Cited on page 8.]
- Homan, J., & Belloni, T. 2005, *Astrophysics and Space Science*, 300, 107 [Cited on page 26.]
- Homan, J., Wijnands, R., van der Klis, M., et al. 2001, *The Astrophysical Journal Supplement Series*, 132, 377 [Cited on page 24.]
- Huang, K. 1987, *Statistical Mechanics*, 2nd Edition [Cited on page 10.]
- Jourdain, E., & Roques, J. P. 2009, *The Astrophysical Journal*, 704, 17 [Cited on pages 111, 123, 124, and 179.]
- . 2020, *The Astrophysical Journal*, 899, 131 [Cited on page 97.]
- Jourdain, E., Roques, J. P., Chauvin, M., & Clark, D. J. 2012a, *Astrophysical Journal*, 761, 27 [Cited on pages 40 and 186.]

- Jourdain, E., Roques, J. P., & Malzac, J. 2012b, *The Astrophysical Journal*, 744, 64 [Cited on pages xvi, 37, and 39.]
- Kaaret, P. 2014, arXiv:1408.5899 [Cited on page 64.]
- Kaaret, P., Feng, H., & Roberts, T. P. 2017, *Annual Review of Astronomy and Astrophysics*, 55, 303 [Cited on page 1.]
- Kalemci, E., Tomsick, J. A., Rothschild, R. E., et al. 2006, *The Astrophysical Journal*, 639, 340 [Cited on page 27.]
- Kalogera, V., & Baym, G. 1996, *The Astrophysical Journal Letters*, 470, L61 [Cited on page 7.]
- Kashyap, V. L., van Dyk, D. A., Connors, A., et al. 2010, *The Astrophysical Journal*, 719, 900 [Cited on pages 85 and 86.]
- Kass, R. E., & Raftery, A. E. 1995, *Journal of the American Statistical Association*, 90, 773 [Cited on page 88.]
- Kazanas, D., Hua, X.-M., & Titarchuk, L. 1997, *The Astrophysical Journal*, 480, 735 [Cited on page 17.]
- Kirsch, M. G., Briel, U. G., Burrows, D., et al. 2005, in *Society of Photo-Optical Instrumentation Engineers (SPIE) Conference Series*, Vol. 5898, UV, X-Ray, and Gamma-Ray Space Instrumentation for Astronomy XIV, ed. O. H. W. Siegmund, 22–33 [Cited on page 97.]
- Knoll, G. F. 2000, *Radiation detection and measurement* [Cited on page 48.]
- Kole, M. 2019, in *International Cosmic Ray Conference*, Vol. 36, 36th International Cosmic Ray Conference (ICRC2019), 572 [Cited on page 173.]
- Kormendy, J., & Ho, L. C. 2013, *Annual Review of Astronomy and Astrophysics*, 51, 511 [Cited on page 8.]
- Kormendy, J., & Richstone, D. 1995, *Annual Review of Astronomy and Astrophysics*, 33, 581 [Cited on page 8.]

- Kotov, Y., Yurov, V., Glyanenko, A., et al. 2016, *Advances in Space Research*, 58, 635 [Cited on page 173.]
- Krawczynski, H., Garson, A., Guo, Q., et al. 2011, *Astroparticle Physics*, 34, 550 [Cited on page 70.]
- Krawczynski, H., Muleri, F., Dovčiak, M., et al. 2022, arXiv e-prints, arXiv:2206.09972 [Cited on pages 151, 185, and 186.]
- Kuiper, L., Hermsen, W., Cusumano, G., et al. 2001, *Astronomy & Astrophysics*, 378, 918 [Cited on page 97.]
- Kumar, A., Chattopadhyay, T., Vadawale, S. V., et al. 2021, arXiv e-prints, arXiv:2102.13593 [Cited on page 82.]
- . 2022, arXiv e-prints, arXiv:2208.11476 [Cited on page 82.]
- Laplace, P. S. 1799, *Allgemeine Geographische Ephemeriden*, 4, 1 [Cited on page 6.]
- Lasota, J.-P. 2001, *New Astronomy Reviews*, 45, 449 [Cited on page 14.]
- Laurent, P., Rodriguez, J., Wilms, J., et al. 2011, *Science*, 332, 438 [Cited on pages 36 and 40.]
- Leahy, D. A., Darbro, W., Elsner, R. F., et al. 1983, *The Astrophysical Journal*, 266, 160 [Cited on page 61.]
- Lei, F., Dean, A. J., & Hills, G. L. 1997, *Space Science Reviews*, 82, 309 [Cited on pages 28, 64, and 81.]
- Lewin, W. H. G., & Livingston, W. 1995, *Journal of the British Astronomical Association*, 105, 284 [Cited on page 1.]
- Li, L.-X., Narayan, R., & McClintock, J. E. 2009, *The Astrophysical Journal*, 691, 847 [Cited on page 31.]
- Ling, J. C., & Wheaton, W. A. 2003, *The Astrophysical Journal*, 598, 334 [Cited on page 123.]

- Llopart, X., Ballabriga, R., Campbell, M., Tlustos, L., & Wong, W. 2007, *Nuclear Instruments and Methods in Physics Research A*, 581, 485 [Cited on page 68.]
- Long, K. S., Chanan, G. A., & Novick, R. 1980, *The Astrophysical Journal*, 238, 710 [Cited on page 40.]
- Longair, M. S. 2011, *High Energy Astrophysics* [Cited on page 11.]
- Lubiński, P., Filothodoros, A., Zdziarski, A. A., & Pooley, G. 2020, *The Astrophysical Journal*, 896, 101 [Cited on pages xxii, xxvi, 93, 94, 133, 136, 137, 138, 139, 140, 148, 149, 179, and 184.]
- Lynden-Bell, D. 1969, *Nature*, 223, 690 [Cited on page 7.]
- Magdziarz, P., & Zdziarski, A. A. 1995, *Monthly Notices of Royal Astronomical Society*, 273, 837 [Cited on page 60.]
- Malzac, J. 2018, *Nature Astronomy*, 2, 623 [Cited on pages xvi and 32.]
- Markoff, S., Falcke, H., & Fender, R. 2001, *Astronomy & Astrophysics*, 372, L25 [Cited on pages 5, 36, and 177.]
- Matt, G., Perola, G. C., & Piro, L. 1991, *Astronomy & Astrophysics*, 247, 25 [Cited on page 34.]
- McClintock, J. E., Narayan, R., & Steiner, J. F. 2014, *Space Science Reviews*, 183, 295 [Cited on page 38.]
- McClintock, J. E., Shafee, R., Narayan, R., et al. 2006, *The Astrophysical Journal*, 652, 518 [Cited on pages 8, 14, and 30.]
- McClintock, J. E., Narayan, R., Davis, S. W., et al. 2011, *Classical and Quantum Gravity*, 28, 114009 [Cited on page 30.]
- McConnell, M. L., Ryan, J. M., Smith, D. M., Lin, R. P., & Emslie, A. G. 2002, *Solar Physics*, 210, 125 [Cited on pages xvi and 39.]

- Meszaros, P., Novick, R., Szentgyorgyi, A., Chanan, G. A., & Weisskopf, M. C. 1988, *Astrophysical Journal*, 324, 1056 [Cited on page 28.]
- Michel, T., & Durst, J. 2008, *Nuclear Instruments and Methods in Physics Research Section A: Accelerators, Spectrometers, Detectors and Associated Equipment*, 594, 188 [Cited on page 68.]
- Michell, J. 1784, *Philosophical Transactions of the Royal Society of London Series I*, 74, 35 [Cited on page 6.]
- Miller, J. M. 2007, *Annual Review of Astronomy and Astrophysics*, 45, 441 [Cited on page 30.]
- Miller-Jones, J. C. A., Bahramian, A., Orosz, J. A., et al. 2021, *Science*, 371, 1046 [Cited on pages 37, 38, and 39.]
- Miniutti, G., & Fabian, A. C. 2004, *Monthly Notices of Royal Astronomical Society*, 349, 1435 [Cited on page 31.]
- Mitsuda, K., Inoue, H., Koyama, K., et al. 1984, *Publications of the Astronomical Society of Japan*, 36, 741 [Cited on page 59.]
- Montgomery, C., Orchiston, W., & Whittingham, I. 2009, *Journal of Astronomical History and Heritage*, 12, 90 [Cited on page 6.]
- Muñoz-Darias, T., Motta, S., & Belloni, T. M. 2011, *Monthly Notices of Royal Astronomical Society*, 410, 679 [Cited on pages xvi, 24, and 25.]
- Narayan, R., & Yi, I. 1995, *The Astrophysical Journal*, 452, 710 [Cited on page 17.]
- Niedźwiecki, A., Szanecki, M., & Zdziarski, A. A. 2019, *Monthly Notices of Royal Astronomical Society*, 485, 2942 [Cited on page 59.]
- Niedźwiecki, A., & Zdziarski, A. A. 2018, *Monthly Notices of the Royal Astronomical Society*, 477, 4269 [Cited on page 60.]
- Ninkov, Z., Walker, G. A. H., & Yang, S. 1987, *The Astrophysical Journal*, 321, 425 [Cited on pages 37 and 39.]

- Novick, R. 1975, *Space Science Reviews*, 18, 389 [Cited on pages 28 and 67.]
- Nowak, M. A. 2000, *Monthly Notices of Royal Astronomical Society*, 318, 361 [Cited on page 62.]
- Oda, M., Gorenstein, P., Gursky, H., et al. 1971, *The Astrophysical Journal Letters*, 166, L1 [Cited on page 46.]
- Oh, K., Koss, M., Markwardt, C. B., et al. 2018, *The Astrophysical Journal Supplement Series*, 235, 4 [Cited on page 114.]
- Oppenheimer, J. R., & Snyder, H. 1939, *Physical Review*, 56, 455 [Cited on page 7.]
- Oppenheimer, J. R., & Volkoff, G. M. 1939, *Physical Review*, 55, 374 [Cited on page 7.]
- Orosz, J. A., McClintock, J. E., Aufdenberg, J. P., et al. 2011, *The Astrophysical Journal*, 742, 84 [Cited on page 37.]
- Otte, N. 2006, in IX International Symposium on Detectors for Particle, Astroparticle and Synchrotron Radiation Experiments, SNIC Symposium, Stanford, California, 1–9 [Cited on page 154.]
- Paczynski, B. 1974, *Astronomy & Astrophysics*, 34, 161 [Cited on page 37.]
- Paul, B. 2013, *International Journal of Modern Physics D*, 22, 41009 [Cited on page 49.]
- Pence, W. D., Chiappetti, L., Page, C. G., Shaw, R. A., & Stobie, E. 2010, *Astronomy & Astrophysics*, 524, A42 [Cited on page 56.]
- Penrose, R. 1965, *Physical Review Letters*, 14, 57 [Cited on page 7.]
- Pottschmidt, K., Wilms, J., Nowak, M. A., et al. 2003a, *Astronomy & Astrophysics*, 407, 1039 [Cited on page 38.]
- . 2003b, *Astronomy & Astrophysics*, 407, 1039 [Cited on pages 141 and 142.]
- . 2003c, *Astronomy & Astrophysics*, 407, 1039 [Cited on page 141.]

- Prendergast, K. H., & Burbidge, G. R. 1968, *The Astrophysical Journal Letters*, 151, L83 [Cited on page 8.]
- Pringle, J. E., & Rees, M. J. 1972, *Astronomy & Astrophysics*, 21, 1 [Cited on pages 8 and 36.]
- Puls, J., Vink, J. S., & Najarro, F. 2008, *The Astronomy and Astrophysics Review*, 16, 209 [Cited on pages 2 and 39.]
- Ramadevi, M. C., Seetha, S., Bhattacharya, D., et al. 2017, *Experimental Astronomy*, 44, 11 [Cited on page 48.]
- Rees, M. J., & Gunn, J. E. 1974, *MNRAS*, 167, 1 [Cited on page 28.]
- Reid, M. J., McClintock, J. E., Narayan, R., et al. 2011, *The Astrophysical Journal*, 742, 83 [Cited on page 37.]
- Reig, P. 2011, *Astrophysics and Space Science*, 332, 1 [Cited on page 1.]
- Reis, R. C., Fabian, A. C., Ross, R. R., & Miller, J. M. 2009, *Monthly Notices of Royal Astronomical Society*, 395, 1257 [Cited on page 31.]
- Remillard, R. A., & McClintock, J. E. 2006, *Annual Review of Astronomy and Astrophysics*, 44, 49 [Cited on page 8.]
- Romero, G. E., Vieyro, F. L., & Chaty, S. 2014, *Astronomy & Astrophysics*, 562, L7 [Cited on page 36.]
- Roming, P. W. A., Kennedy, T. E., Mason, K. O., et al. 2005, *Space Science Reviews*, 120, 95 [Cited on page 53.]
- Russell, T. D., Soria, R., Miller-Jones, J. C. A., et al. 2014, *Monthly Notices of Royal Astronomical Society*, 439, 1390 [Cited on pages 40, 185, and 187.]
- Rybicki, G. B., & Lightman, A. P. 1985, *Radiative processes in astrophysics*. [Cited on page 28.]
- Salpeter, E. E. 1964, *The Astrophysical Journal*, 140, 796 [Cited on page 7.]
- Schatzman, E. L. 1958, *White dwarfs* [Cited on page 7.]

- Schmidt, M. 1963, *Nature*, 197, 1040 [Cited on page 7.]
- Schnittman, J. D., & Krolik, J. H. 2009, *The Astrophysical Journal*, 701, 1175 [Cited on page 31.]
- . 2010, *Astrophysical Journal*, 712, 908 [Cited on pages xvi, 32, 33, 35, and 149.]
- Schwarzschild, K. 1916, *Sitzungsberichte der Königlich Preußischen Akademie der Wissenschaften* (Berlin, 189 [Cited on page 6.]
- . 1999, arXiv e-prints, physics/9905030 [Cited on page 6.]
- Seward, F. D., & Charles, P. A. 2010, *Exploring the X-ray Universe* [Cited on page 45.]
- Shafee, R., McClintock, J. E., Narayan, R., et al. 2006a, *The Astrophysical Journal Letters*, 636, L113 [Cited on page 30.]
- . 2006b, *The Astrophysical Journal Letters*, 636, L113 [Cited on page 31.]
- Shakura, N. I., & Sunyaev, R. A. 1973, *Astronomy & Astrophysics*, 500, 33 [Cited on pages 3, 18, and 59.]
- Shapiro, S. L., & Teukolsky, S. A. 1983, *Black holes, white dwarfs, and neutron stars : the physics of compact objects* [Cited on page 30.]
- Shields, G. A. 1999, *Publications of the Astronomical Society of the Pacific*, 111, 661 [Cited on page 7.]
- Shionoya, S., Yen, W. M., & Yamamoto, H. 2018, *Phosphor handbook* (CRC press) [Cited on page 157.]
- Shipman, H. L. 1975, *Astrophysical Letters*, 16, 9 [Cited on page 8.]
- Shklovsky, I. S. 1967, *The Astrophysical Journal Letters*, 148, L1 [Cited on page 7.]
- Silver, E., Holley, J., Ziock, K., et al. 1990, *Optical Engineering*, 29, 759 [Cited on page 66.]

- Singh, K. P. 2022, arXiv e-prints, arXiv:2203.04610 [Cited on page 49.]
- Singh, K. P., Tandon, S. N., Agrawal, P. C., et al. 2014, in Society of Photo-Optical Instrumentation Engineers (SPIE) Conference Series, Vol. 9144, Society of Photo-Optical Instrumentation Engineers (SPIE) Conference Series [Cited on page 49.]
- Singh, K. P., Stewart, G. C., Chandra, S., et al. 2016, in Society of Photo-Optical Instrumentation Engineers (SPIE) Conference Series, Vol. 9905, Space Telescopes and Instrumentation 2016: Ultraviolet to Gamma Ray, ed. J.-W. A. den Herder, T. Takahashi, & M. Bautz, 99051E [Cited on pages 48 and 144.]
- Singh, K. P., Stewart, G. C., Westergaard, N. J., et al. 2017, *Journal of Astrophysics and Astronomy*, 38, 29 [Cited on pages 48 and 144.]
- Stark, R. F., & Connors, P. A. 1977, *Nature*, 266, 429 [Cited on page 62.]
- Stiele, H., Yu, W., & Kong, A. K. H. 2016, *The Astrophysical Journal*, 831, 34 [Cited on page 60.]
- Stirling, A. M., Spencer, R. E., de la Force, C. J., et al. 2001, *Monthly Notices of Royal Astronomical Society*, 327, 1273 [Cited on page 38.]
- Strickman, M. S., Johnson, W. N., & Kurfess, J. D. 1979, *The Astrophysical Journal Letters*, 230, L15 [Cited on page 123.]
- Sunyaev, R. A., & Titarchuk, L. G. 1980, *Astronomy & Astrophysics*, 86, 121 [Cited on page 148.]
- Sunyaev, R. A., & Truemper, J. 1979, *Nature*, 279, 506 [Cited on page 148.]
- Tan, C. 2021, *Journal of Physics: Conference Series*, 2012, 012119 [Cited on page 1.]
- Tananbaum, H., Gursky, H., Kellogg, E., & Giacconi, R. 1971, *The Astrophysical Journal Letters*, 168, L25 [Cited on page 46.]
- Tananbaum, H., Gursky, H., Kellogg, E., Giacconi, R., & Jones, C. 1972, *The Astrophysical Journal Letters*, 177, L5 [Cited on page 23.]

- Tandon, S. N., Subramaniam, A., Girish, V., et al. 2017, *The Astronomical Journal*, 154, 128 [Cited on page 48.]
- Terrell, N. James, J. 1972, *The Astrophysical Journal Letters*, 174, L35 [Cited on pages 17 and 23.]
- Tetarenko, B. E., Sivakoff, G. R., Heinke, C. O., & Gladstone, J. C. 2016a, *The Astrophysical Journal Supplement Series*, 222, 15 [Cited on page 13.]
- . 2016b, *The Astrophysical Journal Supplement Series*, 222, 15 [Cited on page 15.]
- Thorne, K. S. 1974, *The Astrophysical Journal*, 191, 507 [Cited on page 4.]
- Thorne, K. S., & Price, R. H. 1975, *The Astrophysical Journal Letters*, 195, L101 [Cited on page 8.]
- Toraskar, J. R. 1975, *Applied Optics*, 14, 1727 [Cited on page 66.]
- Trimble, V., Rose, W. K., & Weber, J. 1973, *Monthly Notices of Royal Astronomical Society*, 162, 1P [Cited on page 37.]
- Tsunemi, H., Hayashida, K., Tamura, K., et al. 1992, *Nuclear Instruments and Methods in Physics Research A*, 321, 629 [Cited on page 68.]
- Uttley, P., McHardy, I. M., & Vaughan, S. 2005, *Monthly Notices of Royal Astronomical Society*, 359, 345 [Cited on page 17.]
- Vadawale, S. V., Chattopadhyay, T., & Pendharkar, J. 2012, in *Society of Photo-Optical Instrumentation Engineers (SPIE) Conference Series*, Vol. 8443, *Society of Photo-Optical Instrumentation Engineers (SPIE) Conference Series* [Cited on page 123.]
- Vadawale, S. V., Chattopadhyay, T., Rao, A. R., et al. 2015, *Astronomy & Astrophysics*, 578, A73 [Cited on pages 50, 72, 74, 78, 81, 82, and 116.]
- Vadawale, S. V., Rao, A. R., & Chakrabarti, S. K. 2001, *Astronomy & Astrophysics*, 372, 793 [Cited on pages 5, 36, and 177.]

- Vadawale, S. V., Rao, A. R., Bhattacharya, D., et al. 2016, in Society of Photo-Optical Instrumentation Engineers (SPIE) Conference Series, Vol. 9905, Space Telescopes and Instrumentation 2016: Ultraviolet to Gamma Ray, ed. J.-W. A. den Herder, T. Takahashi, & M. Bautz, 99051G [Cited on pages 48 and 49.]
- Vadawale, S. V., Chattopadhyay, T., Mithun, N. P. S., et al. 2018, *Nature Astronomy*, 2, 50 [Cited on pages 63, 72, 74, 78, 81, 82, and 116.]
- Vaishnava, C. S., Mithun, N. P. S., Vadawale, S. V., et al. 2022, *Journal of Astronomical Telescopes, Instruments, and Systems*, 8, 038005 [Cited on page 131.]
- van der Klis, M. 1989, in NATO Advanced Study Institute (ASI) Series C, Vol. 262, Timing Neutron Stars, ed. H. Ögelman & E. P. J. van den Heuvel, 27 [Cited on page 60.]
- van der Klis, M. 1997, in *Statistical Challenges in Modern Astronomy II*, ed. G. J. Babu & E. D. Feigelson, 321 [Cited on page 62.]
- van Paradijs, J., & McClintock, J. E. 1995, in *X-ray Binaries*, 58–125 [Cited on pages 29 and 42.]
- Vaughan, S., Edelson, R., Warwick, R. S., & Uttley, P. 2003, *Monthly Notices of Royal Astronomical Society*, 345, 1271 [Cited on page 62.]
- Walton, D. J., Tomsick, J. A., Madsen, K. K., et al. 2016, *The Astrophysical Journal*, 826, 87 [Cited on page 38.]
- Wang, Y., Guo, J., Li, G., Roussos, E., & Zhao, J. 2022, *The Astrophysical Journal*, 928, 157 [Cited on page 121.]
- Webster, B. L., & Murdin, P. 1972, *Nature*, 235, 37 [Cited on pages 8 and 36.]
- Weisskopf, M. C., Cohen, G. G., Kestenbaum, H. L., et al. 1976, *Astrophysical Journal Letter*, 208, L125 [Cited on pages 63 and 67.]
- Weisskopf, M. C., Elsner, R. F., Hanna, D., et al. 2006, ArXiv Astrophysics e-prints, astro-ph/0611483 [Cited on page 28.]

- Wilms, J., Allen, A., & McCray, R. 2000, *The Astrophysical Journal*, 542, 914 [Cited on page 58.]
- Wilms, J., Pottschmidt, K., Nowak, M. A., et al. 2004, in American Institute of Physics Conference Series, Vol. 714, X-ray Timing 2003: Rossi and Beyond, ed. P. Kaaret, F. K. Lamb, & J. H. Swank, 116–119 [Cited on page 146.]
- Wilson, C. A., Finger, M. H., & Camero-Arranz, A. 2008, *The Astrophysical Journal*, 678, 1263 [Cited on page 15.]
- Winkler, C., Courvoisier, T. J. L., Di Cocco, G., et al. 2003, *Astronomy & Astrophysics*, 411, L1 [Cited on page 133.]
- Wolfe, A. M., & Burbidge, G. R. 1970, *The Astrophysical Journal*, 161, 419 [Cited on page 8.]
- Wonders, Marc A., Chichester, David L., & Flaska, Marek. 2018, EPJ Web Conf., 170, 07015 [Cited on page 156.]
- Yadav, J. S., Misra, R., Verdhan Chauhan, J., et al. 2016a, *The Astrophysical Journal*, 833, 27 [Cited on pages 48, 140, and 144.]
- Yadav, J. S., Agrawal, P. C., Antia, H. M., et al. 2016b, in Society of Photo-Optical Instrumentation Engineers (SPIE) Conference Series, Vol. 9905, Space Telescopes and Instrumentation 2016: Ultraviolet to Gamma Ray, ed. J.-W. A. den Herder, T. Takahashi, & M. Bautz, 99051D [Cited on pages 48, 140, and 144.]
- Yan, Z., & Yu, W. 2015, *The Astrophysical Journal*, 805, 87 [Cited on page 15.]
- Ye, Y., Zou, H., Zong, Q., et al. 2017, *Space Weather*, 15, 1548 [Cited on page 116.]
- Young, A. J., Fabian, A. C., Ross, R. R., & Tanaka, Y. 2001, *Monthly Notices of Royal Astronomical Society*, 325, 1045 [Cited on page 22.]
- Zdziarski, A. A., & Gierliński, M. 2004, *Progress of Theoretical Physics Supplement*, 155, 99 [Cited on page 31.]

- Zdziarski, A. A., Johnson, W. N., & Magdziarz, P. 1996, *Monthly Notices of Royal Astronomical Society*, 283, 193 [Cited on page 59.]
- Zdziarski, A. A., Pjanka, P., Sikora, M., & Stawarz, L. 2014, MNRAS, 442, 3243 [Cited on page 40.]
- Zdziarski, A. A., Skinner, G. K., Pooley, G. G., & Lubiński, P. 2011, *Monthly Notices of Royal Astronomical Society*, 416, 1324 [Cited on page 133.]
- Zdziarski, A. A., Szanecki, M., Poutanen, J., Gierliński, M., & Biernacki, P. 2020, *Monthly Notices of Royal Astronomical Society*, 492, 5234 [Cited on page 60.]
- Zeldovich, Y. B., & Guseynov, O. H. 1966, *The Astrophysical Journal*, 144, 840 [Cited on page 46.]
- Zhang, S. N., Cui, W., & Chen, W. 1997, *The Astrophysical Journal Letters*, 482, L155 [Cited on page 30.]
- Życki, P. T., Done, C., & Smith, D. A. 1999, *Monthly Notices of Royal Astronomical Society*, 309, 561 [Cited on page 59.]